Title

Biohybrid Microrobots: Design, Fabrication, Characterization and Applications

Author

Zhang, Fangyu

Publication Date

2022

UNIVERSITY OF CALIFORNIA SAN DIEGO

Biohybrid Microrobots:

Design, Fabrication, Characterization and Applications

A Dissertation submitted in partial satisfaction of the requirements for the degree

Doctor of Philosophy

in

NanoEngineering

by

Fangyu Zhang

Committee in charge:

Professor Joseph Wang, Chair
Professor Liangfang Zhang, Co-Chair
Professor Shengqiang Cai
Professor Nicole Steinmetz
Professor Michael Tolley

2022

The Dissertation of Fangyu Zhang is approved, and it is acceptable in quality and form for publication on microfilm and electronically.

University of California San Diego

2022

DEDICATION

To my mom and dad

TABLE OF CONTENTS

LIST OF FIGURES

ACKNOWLEDGEMENTS

I would first like to offer my sincerest thanks and praise to my advisor, Professor Joseph Wang. I heard of his research and learned about his papers when I was doing my Master's at Cornell. His tremendous work on micromotors which can autonomously move by harvesting the energy from the surroundings inspired me to step into such a fantastic micro world. It was one of the most exciting moments in my life when he offered me an incredible opportunity to complete my Ph.D. study with him on 1st November 2017. Starting from that date, he gave me immense guidance, encouragement, and inspiration to lead me toward the success of the research. Over the past 5 years, he taught me everything about how to be a successful scientific researcher including conceptualization, experimental design, formal analysis, writing, communication, team building, and collaboration. He has motivated me and helped me achieve more than I ever could have imagined as a graduate student because of the passion and commitment he put into his students. His dedication to the pursuit of knowledge, innovation, and true findings always influences my attitude and sense toward the beauty of science and inspires me to be a great scientist like him.

I would like to thank Prof. Liangfang Zhang, who is my co-advisor and main collaborator. His great mind and deep insights encourage me to chase and deal with the grand challenges in the field. His useful suggestions, constructive criticism, and encouraging words always drag me out of the stuck and guide me in the right direction when I was frustrated by the project delays. His magnificent vision and foresight not only open my mind to a new scientific world but also give me significant support in my career development.

During the past 5 years of study at UCSD, I went through an extraordinary life and met many great people whom I learned and worked with. I would thank Berta Esteban Fernandes de Avila for her great help and extreme devotion to many challenging projects. I would give a special thanks to Jia Zhuang for his passion and spirit which encourage me to tackle difficulties boldly. It was the best memory to discuss projects and life with him. I acknowledge Zhengxing Li, who worked with me on several projects, for his endeavors to keep pushing forward. I would also be appreciative of the friendship and collaboration with Lu Yin, Songsong Tang, Yaou Duan, Emil Karshalev, Rodolfo Mundaca-Uribe, Hazhir Teymourian, Farshad Tehrani, Hua Gong, Qiangzhe Zhang, Fernando Soto, Hao Luan, Chuanrui Chen, Zhongyuan Guo, Zhidong Zhou, Ronnie Fang, Weiwei Gao and many more graduate students and postdocs for their outstanding contribution to various projects.

I would also like to thank my committee, Professor Shengqiang Cai, Professor Nicole Steinmetz, and Professor Michael Tolley, who gave me support and guidance. I thank Professor Victor Nizet for his helpful and valuable advice in solving the challenges. I highly appreciate Prof. Tao Deng and Prof. Jiajun Gu, who were my advisers in my undergraduate study, for giving me generous support throughout my academic career.

Finally, I would like to give the utmost thanks to my mother and father. I can’t complete the Ph.D. study and stand here without your endless support and love.

Chapter 1.1 is based, in part, on the material as it appears in Chemical Reviews, 2021, by Fernando Soto, Emil Karshalev, Fangyu Zhang, Berta Esteban Fernandez de Avila, Amir Nourhani, and Joseph Wang. The dissertation author was the primary investigator and author of this paper.

Chapter 1.3 is based, in part, on the material as it appears in Advanced Materials, 2021, by Fangyu Zhang, Rodolfo Mundaca-Uribe, Nelly Askarinam, Zhengxing Li, Weiwei Gao, Liangfang Zhang, Joseph Wang. The dissertation author was the primary investigator and author of this paper.

Chapter 2.1, in full, is a reprint of the material as it appears in Nature Materials, 2022, by Fangyu Zhang, Jia Zhuang, Zhengxing Li, Hua Gong, Berta Esteban-Fernández de Ávila, Yaou Duan, Qiangzhe Zhang, Jiarong Zhou, Lu Yin, Emil Karshalev, Weiwei Gao, Victor Nizet, Ronnie H. Fang, Liangfang Zhang, Joseph Wang. The dissertation author was the primary investigator and author of this paper.

Chapter 2.2, in full, is a reprint of the material as it appears in Science Robotics, 2022, by Fangyu Zhang, Zhengxing Li, Yaou Duan, Amal Abbas, Rodolfo Mundaca-Uribe, Lu Yin, Hao Luan, Weiwei Gao, Ronnie H. Fang, Liangfang Zhang, Joseph Wang. The dissertation author was the primary investigator and author of this paper.

Chapter 2.3, in full, is a reprint of the material as it may appear in Science Advances, 2022, by Fangyu Zhang, Zhengxing Li, Yaou Duan, Hao Luan, Lu Yin, Zhongyuan Guo, Chuanrui Chen, Mingyao Xu, Weiwei Gao, Ronnie H. Fang, Liangfang Zhang, Joseph Wang. The dissertation author was the primary investigator and author of this paper.

Chapter 2.4, in full, is a reprint of the material as it appears in Journal of the American Chemical Society, 2021, by Fangyu Zhang, Zhengxing Li, Lu Yin, Qiangzhe Zhang, Nelly Askarinam, Rodolfo Mundaca-Uribe, Emil Karshalev, Weiwei Gao, Liangfang Zhang, Joseph Wang. The dissertation author was the primary investigator and author of this paper.

Chapter 3.1, in full, is a reprint of the material as it appears in Advanced Materials, 2019, by Fangyu Zhang, Rodolfo Mundaca-Uribe, Hua Gong, Berta Esteban-Fernández de Ávila, Mara Beltrán-Gastélum, Emil Karshalev, Amir Nourhani, Yao Tong, Bryan Nguyen, Mathieu Gallot, Yue Zhang, Liangfang Zhang, Joseph Wang. The dissertation author was the primary investigator and author of this paper.

Chapter 3.2, in full, is a reprint of the material as it appears in Science Robotics, 2020, by Songsong Tang, Fangyu Zhang, Hua Gong, Fanan. Wei, Jia. Zhuang, Emil Karshalev, Berta Esteban-Fernández de Ávila, Chuying Huang, Zhidong Zhou, Zhengxing Li, Lu Yin, Haifeng Dong, Ronnie H. Fang, Xueji Zhang, Liangfang Zhang, Joseph Wang. The dissertation author was the primary investigator and author of this paper.

Chapter 3.3, in full, is a reprint of the material as it appears in ACS Nano, 2019, by Fangyu Zhang, Jia. Zhuang, Berta Esteban-Fernández de Ávila, Songsong Tang, Qiangzhe Zhang, Ronnie H. Fang, Liangfang Zhang, Joseph Wang. The dissertation author was the primary investigator and author of this paper.

Chapter 4.2 is based, in part, on the material as it appears in Advanced Materials, 2021, by Fangyu Zhang, Rodolfo Mundaca-Uribe, Nelly Askarinam, Zhengxing Li, Weiwei Gao, Liangfang Zhang, Joseph Wang. The dissertation author was the primary investigator and author of this paper.

VITA

2013 Bachelor of Science, Shanghai Jiao Tong University

2016 Master of Science, Cornell University

2022 Doctor of Philosophy, University of California San Diego

PUBLICATIONS

1. **F. Zhang**, J. Zhuang, Z. Li, H. Gong, B. E. Ávila, Y. Duan, Q. Zhang, J. Zhou, L. Yin, E. Karshalev, W. Gao, V. Nizet, R. H. Fang, L. Zhang, J. Wang. Nanoparticle-modified microrobots for in vivo antibiotic delivery to treat acute bacterial pneumonia. **Nature Materials** 2022, 21, 1324.

2. **F. Zhang**, Z. Li, Y. Duan, A. Abbas, R. Mundaca-Uribe, L. Yin, H. Luan, W. Gao, R. H. Fang, L. Zhang, J. Wang. Algae Motors in a Capsule for Effective Gastrointestinal Delivery. **Science Robotics** 2022, 7, eabo4160.

3. **F. Zhang**, Z. Li, Y. Duan, H. Luan, L. Yin, Z. Guo, C. Chen, M. Xu, W. Gao, R. H. Fang, L. Zhang, J. Wang. Extremophile-based biohybrid micromotors for biomedical operations in harsh environments. **Science Advances** 2022, in press.

4. **F. Zhang**, Z. Li, L. Yin, Q. Zhang, N. Askarinam, R. Mundaca-Uribe, E. Karshalev, W. Gao, L. Zhang, J. Wang. ACE2 receptor-modified algae-based microrobot for removal of SARS-CoV-2 in wastewater. **Journal of the American Chemical Society** 2021, 143, 12194.

5. **F. Zhang**, R. Mundaca-Uribe, N. Askarinam, Z. Li, W. Gao, L. Zhang, J. Wang. Biomembrane-Functionalized Micromotors: Biocompatible Active Devices for Diverse Biomedical Applications. **Advanced Materials** 2021, 34, 2107177.

6. S. Tang, **F. Zhang**, H. Gong, F. Wei, J. Zhuang, E. Karshalev, B. E. Ávila, C. Huang, Z. Zhou, Z. Li, L. Yin, H. Dong, R. H. Fang, X. Zhang, L. Zhang, J. Wang. Enzyme-powered Janus platelet cell robots for active and targeted drug delivery. **Science Robotics** 2020, 5, eaba6137.

7. **F. Zhang**, R. Mundaca-Uribe, H. Gong, B. E. Ávila, M. B. Gastelum, E. Karshalev, A. Nourhani, Y. Tong, B. Nguyen, M. Gallot, Y. Zhang, L. Zhang, J. Wang. A macrophage–magnesium hybrid biomotor: fabrication and characterization. **Advanced Materials** 2019, 31, 1901828.

8. **F. Zhang**, J. Zhuang, B. E. Ávila, S. Tang, Q. Zhang, R. H. Fang, L. Zhang, J. Wang. A nanomotor-based active delivery system for intracellular oxygen transport. **ACS Nano** 2019, 13, 11996.

9. F. Soto, E. Karshalev, **F. Zhang**, B. E. Avila, A. Nourhani, J. Wang*. Smart Materials for Microrobots. **Chemical Reviews** 2022, 122, 5365.

FIELD OF STUDY

Major Field: Nanoengineering, Bioengineering and Materials Science

Studies in Nanoengineering

Professors Joseph Wang and Liangfang Zhang

ABSTRACT OF THE DISSERTATION

Biohybrid Microrobots:

Design, Fabrication, Characterization and Applications

by

Fangyu Zhang

Doctor of Philosophy in NanoEngineering

University of California San Diego, 2022

Professor Joseph Wang, Chair
Professor Liangfang Zhang, Co-Chair

Bioinspired microrobots capable of actively moving in biological fluids have attracted considerable attention for biomedical applications because of their unique dynamic features that are otherwise difficult to achieve by their static counterparts. This thesis is dedicated to extending the current microrobotics by utilizing natural cells as the basic elements to design biohybrid microrobots and apply them in diverse biomedical and environmental applications. The first section demonstrates the feasibility to combine natural cell-based materials (e.g. microalgae and blood cell) with synthetic components to fabricate biohybrid microrobots towards versatile applications. The second section focuses on design and fabrication of different types of microalgae-based biohybrid microrobots with efficient autonomous motion, effective cargo loading, long lifespan, adaptable utilization and biological function towards operation in different body locations, such as lung, small intestine and stomach. It further explores the possibility of functional algae-based microrobots to perform versatile tasks including pulmonary infection treatment, targeted GI delivery and virus detoxification. The third section explores the use of blood cell as the main composition to establish biohybrid microrobots. By replicating and inheriting the intrinsic biological functions of the cells, the new cell-based microrobots can be applied to neutralize lipopolysaccharide, deliver antibacterial and anticancer drugs, transport oxygen to treat hypoxia. The biohybrid microrobot platform described in this thesis creates new opportunities in the development of autonomous drug delivery vehicles for treating many diseases.

Chapter 1. Introduction

1.1 Opportunities for small scale robotics

Robots have been a transformative force to society by enhancing our capabilities beyond biological limitations and by providing a better life quality for the world population.[1–3] For example, the Da Vinci surgical system operates inside patients with more precision than a freehand physician.[4] Moreover, robots are fundamental to the exploration of extreme environments such as the current NASA Rover.[5] While certain technological advances in materials development have resulted in lightweight yet strong macroscale structures with superior performance, the majority of improvement has been on the software side. On the hardware side, current robotic designs consist of an assembly of discrete mechanical and electronic components with individually prescribed functionalities. Such macroscale robots mainly rely on operator inputs or artificial intelligence software to adapt to their ever-changing environmental conditions. Nature, on the other hand, programs adaptability and multifunctionality directly in the constituent materials. For example, microorganisms contain the necessary tools to adapt to and function in dynamically varying environments and replicate and synthesize an assembly of molecules and cells.[6–8] Inspired by microorganisms, we can learn from nature how to develop cell-sized robots furnished with their own propulsion, intelligence, programmability, and adaptability to the environment.

Tremendous progress in developing synthetic micromotors based on different propulsion mechanisms and designs has been achieved in the last decade.[9-12] Powered by local fuels or external forces, artificial micromotors have been shown to navigate in biological fluids while performing diverse tasks connected to critical biomedical applications ranging from targeted drug delivery to precision surgery. This impressive progress has placed synthetic micromotors at the forefront of biomedical research.[13,14] While several initial successful in vivo animal tests have been reported,[15-17] key challenges need to be addressed before micromotors can be safely and efficiently applied in living systems and translated to practical applications. The performance and effectiveness of these micromotors rely largely on synthetic materials, which are susceptible to immune response and biofouling process in complex biological systems. Practical in vivo applications of synthetic micromotors thus require biocompatible and biomimetic designs, capable of prolonged and efficient operation in the physiological environment without producing any unintended harmful consequences.

1.2 Microalgae-based biohybrid microrobots

Despite the distinct advantages of synthetic micromotors, key challenges, such as improvement of the propulsion in complex biofluid, collective actuation for targeted drug delivery, and realization of fuel-free movement, need to be addressed further towards their practical in vivo operations. Nature has provided us with many examples of realizing collective motion behavior. For example, living microorganisms can efficiently propel in biofluid and complete versatile tasks in a collective mode. Learning from nature, biohybrid micromotors—coupling natural microorganisms (e.g., sperm, bacteria, and microalgae) with artificial substrates—were fabricated in recent years to produce biofunctional devices with new and improved capabilities.[18-22] Among them, magnetic field-driven sperm can be controlled to swim toward an egg for assisted fertilization.[18] Magneto-aerotactic bacteria carrying drug-loaded liposomes has been delivered to tumor hypoxic regions.[20] Phototactic algae were steered under visible light to collectively self-propel for on-demand cargo delivery.[22] Looking forward, the integration of multifunctionality, versatility, and adaptivity of cell membranes with the smart behavior of natural micromotors and the efficient propulsion of synthetic micromotors, will create powerful biohybrid systems with expanded capabilities towards diverse in-vitro and in-vivo operations. Such developments of biomimetic micromotors require close collaborative efforts among researchers from different disciplines. The new capabilities of cell membrane-functionalized micromotors are expected to advance the fields of micromotors and nanomedicine.

Algae are a diverse group of photosynthetic organisms that live primarily in freshwater and marine environments. They are high in photosynthetic pigments like chlorophyll, which can trap light energy from the sun, convert it to chemical energy, and store it as photosynthesis products. These organisms are thought to be among the fastest-growing creatures due to their highly efficient photosynthesis. As a result, algae are abundant in nature and are regarded as a significant source of free oxygen in the atmosphere. Microalgae are currently gaining popularity due to their extensive application potential in the renewable energy, food production, and healthcare industries. Microalgae's distinct morphological characteristics and easily functionalized surfaces enable the attachment of diagnostic or therapeutic agents to their surfaces, making them promising candidates for the development of novel biochemical probes, drug carriers, or biomedical scaffolds.

In the Chapter 2, a thorough discussion of algae-based biohybrid microrobots, ranging from design, fabrication, and applications, will be presented. To achieve the goal, we take a critical look at the existing algae-based technology and highlight the foundation of algae-based biohybrid microrobots from three aspects: inherent properties of microalgae, functionalization of microalgae to form biohybrid systems, and versatile applications using as-fabricated biohybrid microrobots (Fig. 1.1). First, we explain the locomotion modalities of the algae in order to provide an understanding of motility and actuation in the microscopic world. Next, we critically review the desired properties of the artificial constructs and the approaches used to integrate them into the microorganisms. Finally, we describe the important biohybrid microrobot designs used in biomedical and environmental applications and discuss key challenges for improving the concept of biohybrid microrobots.

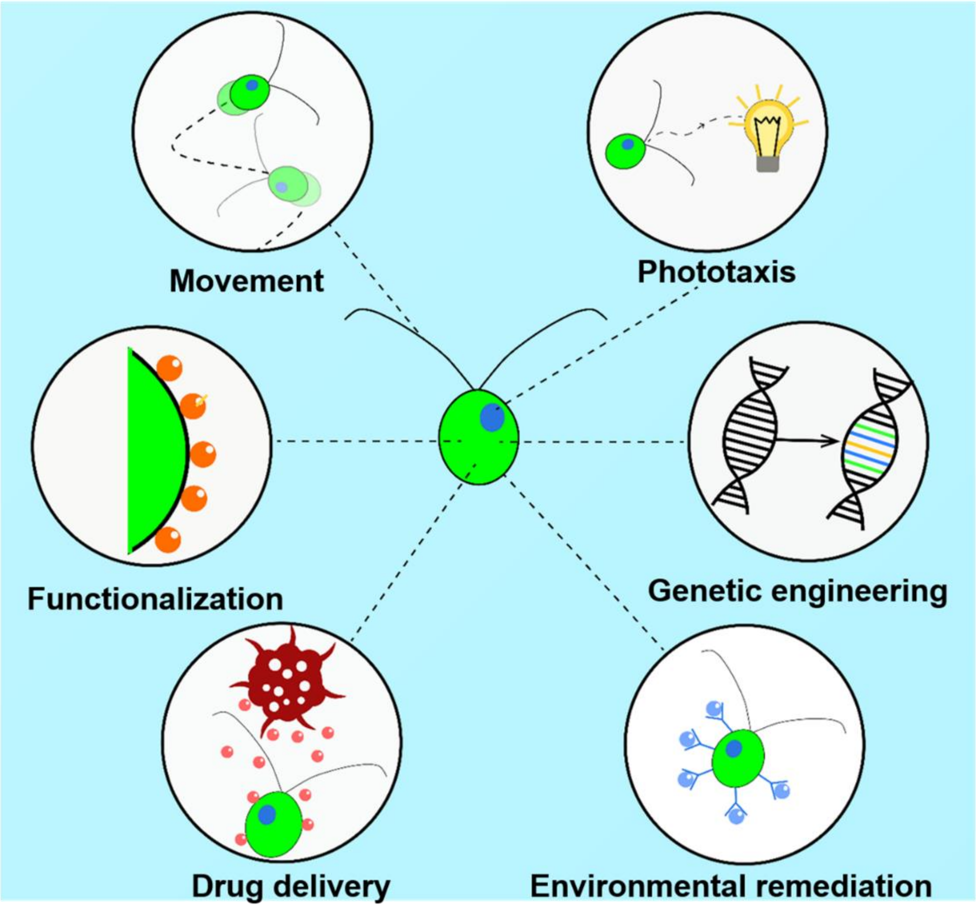

Figure 1.1 Fundamental of microalgae-based micromotors.

1.3 Blood cell-based biohybrid microrobots

Combining the advantages of the dynamic movement of synthetic motors with the versatility and unique biological functions of natural cells leads to cell-like micromotors that enable new opportunities for overcoming many obstacles that synthetic motors currently face in numerous biomedical operations.[17] By taking inspiration from nature, essential biological functions of natural blood cells, such as immune stealth, faithful antigen presentation, cell- or tissue-specific targeting, and selective binding with bacterial toxins or pathogens, can thus be harnessed and imparted to mobile synthetic microsystems. Cell membrane coating also represents a powerful top-down approach for replicating complex protein profiles and biological functions of host cell membrane that are otherwise impractical to achieve with bottom-up synthetic approaches. The cell membrane-synthetic motor coupling results in novel active biocompatible devices, offering synergistic functionalities and new capabilities for a broad range of applications. In particular, recent attention has been given to cell membrane-functionalized micromotors.

In this Chapter 3, the preparation, unique capabilities, and advantages of biomimetic micromotors will be discussed by leveraging the attractive properties of whole cell and cell membrane-derived biomaterials and dynamic synthetic micromotors. Cellular membranes play crucial roles in the interface of cells with their complex surrounding biological environment.[23] The use of natural cell membranes to functionalize micromotors has been shown recently to address major barriers (e.g., biofouling) that hinder in vivo operations of synthetic motors while rendering them with a wide range of new properties and unique capabilities that greatly enhance their performance in biological systems. For instance, the cell membrane-functionalized micromotors can achieve prolonged propulsion in complex biofluids and efficient neutralization of harmful agents through the cell membrane receptors. This new class of biomimetic microscale motors thus combines the merits of synthetic motors with those of natural cell membranes. The diversity of different types of cell membranes and their associated biological functionalities enables the development of numerous biomimetic micromotor platforms with broad applicability. The judicious coupling of these different types of cell membranes with various types of synthetic micromotors has shown robust utility, including active and targeted drug delivery, biodetoxification, immune modulation, and photothermal therapy (Fig. 1.2). As a result, the cell membrane functionalization bestows artificial motors with superb biocompatibility that enables the advancement of micromotor research from laboratory test-tubes to whole living systems. These developments, unique capabilities, and representative applications of cell membrane-functionalized micromotors are reviewed in the following sections, along with the discussion on prospects and new opportunities.

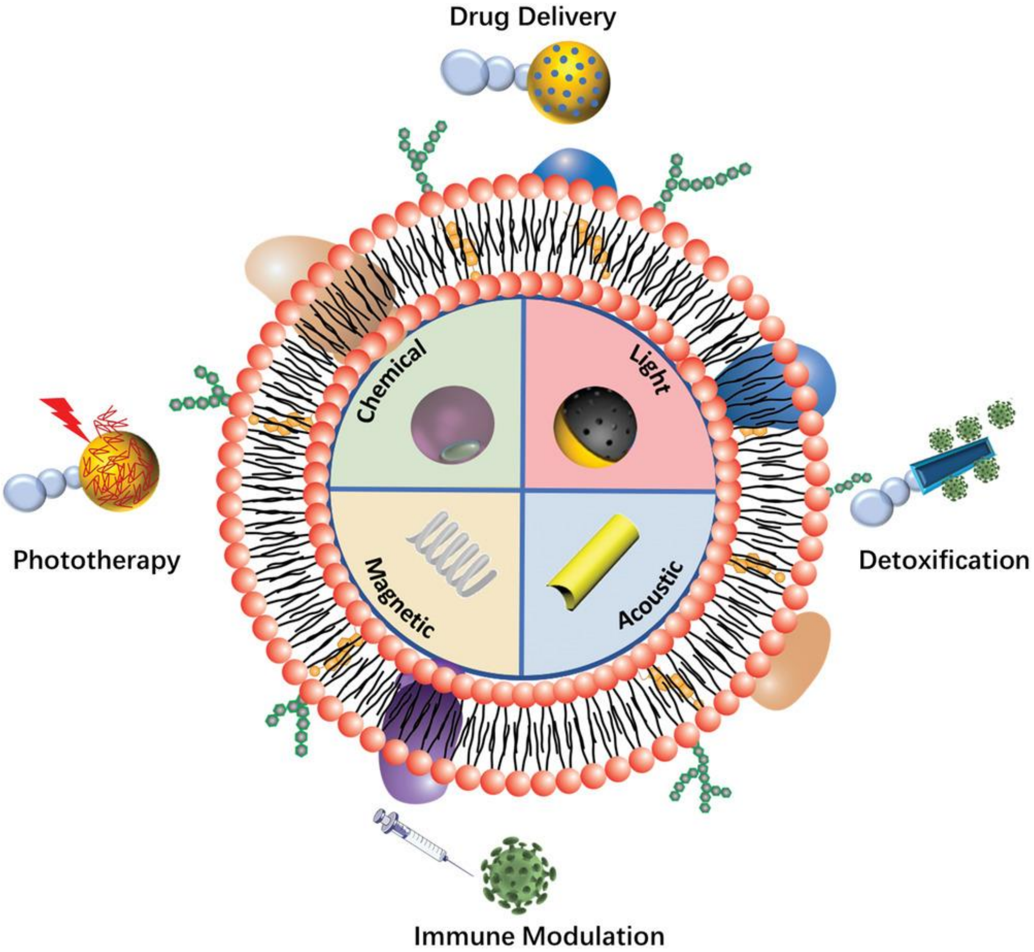

Figure 1.2 Cell membrane-functionalized micromotors for biomedical applications. Schematic illustration of a wide range of synthetic micromotors based on different propulsion mechanisms (inner) that are functionalized with various types of cell membranes (middle) for a variety of biomedical applications, including drug delivery, detoxification, immune modulation, and phototherapy (outer).

Chapter 1.1 is based, in part, on the material as it appears in Chemical Reviews, 2021, by Fernando Soto, Emil Karshalev, Fangyu Zhang, Berta Esteban Fernandez de Avila, Amir Nourhani, and Joseph Wang. The dissertation author was the primary investigator and author of this paper.

Chapter 1.3 is based, in part, on the material as it appears in Advanced Materials, 2021, by Fangyu Zhang, Rodolfo Mundaca-Uribe, Nelly Askarinam, Zhengxing Li, Weiwei Gao, Liangfang Zhang, Joseph Wang. The dissertation author was the primary investigator and author of this paper.

1.4 References

1. Cianchetti, M.; Laschi, C.; Menciassi, A.; Dario, P. Biomedical Applications of Soft Robotics. *Nat. Rev. Mater.* **3**, 143– 153 (2018).

2. Rich, S. I.; Wood, R. J.; Majidi, C. Untethered Soft Robotics. *Nat. Electron.* **1**, 102– 112 (2018).

3. Yang, G. Z.; Bellingham, J.; Dupont, P. E.; Fischer, P.; Floridi, L.; Full, R.; Jacobstein, N.; Kumar, V.; McNutt, M.; Merrifield, R.; Nelson, B. J.; Scassellati, B.; Taddeo, M.; Taylor, R.; Veloso, M.; Wang, Z. L.; Wood, R. The Grand Challenges of Science Robotics. *Sci. Robot.* **3**, eaar7650 (2018).

4. Ngu, J.; Tsang, C.; Koh, D. The Da Vinci Xi: A Review of Its Capabilities, Versatility, and Potential Role in Robotic Colorectal Surgery. *Robot. Surg. Res. Rev.* **4**, 77– 85 (2017).

5. Chien, S.; Wagstaff, K. L. Robotic Space Exploration Agents. *Sci. Robot.* **2**, 4831 (2017).

6. Xia, F.; Jiang, L. Bio-Inspired, Smart, Multiscale Interfacial Materials. *Adv. Mater.* **20**, 2842–2858 (2008).

7. Fu, F.; Shang, L.; Chen, Z.; Yu, Y.; Zhao, Y. Bioinspired Living Structural Color Hydrogels. *Sci. Robot.* **3**, eaar8580 (2018).

8. Wegst, U. G. K.; Bai, H.; Saiz, E.; Tomsia, A. P.; Ritchie, R. O. Bioinspired Structural Materials. *Nat. Mater.* **14**, 23– 36 (2015).

9. Wang, J Nanomachines: Fundamentals and Applications, Wiley-VCH, Weinheim, Germany 2013.

10. Wang, Q.; Zhang, L. External power-driven microrobotic swarm: from fundamental understanding to imaging-guided delivery. *ACS Nano* **15**, 149 (2021).

11. Wang, H.; Pumera, M. Fabrication of micro/nanoscale motors. *Chem. Rev.* **115**, 8704 (2015).

12. Wang, J.; Gao, W. Nano/microscale motors: biomedical opportunities and challenges. *ACS Nano* **6**, 5745 (2012).

13. Li, J.; de Ávila, B. E.-F.; Gao, W.; Zhang, L.; Wang, J. Micro/nanorobots for biomedicine: Delivery, surgery, sensing, and detoxification. *Sci. Robot.* **2**, eaam6431 (2017).

14. Tottori, S.; Zhang, L.; Qiu, F.; Krawczyk, K. K.; Franco-Obregón, A.; Nelson, B. J. Magnetic helical micromachines: fabrication, controlled swimming, and cargo transport. *Adv. Mater.* **24**, 811 (2012).

15. de Ávila, B. E.-F.; Angsantikul, P.; Li, J.; Gao, W.; Zhang, L.; Wang, J. Micromotors go in vivo: from test tubes to live animals. *Adv. Funct. Mater.* **28,** 1705640 (2018).

16. de Ávila, B. E.-F.; Angsantikul, P.; Li, J.; Angel Lopez-Ramirez, M.; Ramírez-Herrera, D. E.; Thamphiwatana, S.; Chen, C.; Delezuk, J.; Samakapiruk, R.; Ramez, V.; Zhang, L.; Wang, J. Micromotor-enabled active drug delivery for in vivo treatment of stomach infection. *Nat. Commun.* **8**, 272 (2017).

17. de Ávila, B. E.-F.; Gao, W.; Karshalev, E.; Zhang, L.; Wang, J. Cell-like micromotors. *Acc. Chem. Res.* **51**, 1901 (2018).

18. Medina-Sanchez, M.; Schwarz, L.; Meyer, A. K.; Hebenstreit, F.; Schmidt, O. G. Cellular cargo delivery: Toward assisted fertilization by sperm-carrying micromotors. *Nano Lett.* **16**, 555 (2016).

19. Singh, A. V.; Hosseinidoust, Z.; Park, B. W.; Yasa, O.; Sitti, M. Microemulsion-based soft bacteria-driven microswimmers for active cargo delivery. *ACS Nano* **11**, 9759 (2017).

20. Felfoul, O.; Mohammadi, M.; Taherkhani, S.; De Lauauze, D.; Xu, Y. Z.; Loghin, D.; Essa, S.; Jancik, S.; Houle, D.; Lafleur, M.; Gaboury, L.; Tabrizian, M.; Kaou, N.; Atkin, M.; Vuong, T.; Batist, G.; Beauchemin, N.; Radzioch, D.; Martel, S. Magneto-aerotactic bacteria deliver drug-containing nanoliposomes to tumour hypoxic regions. *Nat. Nanotechnol.* **11**, 941 (2016).

21. Weibel, D. B.; Garstecki, P.; Ryan, D.; Diluzio, W. R.; Mayer, M.; Seto, J. E.; Whitesides, G. M. Microoxen: Microorganisms to move microscale loads. *Proc. Natl. Acad. Sci. USA* **12**, 11963 (2005).

22. Akolpoglu, M. B.; Dogan, N. O.; Bozuyuk, U.; Ceylan, H.; Kizilel, S.; Sitti, M. High ‐ yield production of biohybrid microalgae for on ‐ demand cargo delivery. *Adv. Sci.* **7**, 2001256 (2020).

23. Fang, R. H.; Kroll, A. V.; Gao, W.; Zhang, L. *Adv. Mater.* **30**, 1706759 (2018).

Chapter 2. Microalgae-based Biohybrid Microrobots

2.1 Microalgae microrobots for drug delivery to infected lung

2.1.1 Introduction

The potential of micro-/nanorobots for biomedical applications has been extensively explored over the last decade[1–3]. Although early microrobot designs, consisting primarily of rigid metallic or polymeric structures, allowed for various in vitro applications, novel platforms based on biocompatible and deformable materials have offered some unique advantages towards in vivo operations, including improved drug delivery, deep-tissue imaging and precision microsurgery[4–6]. The in vivo application of these microrobots has typically been restricted due to limitations in the availability of natural fuels, accessibility to certain organs and tissues, and potential toxicity. Biodegradable zinc- and magnesium-based microrobots have been used for drug delivery in the gastrointestinal tract[7,8]. Magnetically powered microrobots have demonstrated deep penetration in the vitreous humour6 and actuation in the peritoneal cavity[9,10]. Achieving active propulsion in other body locations is difficult, but if successful, would offer unprecedented benefits for the treatment of important diseases.

Here we report a bioinspired microrobot platform consisting of nanoparticle (NP)-modified algae for active therapeutic delivery to treat lung disease. Biohybrid microrobots, which combine the motility of natural organisms with the multifunctionality of synthetic components, have recently been studied as an alternative to purely synthetic microrobots[11,12]. For instance, Magnetococcus marinus, which swims along local magnetic fields and towards low oxygen concentrations, were used for transporting drugs into hypoxic tumor regions[13]. The natural movement of sperm has been leveraged to construct hybrid microrobots with distinct advantages towards assisted fertilization[14]. In our design, we create a biohybrid microrobot consisting of Chlamydomonas reinhardtii microalgae modified with neutrophil membrane-coated and drug-loaded polymeric nanoparticles (denoted as 'algae-NP-robot') for the in vivo treatment of lung infection (Fig. 2.1a). C. reinhardtii-based microswimmers have been recently used as the microcarriers of synthetic cargo, demonstrating efficient movement and biocompatibility[15,16]. They can be facilely cultured and offer self-propulsion based on flagella beating (≥110 μm s^{-1}), intrinsic autofluorescence, phototactic guidance and a long lifespan[17]. Neutrophil membrane-coated NPs are used because of their unique cell-mimicking properties, including shielding payloads from biological environments, reducing immune clearance and enabling specific binding with target pathogens[18]. The unique properties of natural algae are combined with the engineering versatility of biomimetic NPs to yield a hybrid microrobot platform capable of active drug delivery. Among the numerous applicable conditions, we choose to first test the algae-NP-robot for in vivo antibiotic delivery to treat bacterial lung infections. Specifically, ventilator-associated pneumonia (VAP) is an acute and potentially fatal infection characterized by onset 48 h after the initiation of mechanical ventilation in intensive care unit (ICU) settings[19]. VAP represents one of the most common infections among hospital patients, affecting between 10% and 25% of those who are intubated[20], resulting in considerable mortality, prolonged ICU stays and an increased number of days on ventilation[21–23]. Multidrug-resistant pathogens such as Pseudomonas aeruginosa are becoming increasingly prevalent as antibiotics continue to be indiscriminately used and with waning effectiveness[24]. We hypothesized that pulmonary antibiotic delivery efficiency could benefit from the deep tissue penetration and prolonged drug retention enabled by the algae-NP-robot system in an experimental model of VAP.

To transform microalgae into algae-NP-robot, we first modified the algal surface with azido N-hydroxysuccinimide (NHS) ester[25,26], followed by conjugation with dibenzocyclooctyne (DBCO)-modified neutrophil membrane-coated polymeric NPs via click chemistry (Fig. 2.1b). This type of reaction has been used to modify cells for a number of applications[27–29]. The motion and cargo-carrying behavior of the resulting algae-NP-robot in simulated lung fluid (SLF), combined with their uniform distribution, effective inhibition of macrophage phagocytosis and prolonged retention in lung tissue, is verified and highlights the considerable promise of the platform for in vivo drug delivery. Additionally, the therapeutic efficacy and safety of the drug-loaded algae-NP-robot are demonstrated using a murine model of P. aeruginosa lung infection.

2.1.2 Preparation of algae-NP-robot

C. reinhardtii algae were cultivated in a Tris-acetate-phosphate (TAP) medium. For further modification, the algae were conjugated with azido-PEG4-NHS ester, which reacts with primary amines on the algal surface. The algae functionalization was confirmed, and negligible cytotoxicity was observed. We then fabricated neutrophil membrane-coated poly(lactic-co-glycolic acid) (PLGA) NPs[30] for use as a therapeutic payload. For visualization, the hydrophobic dyes 1,1’-dioctadecyl-3,3,3’,3’-tetramethylindocarbocyanine perchlorate (DiI) and 3,3’-dioctadecyloxacarbocyanine perchlorate (DiO) were loaded into the PLGA cores and neutrophil membranes, respectively. The overlap of both fluorescence signals indicated the successful association of the two components (Fig. 2.1c). The NPs were further characterized by dynamic light scattering, transmission electron microscopy (TEM) and immunostaining, verifying their core–shell structure and right-side-out membrane orientation. The surface of the NPs was further reacted with DBCO-PEG4-NHS ester, and successful modification was qualitatively confirmed by fluorescence microscopy using an azide-functionalized dye. Conjugation to the algal surface was achieved through click chemistry by incubating the azido-modified algae with DBCO-modified NPs. Scanning electron microscopy (SEM) imaging confirmed the formation of NP-modified algae (Fig. 2.1d). By optimizing the NP input concentration, 91.2% of the algae population could be conjugated with NPs (Fig. 2.1e). Fluorescence microscopy was used to confirm that the NPs were firmly attached to the algal surface after multiple washing steps (Fig. 2.1f,g).

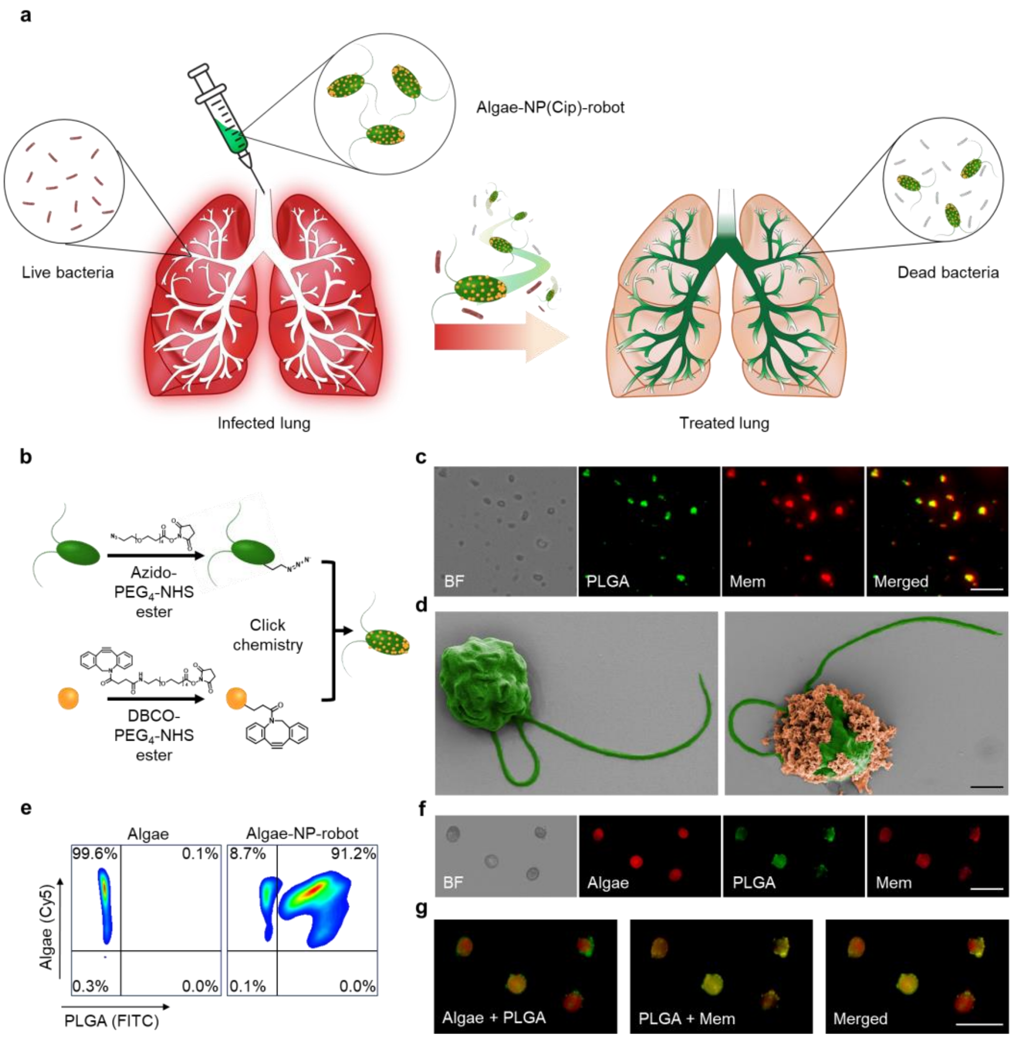

Figure 2.1 Preparation and structural characterization of the algae–nanoparticle hybrid microrobot (denoted as ‘algae-NP-robot’). a, Schematic depicting the use of algae-NP-robot for the treatment of a bacterial lung infection. C. reinhardtii algae is modified with drug-loaded NPs and then administered in vivo for the treatment of P. aeruginosa lung infection. The NP consists of a neutrophil membrane-coated PLGA core. b, Schematic of the functionalization of C. reinhardtii with drug-loaded NP using click chemistry. c, Bright-field (BF) and fluorescent images of the NP, in which the PLGA cores are labelled with DiO (green colour) and the neutrophil membranes are labelled with DiI (red colour). Scale bar, 1 µm. d, Pseudo-coloured SEM images of an unmodified algae (left) and an algae-NP-robot (right). Scale bar, 2 µm. e, Flow cytometry analysis of algae before (left) and after (right) functionalization with DiO-labelled NPs. f, BF and fluorescent images of algae-NP-robot. Autofluorescence of natural algae chloroplast in the Cy5 channel; DiO-labelled PLGA cores in the GFP channel; DiI-labelled cell membranes in the RFP channel. Scale bar, 20 µm. g, Merged images from f. Cy5 and GFP channels (left); GFP and RFP channels (centre); all the three channels (right). Scale bar, 20 µm. In c, f and g, independent experiments were performed (n = 3) with similar results.

2.1.3 Motion behaviour of algae-NP-robot

The speed of algae-NP-robot (104.6 ± 11.2 μm s^{-1}) was similar to that of bare algae (115.5 ± 11.8 μm s^{-1}) in TAP medium at 22 °C, suggesting that NP coupling had a negligible effect on algal motility. As we sought to leverage algae-NP-robot for deep lung delivery, propulsion characteristics in SLF[31] were first evaluated. The motion behaviour of bare algae at room temperature (RT, 22 °C) and at body temperature (BT, 37 °C) in SLF was compared (Fig. 2.2a–c). The bare algae maintained a steady speed of ~115 μm s^{-1} (11.5 body lengths per second) over 1 h at RT but displayed a gradual decrease in speed from ~101 to ~55 μm s^{-1} at BT, indicating that higher temperatures could impact algal motion[32]. The growth rate of bare algae was monitored at both temperatures, and an inhibition of growth was observed at BT[33]. Algae-NP-robot demonstrated similar trends in their motion (Fig. 2.2d–f). To mimic the elevated BT of patients with VAP, an additional test was carried out at 40 °C, and no significant differences were observed compared with algae-NP-robot at BT. Figure 2.2g–l shows the representative tracking trajectories of individual algae-NP-robot over 0, 1 and 2 s intervals and the corresponding mean speed distribution in SLF at different operation times at BT. It is important to note that 95% of the algae remained viable after 1 h of motion in SLF, reflecting the good adaptivity of algae under these conditions. At longer timepoints of 12 and 24 h, approximately 85% and 60% of the algae-NP-robot, respectively, remained motile when exposed to SLF in the dark at BT; this percentage further decreased to less than 20% after 48 h of exposure. Algae-NP-robot did not exert cytotoxicity when incubated with different cell types, and their capacity for phototaxis was unaffected. Overall, these results demonstrate that modification with NPs has a negligible effect on the intrinsic motion behaviour of algae, allowing algae-NP-robot to be employed as an active delivery platform in physiological conditions.

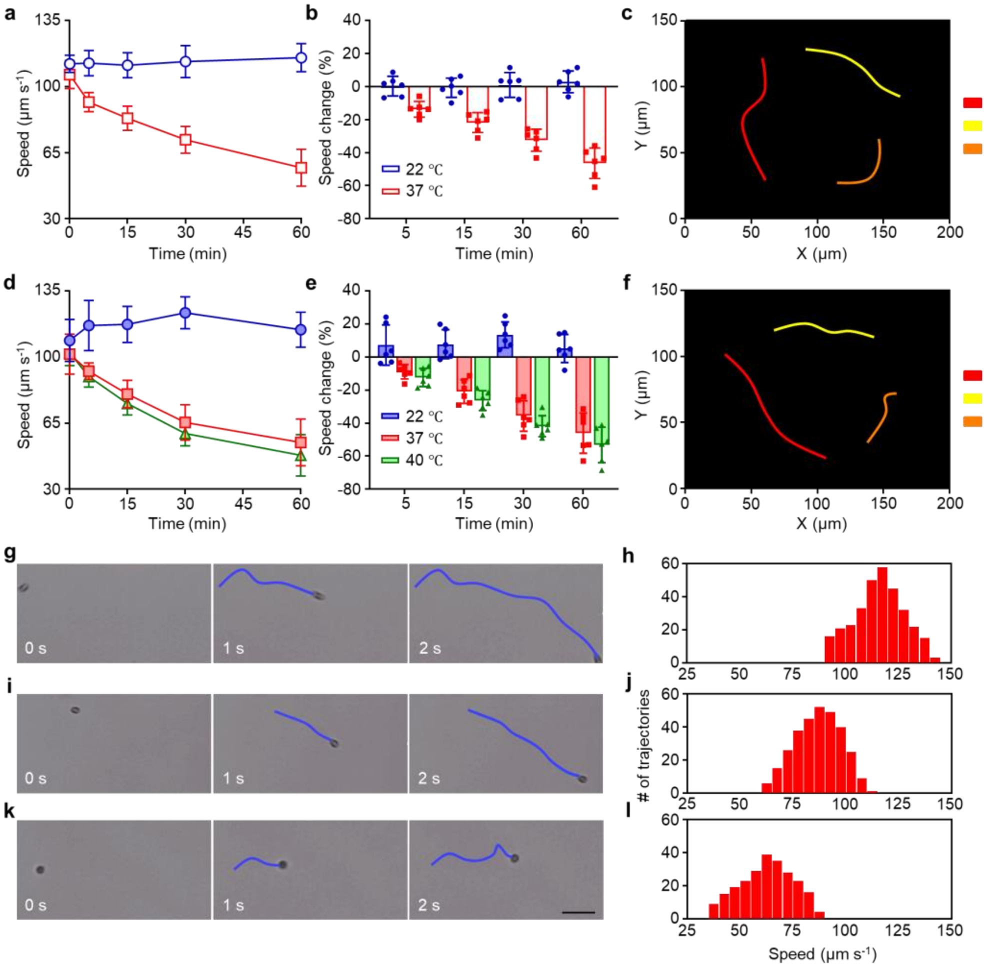

Figure 2.2 Motion behaviour of algae-NP-robot. a–f, Comparison of the speed of bare algae (a and b) and algae-NP-robot (d and e) in simulated lung fluid (SLF) at room temperature (22 °C), body temperature (37 °C) and elevated body temperature (40 °C) (blue, red and green bars, respectively) (n = 6; mean ± standard deviation (s.d.)). Optical tracking trajectories of the motion of bare algae (c) and algae-NP-robot (f) in SLF at 37 °C over 1 s (obtained at 0, 15 and 60 min: red, yellow and orange, respectively). g–l, Representative trajectories (g, i and k) corresponding to 0, 1 and 2 s, respectively, and mean speed distribution (h, j and l) of algae-NP-robot in SLF at 37 °C after 0 min (g and h), 15 min (i and j) and 60 min (k and l). Scale bar, 50 μm.

2.1.4 In vivo distribution, retention and clearance in the lungs

The lung distribution of algae-NP-robot was examined after intratracheal administration[34]. Leveraging autofluorescence from the algae's chloroplasts, the distribution was visualized by ex vivo fluorescence imaging of the excised lungs at various timepoints (Fig. 2.3a). Fluorescence from the algae-NP-robot permeated throughout the lung tissue within 1 h, and the strong signal was retained for at least 24 h. In contrast, NP-modified deflagellated algae (denoted as 'static algae-NP'), incapable of moving, were characterized by SEM and used as a control. The signal of static algae-NP sharply decreased within 4 h and nearly disappeared after 12 h, highlighting the role of active motion in promoting robust lung distribution and retention. To quantitatively compare algal retention, we homogenized the lungs and measured the fluorescence intensity. The total fluorescence of the algae-NP-robot slowly decreased over the course of 72 h and was significantly higher than that of the static algae-NP up to 48 h. After 72 h, the fluorescence intensity returned to near the baseline for both groups. The normalized fluorescence data further verified the slower clearance of algae-NP-robot, as 86% and 65% of the original signal were present at 4 and 24 h, respectively (Fig. 2.3b). In comparison, static algae-NP exhibited greatly reduced signals, with 24% and 8% remaining at 4 and 12 h, respectively. Overall, these data indicate that the motion behaviour of algae-NP-robot greatly improved their lung retention.

To better understand the greatly reduced clearance of algae-NP-robot compared with static algae-NP, we sought to elucidate the potential role of macrophages, an abundant cell population in the lung alveoli capable of clearing exogenous species by phagocytosis[35]. Algae-NP-robot and static algae-NP were mixed with murine J774 macrophages at a 1:1 ratio and incubated at 37 °C in the dark. Figure 2.3c displays the different stages of the algae-NP-robot phagocytosis by macrophages. Algae-NP-robot showed strong autofluorescence from the algae before binding and on contacting the macrophage (0 min). After being taken up by the macrophages via phagocytosis, the algae-NP-robot was gradually degraded, as indicated by a progressive decrease in autofluorescence (15–75 min). By counting the numbers of unbound algae-NP-robot and macrophages at different timepoints, the uptake of algae-NP-robot over time was quantified. As shown in Fig. 2.3d, static algae-NP were internalized significantly faster than their active counterparts, indicating that active motion facilitates escape from macrophage uptake. A cryo-treated algae-NP-robot, incapable of moving, was also taken up faster by macrophages compared with algae-NP-robot, confirming that the physical presence of flagella is not a major factor in the inhibition of phagocytosis. Quantification of the total fluorescence intensity showed that the signal of the algae-NP-robot was consistently higher than that of the static control during 72 h of incubation. Compared with the uptake profiles (Fig. 2.3d), the relative fluorescence profiles of the algae were reversed (Fig. 2.3e). It should be noted that the optical absorbance and fluorescence of the algae-NP-robot without the macrophages was constant, further supporting that macrophage phagocytosis was an important reason for the observed lung-clearance kinetics.

To better understand the clearance mechanism in vivo, flow cytometry analysis of the macrophage uptake was performed at different timepoints after intratracheal administration in mice (Fig. 2.3f,g). A minimal uptake of algae-NP-robot by alveolar macrophages was observed within the first 12 h, and a large increase of uptake was observed at 48 h. In comparison, approximately 20% of the macrophages were positive for static algae-NP uptake after only 1 h, with the uptake peaking at 4 h post-administration before decreasing at later timepoints. The decreased signal is attributed to the degradation of algae after uptake, which destroys their autofluorescence (Fig. 2.3c). These results indicate that alveolar macrophage uptake is a major clearance mechanism for algae in the lungs. The delayed in vivo uptake of the algae-NP-robot by alveolar macrophages corroborates the in vitro findings and could explain the enhanced lung retention that was observed.

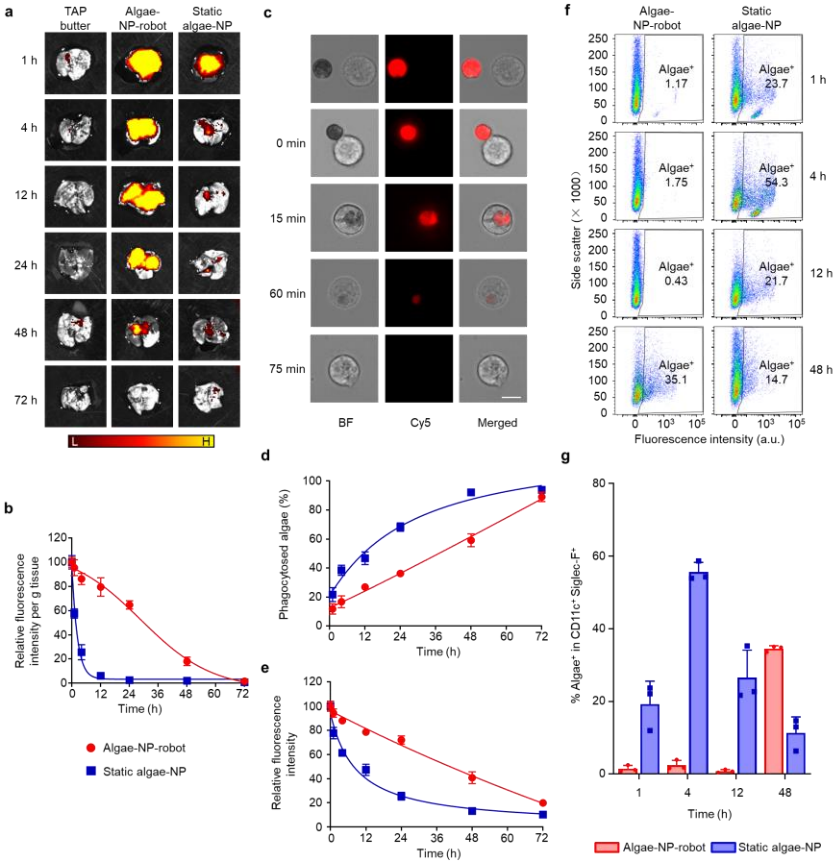

Figure 2.3 Lung distribution of algae-NP-robot. a, Ex vivo fluorescent imaging of lungs at various timepoints after intratracheal administration with TAP medium, algae-NP-robot or static algae-NP (negative control) (H, high signal; L, low signal). b, Normalized intensity per gram of tissue of lung samples collected in a (n = 3; mean + s.d.). c, BF and fluorescence microscopy images of representative algae-NP-robot incubated with macrophages at various stages of their interaction. Scale bar, 10 μm. Independent experiments (n = 3) were performed with similar results. d, Macrophage phagocytosis of static algae-NP or algae-NP-robot over time (n = 3; mean + s.d.). e, Relative fluorescence intensity of algae-NP-robot or static algae-NP over time after incubation with macrophage cells in vitro (n = 3; mean + s.d.). f, Representative flow cytometry dot plots of algae-NP-robot (left) and static algae-NP (right) uptake by alveolar macrophages (CD11c+ Siglec-F+) at various timepoints after intratracheal administration in vivo. g, Comparison of algae-NP-robot and static algae-NP uptake in alveolar macrophages at various timepoints after intratracheal administration in vivo (n = 3; mean + s.d.).

2.1.5 Drug loading and in vivo antibacterial efficacy

Based on the uniform lung distribution and prolonged retention, we postulated that algae-NP-robot may serve as an effective drug carrier for treating infection in the lower respiratory tract. In the study, ciprofloxacin (Cip), a common antibiotic drug used in combinational regimens against susceptible strains of P. aeruginosa, was encapsulated into NP (denoted as ‘NP(Cip)’). The drug loading was optimized to meet the therapeutic threshold for P. aeruginosa[36]. The same method as before was used to fabricate algae conjugated with the drug-loaded NPs (denoted as ‘algae-NP(Cip)-robot’). We then evaluated the Cip loading yield onto the algae (Fig. 2.4a). Using a constant drug input, the total amount of Cip loaded increased linearly with algae number up to approximately 4×10^7 algae and then slowly saturated. The formulation consisting of 6 μg Cip loaded onto 4×10^7 algae was thus selected for subsequent in vitro and in vivo studies. Similar to NP(Cip), algae-NP(Cip)-robot demonstrated an initial burst release of drug over the initial 20 h, followed by a slow release up to 96% by 72 h (Fig. 2.4b). The minimal inhibitory concentration against P. aeruginosa was then evaluated. Bacterial growth was inhibited at a Cip concentration of 62.5 ng ml^{-1} for all the groups (Fig. 2.4c), consistent with what has been previously reported[37]. Figure 2.4d shows the enumerated bacterial colony-forming units (CFU) after treatment with algae-NP(Cip)-robot and with other controls, enabling us to establish the minimal bactericidal concentration. Algae-NP(Cip)-robot had a comparable inhibitory efficacy to free Cip, and the minimal bactericidal concentration of both was determined to be 125 ng ml^{-1}. Bare algae and NPs had negligible effects on the bacteria, supporting the fact that the inhibitory efficacy of algae-NP(Cip)-robot was solely due to the loaded Cip. An in vitro study was also performed to confirm that the algae-NP-robot is able to bind to P. aeruginosa. After 24 h of incubation, a signal from the Hoechst 33342-stained DNA of the bacteria co-localized with that of the DiI-labelled NPs, demonstrating effective binding between the two. The binding efficiency was further quantified by the enumeration of unbound bacteria, revealing that 95% of the initial bacterial input was bound to algae-NP-robot. Such binding is thought to be mediated by protein receptors present on the surface of the NPs[38]. To further verify the unique binding properties of the NPs, PLGA NP cores without membrane coating and liposomes were used, and neither control bound effectively to the bacteria.

Next, we examined the ability of algae-NP(Cip)-robot to treat acute lung infection in vivo. P. aeruginosa was first inoculated to characterize the bacterial dispersion within the lungs. The data demonstrated that the bacteria disseminated throughout the entirety of the lungs within 1 h after intratracheal inoculation, suggesting that algae-NP-robot could be used to efficiently treat conditions like VAP. To investigate the antibacterial efficacy against P. aeruginosa pneumonia, algae-NP(Cip)-robot or control samples were intratracheally administered 30 min after bacterial inoculation. An antibiotic dose of 500 ng Cip was administered per mouse. The lungs were then collected, followed by homogenization for bacterial enumeration 24 h after administration. As illustrated in Fig. 2.4e, the bacterial burden after the algae-NP(Cip)-robot treatment was quantified as 2.6×10^4 CFU g^{-1}, representing a three orders of magnitude reduction compared with the negative control (2.6×10^7 CFU g^{-1}), and a significant reduction compared with static algae-NP(Cip) (6.5×10^5 CFU g^{-1}) and NP(Cip) (3.8×10^5 CFU g^{-1}). A survival study was conducted using the same experimental setup (Fig. 2.4f). The algae-NP(Cip)-robot treatment of infected mice resulted in 100% survival over the entire duration of the 14-day study ($P < 0.0001$, $n = 12$). In stark contrast, all the untreated mice died within three days. The survival rates of mice treated with NP(Cip) or static algae-NP(Cip) were 25.0% and 16.7%, respectively. We concluded that the prolonged lung retention and sustained release characteristics of algae-NP(Cip)-robot enabled the significant improvement in survival compared with the control groups. Subsequently, we compared the efficacy of algae-NP(Cip)-robot with the conventional treatment of intravenous (IV) Cip. The algae-NP(Cip)-robot treatment significantly outperformed IV Cip at the same drug dosage (500 ng per mouse) and achieved similar efficacy compared with IV Cip at a more clinically relevant dosage (1.644 mg per mouse). Additional experiments were performed to quantify the lung bacterial burden at later timepoints following algae-NP(Cip)-robot treatment, revealing a progressive decrease over time and complete clearance after one week (Fig. 2.4g). To verify the effectiveness of algae-NP(Cip)-robot with delayed treatment, we performed an additional study in which mice were treated at progressively longer intervals after a lethal P. aeruginosa challenge (Fig. 2.4h,i). Although the therapeutic efficacy decreased as the treatment interval increased, a significant reduction was still observed even with a 6 h delay.

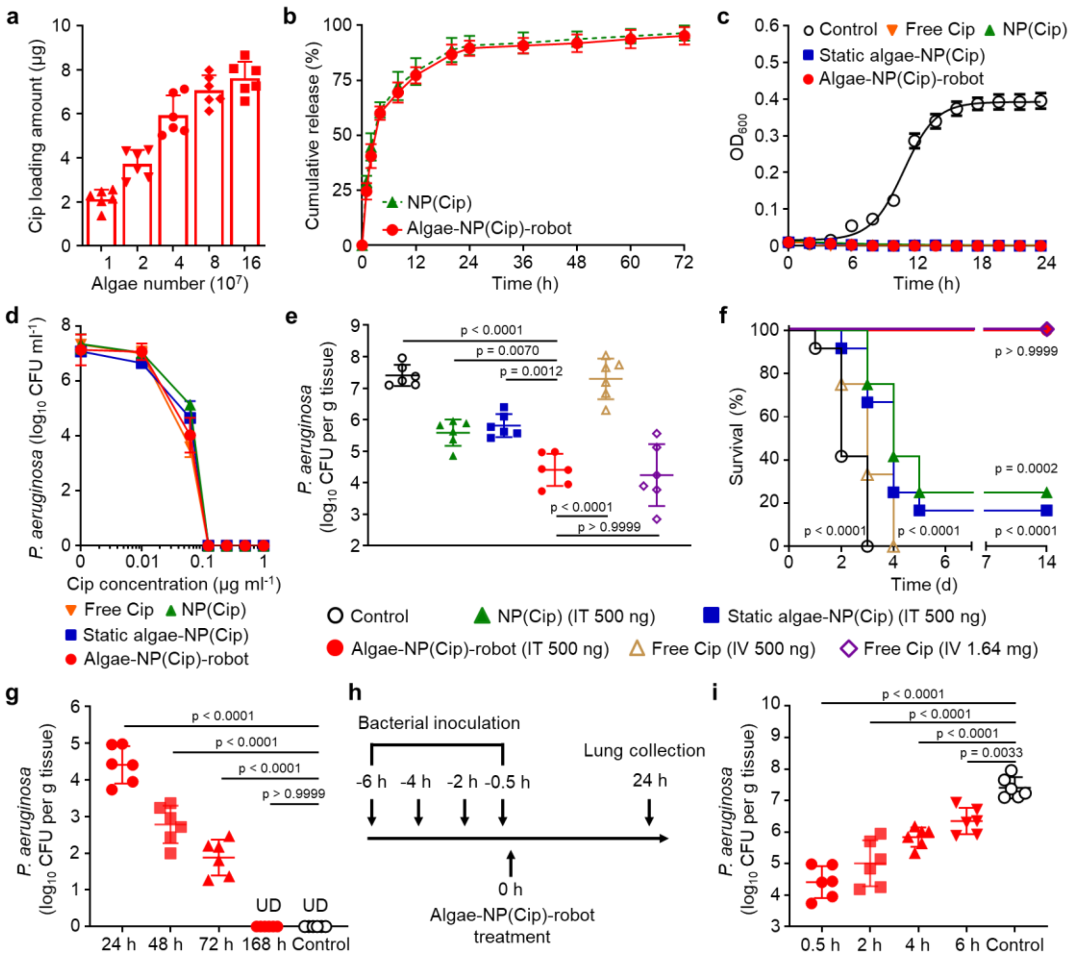

Figure 2.4 In vivo therapeutic efficacy of algae-NP-robot.a, Quantification of Cip loading on different numbers of algae (n = 6; mean + s.d.). b, Cumulative drug release profile of NP(Cip) and algae-NP(Cip)-robot (n = 3; mean + s.d.). c, Optical density at 600 nm (OD600) measurements of P. aeruginosa treated with the control TAP medium, free Cip, NP(Cip), static algae-NP(Cip) and algae-NP(Cip)-robot (n = 3; mean + s.d.). d, In vitro antibacterial activity of free Cip, NP(Cip), static algae-NP(Cip) and algae-NP(Cip)-robot against P. aeruginosa (n = 3; geometric mean + s.d.). e,f, In vivo antibacterial efficacy of the control TAP medium, NP(Cip), static algae-NP(Cip) and algae-NP(Cip)-robot with a dosage of 500 ng by intratracheal (IT) administration and free Cip with the same dosage of 500 ng as used in intratracheal administration and a clinical dosage of 1.64 mg by IV administration in P. aeruginosa-infected mice, as determined by bacterial enumeration (n = 6; geometric mean + s.d.) (e) and survival (n = 12 per group) (f) studies. g, Quantification of bacterial load in the lungs at 24, 48, 72 and 168 h after the algae-NP(Cip)-robot treatment (n = 6; geometric mean + s.d.). UD, undetectable. h,i, Experimental timeline (h) and data (i) for the enumeration of bacterial load in the lungs of mice treated with algae-NP(Cip)-robot at different times after challenge with P. aeruginosa (n = 6; geometric mean + s.d.). One-way analysis of variance for e, g and i and log-rank (Mantel–Cox) test for f.

2.1.6 Biosafety evaluation

Last, to verify the biosafety of algae-NP(Cip)-robot, a comprehensive analysis of blood chemistry and major blood cell populations was conducted 24, 72 and 168 h after administration into the lungs (Fig. 2.5a,b). Compared with mice administered only with the TAP medium, little difference was observed for all the blood parameters. The heart, liver, spleen, lungs and kidneys were also processed by haematoxylin and eosin staining (Fig. 2.5c–e). The overall structural integrity of all the tissues was nearly identical to those from mice administered with the TAP medium, demonstrating no signs of acute toxicity and further supporting the safety of algae-NP(Cip)-robot.

To further evaluate for potential inflammatory responses in the lungs, different cytokines (tumour necrosis factor alpha (TNF-α), interleukin (IL)-1β and IL-6) were analysed 24, 72 and 168 h after the intratracheal administration of algae-NP(Cip)-robot into the lungs. No significant difference in cytokine levels was observed for the algae-NP(Cip)-robot treatment compared with the control group (Fig. 2.5f–h). Histological sections of lung tissues collected over time at 24, 72 and 168 h after administration revealed negligible leucocyte infiltration, normal structures of the lung tissue and no signs of inflammation (Fig. 2.5i). Further in vitro studies verified that algae-NP-robot, in contrast to bacterial flagellin[39], did not trigger the significant production of proinflammatory cytokines by innate immune cells. Together, these data suggest the favourable safety profile of the algae-NP-robot delivery platform.

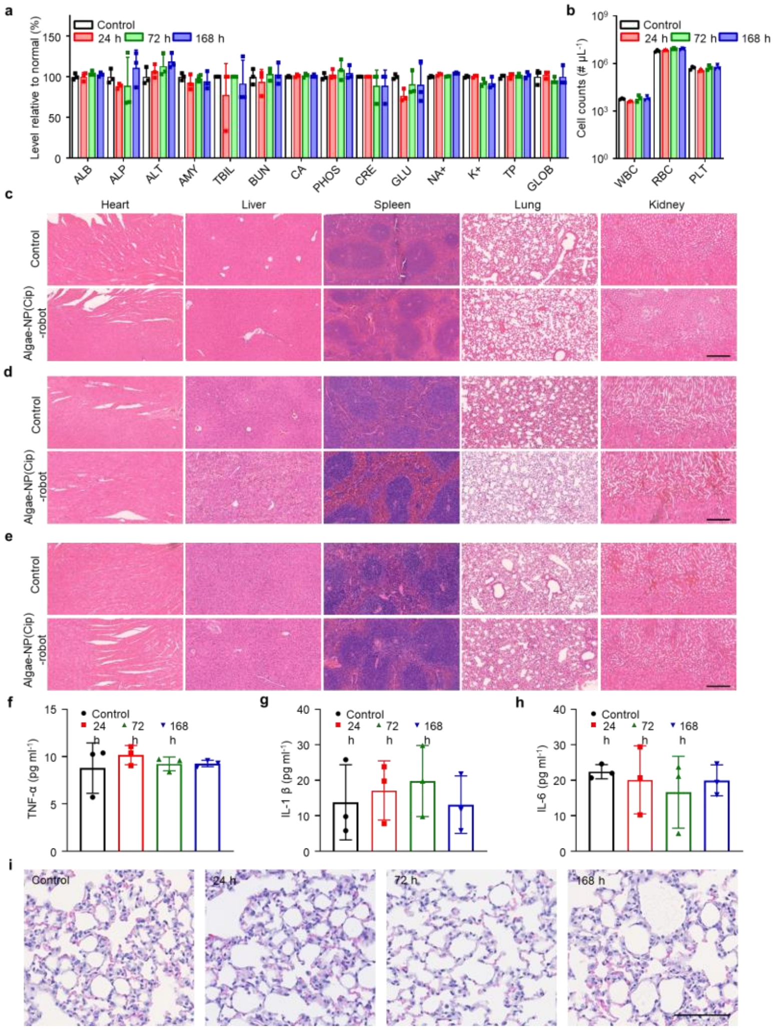

Figure 2.5 In vivo safety evaluation of algae-NP(Cip)-robot. a, Comprehensive blood chemistry panel taken 24 h after the intratracheal administration of TAP medium or 24, 72 and 168 h after that of algae-NP(Cip)-robot (n = 3; mean + s.d.). ALB, albumin; ALP, alkaline phosphatase; ALT, alanine transaminase; AMY, amylase; TBIL, total bilirubin; BUN, blood urea nitrogen; CA, calcium; PHOS, phosphorus; CRE, creatinine; GLU, glucose; NA+, sodium; K+, potassium; TP, total protein; GLOB, globulin. b, Counts of various blood cells 24 h after the intratracheal administration of TAP medium or 24, 72 and 168 h after that of algae-NP(Cip)-robot (n = 3; geometric mean + s.d.). WBC, white blood cells; RBC, red blood cells; PLT, platelets. c–e, Haematoxylin and eosin staining of histology sections from major organs 24 h (c), 72 h (d) and 168 h (e) after the intratracheal administration of TAP medium or algae-NP(Cip)-robot. Scale bars, 250 μm. Independent experiments (n = 3) were performed with similar results. f–h, Cytokines, including TNF-α (f), IL-1β (g) and IL-6 (h), measured in the BALF from healthy control mice or 24, 72 and 168 h after the intratracheal administration of algae-NP(Cip)-robot (n = 3; mean ± s.d.) i, Representative images of haematoxylin and eosin staining on lung histology sections taken from healthy control mice or 24, 72 and 168 h after the intratracheal administration of algae-NP(Cip)-robot. Scale bar, 100 μm. Independent experiments were performed (n = 3) with similar results.

2.1.7 Discussion

The biohybrid microrobot platform described in this work creates new opportunities for active drug delivery to the lungs of ventilated ICU patients. This is due to its distinct advantages in terms of facile large-scale production, autonomous motion and long lifespan in localized environments, intrinsic autofluorescence for easy in vivo observation and potential targeting functionality. Further studies are required to determine if our biohybrid microrobot system can deliver key antibiotics for treating other important bacterial pathogens in VAP, including Acinetobacter baumannii and Staphylococcus aureus, or be extended to the treatment of other ICU conditions such as acute respiratory distress syndrome—a complication of viral pneumonia. Future studies will also test the algae-NP-robot formulation against clinical P. aeruginosa isolates to evaluate its general applicability. In its current iteration for intratracheal administration, the biohybrid microrobot would not be suitable for treating chronic P. aeruginosa infections, such as those that afflict the lungs of cystic fibrosis patients, or for other patients in which mechanical ventilation or bronchoscopy is not indicated by their clinical status. Before human clinical trials, additional validation using large animal models suitable for repeated dosing studies would enable a better evaluation of the algae-NP-robot therapeutic efficacy and safety in comparison to clinical IV antibiotic regimens. Looking forward, it would also be interesting to more precisely understand how algae-based microrobots interact with the immune system, aiming to further improve their retention time in the lungs. Exploring different delivery methods, such as by inhalation or IV administration, or leveraging the inherent phototaxis properties of algae, may expand the scope of the platform across a wider range of applications.

Although the treatment of acute pneumonia using algae-NP-robot probably benefited from uniform dispersion throughout the lungs, biohybrid microrobots can also be integrated with sensory and targeting functionalities for situations in which more precise delivery is required. For example, optogenetics technology that locally induces the light emission of target cells with photoreceptors[40] can be introduced to trigger the inherent phototaxis of algae[41], thus enabling site-specific targeting[42]. The algae can also be genetically engineered with functional proteins on their surface to introduce additional functionalities[43]. Besides algae, other microorganisms with specific sensory or targeting capabilities[13,44] could also be used in the development of autonomous drug delivery vehicles for treating pulmonary diseases.

2.1.8 Experimental section

Algae culture. Green C. reinhardtii algae (strain CC-125 wild-type mt+) were obtained from the Chlamydomonas Resource Center. The algae were transferred from the agar plate to Tris-acetate-phosphate (TAP) medium (Thermo Fisher Scientific) and cultivated at room temperature under cycles of 12 h sunlight and 12 h dark.

Neutrophil cell culture. Human neutrophil-like cells (HL-60, American Type Culture Collection, ATCC CCL-240) were cultured in RPMI 1640 (11875135, Gibco) with 1 v/v% penicillin-streptomycin (15140122, Gibco) and 10 v/v% fetal bovine serum (SH30541.03, Hyclone) in an incubator under 5% CO_2 at a temperature of 37 °C. Cells were regularly tested for mycoplasma.

Neutrophil cell membrane derivation. HL-60 plasma membrane was collected according to an established procedure[23]. Frozen cells were thawed and washed 3 times with 1× PBS. Cells were lysed in a buffer consisting of 30 mM Tris-HCl, 75 mM sucrose, 225 mM D-mannitol, 0.2 mM ethylene glycol-bis(β-aminoethyl ether)-N,N,N',N'-tetraacetic acid, and phosphatase/protease inhibitor mixtures (Sigma Aldrich). Cells were next homogenized using a Kinematica Polytron PT-10/35 probe homogenizer, and the cell membrane was collected through gradient centrifugation. BCA kit (Pierce) was used to quantify the cell membrane content. The final cell membrane was stored in 0.2 mM EDTA at -80 °C for subsequent studies.

Synthesis of polymeric cores. Drug loaded polymeric cores were synthetized following a reported method with slight modifications[45]. Briefly, 50 µl of 25 mg ml^{-1} ciprofloxacin (HCl salt, Sigma Aldrich) solution was emulsified in 500 µl chloroform solution containing 50 mg ml^{-1} poly(lactic-co-glycolic acid) (50:50 PLGA, 0.67 dl g^{-1}, Lactel Absorbable Polymers) using an ultrasonic probe sonicator (Fisher Scientific) operating at a power of 10 W. The sonication lasted for 2 min with alternating cycles of 2 s power on and 2 s power off inside an ice bath. Then, the emulsion was transferred to 10 ml of aqueous solution and sonicated for another 2 min. The emulsion was stirred for 4 h to completely evaporate the chloroform. All samples were centrifuged for 5 min at 16,100g and washed twice with ultrapure water, and lyophilized for future use. The 3,3'-dioctadecyloxacarbocyanine perchlorate (DiO, $\lambda_{ex}/\lambda_{em}$ = 484 nm/501 nm; Thermo Fisher Scientific)-loaded nanoparticles were synthesized by replacing ciprofloxacin with 1 mg ml^{-1} of the dye and then following the same method.

Synthesis of neutrophil membrane-coated nanoparticles. Neutrophil membrane-coated nanoparticles were synthesized by an established procedure[18]. Briefly, the neutrophil membranes were added into solution containing PLGA cores at a polymer to membrane protein weight ratio 1:1. The neutrophil membranes were coated onto PLGA cores through 3 min sonication in a bath sonicator (Fisher Scientific FS30D). The resulting membrane-coated nanoparticles were separated from the solution by 5 min centrifugation at 16,100g and washed twice with ultrapure water.

Characterization of neutrophil membrane-coated nanoparticles. The nanoparticle size and surface charge of neutrophil membrane-coated nanoparticles were measured using dynamic light scattering (ZEN 3600 Zetasizer, Malvern). In addition, the morphology of nanoparticles was verified using transmission electron spectroscopy (FEI 200 kV Sphera). Brightfield and fluorescent images of 1,1'-dioctadecyl-3,3,3',3'-tetramethylindocarbocyanine perchlorate (DiI, $\lambda_{ex}/\lambda_{em}$ = 551 nm/566 nm; Thermo Fisher Scientific)-labeled neutrophil membrane and DiO-loaded PLGA core were taken on a fluorescence microscopy (EVOS FL). To verify the neutrophil membrane orientation after coating, neutrophils (~2.5 × 10^6 cells) and neutrophil membrane-coated nanoparticles (100 µl, 0.5 mg ml^{-1} protein content) were blocked in 1% bovine serum albumin (BSA, Millipore Sigma) for 30 min and then incubated with 1 µl 100 mg ml^{-1} Alexa488 anti-human CD11a (LFA-1) antibody (Biolegend) for 30 min. The total fluorescent intensity of the mixture was measured by BioTek Synergy Mx microplate reader. To separate unbound antibodies, neutrophil samples were spun down at 3000g for 5 min, whereas neutrophil membrane-coated nanoparticles were centrifuged for 5 min in 300 kDa molecular weight cutoff Nanosep tubes at 5000g. The fluorescence intensity of the unbound antibodies was measured in order to determine the amounts bound to the neutrophils and NPs.

Preparation of algae-NP-robot. Green algae were washed with ultrapure water three times to remove any residual TAP buffer, and they were subsequently resuspended in ultrapure water. Then, 1 × 10^7 algae were treated with 20 µM azido-PEG$_4$-NHS ester (Click Chemistry Tools) for 45 min at room temperature. To examine the effective binding of azido groups on the algae surface, the resulting algae were incubated with BDP FL DBCO (Lumiprobe) for 30 min and then subjected to flow cytometry analysis (1×10^4 events were collected for analysis). Then neutrophil membrane-coated PLGA nanoparticles (denoted 'NP') were modified with N_3 bonds for the click chemistry. Here, NP were incubated with 40 μM DBCO-PEG_4-NHS ester for 1 h at room temperature. The presence of triple bonds on the NP surface was confirmed by adding FAM azide, 5-isomer (Lumiprobe) and visualized by fluorescence microscopy. Both of the resulting algae and NP were washed five times with ultrapure water, removing unreacted NHS ester for the following conjugation. To optimize the binding efficiency, we used different concentrations of NP at 0.04 mg ml^{-1}, 0.2 mg ml^{-1}, and 1 mg ml^{-1} for conjugation. During the conjugation, DBCO-modified NP were incubated with azido-functionalized algae for 45 min. After 3 min centrifugation at 300g and three washes with TAP medium, the resulting algae-NP-robot were collected for further characterization. Static algae-NP were prepared by removing the flagella from the algae using 0.5 M acetic acid, followed by the same procedure for NP conjugation. Cryo-treated algae-NP-robots were prepared by a cryogenic treatment in which the algae-NP-robot was immersed into liquid nitrogen for 45 seconds to maintain the structure of the algae.

Characterization of algae-NP-robot. To perform scanning electron microscopy (SEM) characterization, algae-NP-robots were first fixed with 2.5% glutaraldehyde overnight at 4 °C and then washed in ultrapure water. After overnight drying, algae-NP-robots were coated with palladium for SEM characterization using an acceleration voltage of 3 KV (Zeiss Sigma 500 SEM instrument). The bare algae and static algae-NP were treated and examined using the same methodology. The attachment of NP to algae was captured by fluorescence microscopy (EVOS FL) with three individual fluorescence channels, Cy5, RFP and GFP, which corresponded to the autofluorescence of algae, the DiI-labeled neutrophil membrane, and the DiO-loaded PLGA cores, respectively.

Algae viability study. To evaluate algae viability, algae were stained in 5 μM SYTOX green fluorescent probe (Thermo Fisher). The bright green fluorescence of dead algae was examined by fluorescence microscopy. Based on previously reported methods[46], the solution was measured for SYTOX fluorescence intensity ($\lambda_{ex}/\lambda_{em}$ = 504 nm/523 nm) using a plate reader. No washing steps were required due to the specific staining of the nucleic acid of dead algae.

Motion analysis. The motion of algae-NP-robot and bare algae control was evaluated in simulated lung fluid (SLF). The speed of algae-NP-robot in the SLF was measured in the dark at 37 °C, and changes in the motion were evaluated at 1 h, 12 h, 24 h, and 48 h. The speed of algae-NP-robot was also measured over 1 h at an elevated body temperature at 40 °C. The movies of the motion were recorded by optical microscope (Nikon Eclipse Instrument Inc. Ti-S/L 100). An NIS Element tracking module was used to measure the corresponding algae speed in SLF.

Binding of NPs or liposomes with bacteria. Neutrophil membrane-coated DiO-loaded PLGA nanoparticles (denoted 'NPs') and DiO-loaded PLGA nanoparticle cores without membrane coating were prepared as before. Liposomes were synthesized through an extrusion-based method. Briefly, L-α-phosphatidylcholine (EggPC, Avanti Polar Lipids 840051) and cholesterol (Avanti Polar Lipids 700100) were dissolved in chloroform and mixed at a weight ratio of 9:1. To label the liposomes, DiO was dissolved in chloroform and added to the lipid mixture to reach a weight percentage of 2% DiO. The chloroform was evaporated in nitrogen gas. The dried lipid film was hydrated with sterile PBS to reach a total lipid concentration of 5 mg ml^{-1}. The lipid solution was vortexed for 1 min, followed by sonication in a bath sonicator. The re-hydrated lipids were further extruded through a polycarbonate membrane with 100 nm pore size to form liposomes. To compare the binding effect, 1 mg of NPs, 1 mg PLGA nanoparticle cores without membrane coating and 1 mg of liposomes were incubated with 1 × 10^7 ml^{-1} P. aeruginosa overnight, respectively. The unbound NPs, liposomes and PLGA nanoparticle cores without membrane coating were removed through three washing steps by centrifuging at 700g for 2 min. Brightfield and fluorescent images of the three groups were taken on a Life Technologies EVOS FL fluorescence microscope. Fluorescence values from DiO ($\lambda_{ex}/\lambda_{em}$ = 484 nm/501 nm) were quantified using a BioTek Synergy Mx microplate reader. To perform SEM characterization, samples were initially fixed overnight with 2.5% glutaraldehyde at 4 °C, followed by washing with ultrapure water. After overnight drying, samples were coated with palladium for SEM characterization using an acceleration voltage of 3 KV (Zeiss Sigma 500 SEM instrument).

Binding of algae-NP-robot with bacteria. The PLGA core and neutrophil membrane were labeled with DiO and DiI, respectively. The algae-NP-robot was prepared as before. P. aeruginosa was labeled with Hoechst 33342 (Thermo Fisher Scientific) for 30 min at room temperature. The free dye was removed through three washing steps by centrifuging at 3000g for 5 min. To explore the binding effect between algae-NP-robot and bacteria, 1 × 10^5 ml^{-1} algae-NP-robot were incubated with 1 × 10^7 ml^{-1} P. aeruginosa overnight. The unbound bacteria were removed through five washing steps by centrifuging at 200g for 2 min. After fixation in 2.5% glutaraldehyde, brightfield and fluorescent images of the binding between algae-NP-robot and P. aeruginosa were taken on a Life Technologies EVOS FL fluorescence microscope. To quantify binding efficiency, 5 × 10^6 ml^{-1} algae-NP-robots were incubated with 5 × 10^6 CFU ml^{-1} P. aeruginosa for 1 h. Colonies of total bacterial input and unbound bacteria were counted after 24 h of culture on agar plates.

Cytotoxicity test. To evaluate cytotoxicity, J774A.1 cells (ATCC TIB-67) and NL20 cells (ATCC CRL-2503) were seeded in 96-well plates at 1× 10^4 cells per well. The cells were then incubated with algae-NP-robot with an algae/ cell ratio of 0.0625, 0.125, 0.25, 0.5, 1.0, 2.0, 4.0, 8.0, 16.0, 32.0, and 64.0 for 24 hours. CellTiter AQueous One Solution cell proliferation assay (Promega) was used to evaluate cell viability, according to the manufacturer's instructions.

Phototaxis of algae-NP-robot. A small 2 µl droplet of algae-NP-robot was placed on a glass slide without further modification. After 5 s of random motion, the algae-NP-robot sample was illuminated with white light from the top for 30 s. The video was recorded using an optical microscope.

Intratracheal administration. The intratracheal administration was performed using a modified method based on a previous paper[34]. Specifically, male CD-1 mice (Charles River Labs) were placed under anesthesia with a ketamine (Pfizer) and xylazine (Lloyd Laboratories) cocktail administered at 100 mg/kg and 20 mg kg^{-1}, respectively. To prepare the inoculation, a certain volume of test materials (50 µl algae-NP-robot, static algae-NP, NP, and TAP medium) was injected into the PTFE feeding tube (cut 6-8 inches in length) by an insulin needle. Then, the feeding tube was inserted 0.5–1.0 cm into the trachea and the inoculum of test materials was administered into the lungs. To avoid escape of the test materials from the lungs, the feeding tube was left in place for 30 seconds.

Ex vivo lung imaging and retention quantification. All animal experiments were approved by the Institutional Animal Care and Use Committee of the University of California San Diego and performed under the National Institutes of Health (NIH) guidelines. Male CD-1 mice (Charles River Labs) were placed under anesthesia with a ketamine and xylazine cocktail. They were subsequently intratracheally administrated with TAP buffer, 5 × 10^6 algae-NP-robot, or 5 × 10^6 static algae-NP. After certain timepoints (1, 4, 12, 24, 48, and 72 h), the mice were euthanized, and their lungs were excised for analysis. Fluorescent ex vivo lung images were obtained with the Xenogen IVIS 200 system. Subsequently, the lung samples were homogenized, and fluorescence values were measured on a BioTek Synergy Mx microplate reader. Bacterial dispersion studies were performed with a similar method. Briefly, P. aeruginosa bacteria were labeled with DiD after overnight incubation. Following anesthesia, the mice were intratracheally inoculated with 5 × 10^6 CFU of DiD labeled P. aeruginosa. After 1 h inoculation, the mice were euthanized, and their lungs were excised for IVIS imaging analysis.

In vitro macrophage phagocytosis. J774A.1 macrophage cells were cultured using Dulbecco's modified Eagle medium (DMEM, Invitrogen) in a 24-well plate at density of 1 × 10^6 cells per well. Algae-NP-robots were then added at a robot/macrophage ratio of 1:1 and incubated at 37 °C. After certain timepoints (1, 4, 12, 24, 48, and 72 h), the mixture was analyzed by fluorescence microscopy and fluorescence values were quantified using a BioTek Synergy Mx microplate reader. Static algae-NP and cryo-treated algae-NP-robot controls were tested and quantified following the same method.

Algae-NP-robot clearance in vivo. At various timepoints (1 h, 4 h, 12 h, and 48 h) before the study, male CD-1 mice were intratracheally inoculated with equivalent amounts of algae-NP-robot or static algae-NP. Then, mice were euthanized by carbon dioxide asphyxiation and the trachea was exposed. A catheter made by tightly fitting a 23-gauge needle into PTFE tubing (Cole Parmer) was inserted into the trachea and secured with sutures. Bronchoalveolar lavage was then collected from each mouse by repeatedly washing the lungs five times with 1 ml of 0.5% (v/v) fetal bovine serum

(Gibco) and 2 mM EDTA in PBS and immediately stored on ice. Cells were spun down at 700g for 5 min, and red blood cells were lysed using a commercial buffer (Biolegend) following the manufacturer's instructions. Subsequently, nonspecific binding on the cells was blocked with 1% (w/v) BSA in PBS for 15 min and then probed with Pacific Blue conjugated anti-mouse CD11c (N418, Biolegend) and PE-conjugated anti-mouse Siglec-F (S17007L, Biolegend) antibodies for 30 min on ice. Unbound antibodies were washed out twice with 1% BSA in PBS and the cells were resuspended in 1% BSA in PBS for flow cytometry analysis. Data was acquired with a BD FACSCanto II flow cytometer and analyzed using the FlowJo software.

Ciprofloxacin (Cip) loading and release measurement. A total of 1 ml of algae at different concentrations (1×10^7 ml^{-1}, 2×10^7 ml^{-1}, 4×10^7 ml^{-1}, 8×10^7 ml^{-1}, and 16×10^7 ml^{-1}) was conjugated with 1 mg NP(Cip) by click chemistry, followed by removal of free NP(Cip) by three washes at 300 g for 2 min. Then, the algae-NP(Cip)-robots were suspended in 1 ml of TAP for further use. After fabrication of algae-NP(Cip)-robot, the solution was measured for Cip fluorescence intensity ($\lambda_{ex}/\lambda_{em}$ = 270 nm/440 nm). A standard calibration curve was made by measuring serial dilutions of Cip solution (0-10 μg ml^{-1}), and the Cip concentration was determined by comparing with the standard calibration curve. The Cip release was conducted with 1 ml of algae-NP(Cip)-robot at 37 °C within 72 h. Cip concentration was determined also by fluorescence measurement.

In vitro antibacterial activity of algae-NP(Cip)-robot. A volume of 1 ml of P. aeruginosa PAO1 strain (ATCC, BAA-47) at 5×10^6 CFU (colony-forming unit) ml^{-1} was mixed with TAP, free Cip, NP(Cip), static algae-NP(Cip), or algae-NP(Cip)-robot at an equivalent Cip amount. To quantify the minimal inhibitory concentration (MIC) of Cip, various concentrations of Cip were used:

31.25 ng ml^{-1}, 62.5 ng ml^{-1}, 125 ng ml^{-1}, 250 ng ml^{-1}, 500 ng ml^{-1}, and 1 μg ml^{-1}. The bacterial growth was quantified by measuring their absorbance at 600 nm (OD_{600}).

In vivo enumeration study. P. aeruginosa was first streaked onto a Luria broth (LB; Sigma-Aldrich) agar plate and cultured overnight at 37 °C. A single colony was inoculated in 50 ml of LB, and further cultured for 10 h at 37 °C on shaker. The bacteria were collected after spinning down at 5,000g for 20 min, washing with PBS, and resuspending in PBS to a final concentration of 2×10^8 CFU ml^{-1}. Male CD-1 mice were placed under anesthesia with a ketamine and xylazine cocktail. They were intratracheally inoculated with 5×10^6 CFU of P. aeruginosa and subsequently intratracheally administered with TAP buffer, NP(Cip), 5×10^6 algae-NP(Cip)-robot, or 5×10^6 static algae-NP(Cip) at an equivalent Cip amount (500 ng). After 24 h, 48 h, 72 h, and 168 h, the mice were euthanized, and their lungs were collected for quantification of bacterial load. In a separate enumeration study, treatment with the algae-NP(Cip)-robot was delayed for 30 min, 2 h, 4 h, and 6 h after the bacterial challenge, and lung samples were collected after another 24 h for enumeration. To compare with the IV treatment, an equivalent Cip amount (500 ng) and a clinical dose (1.64 mg) were intravenous injected separately into mice 30 min after bacterial inoculation. Bacterial enumeration was performed using the same protocol.

In vivo survival study. Male CD-1 mice were placed under anesthesia using a ketamine and xylazine cocktail. They were intratracheally inoculated with 5×10^6 CFU of P. aeruginosa and then intratracheally administered with TAP buffer, NP-Cip, 5×10^6 algae-NP(Cip)-robot, or 5×10^6 static algae-NP(Cip) at an equivalent Cip amount (500 ng). To compare with the IV treatment, an equivalent Cip amount (500 ng) and a clinical dose (1.64 mg) were intravenous injected separately into mice 30 min after bacterial inoculation. Survival of each mouse was monitored on a daily basis.

In vivo safety studies. Mice were euthanized at 24 h, 72 h, and 168 h after intratracheal administration of TAP buffer or 5 × 10^6 algae-NP(Cip)-robot for sample collection. For the comprehensive metabolic panel and blood cell counts, serum and whole blood were collected. Lab tests were carried out by the UC San Diego Animal Care Program Diagnostic Services Laboratory. For histological analysis, H&E staining was performed on major organs. To evaluate the cytokine levels, bronchoalveolar lavage fluid (BALF) was collected by washing the lungs five times using 1 ml of 0.5% (v/v) fetal bovine serum (Gibco) and 2 mM EDTA in PBS through a 23-gauge needle into PTFE tubing (Cole Parmer) inserted into the trachea. For cytokine analysis, the BALF was centrifuged at 700g for 5 min to collect the supernatant. Cytokine concentrations in BALF were measured in triplicate by multiplexed sandwich enzyme-linked immunosorbent assay (ELISA) kit (BioLegend). The histology sections of lung tissue were evaluated by the Tissue Technology Shared Resources, UC San Diego Moores Cancer Center. All histological assessments were performed in a blinded manner to prevent observer bias.

In vitro cytokine production. J774A.1 macrophage cells were cultured in DMEM in a 6-well plate at 1 × 10^6 cells per well. They were subsequently incubated with 5 × 10^6 algae-NP-robot, 5 × 10^6 cryo-treated algae-NP-robot, 5 × 10^6 static algae-NP, or 100 ng ml^{-1} flagellin isolated from Salmonella Typhimurium bacteria (InvivoGen) for 24 h. Cytokine levels were determined by ELISA kits (BioLegend).

Chapter 2.1, in full, is a reprint of the material as it appears in Nature Materials, 2022, by Fangyu Zhang, Jia Zhuang, Zhengxing Li, Hua Gong, Berta Esteban-Fernández de Ávila, Yaou Duan, Qiangzhe Zhang, Jiarong Zhou, Lu Yin, Emil Karshalev, Weiwei Gao, Victor Nizet, Ronnie H. Fang, Liangfang Zhang, Joseph Wang. The dissertation author was the primary investigator and author of this paper.

2.1.9 References

1. Li, J., Esteban-Fernández de Ávila, B., Gao, W., Zhang, L., Wang, J. Micro/nanorobots for biomedicine: delivery, surgery, sensing, and detoxification. Sci. Robot. **2,** eaam6431 (2017).

2. Gao, C., Wang, Y., Ye, Z., Lin, Z., Ma, X., He, Q. Biomedical micro-/nanomotors: from overcoming biological barriers to in vivo imaging. Adv. Mater. 2000512 (2020).

3. Wu, Z., Chen, Y., Mukasa, D., Pak, O. S., Gao, W. Medical micro/nanorobots in complex media. Chem. Soc. Rev. **49**, 8088-8112 (2020).

4. Esteban-Fernández de Ávila, B., Angsantikul P., Li, J., Angel Lopez-Ramirez, M., Ramírez-Herrera, D. E., Thamphiwatana, S., Chen, C., Delezuk, J., Samakapiruk, R., Ramez, V., Obonyo, M., Zhang, L., Wang, J. Micromotor-enabled active drug delivery for in vivo treatment of stomach infection. Nat. Commun. **8,** 272 (2017).

5. Wu, Z., Li, L., Yang, Y., Hu, P., Li, Y., Yang, S. Y., Wang, L., Gao, W. A microrobotic system guided by photoacoustic computed tomography for targeted navigation in intestines in vivo. Sci. Robot. **4,** eaax0613 (2019).

6. Wu, Z., Troll, J., Jeong, H. H., Wei, Q., Stang, M., Ziemssen, F., Wang, Z., Dong, M., Schnichels, S., Qiu, T., Fischer, P.A swarm of slippery micropropellers penetrates the vitreous body of the eye. Sci. Adv. **4,** eaat4388 (2018).

7. Gao, W., Dong, R., Thamphiwatana, S., Li, J., Gao, W., Zhang, L., Wang, J. Artificial micromotors in the mouse’s stomach: a step toward in vivo use of synthetic motors. ACS Nano **9,** 117-123 (2015).

8. Wei, X., Beltrán-Gastélum, M., Karshalev, E., Esteban-Fernández de Ávila, B., Zhou, J., Ran, D., Angsantikul P., Fang, R. H., Zhang, L.Biomimetic micromotor enables active delivery of antigens for oral vaccination. Nano Lett. **19,** 1914-1921 (2019).

9. Servant, A., Qiu, F., Mazza, M., Kostarelos, K., Nelson, B. J. Controlled in vivo swimming of a swarm of bacteria-like microrobotic flagella. Adv. Mater. **27,** 2981 (2015).

10. Yan, X., Zhou, Q., Vincent, M., Deng, Y., Yu, J., Xu, J., Xu, T., Tang, T., Bian, L., Wang, Y. J., Kostarelos, K., Zhang, L. Multifunctional biohybrid magnetite microrobots for imaging-guided therapy. Sci. Robot. **2,** eaaq1155 (2017).

11. Sun, L. Yu, Y., Chen, Z., Bian, F., Ye, F., Sun, L., Zhao, Y. Biohybrid robotics with living cell actuation. Chem. Soc. Rev. **49,** 4043-4069 (2020).

12. Ricotti, L. Trimmer, B., Feinberg, A. W., Raman, R., Parker, K. K., Bashir, R., Sitti, M., Martel, Sylvain., Dario, P., Menciassi, A. Biohybrid actuators for robotics: A review of devices actuated by living cells. Sci. Robot. **2**, eaaq0459 (2017)

13. Felfoul, O. Mohammadi, M., Taherkhani, S., De Lauauze, D., Xu, Y. Z., Loghin, D., Essa, S., Jancik, S., Houle, D., Lafleur, M., Gaboury, L., Tabrizian, M., Kaou, N., Atkin, M., Vuong, T., Batist, G., Beauchemin, N., Radzioch, D., Martel, S. Magneto-aerotactic bacteria deliver drug-containing nanoliposomes to tumour hypoxic regions. Nat. Nanotechnol. **11,** 941-947 (2016).

14. Medina-Sánchez, M., Schwarz, L., Meyer, A. K., Hebenstreit, F., Schmidt, O. G. Cellular cargo delivery: toward assisted fertilization by sperm carrying micromotors. Nano Lett. **16,** 555-561 (2015).

15. Weibel, D. B. Garstecki, P., Ryan, D., Diluzio, W. R., Mayer, M., Seto, J. E., Whitesides, G. M. Microoxen: microorganisms to move microscale loads. PNAS **102,** 11963 (2005).

16. Yasa, O., Erkoc, P., Alapan, Y., Sitti, M. Microalga-powered microswimmers toward active cargo delivery. Adv. Mater. **30,** 1804130 (2018).

17. Silflow, C. D., Lefebvre, P. A. Assembly and motility of eukaryotic cilia and flagella. Lessons from chlamydomonas reinhardtii. Plant Physiol. **127,** 1500-1507 (2001).

18. Zhang, Q., Dehaini, D., Zhang, Y., Zhou, J., Chen, X., Zhang, L., Fang, R. H., Gao, W., Zhang, L. Neutrophil membrane-coated nanoparticles inhibit synovial inflammation and alleviate joint damage in inflammatory arthritis. Nat. Nanotechnol. **13,** 1182 (2018).

19. Metersky, M. L., Kalil, A. C. Management of ventilator-associated pneumonia: guidelines. Clin. Chest Med. **39**, 797-808 (2018).

20. Schreiber, M. P., Shorr, A. F. Challenges and opportunities in the treatment of ventilator-associated pneumonia. Expert Rev. Anti. Infec. Ther. **15**, 23-32 (2017).

21. Muscedere, J., Sinuff, T., Heyland, D. K., Dodek, P. M., Keenan, S. P., Wood, G., Jiang, X., Day, A. G., Laporta, D., Klompas, M., Canadian Critical Care Trials Group. The clinical impact and preventability of ventilator-associated conditions in critically ill patients who are mechanically ventilated. Chest. **144**, 1453-1460 (2013).

22. Melsen, W. G., Rovers, M.M., Groenwold, R.H., Bergmans, D.C., Camus, C., Bauer, T.T., Hanisch, E.W., Klarin, B., Koeman, M., Krueger, W.A. and Lacherade, J.C., Lorente, L., Memish, Z. A., Morrow, L. E., Nardi, G., van Nieuwenhoven, C. A., OKeefe, G. E., Nakos, G., Scannapieco, F. A., Seguin, P., Staudinger, T., Topeli, A., Ferrer, M., Bonten, M. JM. Attributable mortality of ventilator-associated pneumonia: a meta-analysis of individual patient data from randomised prevention studies. Lancet Infect. Dis. **13**, 665-671 (2013).

23. Kharel, S., Bist, A., Mishra, S. K. Ventilator-associated pneumonia among ICU patients in WHO Southeast Asian region: A systematic review. PloS one **16**, e0247832 (2021).

24. Vincent, J.-L., de Souza Barros, D., Cianferoni, S., Diagnosis, management and prevention of ventilator-associated pneumonia. Drugs. **70**, 1927-1944 (2010).

25. Kerschgens, I. P., Gademann, K. Antibiotic algae by chemical surface engineering. ChemBioChem **19,** 439-443 (2018).

26. Szponarski, M., Schwizer, F., Ward, T. R., Gademann, K. On-cell catalysis by surface engineering of live cells with an artificial metalloenzyme. Commun. Chem. **1,** 84 (2018).

27. Shi, P., Ju, E., Yan, Z., Gao, N., Wang, J., Hou, J., Zhang, Y., Ren, J. Qu, X. Spatiotemporal control of cell–cell reversible interactions using molecular engineering. Nat. Commun. **7,** 13088 (2016).

28. Wang, H., Sobral, M. C., Zhang, D. K., Cartwright, A. N., Li, A. W., Dellacherie, M. O., Tringides, C. M., Koshy, S. T., Wucherpfennig, K. W., Mooney, D. J. Metabolic labeling and targeted modulation of dendritic cells. Nat. Mater. **19,** 1244-1252 (2020).

29. Hu, Q., Sun, W., Wang, J., Ruan, H., Zhang, X., Ye, Y., Shen, S., Wang, C., Lu, W., Cheng, K. and Dotti, G., Zeidner, J. F., Wang, J., Gu, Z. Conjugation of haematopoietic stem cells and platelets decorated with anti-PD-1 antibodies augments anti-leukaemia efficacy. Nat. Biomed. Eng. **2,** 831 (2018).

30. Fang, R. H., Kroll, A.V., Gao, W., Zhang, L. Cell membrane coating nanotechnology. Adv. Mater. **30,** 1706759 (2018).

31. Kumar. A., Terakosolphan, W., Hassoun, M., Vandera, K.K., Novicky, A., Harvey, R., Royall, P.G., Bicer, E.M., Eriksson, J., Edwards, K. and Valkenborg, D., Nelissen, I., Hassall, D., Mudway, I. S., Forbes, B. A biocompatible synthetic lung fluid based on human respiratory tract lining fluid composition. Pharm. Res. **34,** 2454-2465 (2017).

32. Tanaka, Y., Nishiyama, Y., Murata, N. Acclimation of the photosynthetic machinery to high temperature in chlamydomonas reinhardtii requires synthesis de novo of proteins encoded by the nuclear and chloroplast genomes. Plant. Physiol. **124,** 441-449 (2000).

33. Singh, S. P., Singh, P. Effect of temperature and light on the growth of algae species: a review. Renew. Sust. Energ. Rev. **50**, 431-444 (2015).

34. Ortiz-Munoz, G., Looney, M. R. Non-invasive intratracheal instillation in Mice. Bio. Protoc. 5, e1504 (2015).

35. Sibille, Y., Reynolds, H. Y. Macrophages and polymorphonuclear neutrophils in lung defense and injury. Am. Rev. Respir. Dis. **141**, 471-501 (1990).

36. Justo, J. A., Danziger, L. H., Gotfried, M. H. Efficacy of inhaled ciprofloxacin in the management of non-cystic fibrosis bronchiectasis. Ther. Adv. Respir. Dis. **7,** 272-287 (2013).

37. Oliver, A., Levin, B. R., Juan, C., Baquero, F., Blázquez, J. Hypermutation and the Preexistence of Antibiotic-Resistant Pseudomonas aeruginosa Mutants: Implications for Susceptibility Testing and Treatment of Chronic Infections. Antimicrob. Agents Chemother. **48**, 4226 (2004).

38. Lovewell, R. R., Patankar, Y. R., Berwin, B. Mechanisms of phagocytosis and host clearance of Pseudomonas aeruginosa. Am. J. Physiol. Lung Cell. Mol. Physiol. **306,** L591–L603 (2014).

39. Hayashi, F., Smith, K. D., Ozinsky, A., Hawn, T. R., Yi, E. C., Goodlett, D. R., Eng, J. K., Akira, S., Underhill, D. M., Aderem, A. The innate immune response to bacterial flagellin is mediated by Toll-like receptor 5. Nature **410**, 1099 (2001).

40. Boyden, E., Zhang, F., Bamberg, E., Nagel, G., Deisseroth, K. Millisecond-timescale, genetically targeted optical control of neural activity. Nat. Neurosci. **8**, 1263–1268 (2005).

41. Sineshchekov, O. A., Jung, K-H., Spudich, J. L. Two rhodopsins mediate phototaxis to low- and high-intensity light in Chlamydomonas reinhardtii. PNAS **99**, 8689-8694 (2002).

42. Akolpoglu, M. B., Dogan, N. O., Bozuyuk, U., Ceylan, H., Kizilel, S., Sitti, M. High-Yield Production of Biohybrid Microalgae for On-Demand Cargo Delivery. Adv Sci. **7**, 2001256 (2020).

43. Delalat, B., Sheppard, V. C., Rasi Ghaemi, S., Rao, S., Prestidge, C. A., McPhee, G., Rogers, M. L., Donoghue, J. F., Pillay, V., Johns, T. G., Kröger, N. Targeted drug delivery using genetically engineered diatom biosilica. Nat. Commun. **6**, 8791 (2015).

44. Martel, S., Mohammadi, M., Felfoul, O., Lu, Z., Pouponneau, P. Flagellated magnetotactic bacteria as controlled MRI-trackable propulsion and steering systems for medical nanorobots operating in the human microvasculature. IJRR **28**, 571-582 (2009).

45. Zhang, Y., Zhang, J., Chen, M., Gong, H., Thamphiwatana, S., Eckmann, L., Gao, W., Zhang, L. A bioadhesive nanoparticle–hydrogel hybrid system for localized antimicrobial drug delivery. ACS Appl. Mater. Inter. 8, 18367 (2016).

46. Sato, M., Murata, Y., Mizusawa, M., Iwahashi, H., Oka, S.-i. A Simple and rapid dual fluorescence viability assay for microalgae. Microbiol. Cult. Coll. 20, 53-59 (2004).

2.2 Microalgae microrobots embedded in capsule for targeted intestinal delivery

2.2.1 Introduction

Oral delivery to the gastrointestinal (GI) tract has been one of the most widely used approaches or drug administration due to its high patient compliance, noninvasiveness, simplicity, and low cost[1,2]. Despite their potential advantages, oral drug formulations face several barriers within the GI tract, including poor stability in gastric fluid, limited drug interaction with the intestinal lining, and low solubility[3]. Several engineered systems, based on microinjectors and microneedles, have been described recently for improving the oral delivery of large biological macromolecules via mechanical penetration mechanisms[4,5]. Other platforms, including bioadhesive patches, responsive hydrogels, mucus-penetrating particles, ionic liquids, and microgrippers, have been reported for enhancing GI delivery via improved tissue adhesion, prolonged retention, and improved drug localization[6–10]. The use of micromotors is another promising and effective approach for the active transport of therapeutic agents to specific sites of interest[11–14]. A variety of synthetic micromotors, capable of propelling to hard-to-reach locations within the body, have been developed for active drug delivery and for other biomedical applications, including biosensing and microsurgery[15–19]. Early in vivo studies using micromotors focused primarily on the GI tract, which can provide a favorable environment for movement[19, 20]. These pioneering studies used chemically powered micromotors based on magnesium (Mg) or zinc microengines for the enhanced delivery of antibiotics, vaccines, and micronutrients[19–22]. These self-propelled micromotors hold particular promise for the local delivery of drug payloads toward the treatment of GI diseases and disorders.[19] Although these active platforms substantially enhanced delivery efficacy compared with corresponding static microcarriers, they suffer from short lifetimes of operation up to about 15 min once in contact with GI fluid. This decreases the potential of these synthetic micromotors to interact with GI mucosa and limits their overall retention, thus leading to decreased drug bioavailability. To address this limitation, active micromotor-based GI drug delivery systems with improved characteristics need to be developed.

Here, we report an algae motor–loaded capsule system that combines the efficient long-lasting movement of natural algae in the small intestine with the protective capabilities of oral capsules, thus enabling prolonged retention within the intestinal mucosa toward greatly improved GI delivery. Microorganisms such as bacteria, sperm, and microalgae have evolved over millions of years to develop robust actuation systems that enable autonomous motion[23]. These natural cellular systems have recently emerged as attractive cargo carriers that are capable of transporting therapeutics to hard-to-reach body locations.[24,25] Combining these motile microorganisms with synthetic materials results in biohybrid systems capable of performing multiple tasks.[26–28] Whereas sperm and bacteria have been used for over a decade in diverse biomedical applications ranging from cancer therapy to assisted fertilization,[29–31] microalgae swimmers have rarely been explored as robotic actuators.[32] Microalgae are eukaryotic swimmers that are facile to culture, and they offer attractive properties for biomedical applications, including efficient propulsion (>100 μm/s), autofluorescence, and phototactic guidance capabilities.

We chose Chlamydomonas reinhardtii as a model microalgal swimmer for active payload delivery in the GI tract because of its many attractive properties, including cytocompatibility, cost-effective scalable production, good adaptability and motility in diverse aqueous environments, abundance of reactive surface groups for functionalization, and autofluorescence for ease of tracking in vivo.[27, 32–34] C. reinhardtii swims by beating its two flagella synchronously at a frequency of 50 Hz,[35] reaching high speeds up to about 200 μm/s.[32, 36] We demonstrate that C. reinhardtii display substantially longer propulsion in intestinal fluid compared with synthetic chemically powered Mg micromotors, which are the only type of self-propelled microrobot swimmers that have been reported for in vivo operation in the GI tract.[19–22] To protect the algae motors from the harsh gastric environment, we embedded them inside a protective capsule (Fig. 2.6, a to c), which was prepared with an inner hydrophobic coating to entrap aqueous solution for maintaining algae viability along with an outer pH-responsive enteric polymer coating. Upon release from the capsule, the algae display constant motility in intestinal fluid (Fig. 2.6d). Compared with the short lifetime of commonly used Mg micromotors, the algae motors remain motile for more than 12 hours at body temperature. In vivo, this prolonged movement leads to notably improved intestinal distribution (Fig. 2.6e), resulting in enhanced retention of a model chemotherapeutic doxorubicin (Dox) conjugated to the algae motors. Overall, our findings indicate that natural algae–based active carriers hold great promise for oral drug delivery to enhance the treatment of GI diseases.

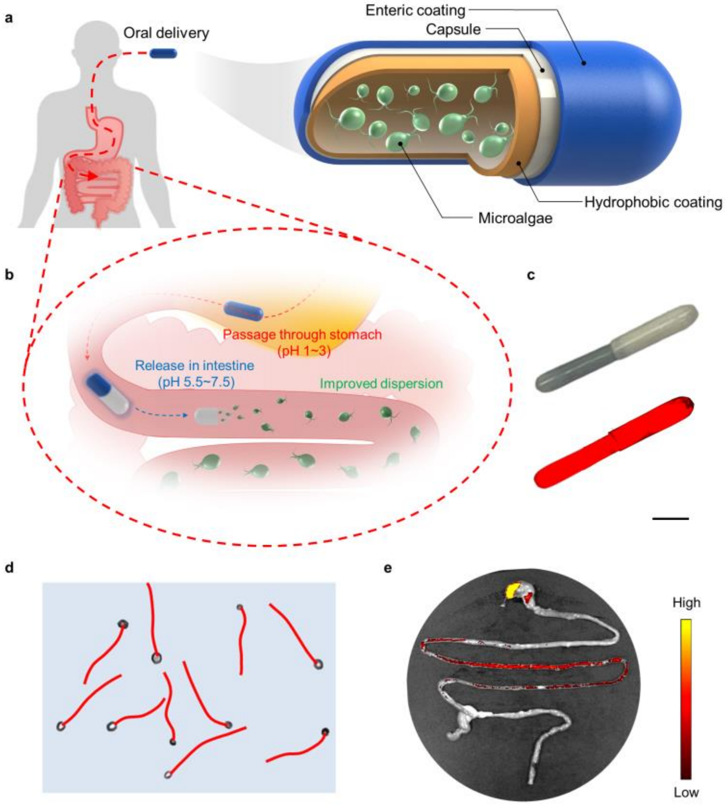

Figure 2.6 Schematic of algae motors in a capsule for GI tract delivery. a, Algae motors loaded within protective capsules containing an inner hydrophobic coating layer and an outer enteric coating layer can be used for oral delivery applications. b, The algae motor–loaded capsule first enters the stomach, where the enteric coating protects it from degradation at acidic gastric pH. Upon entering the intestines, the enteric coating is dissolved in the nearly neutral pH and the capsule is degraded, leading to complete release of the algae motors. c, Bright-field (top) and fluorescent (bottom) images of an algae motor-loaded capsule. Scale bar, 2 mm. d, Representative tracking trajectories demonstrating the autonomous movement of algae motors in simulated intestinal fluid. e, Representative biodistribution of fluorescently labeled algae motors in the GI tract 5 hours after administration in a capsule by oral gavage.

2.2.2 Movement of algae-based micromotors in simulated intestinal fluid

We first studied the motion properties of C. reinhardtii, which are commonly used as a model algal species,[37] and compared them with those of Mg micromotors (Fig. 2.7a). Simulated intestinal fluid (SIF), mainly composed of potassium dihydrogen phosphate at pH 6.8, was used to test the movement of the algae and Mg micromotors. In SIF, the natural algae motors exhibited a stable speed profile of about 120 μm/s that lasted for a minimum of 12 hours. This consistent motile behavior is ascribed to the coordinated, self-sustained beating of algae flagella[38] even under suboptimal survival conditions, such as SIF. In contrast, the speed of Mg micromotors in SIF markedly decreased from an initial 180 to 80 μm/s after 15 min before reaching 0 μm/s after another 15 min. This sharp drop in speed reflects the rapid dissolution and depletion of the Mg engine during propulsion. The percentage of motile Mg motors also dropped to 20% after 15 min of propulsion, whereas 89% of the algae motors remained moving after 12 hours (Fig. 2.7b). In tracing their motion, the movement patterns of algae tracked over 2-s intervals appeared consistent over the course of 12 hours (Fig. 2.7c), whereas no movement was observed for Mg motors after 30 min (Fig. 2.7d). These data illustrated that the algae motors could self-propel efficiently in SIF and maintain consistently fast motility over long periods of time, thereby supporting their potential for active GI delivery applications.

To demonstrate their potential for drug delivery, we modified the algae motors with two different cargos: a fluorescent dye and polymeric nanoparticles (NPs). The green dye fluorescein (excitation/emission = 494 nm/518 nm) was first chemically conjugated to the surface of the algae .[39] After dye conjugation, the algae could be fluorescently tracked (Fig. 2.7, g and h), and the median speed calculated from 100 individual algae was nearly identical to that of unmodified algae (Fig. 2.7, e and f) and consistent with previously reported values.[32,36] Similarly, red blood cell (RBC) membrane–coated poly(lactic-co-glycolic acid) (PLGA) NPs[40] were linked to the algae via click chemistry. To visualize the NPs on the algae, we encapsulated the fluorescent dye 1,1'-dioctadecyl-3,3,3',3'-tetramethylindocarbocyanine (DiI; excitation/emission = 550 nm/567 nm) inside the PLGA core during the fabrication process. The NP-modified algae motors (denoted “algae-NP motors”) exhibited a similar swimming pattern and speed distribution profile in SIF compared with unmodified algae motors (Fig. 2.7, i and j). In addition, the intrinsic phototaxis of the algae was not compromised after the NP functionalization. The data here confirmed that different payloads, ranging from small molecules to NPs, can be successfully loaded onto algae motors without affecting their propulsion characteristics, further highlighting the active GI delivery potential of algae-based motor systems.

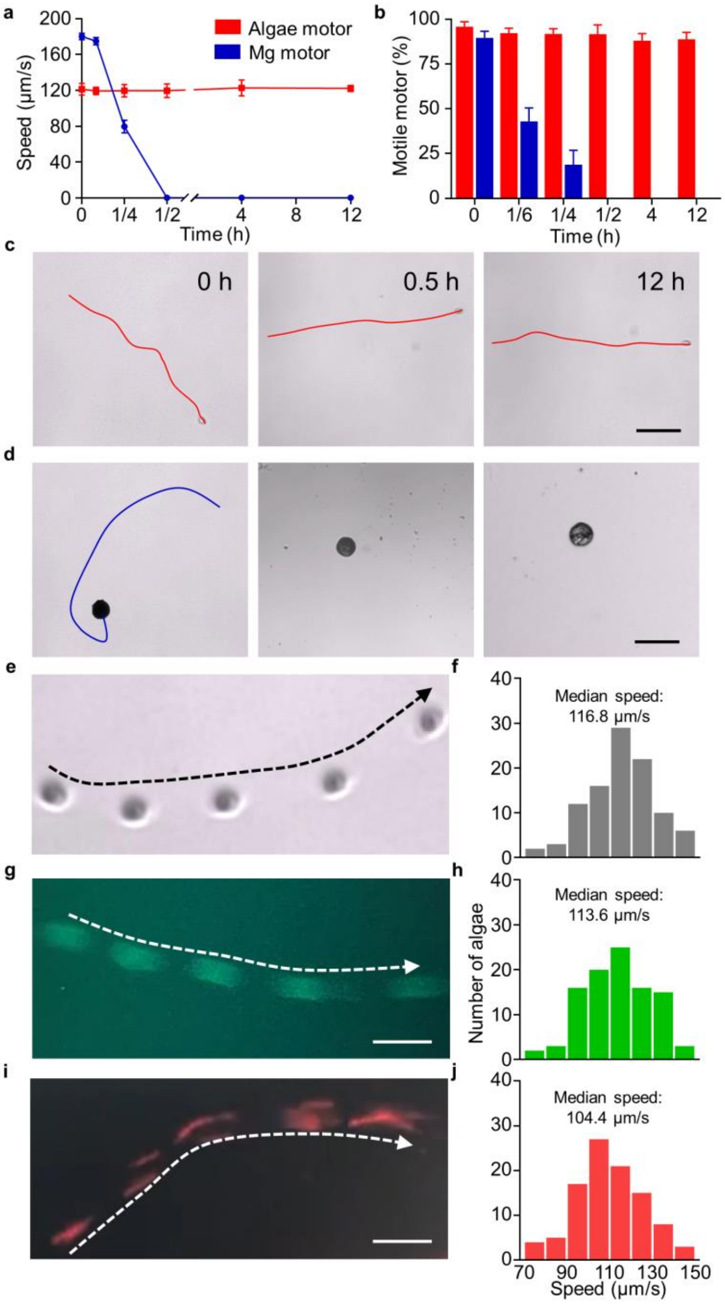

Figure 2.7 Motility of algae motors and Mg motors in SIF at room temperature. a, Speed of algae motors and Mg motors in SIF during 12 hours of operation (n = 5, means ± SD). b, The percentage of motile motors in SIF during a 12-hour period (n = 5, means + SD). c,d, Time-lapse snapshots and trajectories of algae motors (c) and Mg motors (d) over a span of 2 s at different time points during operation. Scale bars, 50 µm. e-j, Time-lapse images showing trajectories over a span of 1 s and corresponding speed distributions of unmodified algae (e and f), fluorescein-labeled algae motors (g and h), and algae motors carrying DiI-loaded RBC membrane–coated NPs (i and j) (n = 100). Scale bars, 20 µm.

2.2.3 Formulation of algae motors into protective capsules

To effectively use algae motors for delivery to the GI tract in vivo, it is necessary to overcome the harsh acidic environment of the stomach, which can degrade the algae before they reach the small intestines. To address this, we modified a commercial capsule to encapsulate viable algae in an internal aqueous medium for safe passage through the stomach. First, an organosilicon solution, consisting of 4% octadecyltrimethoxysilane (OTMS),[41] was prepared to create a thin hydrophobic coating on the inside of the capsule via a thermal evaporation technique. To test the stability of a capsule with this internal coating, we encapsulated an aqueous solution containing rhodamine dye. Visually, the capsule remained unchanged, whereas notable deformation was observed for a control uncoated capsule. By changing the number of coating layers, we could modulate the degradation of the capsules, which is reflected by the release of the dye, with 10 layers of coating offering the longest delay in release in SIF. Second, the exterior surface of the capsule was coated with Eudragit L100-55, a pH-responsive polymer commonly used for protecting oral medication from harsh gastric acid conditions; previous studies have demonstrated the utility of Eudragit L100-55 as an enteric coating for enhancing the delivery of micromotors to the intestines.[42] To imitate physiological conditions in the stomach, we used simulated gastric fluid (SGF) at pH 1.5, containing sodium chloride and hydrochloric acid. In our case, three layers of coating using a 7% (w/v) polymer solution offered full protection of the encapsulated cargo from SGF. Upon changing from SGF to SIF, burst cargo release was observed within 10 min because of dissolution of the enteric coating at higher pH values. These results confirmed that it was possible to load cargo in aqueous solutions using suitably coated capsules for the GI delivery of algae motors.

Next, we investigated the encapsulation of live algae into the modified capsules and their release in vitro. Algae were suspended in tris-acetate-phosphate (TAP) medium and loaded into capsules with 10 inner OTMS layers and 3 outer enteric coating layers. For visualization, the OTMS and enteric coating layers were labeled with 3’,3’-dioctadecyloxacarbocyanine (DiO; excitation/emission = 484 nm/501 nm) and Pacific Blue (excitation/emission = 410 nm/455 nm), respectively. Under fluorescence microscopy, a strong signal was observed for both coating layers along with the autofluorescence of the algae (excitation/emission = 647 nm/680 nm), confirming the successful encapsulation of algae motors into the fabricated capsule platform (Fig. 2.8a). In SGF, it was demonstrated that there was no release of algae from the capsules, whereas the algae motors could be released over time in SIF (Fig. 2.8b). The release in SIF was gradual for about 30 min, after which most of the algae was released by 45 min from the start of the experiment. The total number of released algae reached 9.15×10^5 after 45 min (Fig. 2.8, c and d). Motion tracking of algae motors within the capsule and algae motors released from the capsule revealed similar patterns of movement (Fig. 2.8e). The median speed calculated from 100 individual algae also remained unchanged throughout the fabrication process and after release from the capsules (Fig. 2.8, f and g). These data indicated that the algae motors could be effectively encapsulated and then released from the modified capsule with negligible effect on their swimming performance.

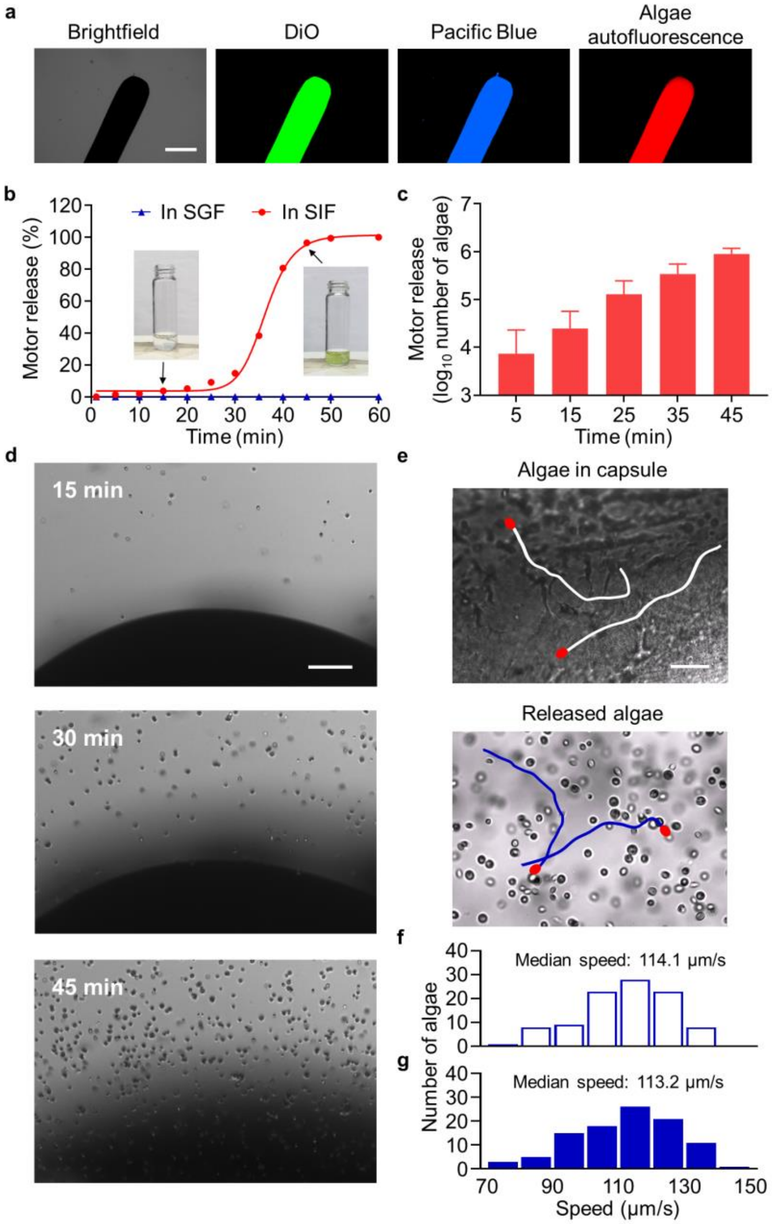

Figure 2.8 Loading and release of algae motors in a capsule in vitro. a, Bright-field and fluorescence microscopy images of autofluorescence of algae motors (red) in a capsule formulation fabricated with a DiO-labeled OTMS inner coating (green) and a Pacific Blue–labeled enteric outer coating (blue). Scale bar, 1 mm. b, Release profile of algae motors from a capsule in SGF (blue line) and SIF (red line). Inset images correspond to t = 15 min (left) and t = 45 min (right). c, Quantification of algae release from capsules over time in SIF (n = 3, means + SD). d, Time-lapse images (t = 15, 30, and 45 min) showing the release of algae motors from a capsule in SIF. Scale bar, 100 µm. e, Representative tracking lines (captured from movie S7) of encapsulated algae motors in TAP medium and released algae motors in SIF. Scale bar, 50 µm. f,g, Speed distribution of the encapsulated algae motors (f) and released algae motors (g) from (e) (n = 100).

After evaluating the release of algae motors from the capsules under in vitro conditions, we investigated the delivery capabilities of the platform within the GI tract. First, mimicking the physiological conditions of the intestines, the motion behavior of algae motors and Mg motors was evaluated in SIF at 37°C in vitro (Fig. 2.9, a and b). The speed of the algae motors was affected by the elevated temperature, decreasing from 113 to 83 μm/s within 15 min of self-propulsion and further dropping to 40 μm/s after 12 hours. At the experimental endpoint, about 70% of the algae remained motile, indicating that they could survive for prolonged periods of time even under unfavorable conditions. In comparison, the conventional Mg motors rapidly lost their movement, with only 33% still propelling at a high speed of 180 μm/s after 5 min. After another 10 min, only 8% remained motile, with an average speed of 80 μm/s. This fast drop in speed and the fraction of motors displaying active motion reflected the rapid depletion of the Mg engine. The algae motors also exhibited the ability to swim in viscous simulated mucus[43] over an extended period of time, whereas the Mg motors did not. These findings illustrated the greatly improved behavior of the algae motors compared with their Mg-based counterparts for potential GI applications requiring prolonged propulsion.

2.2.4 In vivo biodistribution of algae motors after oral delivery

After the in vitro tests, a study was carried out to assess the in vivo biodistribution and retention of the algae motors when delivered orally in capsule form. To facilitate imaging and quantification in biological tissue, we labeled the algae motors and Mg motors with the same fluorescent dye. The algae motors were directly conjugated with fluorescein, whereas the Mg motors were first coated with poly-l-lysine,[44] then conjugated with the dye. As a result, both motors could be easily visualized under fluorescence microscopy and displayed near-identical signals that did not diminish after 6 hours in SIF at 37°C. Next, the algae motors and Mg motors were embedded in the protective capsules and administered by oral gavage to mice. At 5 hours after administration, the mice were euthanized, and their GI tracts were imaged ex vivo (Fig. 2.9c). Whereas a narrow distribution was observed from the fluorescent signal of the Mg motors, the signal for the algae motors was more broadly distributed through the intestines. Quantification of the total radiant efficiency within the small intestines corroborated the improved retention of the algae motors compared with the Mg motors (Fig. 2.9d). The observed differences in biodistribution suggested that algae, with their long-lasting movement properties, could be effective at delivering drug payloads locally within the GI tract.

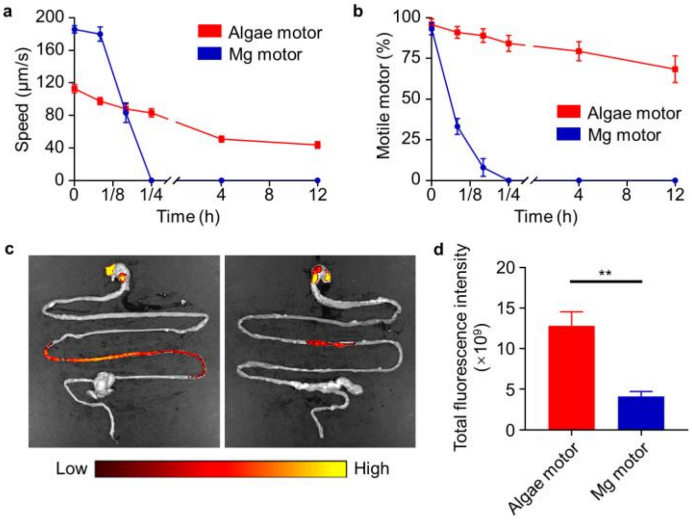

Figure 2.9 Comparison of the distribution of algae motors and Mg motors in the GI tract. a, Speed of algae motors and Mg motors at 37°C in SIF during 12 hours of operation (n = 5, means ± SD). b, Percentage of motile algae motors and Mg motors at 37°C in SIF during 12 hours of operation (n = 5, means ± SD). c, Representative images of the GI tracts of mice 5 hours after oral administration of fluorescein-labeled algae motors in a capsule (left) or Mg motors in a capsule (right). d, Quantitative analysis of total fluorescence intensity within the small intestine from the images in (C) (n = 3, means + SD). Student's two-tailed t test, $^{**}P < 0.01$.

2.2.5 In vivo delivery of therapeutic drugs using algae motor capsules

To better understand the mechanism behind the improved biodistribution and retention of algae motors within the small intestine, we compared our algae motor capsule formulation with different control groups, including TAP medium only (negative control), free algae without a capsule, and static algae in a capsule. To prepare the static algae control, we deflagellated live algae using acetic acid and resuspended them in phosphate-buffered saline (PBS) for encapsulation. Optical visualization and scanning electron microscopy (SEM) images confirmed successful deflagellation and that the resulting static algae lost their motion capabilities in SIF at 37°C. The intrinsic fluorescence of chlorophyll a in algal chloroplasts allows for noninvasive fluorescence imaging of algae without the need for chemical modification .[45] We then proceeded to perform ex vivo fluorescence imaging on the GI tracts of mice receiving the various formulations with equivalent fluorescence to determine the influence of active movement and capsule protection on biodistribution (Fig. 2.10a). At 5 hours after oral administration, algae motors delivered inside capsules were more broadly distributed across the intestines compared with static algae that were also encapsulated. This result highlighted the importance of self-propulsion, which likely helped to increase the interaction of the algae with the intestinal wall, thus leading to enhanced retention. In addition, there was almost no signal observed in the intestines after administration of free algae, demonstrating the necessity of using the capsules to protect from the harsh stomach acid. Quantification of the fluorescent signal from each sample further supported the imaging results, as the fluorescence from the encapsulated algae motor group was 3.5-fold greater than that of the encapsulated static algae group (Fig. 2.10b). To control for the background signal from food contaminants within the stomach,[42,46] we delivered capsules containing algae motors labeled with Cyanine7 (Cy7; excitation/emission = 750 nm/773 nm) orally, and it was confirmed that most of the algae were distributed within the intestine.

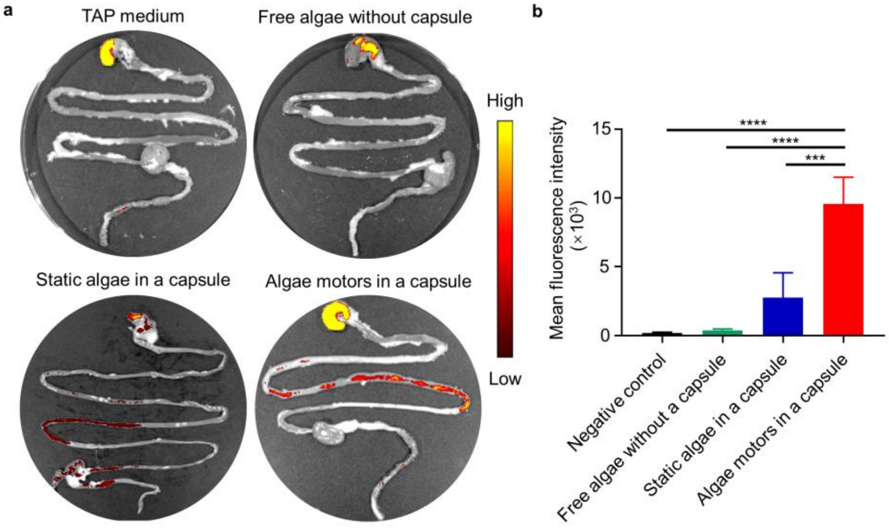

Figure 2.10 GI tract delivery of algae motors in comparison with other algae controls. a, Representative ex vivo fluorescence images of GI tissues of mice 5 hours after oral administration with TAP medium as a negative control, free algae without a capsule, static algae in a capsule, and algae motors in a capsule. b, Quantitative analysis of the mean fluorescence from the experiment in (a) (n = 3, means + SD). One-way ANOVA, ***P < 0.001 and ****P < 0.0001.

We next explored the feasibility of using algae motors for delivering therapeutic drugs to the GI tract. Dox, a commonly used frontline chemotherapeutic agent,[47] was selected as a model drug payload. First, RBC membrane–coated NPs were loaded with Dox [denoted “NP(Dox)”] via a double emulsion solvent evaporation technique.[48,49] Transmission electron microscopy (TEM) imaging confirmed the core-shell structure of the NPs. Fluorescence imaging showed colocalization of the Dox-loaded PLGA cores and the DiO-labeled RBC membrane coating, verifying successful drug loading. Next, NP(Dox) was linked to the algae [denoted "algae-NP(Dox)"] by click chemistry (Fig. 2.11a). Fluorescence and SEM imaging confirmed the effective binding of NP(Dox) to the algae (Fig. 2.11, b and c). To test the Dox loading onto the algae, we incubated 1×10^6 algae with different concentrations of NP(Dox). The Dox loading yield onto the algae was measured at different NP(Dox) inputs, and the maximum loading amount (15 μg) was obtained with a 50-μg input of Dox, corresponding to a 30% loading efficiency per 10^6 cells (Fig. 2.11d). It was also confirmed that Dox, either in free form or nanoparticulate form, did not influence the viability of the algae. The mean and median speed of algae-NP(Dox) measured from 100 individual algae motors were 108.69 and 108.78 μm/s, respectively, and these values were comparable with those of the bare algae (Fig. 2.11, e and f). Furthermore, it was demonstrated that the drug release profile of NP(Dox) was not affected by binding to the algae motors (Fig. 2.11g). After loading onto algae motors, the NP(Dox) payload retained its cytotoxic activity, as it was demonstrated that algae-NP(Dox) could inhibit the growth of B16F10 melanoma cell lines in vitro (Fig. 2.11h). Algae-NP(Dox) and NP(Dox), both loaded into protective capsules, were then administered at the same drug dosage, followed by extraction of the intestines to quantify Dox concentration (Fig. 2.11i). Compared with the tissue homogenates of mice administered with NP(Dox), the samples from mice receiving algae-NP(Dox) exhibited significantly higher drug levels at all of the time points (3, 6, and 9 hours) that were tested. These data further supported the benefits of using algae motors with prolonged active self-propulsion to enhance the delivery and retention of therapeutic payloads in the small intestinal tissues. Future studies will focus on evaluating the potential of algae motors for drug delivery to treat diseases in suitable animal models, such as for inflammatory bowel disease and bacterial gastroenteritis.

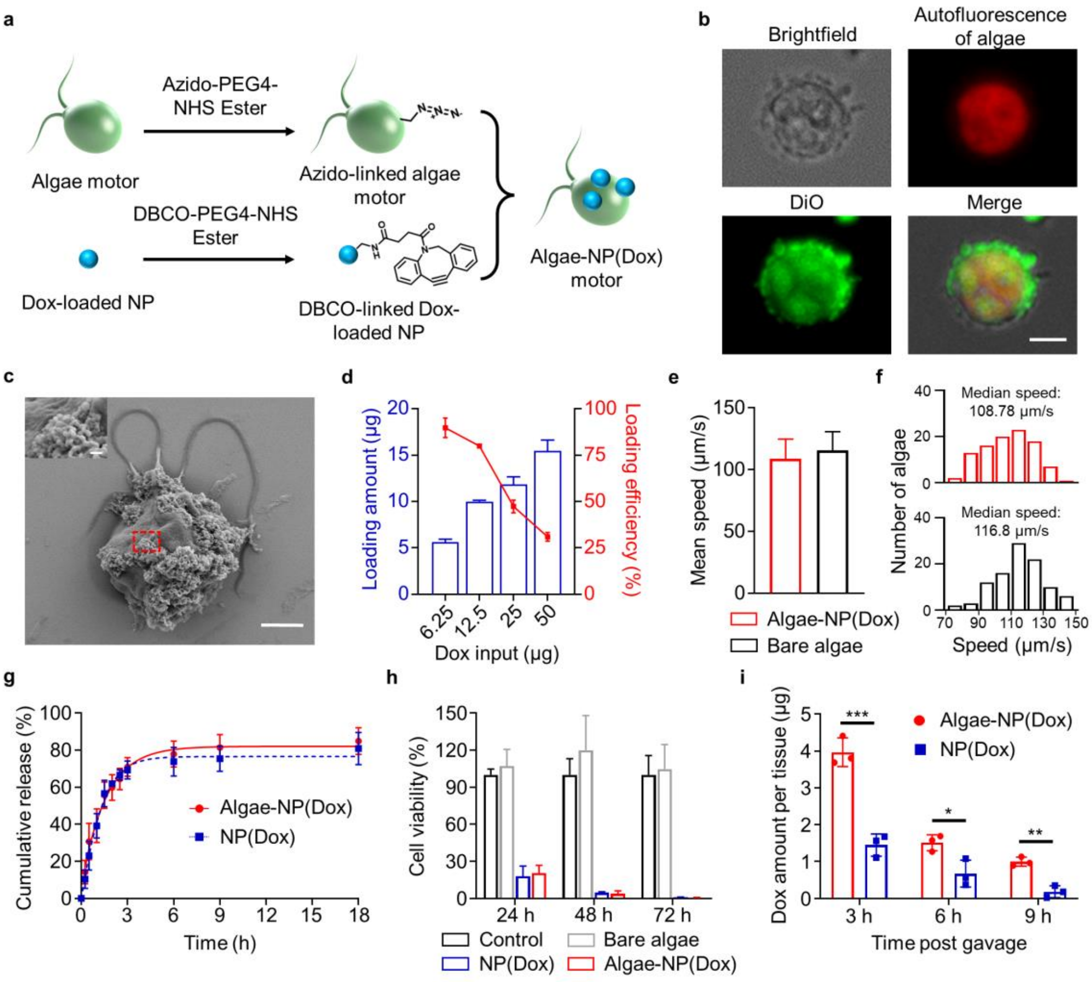

Figure 2.11 Characterization of drug-loaded algae motors. a, Schematic illustration of the fabrication process for the algae-NP(Dox) motor. b, Bright-field and fluorescence microscopy images visualizing the autofluorescence of algae chloroplasts (red) and DiO-labeled RBC membrane (green) to demonstrate the loading of Dox-loaded NPs onto an algae motor. Scale bar, 5 μm. c, SEM image of an algae motor loaded with NP(Dox). Scale bar, 2.5 μm. Inset shows a zoomed-in view corresponding to the dashed red box. Scale bar, 200 nm. d, Quantification of drug loading amount and loading efficiency of 1 × 10^6 algae-NP(Dox) at different Dox inputs (n = 3, means ± SD). e,f, Mean (e) and median (f) speed of algae-NP(Dox) motor and bare algae. The speed was measured from 100 individual alga. g, The cumulative drug release profiles from the algae-NP(Dox) motor and NP(Dox) (n = 3, means ± SD). h, Viability of B16-F10 cancer cell lines after 24, 48, and 72 hours of incubation with blank solution, bare algae, NP(Dox), and algae-NP(Dox) motor (n = 3, means ± SD). i, Quantification of the total Dox content per small intestine at different times after administration of the algae-NP(Dox) motor and NP(Dox) in a capsule (n = 3, means ± SD). Student's multiple t test, $^*P < 0.05$, $^{**}P < 0.01$, and $^{***}P < 0.001$.

2.2.6 In vivo toxicity evaluation of algae motor capsules

Last, we evaluated the in vivo safety profile of the algae motor capsule platform after oral administration. A comprehensive blood chemistry panel and blood cell count were conducted 24 hours after administration (Fig. 2.12, a and b). Compared with untreated control mice, the levels of all serum biochemistry markers and numbers of blood cells (RBCs, white blood cells, and platelets) in the mice receiving algae motor capsule treatment remained at normal levels. A longer-term safety study in which mice were administered with one algae motor capsule on days 0, 2, 4, and 6 also yielded the same result, whereby negligible toxicity, indicated by the minor changes in metabolic biomarkers and blood cell counts, to the mice was observed. Histological analysis of GI tract tissue sections from algae motor-treated mice stained with hematoxylin and eosin (H&E) revealed that structural integrity was preserved and that there was no immune cell infiltration into the mucosa or submucosa, indicating the lack of an inflammatory response (Fig. 2.12c). There was also no observable inflammation or pathological changes on H&E-stained sections from other major organs such as the heart, lungs, liver, kidneys, and spleen (Fig. 2.12d). Overall, these results suggested that the algae motor capsule platform is safe to use for oral drug administration.

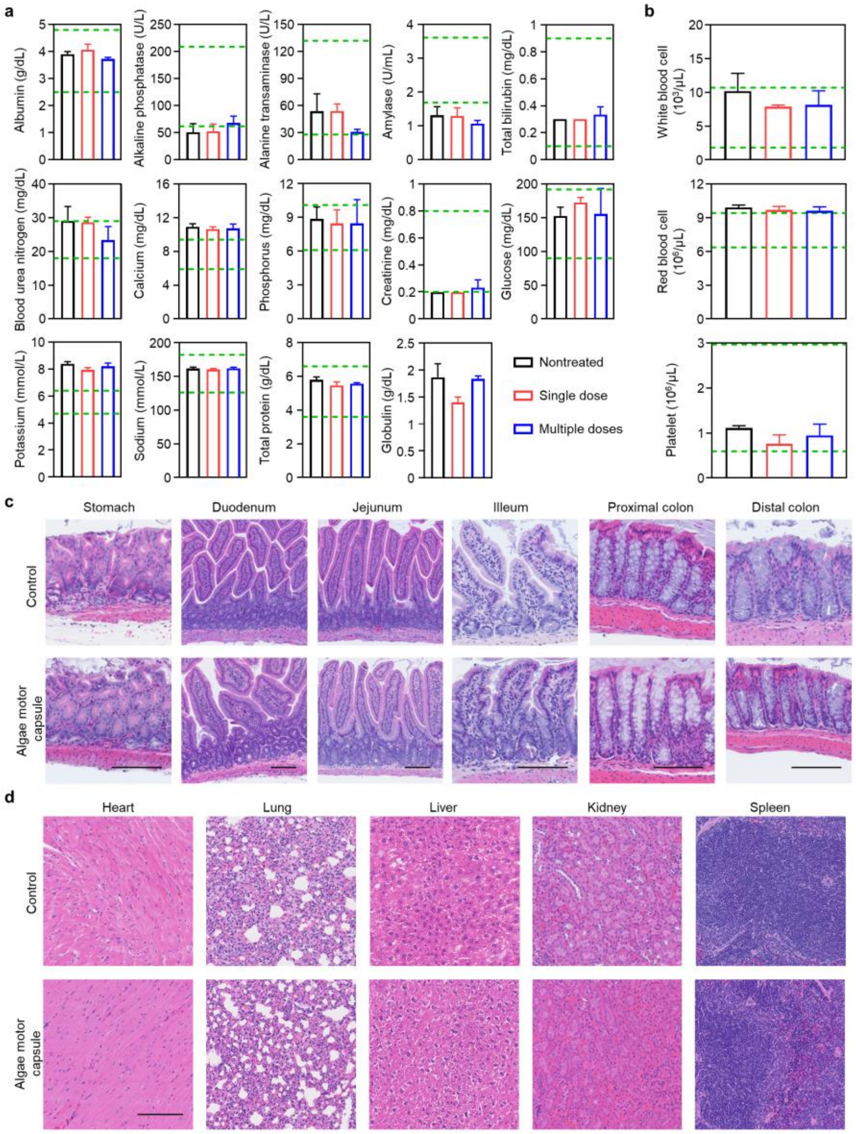

Figure 2.12 In vivo safety analysis of algae motors after oral administration. a,b, Comprehensive blood chemistry panel (a) and blood cell counts (b) taken from nontreated mice, mice with single-dose treatment, and mice with multiple-dose treatment (n = 3, means + SD). For single-dose evaluation, mice were orally administered with one algae motor capsule on day 0, and blood samples were collected on day 1. For multiple-dose evaluation, mice were orally administered with one algae motor capsule on days 0, 2, 4, and 6. Blood samples were collected on day 7. The green dashed lines indicate the mouse reference ranges of each analyte. c, Representative H&E-stained histological sections from different sections of the GI tract from nontreated mice and mice treated with the algae motors in a capsule 24 hours after oral administration. Scale bars, 100 µm. d, H&E-stained histological sections of major organs, including the heart, lungs, liver, kidneys, and spleen, from nontreated mice and mice treated with the algae motors in a capsule 24 hours after oral administration. Scale bar, 250 µm.

2.2.7 Discussion

The development of microorganism-based micromotors for addressing key health care issues is still in its infancy.[25] Although various in vitro studies have illustrated the use of bacteria-based drug delivery systems, there are major risks associated with their in vivo use when considering factors such as pathogenicity or immunogenicity.[24] As an alternative cell type, microalgae are nonpathogenic and have been explored in the development of biohybrid systems.[36,50] Microalgal swimmers recently have been used as biomedical robotic actuators, primarily under in vitro settings.[32] Early in vivo studies have mainly focused on the therapeutic delivery of algae-derived compounds.[51] More recently, a few studies have reported the use of algae as drug carriers for in vivo operation.[45,52] For example, the spiral structure of Spirulina platensis was leveraged to passively prolong retention of curcumin in the intestines for the improved treatment of colon cancer and colitis.[45] In addition, a magnetic NP-loaded microalgae biohybrid imaging system was reported recently, and a swarm of these microswimmers could be externally controlled by a magnetic field and tracked using magnetic resonance imaging.[50] Despite these advances, there have been no studies exploiting the intrinsic self-propulsion of algae for enhanced GI delivery.

In the present study, several key points have been considered to tackle the challenges facing algae-based active GI delivery: protection from the harsh acidic environment of the stomach en route to the intestines, selection of a suitable algal strain with long-lasting self-propulsion in intestinal fluid, and cargo/drug loading capability. By addressing these issues, we demonstrated here an algae motor capsule system for effective intestinal targeting and prolonged tissue retention. Compared with the short lifetime of current Mg-based micromotors, the algae motors displayed prolonged propulsion in GI fluid toward enhanced local delivery for the treatment of potential GI diseases and disorders. To achieve intestinal delivery, we fabricated an enteric-coated capsule modified with an inner hydrophobic organosilicon layer to effectively protect encapsulated algae from the harsh gastric fluid while maintaining their viability. The capsule fabrication, encapsulation, and release processes had a negligible effect on the viability of the algae motors. Modifying capsules in the manner described here provides an effective approach for delivering motile living organisms in aqueous media to the GI tract. To demonstrate the distinct advantages of the platform for in vivo intestinal delivery, we administered algae motor capsules orally, and their biodistribution and retention properties were compared with various controls. The algae motors displayed broader distribution and stronger retention in the GI tract compared with synthetic Mg motors. This was likely mediated by the prolonged motion of the live algae, because it was shown that static algae that were incapable of propulsion exhibited considerably less retention in the intestines. We also demonstrated that the ability of the algae motor capsule system could also be used for the delivery of a model anticancer drug to the GI tract. Moreover, the platform displayed a favorable biosafety profile after oral administration.

The characteristics of the algae motor in a capsule formulation, particularly its long-lasting self-propulsion, can be leveraged for microrobotic biomedical applications beyond the treatment of GI diseases and disorders, ranging from GI detoxication to imaging and sensing. There are several approaches in which algae motors could be improved to enhance their utility for GI delivery applications. For example, the incorporation of imaging agents could enable direct visualization of algae movement as they operate within the intestines. A recent report described a photoacoustic computed tomography–guided microrobotic system for realizing real-time navigation and monitoring of synthetic Mg motors in the intestines in vivo.[53] In another example, positron emission tomography combined with computed tomography was used to evaluate the swarm behavior of enzyme-powered nanomotors in the bladder.[17] By conjugating magnetic microparticles to the algae surface,[32] an external magnetic navigation system could be used to precisely guide and track algae motors to target sites. Whereas the current work focused on demonstrating the potential of algae motor capsules for enhancing intestinal delivery, future work will be required to confirm the therapeutic advantages of the platform in clinically relevant disease models, such as those for bacterial GI infection, irritable bowel disease, or colon cancer. Microalgae can also be engineered to express biologic payloads that can be produced in situ after oral administration.[54,55] The properties of the capsules can be tuned to more precisely target specific regions of the GI tract.[42] Overall, functionalized algae motors, loaded within a protective capsule, represent an attractive biohybrid motor system that can be applied across a wide range of biomedical applications.

2.2.8 Experimental section

Algae culture. The green algae C. reinhardtii (strain CC-125 wild-type mt+) were obtained from the Chlamydomonas Resource Center. The algae were transferred from the agar plate to TAP medium (Thermo Fisher Scientific) and cultured at room temperature under cycles of 12-hour sunlight and 12-hour dark.

Preparation of Mg micromotors. Mg micromotors were fabricated using 20 ± 5–µm commercial Mg microparticles (FMW20, Tangshan Weihao Magnesium Powder Co.) as the core. The Mg microparticles were washed two times with acetone and dried under an N2 current to remove impurities. Then, ~10 mg of Mg microparticles were dispersed onto glass slides, which were previously coated with 100 µl of 0.5% polyvinylpyrrolidone ethanolic solution (Spectrum Chemical). A coating of TiO2 was deposited onto the Mg microparticles by atomic layer deposition at 100°C for 3000 cycles using a Beneq TFS 200 System, leaving a small opening at the contact point between the Mg particles and the glass slide. Last, the Mg micromotors were released by gentle scratching from the glass slide. For surface modification with a fluorescent dye, 0.5 mg of Mg micromotors were first mixed with 0.1% poly-l-lysine (Sigma-Aldrich) aqueous solution for 30 min. Then, 2 µg of 5/6-carboxyfluorescein succinimidyl ester (NHS-fluorescein; Thermo Fisher Scientific) was mixed with the motors in PBS buffer for 1 hour. The resulting fluorescein-labeled Mg micromotors were centrifuged at 3000g for 3 min, washed with ultrapure water, and dried for further use.

Preparation of fluorescent dye–labeled algae. Green algae were washed three times with ultrapure water to remove TAP medium and then suspended in HEPES buffer (Thermo Fisher Scientific). Then, 2 µg of NHS-fluorescein was added to 1 ml of algae at 2×10^6 per ml and incubated for 1 hour at room temperature. After dye conjugation, the modified algae were washed three times with TAP medium to remove free dye, and then they were suspended in TAP medium for further use. Near-infrared dye-labeled algae were prepared with a similar method by replacing NHS-fluorescein with NHS-Cy7 (Lumiprobe).

Synthesis of Dox-loaded polymeric NPs. Dox-loaded polymeric NPs were synthesized following a published method with slight modification (49). First, 50 µl of 25 mg/ml Dox-HCl (Sigma-Aldrich) solution was emulsified in 500 µl of a chloroform solution containing PLGA (50 mg/ml; 50:50, 0.66 dl/g; LACTEL Absorbable Polymers) using a Fisher Scientific FB120 ultrasonic probe sonicator operating at a power of 10 W. The process lasted for 2 min with alternating cycles of 2-s power on and 2-s power off in an ice bath. Then, the emulsion was transferred to 5 ml of tris-HCl (Teknova) aqueous solution and sonicated for another 2 min. The emulsion was stirred for 3 hours to completely remove the chloroform. The NPs were centrifuged at 16,100g for 5 min, washed three times with ultrapure water, and lyophilized for further use. NPs loaded with DiI (Thermo Fisher Scientific) were prepared using a similar procedure by replacing Dox with the dye.

Synthesis of cell membrane–coated NPs. RBC membrane–coated NPs were synthesized by a membrane cloaking technique (40). RBC membrane was mixed with PLGA cores at a 1:1 membrane protein to polymer weight ratio. The mixture was sonicated in a Fisher Scientific FS30D ultrasonic bath sonicator for 3 min. The NPs were isolated by centrifugation for 5 min at 16,100g and washed three times with ultrapure water. To characterize NP morphology, we deposited samples onto a carbon-coated 400-mesh copper grid and stained them with 1 weight % of uranyl acetate (Electron Microscopy Sciences), followed by imaging on a JEOL 1200 EX II TEM.

Preparation of algae-NP motors. To attach NPs onto algae, we washed 1×10^7 green algae three times with ultrapure water and treated them with 20 μM dibenzocyclooctyne-(polyethylene glycol)4-N-hydroxysuccinimidyl ester (DBCO-PEG4-NHS; Click Chemistry Tools) for 1 hour at room temperature. The NPs were incubated with 20 μM azide-PEG4-NHS for 1 hour at room temperature. Both the algae and NPs were washed five times with ultrapure water to remove the unreacted NHS ester. Then, the modified algae and NPs were mixed together and vortexed for 3 hours to complete the click chemistry reaction. After conjugation, the resulting algae-NP motors were separated by centrifugation for 3 min at 500g, washed three times with TAP medium, and resuspended in TAP medium for further use. NP(Dox) conjugation onto the algae followed a similar method by replacing NPs with NP(Dox). To evaluate the NP(Dox) loading efficiency, we conjugated algae motors at 1 × 10^6/ml to NP(Dox) with Dox content at different concentrations (6.25, 12.5, 25, and 50 μg/ml). After fabrication of the algae-NP(Dox) motor, Dox content in unbound NP(Dox) was quantified by measuring the absorbance at 480 nm using a ultraviolet-visible spectrometer. The Dox loading amount on the algae motor was calculated by subtracting the unbound Dox from the Dox input.

Phototaxis of algae-NP motors. Phototaxis studies were conducted in three-dimensional printed microfluidic channels with a 5-mm by 4-mm by 2-mm chamber. Before testing, the channel was prefilled with 50 μl of TAP medium. Then, the algae-NP motors were added to one side of the channel, whereas the other side was illuminated using a light-emitting diode white light for 500 s. As a control, algae motors were added to one side without a light source on the other side. Time-lapse videos were recorded at 10 s per frame using an Invitrogen EVOS FL fluorescence microscope with a 2× objective.

Influence of Dox on algae viability. To evaluate the influence of free drug, we suspended algae motors at 1 × 10^6/ml into solutions containing different concentrations (0, 5, 10, and 25 μg/ml) of Dox. After 24 hours of incubation, each sample was collected, washed three times with ultrapure water to remove free drug, and resuspended into ultrapure water. Next, the samples were stained in 5 μM SYTOX fluorescent probe (Thermo Fisher Scientific) to measure algae viability. A similar method was used to test the viability of algae after conjugation of NP(Dox).

In vitro anticancer activity of algae-NP(Dox) motors. B16-F10 mouse melanoma cell lines (CRL-6475, American Type Culture Collection) were seeded into a 96-well plate at 5 × 10^4 per well and further incubated with free Dulbecco’s modified Eagle’s medium, free Dox, free algae, and algae-

NP(Dox) motors for 24, 48, and 72 hours. All drug-containing wells used the same Dox concentration of 50 μg/ml. An MTS assay (Promega) was used to evaluate the cell viability per the manufacturer’s protocol.

Algae motility analysis. To evaluate their motion, we suspended unmodified algae motors, fluorescein-conjugated algae motors, and algae-NP motors in SIF (RICCA Chemical). Then, the algae were observed at 0 min, 5 min, 15 min, 30 min, 4 hours, and 12 hours at room temperature (22°C). In a separate experiment, algae were observed at 0 min, 5 min, 10 min, 15 min, 4 hours, and 12 hours at body temperature (37°C). For Mg micromotor motion analysis, the motors were uniformly dispersed on a glass slide, followed by addition of SIF solution. Motion was evaluated at the same time points as above, and SIF was continuously supplemented to prevent the motors from drying. To test the influence of NP(Dox) on motility, we measured the motion of algae-NP(Dox) motors in SIF. To evaluate the operation of algae motors in a mucus-rich environment, we analyzed their motion behavior in a simulated porcine small intestinal mucus containing mucin (20 mg/ml; Alfa Aesar) (43). Bright-field movies were captured by a Nikon Eclipse Ti-S/L100 inverted optical microscope coupled with different objectives (10× and 20×) and a Hamamatsu digital camera C11440. Meanwhile, fluorescent movies were captured using a Sony RX100 V camera on an Invitrogen EVOS FL fluorescence microscope with different objectives (20× and 40×) in two fluorescence channels, green fluorescent protein (GFP) and red fluorescent protein, corresponding to fluorescein and DiI. An NIS Element tracking module was used to measure the speed of the motors in SIF.

Characterization of algae-NP motors. To confirm NP binding on the surface of the algae motors, we labeled the RBC membrane on the NPs beforehand with DiO (Thermo Fisher Scientific).

Fluorescence microscopy images were captured by using an Invitrogen EVOS FL microscope in two fluorescence channels, Cy5 and GFP, corresponding to the autofluorescence of the algae and DiO. To further confirm the structure of algae-NP motors, we performed SEM to visualize their morphology. The algae-NP motors were first fixed with a 2.5% glutaraldehyde solution (Sigma-Aldrich) overnight at 4°C and then washed three times with ultrapure water. The samples were sputtered with palladium for imaging on a Zeiss Sigma 500 SEM instrument using an acceleration voltage of 3 kV.

Fabrication of algae motor capsules. Mouse-specific size M gel capsules were supplied by Torpac. To perform the hydrophobic inner coating, we prepared 4% (w/w) of OTMS (Tokyo Chemical Industry) solution in pure ethanol and stirred it at room temperature for 2 hours. An insulin syringe was used to fill the capsule with ~4 µl of the OTMS solution, followed by a curing process at 120°C for 1 hour to completely evaporate the solvent. This process was repeated for up to 10 times to add more coating layers, and the capsules were stored at room temperature. For algae motor encapsulation, 4 µl of algae at a concentration of 2.5×10^5 per µl in TAP medium was slowly injected into the capsule using a primed syringe pump. After algae encapsulation, the commercial enteric coating polymer Eudragit L100-55 (Evonik Industries) was selected to coat the capsule for protection from gastric acid. First, the enteric coating polymer was dissolved at 7% (w/v) in ethanol solution by stirring at room temperature overnight. The capsules were then immersed into the enteric coating solution with a dip-coating approach, followed by solvent evaporation for a total of three times. After enteric coating, the capsules were stored at room temperature. To evaluate the release of algae motors from the capsule formulation, we immersed the loaded capsules either into SGF at pH 1.5 comprising 0.2% (w/w) sodium chloride and 0.31% (w/w) hydrochloric acid or into SIF at pH 6.8 containing 0.68% (w/w) potassium dihydrogen phosphate and 0.15% (w/w) sodium hydroxide under stirring at 700 rpm. For biodistribution studies, the static algae control (1 × 10^6), fluorescein-conjugated algae (2 × 10^6), fluorescein-labeled Mg motors (0.5 mg), and algae-NP(Dox) motors (5 μg of Dox) were encapsulated by a similar process. To generate the static algae control, we rapidly treated live algae with 0.5 M acetic acid to remove their flagella. To quantify the autofluorescence of algae motor and static algae samples, we used a Tecan Infinite M200 plate reader.

Animal care. Mice were housed in an animal facility at the University of California San Diego (UCSD) under federal, state, local, and National Institutes of Health (NIH) guidelines. Six-week-old CD-1 male mice were purchased from Charles River Labs. Mice were maintained in standard housing with cycles of 12-hour light and 12-hour dark, ambient temperature, and normal humidity. All animal experiments were performed in accordance with NIH guidelines and approved by the Institutional Animal Care and Use Committee of UCSD.

Pharmacokinetics and biodistribution studies. To characterize the biodistribution of algae motors, we fed male CD-1 mice an alfalfa-free diet (LabDiet, St. Louis, MO, USA) starting 1 week before the experiments. To compare the biodistribution between fluorescein-labeled algae motors (2 × 10^6) and Mg-based motors (0.5 mg), we administered mice with the corresponding capsules containing the motors labeled with equal amounts of dye. To evaluate the influence of active propulsion and capsule protection, we administered mice with encapsulated active algae (1 × 10^6), encapsulated static algae (1 × 10^6), unencapsulated active algae (1 × 10^6), or PBS by oral gavage. The mice were euthanized at 5 hours after administration. The entire GI tracts were then collected, rinsed with PBS, and imaged using a Xenogen IVIS 200 system. For quantitative fluorescent measurements, the collected tissues were weighed and then homogenized in PBS. The fluorescent signals were quantified using a Tecan Infinite M200 plate reader. To evaluate drug retention, we administered male CD-1 mice with algae-NP(Dox) motor capsules (5 μg of Dox), NP(Dox) capsules (5 μg of Dox), and PBS via oral gavage. At 3, 6, and 9 hours after oral administration, the GI tracts were then collected, weighed, and then homogenized in PBS. The amount of Dox was quantified using a Tecan Infinite M200 plate reader based on absorbance readings at 480 nm.

In vivo safety studies. Mice were euthanized at 24 hours after oral administration of TAP medium or encapsulated algae motors (1×10^6). For the comprehensive metabolic panel, aliquots of blood were allowed to coagulate, and the serum was collected by centrifugation. To obtain blood cell counts, we collected whole blood into potassium EDTA collection tubes (Sarstedt). For long-term safety, mice were administered algae motors in a capsule on days 0, 2, 4, and 6, and they were euthanized for analysis on day 7. Laboratory tests were performed by the UCSD Animal Care Program Diagnostic Services Laboratory. To perform the histological analysis, we sectioned different parts of the GI tract and major organs and stained them with H&E (Leica Biosystems), followed by imaging using a Hamamatsu Nanozoomer 2.0-HT slide scanning system.

Statistical analysis. All experiments were repeated as independent experiments several times, as shown by the figure captions. The results are reported as means ± SD. A two-tailed, Student's t test was used for testing the significance between two groups. A one-way analysis of variance (ANOVA) with Dunnett's test was performed to test the significance for multiple comparisons. Statistical significance is indicated as $^{*}P < 0.05$, $^{**}P < 0.01$, $^{***}P < 0.001$, and $^{****}P < 0.0001$. No data were excluded from the analysis. Samples were randomly allocated to different experimental groups. Organisms were cultured and maintained in the same environment and randomly allocated to each group. Investigators were not blinded during data collection and analysis.

Chapter 2.2, in full, is a reprint of the material as it appears in Science Robotics, 2022, by Fangyu Zhang, Zhengxing Li, Yaou Duan, Amal Abbas, Rodolfo Mundaca-Uribe, Lu Yin, Hao Luan, Weiwei Gao, Ronnie H. Fang, Liangfang Zhang, Joseph Wang. The dissertation author was the primary investigator and author of this paper.

2.2.9 References

1. J. Li, B. E.-F. de Ávila, W. Gao, L. Zhang, J. Wang, Micro/nanorobots for biomedicine: Delivery, surgery, sensing, and detoxification. *Sci. Robot.* **2**, eaam6431 (2017).

2. S. Hua, Advances in oral drug delivery for regional targeting in the gastrointestinal tract-influence of physiological, pathophysiological and pharmaceutical factors. Front. Pharmacol. 11, 524 (2020).

3. L. M. Ensign, R. Cone, J. Hanes, Oral drug delivery with polymeric nanoparticles: the gastrointestinal mucus barriers. *Adv. Drug Deliv. Rev.* **64**, 557-570 (2012).

4. A. Abramson, M. R. Frederiksen, A. Vegge, B. Jensen, M. Poulsen, B. Mouridsen, M. O. Jespersen, R. K. Kirk, J. Windum, F. Hubálek, J. J. Water, J. Fels, S. B. Gunnarsson, A. Bohr, E. M. Straarup, M. W. Hvitfeld Ley, X. Lu, J. Wainer, J. Collins, S. Tamang, K. Ishida, A. Hayward, P. Herskind, S. T. Buckley, N. Roxhed, R. Langer, U. Rahbek, G. Traverso, Oral delivery of systemic monoclonal antibodies, peptides and small molecules using gastric auto-injectors. *Nat. Biotechnol.* **40,** 103-109 (2022).

5. A. Abramson, E. Caffarel-Salvador, V. Soares, D. Minahan, R. Y. Tian, X. Lu, D. Dellal, Y. Gao, S. Kim, J. Wainer, J. Collins, S. Tamang, A. Hayward, T. Yoshitake, H-C, Lee, J. Fujimoto, J. Fels, M. R. Frederiksen, U. Rahbek, N. Roxhed, R. Langer, G. Traverso. A luminal

unfolding microneedle injector for oral delivery of macromolecules. *Nat. Med.* **25,** 1512–1518 (2019).

6. J. Wu, H. Yuk, T. L. Sarrafian, C. F. Guo, L. G. Griffiths, C. S. Nabzdyk, X. Zhao, An off-the-shelf bioadhesive patch for sutureless repair of gastrointestinal defects. *Sci. Transl. Med.* **14,** eabh2857 (2022).

7. X. Liu, C. Steiger, S. Lin, G. A. Parada, J. Liu, H. F. Chan, H. Yuk, N. V. Phan, J. Collins, S. Tamang, G. Traverso, X. Zhao, Ingestible hydrogel device. *Nat. Commun.* **10,** 493 (2019).

8. N. G. Lamson, A. Berger, K. C. Fein, K. A. Whitehead, Anionic nanoparticles enable the oral delivery of proteins by enhancing intestinal permeability. *Nat. Biomed. Eng.* **4,** 84–96 (2020).
9. P. Angsantikul, K. Peng, A. M. Curreri, Y. Chua, K. Z. Chen, J. Ehondor, S. Mitraotri, Ionic liquids and deep eutectic solvents for enhanced delivery of antibodies in the gastrointestinal tract. *Adv. Funct. Mater.* **31,** 2002912 (2020).

10. A. Ghosh, L. Li, R. P. Dash, N. Gupta, J. Lam, Q. Jin, V. Akshintala, G. Pahapale, W. Liu, A. Sarkar, R. Rais, D. H. Gracias, F. M. Selaru, Gastrointestinal-resident, shape-changing microdevices extend drug release in vivo. *Sci. Adv.* **6,** eabb4133 (2020).

11. C. Gao, Y. Wang, Z. Ye, Z. Lin, X. Ma, Q. He, Biomedical micro-/nanomotors: From overcoming biological barriers to in vivo imaging. *Adv. Mater.* **33**, 2000512 (2020).

12. C. K. Schmidt, M. Medina-Sánchez, R. J. Edmondson, O. G. Schmidt, Engineering microrobots for targeted cancer therapies from a medical perspective. *Nat. Commun.* **11**, 1-18 (2020).

13. Z. Wu, Y. Chen, D. Mukasa, O. S. Pak, W. Gao, Medical micro/nanorobots in complex media. *Chem. Soc. Rev.* **49**, 8088-8112 (2020).

14. B. Wang, K. Kostarelos, B. J. Nelson, L. Zhang, Trends in micro-/nanorobotics: Materials development, actuation, localization, and system integration for biomedical applications. *Adv. Mater.* **33**, 2002047 (2020).

15. B. Wang, K. F. Chan, K. Yuan, Q. Wang, X. Xia, L. Yang, H. Ko, Y.-X. J. Wang, J. J. Y. Sung, P. W. Y. Chiu, L. Zhang, Endoscopy-assisted magnetic navigation of biohybrid soft microrobots with rapid endoluminal delivery and imaging. *Sci. Robot.* **6**, eabd2813 (2021).

16. H. Zhang, Z. Li, C. Gao, X. Fan, Y. Pang, T. Li, Z. Wu, H. Xie, Q. He, Dual-responsive biohybrid neutrobots for active target delivery. *Sci. Robot.* **6**, eaaz9519 (2021).

17. A. C. Hortelao, C. Simó, M. Guix, S. Guallar-Garrido, E. Julián, D. Vilela, L. Rejc, P. Ramos-Cabrer, U. Cossío, V. Gómez-Vallejo, T. Patiño, J. Llop, S. Sánchez, Swarming behavior and in vivo monitoring of enzymatic nanomotors within the bladder. *Sci. Robot.* **6**, eabd2823 (2021).

18. Z. Wu, J. Troll, H.-H. Jeong, Q. Wei, M. Stang, F. Ziemssen, Z. Wang, M. Dong, S. Schnichels, T. Qiu, P. Fischer, A swarm of slippery micropropellers penetrates the vitreous body of the eye. *Sci. Adv.* **4**, eaat4388 (2018).

19. B. E.-F. de Ávila, P. Angsantikul, J. Li, M. A. Lopez-Ramirez, D. E. Ramírez-Herrera, S. Thamphiwatana, C. Chen, J. Delezuk, R. Samakapiruk, V. Ramez, M. Obonyo, L. Zhang, J. Wang, Micromotor-enabled active drug delivery for in vivo treatment of stomach infection. *Nat. Commun.* **8**, 272 (2017).

20. X. Wei, M. Beltrán-Gastélum, E. Karshalev, B. Esteban-Fernández de Ávila, J. Zhou, D. Ran, P. Angsantikul, R. H. Fang, J. Wang, L. Zhang, Biomimetic micromotor enables active delivery of antigens for oral vaccination. *Nano Lett.* **19**, 1914-1921 (2019).

21. L. Cai, C. Zhao, H. Chen, L. Fan, Y. Zhao, X. Qian, R. Chai, Suction-cup-inspired adhesive micromotors for drug delivery. *Adv. Sci.* **9**, 2103384 (2021).

22. E. Karshalev, Y. Zhang, B. Esteban-Fernández de Ávila, M. Beltrán-Gastélum, Y. Chen, R. Mundaca-Uribe, F. Zhang, B. Nguyen, Y. Tong, R. H. Fang, L. Zhang, J. Wang, Micromotors for active delivery of minerals toward the treatment of iron deficiency anemia. *Nano Lett.* **19**, 7816-7826 (2019).

23. J. Wang, Nanomachines: Fundamentals and applications (John Wiley & Sons, 2013).

24. Z. Hosseinidoust, B. Mostaghaci, O. Yasa, B.-W. Park, A. V. Singh, M. Sitti, Bioengineered and biohybrid bacteria-based systems for drug delivery. *Adv. Drug Deliv. Rev.* **106**, 27-44 (2016).

25. L. Ricotti, B. Trimmer, A. W. Feinberg, R. Raman, K. K. Parker, R. Bashir, M. Sitti, S. Martel, P. Dario, A. Menciassi, Biohybrid actuators for robotics: A review of devices actuated by living cells. *Sci. Robot.* **2**, eaaq0495 (2017).

26. V. Magdanz, S. Sanchez, O. G. Schmidt, Development of a sperm-flagella driven micro-bio-robot. *Adv. Mater.* **25**, 6581-6588 (2013).

27. F. Zhang, Z. Li, L. Yin, Q. Zhang, N. Askarinam, R. Mundaca-Uribe, F. Tehrani, E. Karshalev, W. Gao, L. Zhang, J. Wang, ACE2 receptor-modified algae-based microrobot for removal of SARS-CoV-2 in wastewater. *J. Am. Chem. Soc.* **143**, 12194-12201 (2021).

28. O. Felfoul, M. Mohammadi, S. Taherkhani, D. De Lanauze, Y. Z. Xu, D. Loghin, S. Essa, S. Jancik, D. Houle, M. Lafleur, L. Gaboury, M. Tabrizian, N. Kaou, M. Atkin, T. Vuong, G. Batist, N. Beauchemin, D. Radzioch, S. Martel, Magneto-aerotactic bacteria deliver drug-containing nanoliposomes to tumour hypoxic regions. *Nat. Nanotechnol.* **11**, 941 (2016).

29. H. Xu, M. Medina-Sánchez, V. Magdanz, L. Schwarz, F. Hebenstreit, O. G. Schmidt, Sperm-hybrid micromotor for targeted drug delivery. *ACS Nano* **12**, 327-337 (2017).

30. M. Medina-Sánchez, L. Schwarz, A. K. Meyer, F. Hebenstreit, O. G. Schmidt, Cellular cargo delivery: Toward assisted fertilization by sperm-carrying micromotors. *Nano Lett.* **16**, 555-561 (2015).

31. S. Xie, L. Zhao, X. Song, M. Tang, C. Mo, X. Li, Doxorubicin-conjugated Escherichia coli Nissle 1917 swimmers to achieve tumor targeting and responsive drug release. *J. Control. Release* **268**, 390-399 (2017).

32. O. Yasa, P. Erkoc, Y. Alapan, M. Sitti, Microalga-powered microswimmers toward active cargo delivery. *Adv. Mater.* **30**, 1804130 (2018).

33. M. B. Akolpoglu, N. O. Dogan, U. Bozuyuk, H. Ceylan, S. Kizilel, M. Sitti, High-yield production of biohybrid microalgae for on-demand cargo delivery. *Adv. Sci.* **7**, 2001256 (2020).

34. I. P. Kerschgens, K. Gademann, Antibiotic algae by chemical surface engineering. *ChemBioChem* **19**, 439-443 (2018).

35. T. J. Böddeker, S. Karpitschka, C. T. Kreis, Q. Magdelaine, O. Bäumchen, Dynamic force measurements on swimming Chlamydomonas cells using micropipette force sensors. *J. R. Soc. Interface* **17**, 20190580 (2020).

36. D. B. Weibel, P. Garstecki, D. Ryan, W. R. DiLuzio, M. Mayer, J. E. Seto, G. M. Whitesides, Microoxen: Microorganisms to move microscale loads. *Proc. Natl. Acad. Sci. U.S.A.* **102**, 11963-11967 (2005).

37. B. P.-H. Huang, Chlamydomonas reinhardtii: A model system for the genetic analysis of flagellar structure and motility. *Int. Rev. Cytol.* **99**, 181-215 (1986).

38. K. Y. Wan, R. E. Goldstein, Coordinated beating of algal flagella is mediated by basal coupling. *Proc. Natl. Acad. Sci. U.S.A.* **113**, E2784-E2793 (2016).

39. S. Kalkhof, A. Sinz, Chances and pitfalls of chemical cross-linking with amine-reactive N-hydroxysuccinimide esters. *Anal. Bioanal. Chem.* **392**, 305-312 (2008).

40. C.-M. J. Hu, L. Zhang, S. Aryal, C. Cheung, R. H. Fang, L. Zhang, Erythrocyte membrane-camouflaged polymeric nanoparticles as a biomimetic delivery platform. *Proc. Natl. Acad. Sci. U.S.A.* **108**, 10980-10985 (2011).

41. J. D. Cox, M. S. Curry, S. K. Skirboll, P. L. Gourley, D. Y. Sasaki, Surface passivation of a microfluidic device to glial cell adhesion: a comparison of hydrophobic and hydrophilic SAM coatings. *Biomaterials* **23**, 929-935 (2002).

42. J. Li, S. Thamphiwatana, W. Liu, B. Esteban-Fernández de Ávila, P. Angsantikul, E. Sandraz, J. Wang, T. Xu, F. Soto, V. Ramez, X. Wang, W. Gao, L. Zhang, J. Wang, Enteric micromotor

can selectively position and spontaneously propel in the gastrointestinal tract. *ACS Nano* **10**, 9536-9542 (2016).

43. M. Boegh, H. M. Nielsen, Mucus as a Barrier to Drug Delivery – Understanding and Mimicking the Barrier Properties. *Basic & Clinical Pharmacology & Toxicology* **116,** 179-186 (2015).

44. F. Zhang, R. Mundaca-Uribe, H. Gong, B. Esteban-Fernández de Ávila, M. Beltrán-Gastélum, E. Karshalev, A. Nourhani, Y. Tong, B. Nguyen, M. Gallot, Y. Zhang, L. Zhang, J. Wang, A macrophage–magnesium hybrid biomotor: Fabrication and characterization. *Adv. Mater.* **31**, 1901828 (2019).

45. D. Zhong, D. Zhang, W. Chen, J. He, C. Ren, X. Zhang, N. Kong, W. Tao, M. Zhou, Orally deliverable strategy based on microalgal biomass for intestinal disease treatment. *Sci. Adv.* **7**, eabi9265 (2021).

46. Y. Inoue, K. Izawa, S. Kiryu, A. Tojo, K. Ohtomo, Diet and Abdominal Autofluorescence Detected by in Vivo Fluorescence Imaging of Living Mice. *Mol. Imaging* **7,** 21-27 (2008).

47. O. Tacar, P. Sriamornsak, C. R. Dass, Doxorubicin: An update on anticancer molecular action, toxicity and novel drug delivery systems. *J. Pharm. Pharmacol.* **65**, 157-170 (2013).

48. R. H. Fang, A. V. Kroll, W. Gao, L. Zhang, Cell membrane coating nanotechnology. *Adv. Mater.* **30**, 1706759 (2018).

49. N. Yang, Y. Ding, Y. Zhang, B. Wang, X. Zhao, K. Cheng, Y. Huang, M. Taleb, J. Zhao, W.-F. Dong, Surface functionalization of polymeric nanoparticles with umbilical cord-derived mesenchymal stem cell membrane for tumor-targeted therapy. *ACS Appl. Mater. Interfaces* **10**, 22963-22973 (2018).

50. X. Yan, Q. Zhou, M. Vincent, Y. Deng, J. Yu, J. Xu, T. Xu, T. Tang, L. Bian, Y.-X. J. Wang, K. Kostarelos, L. Zhang, Multifunctional biohybrid magnetite microrobots for imaging-guided therapy. *Sci. Robot.* **2**, eaaq1155 (2017).

51. H.-M. D. Wang, X.-C. Li, D.-J. Lee, J.-S. Chang, Potential biomedical applications of marine algae. *Bioresour. Technol.* **244**, 1407-1415 (2017).

52. Y. Qiao, F. Yang, T. Xie, Z. Du, D. Zhong, Y. Qi, Y. Li, W. Li, Z. Lu, J. Rao, Y. Sun, M. Zhou, Engineered algae: A novel oxygen-generating system for effective treatment of hypoxic cancer. *Sci. Adv.* **6**, eaba5996 (2020).

53. Z. Wu, L. Li, Y. Yang, P. Hu, Y. Li, S.-Y. Yang, L. V. Wang, W. Gao, A microrobotic system guided by photoacoustic computed tomography for targeted navigation in intestines in vivo. *Sci. Robot.* **4**, eaax0613 (2019).

54. B. W. Jester, H. Zhao, M. Gewe, T. Adame, L. Perruzza, D. T. Bolick, J. Agosti, N. Khuong, R. Kuestner, C. Gamble, K. Cruickshank, J. Ferrara, R. Lim, T. Paddock, C. Brady, S. Ertel, M. Zhang, A. Pollock, J. Lee, J. Xiong, M. Tasch, T. Saveria, D. Doughty, J. Marshall, D. Carrieri, L. Goetsch, J. Dang, N. Sanjaya, D. Fletcher, A. Martinez, B. Kadis, K. Sigmar, E. Afreen, T. Nguyen, A. Randolph, A. Taber, A. Krzeszowski, B. Robinett, D. B. Volkin, F. Grassi, R. Guerrant, R. Takeuchi, B. Finrow, C. Behnke, J. Roberts, Development of spirulina for the manufacture and oral delivery of protein therapeutics. *Nat. Biotechnol.* **40,** 974 (2022).

55. M. A. Scranton, J. T. Ostrand, F. J. Fields, S. P. Mayfield, Chlamydomonas as a model for biofuels and bio-products production. *The Plant Journal* **82,** 523-531 (2015).

2.3 Acidophilic microalgae microrobots for targeted gastrointestinal delivery

2.3.1 Introduction

The operation and navigation of robots in extreme environments have been listed as one of the ten grand challenges facing robotics in the next decade[1]. Recent robotic research along these lines has focused primarily on developing macroscale robots for operation in challenging environments, such as deep oceans with high pressure[2], polar regions with low temperature[3], and deserts with high temperature[4]. Upon scaling to the microscale regime, robots face additional challenges associated with propulsion in a low Reynolds number medium. Over the past decade, various microrobotic platforms have been developed to meet the propulsion requirements for diverse biomedical and environmental applications using three motion mechanisms, including energy harvesting from external fields[5-9], reaction with fuels present in the local surroundings[10-15], or utilizing the intrinsic motility and natural taxis behavior of living biological organisms[16-20]. Microrobotic platforms can provide distinctive advantages for in vivo operations by leveraging their active propulsion to deliver therapeutics to specific sites within the body[21-26]. Notably, micromotors have recently emerged as powerful tools for effective oral drug delivery, helping to address several limitations of traditional oral drug formulations such as poor drug absorption, short retention, and low bioavailability[27,28]. However, the extended operation of micromotors in the highly acidic gastric environment is still challenging and requires the development of innovative solutions[29].

Although several studies have aimed at integrating self-actuating mechanical devices in millimeter-sized robotic pills for application in the harsh conditions of the GI tract[30-32], effective and long-term operation of micromotors in an extremely acidic medium ($pH < 3$) remains highly challenging owing to its ability to corrode or degrade various types of micromotor platforms. There are only few reports on the influence of extremely acidic conditions on the movement of micromotors. For example, coating magnetically powered microswimmers with Al_2O_3 films was reported to enhance their propulsion in acidic conditions[33]. Al/Pd spherical micromotors were shown to operate in a wide range of pH conditions[34]. Finally, the self-propulsion of zinc microrockets and magnesium-based Janus micromotors in the gastric environment has led to enhanced therapeutic GI delivery[35,36]. Although synthetic micromotors have demonstrated utility for GI applications, their short lifetimes in acidic conditions limit their practical use to only short segments within the GI tract. Prolonged operation in the gastric and intestinal fluid can endow micromotors with the ability to actively drive therapeutic payloads to widely distributed areas over the entire GI tract and enhance the dispersion and retention of drugs for treating diseases and disorders. It is clear that realizing efficient and prolonged micromotor operation in a highly acidic medium remains an important unmet need, particularly for biomedical applications in the gastric environment.

In this work, we demonstrate an extremophile-based biohybrid micromotor capable of continuous and prolonged operation in extremely low pH environments. Many extremophiles, capable of surviving under extreme physical or chemical conditions, are found in some of the harshest environments on earth[37]. Among them, acidophilic microalgae have been shown to support the ecosystems of extremely acidic environments scattered around the globe associated with sulfur springs, volcanic vents, and acid mine drainages[38]. Such acidophilic algae evolved from their respective neutrophilic ancestors to thrive at low pH by reducing their proton influx and increasing their proton pump efficiency[39,40]. Here, we demonstrated the efficient and prolonged motion behavior of acidophilic algae in strong hydrochloric acid down to pH 1 and their tremendous potential for microrobotic gastrointestinal (GI) delivery applications. Specifically, we relied on *Chlamydomonas pitschmannii*, an acidophilic alga isolated from an acid mine drainage[41]. *C. pitschmannii* displayed a negligible change in speed over an extremely broad pH range, from pH 1 to 10, compared to the neutrophilic alga *Chlamydomonas reinhardtii*, which was incapable of swimming in acidic medium (pH < 4) and rapidly degraded (Fig. 2.13a,b). Notably, the movement of *C. pitschmannii* in acidic medium was maintained over an extended period of at least 72 h (Fig. 2.13c). We further evaluated the performance of the acidophilic biomotors in gastric fluid (pH 1.5) and intestinal fluid (pH 6.5) and tracked their *in vivo* biodistribution to establish their potential for biomedical applications involving GI tract delivery (Fig. 2.13d,e). Multifunctional biohybrid algae motors were fabricated by decorating the acidophilic algae with polymeric nanoparticles, which were loaded with a green fluorescent dye for visualization purposes (Fig. 2.13f). The binding between nanoparticles and *C. pitschmannii* algae was clearly observed by electron microscopy (Fig. 2.13g). Finally, by tuning the surface properties of the cargo, selective targeting to the stomach or broad GI tract delivery could be achieved. The effective and long-term movement of cargo-loaded acidophilic algae motors over a wide range of pH conditions, including harsh acidic media, along with their strong retention in the GI tract, suggests that the platform holds considerable promise for future biomedical applications in the GI tract. Further work on extremophile-based multifunctional biohybrid micromotors could lead to the development of novel microrobotic platforms capable of excelling in a variety of harsh environments.

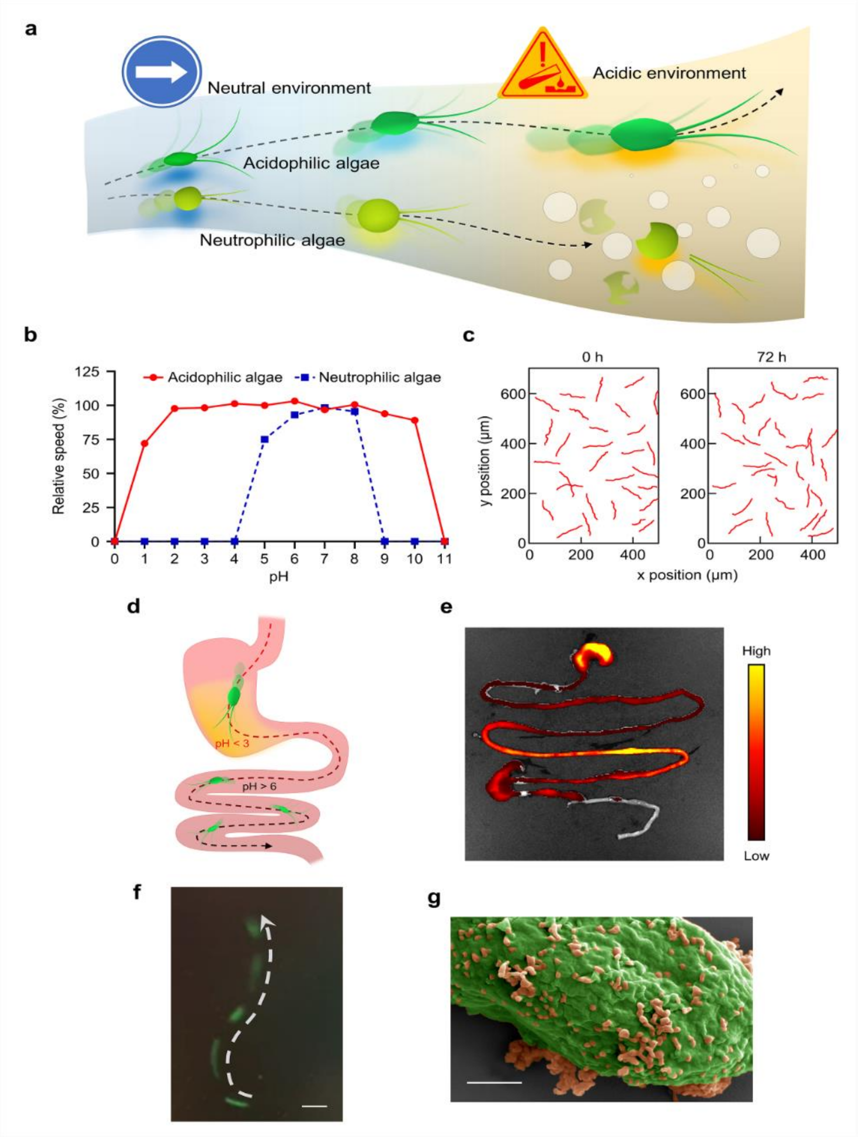

Figure 2.13 Schematics of acidophilic algae micromotors for biomedical applications. a. Acidophilic algae motors are capable of prolonged motion in both neutral and acidic environments, whereas neutrophilic algae are incapable of operating in highly acidic environments. b. The relative speed of acidophilic algae and neutrophilic algae over a range of pH values compared to their speed in optimal culture conditions (modified acidic medium at pH 3.5 for acidophilic algae; TAP at pH 7 for neutrophilic algae). c. 2D motion trajectories of acidophilic algae motors over a period of 1 s before and 72 h after swimming in HCl at pH 1.5. d. Acidophilic algae motors can operate throughout the entire GI tract for in vivo delivery applications. e. Representative biodistribution of acidophilic algae motors in the GI tract at 2 h after administration by oral gavage. f. 1-second motion trajectory of acidophilic algae-based biohybrid motors carrying dye-labeled nanoparticles in HCl at pH ~1.5. Scale bar, 10 μm. g. Representative pseudocolored scanning electron microscopy image of a nanoparticle-functionalized acidophilic algae motor. Scale bar, 1 μm.

2.3.2 Motion behavior of acidophilic algae

C. pitschmannii CPCC 354 was selected as a model acidophilic algae strain, and its swimming behavior was characterized in extremely acidic conditions. To evaluate their movement, the algae were cultured in a modified acidic medium (MAM)[42] (pH 3.5) to a density of 1×10^6/ml, followed by transfer to hydrochloric acid for speed measurement. The algae exhibited constant swimming with a speed of 95-105 μm/s (corresponding to ~10 body length/s) in an extremely acidic environment at pH 1.5 (Fig. 2.14a). Their movement was also tracked over a 5 s period under the same condition in order to visualize a representative trajectory (Fig. 2.14b). When investigating the tolerance range of the algae to extreme acid, we found that they displayed a significant decrease in speed and loss of activity after 1 h of motion at pH 1 (Fig. 2.14c). Furthermore, the effect of the anion was evaluated by immersing the algae in different common strong acids (HCl, H_2SO_4, and HNO_3) adjusted to pH 1.5 (Fig. 2.14d). The detrimental effect of nitric acid on the algae motion could be explained by its strong oxidizing capacity compared to the other two acids.

Interestingly, we observed that the acidophilic algae could not only resist extreme acidic conditions (pH < 3), but they were also able to survive in neutral and alkaline environments (Fig. 2.14e). After 30 min of adaptation, the acidophilic algae displayed efficient movement across a broad pH range from 1 to 10 (Fig. 2.14f). In comparison, a model neutrophilic algae *C. reinhardtii*, which have been commonly used as microorganism-based micromotors for various environmental and biomedical applications[17,20,26,43], were unable to tolerate extreme acidic pH and could swim only over a narrow pH range between 5 to 8 (Fig. 2.14f). The contrast between the two types of algae was further highlighted by visualizing their trajectories at pH 1.5, 4, and 7 after various periods of time (Fig. 2.14g,h). Only slight speed differences were observed for the acidophilic algae at all pH values after 24 h, whereas the motility of neutrophilic algae rapidly diminished at pH 1.5 and 4.

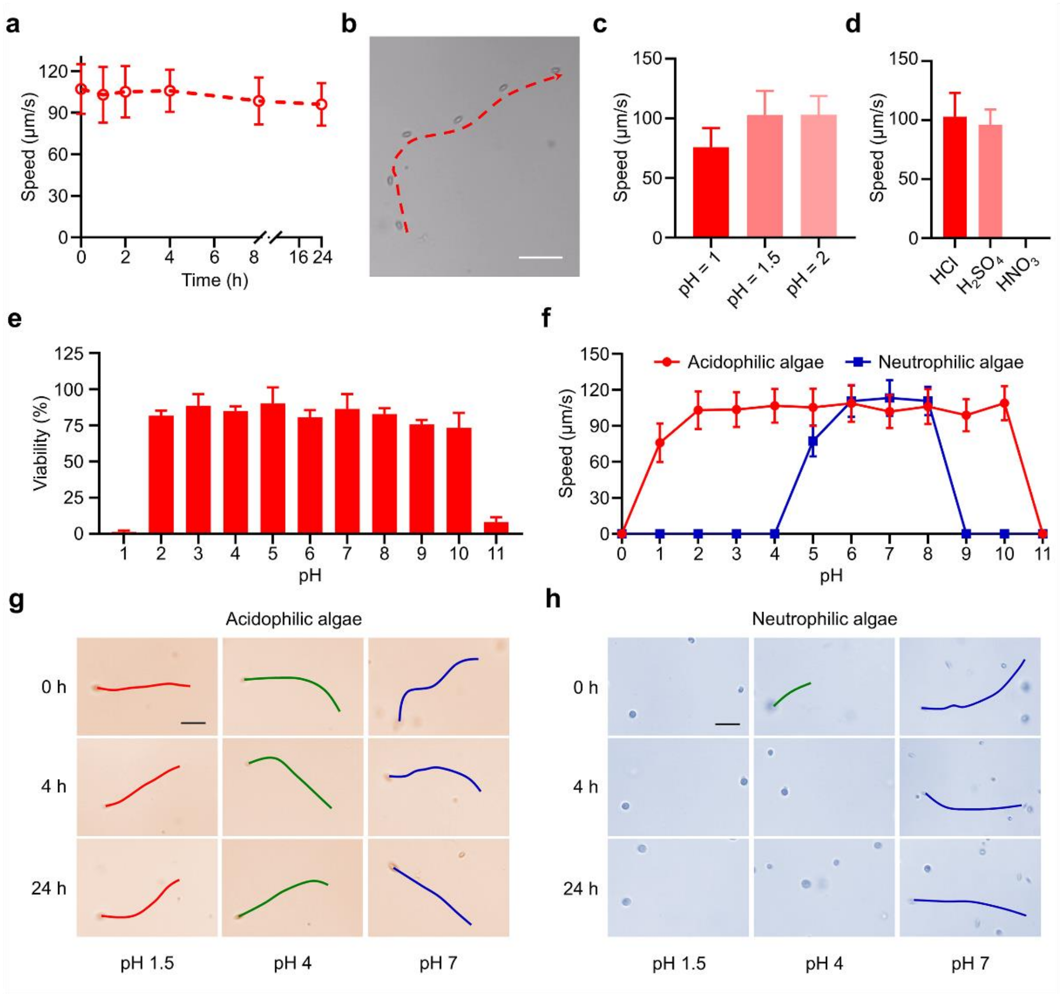

Figure 2.14 Motion behavior of acidophilic algae biomotors in extremely acidic conditions. a. Speed of acidophilic algae biomotors at different timepoints (0, 1, 2, 4, 8, and 24 h) in HCl at pH 1.5. b. The representative trajectory of an acidophilic alga biomotor over a period of 5 s in HCl at pH 1.5. Scale bar, 100 μm. c. Swimming speed of algae biomotors upon 1 h of exposure to HCl at pH 1, 1.5, and 2 (n = 100, mean + s.d.). d. Swimming speed of acidophilic algae biomotors in different acidic mediums (HCl, H2SO4, and HNO3) at pH 1.5 (n = 100, mean + s.d.). e. Viability of acidophilic algae in different media at pH values from 1 to 11 (n = 3, mean + s.d.). f. Speed comparison of acidophilic algae with neutrophilic algae at pH between 0 to 11 (n = 100, mean ± s.d.). Speed was measured from 100 individual algae. g,h. Representative trajectories over a period

of 2 s for acidophilic algae (g) and neutrophilic algae (h) after various durations (0 h, 4 h, and 24 h) of exposure to HCl at pH 1.5, 4, and 7. Scale bar, 50 μm.

2.3.3 Biodistribution and retention of acidophilic algae in the GI tract

The oral route of administration is the most common approach for drug delivery to treat GI disease[44]. A major challenge of GI delivery is overcoming the physiological barrier caused by the extreme acidity within the stomach. To investigate the potential of acidophilic algae biomotors for improved GI delivery, we first tested their motion ability and viability in vitro in simulated gastric (pH ~1.5) and intestinal (pH ~6.5) fluids. They exhibited good adaptation in both physiological fluids, and their self-propulsion (~100 μm/s) was unaffected after 8 h of constant movement, indicating great promise for in vivo GI operation. In comparison, the neutrophilic algae lost their motion ability rapidly upon transfer from the culture medium to gastric fluid at room temperature. We also observed for any changes in morphology using electron microscopy after incubation in strong gastric acid. The acidophilic algae displayed an intact structure after 2 h of motion, whereas the neutrophilic algae were structurally damaged after the same period of time. To further mimic the physiological conditions in the stomach[45], we assessed the speed and lifetime of acidophilic algae in simulated gastric fluid containing 1 mg/ml of pepsin at body temperature (37 °C) and found that the algae maintained speeds of 65 μm/s and 35 μm/s after 1 h and 2 h of incubation, respectively. These results supported the potential of the acidophilic algae for active transport throughout the GI tract, whereas the regular neutrophilic algae would be unable to traverse the harsh acidic medium in the stomach.

Next, we demonstrated the distinct advantages of acidophilic algae biomotors for GI delivery by examining their biodistribution and retention after oral administration using a murine model. Ex vivo fluorescence imaging was conducted to determine the influence of acid tolerance on algae localization within the GI tract (Fig. 2.15a-c). In order to visualize and track the algae, their surfaces were covalently bound with the near-infrared fluorescent dye Cy7 (λex/λem = 750 nm/773 nm)[46], which did not hinder their motion behavior in GI fluid. Before oral gavage, we confirmed that the dye-conjugated acidophilic algae, neutrophilic algae, and alkaline-treated static acidophilic algae were similar in number and fluorescence intensity. At various timepoints (0.5 h, 2 h, 5 h, 10 h, and 24 h) after oral administration, the mice were euthanized, and their GI tracts were isolated to visualize the location of algae. As shown in Fig. 3a, the acidophilic algae displayed a strong signal throughout the entire GI tract, showing sustained retention in the stomach as well as wide distribution in the lower GI tract within the first 5 h. In comparison, the signals from the neutrophilic algae (Fig. 2.15b) and the static acidophilic algae (Fig. 2.15c) diminished rapidly within 2 h after administration. These results emphasized the importance of the acid tolerance and self-propulsion properties of acidophilic algae, which enabled efficient operation in the stomach and effective distribution in the lower GI tract. The visual observations were further corroborated by quantifying the total radiant efficiency in the stomach (Fig. 2.15d) or in the small intestine and colon (Fig. 2.15e) at different timepoints.

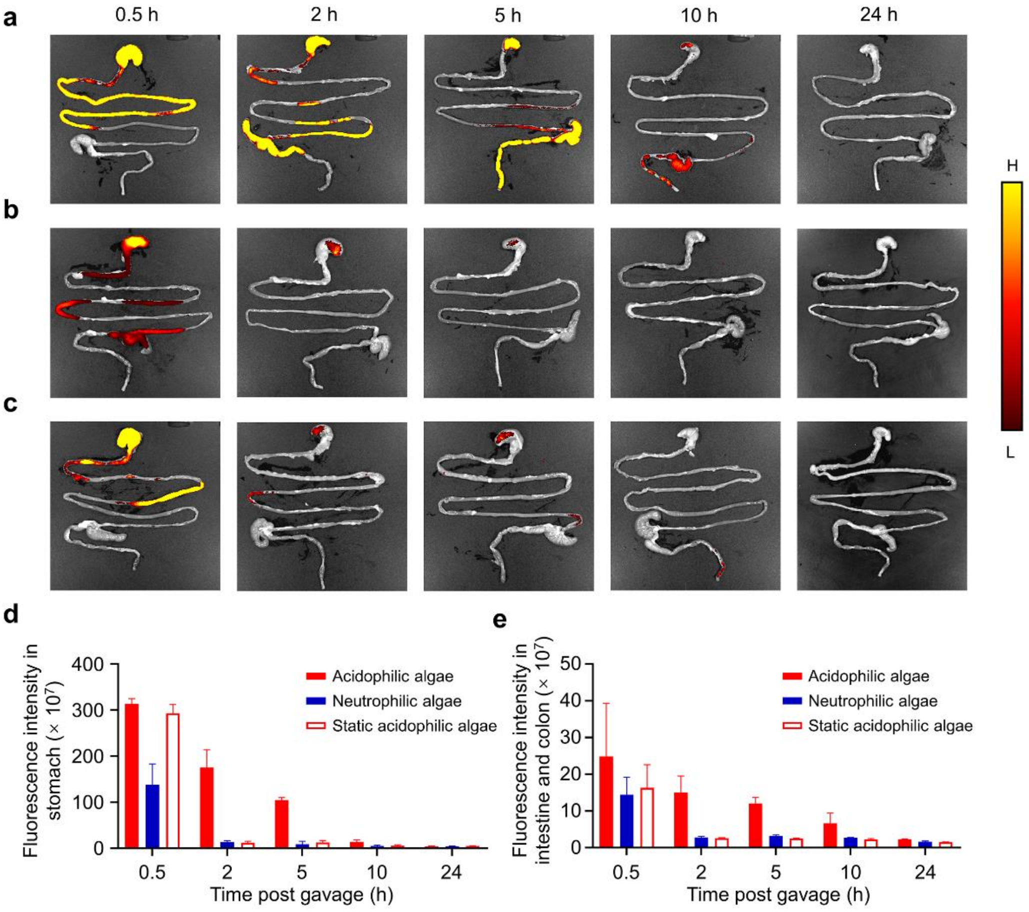

Figure 2.15 Biodistribution of acidophilic algae biomotors in the GI tract. a-c. Mice were orally gavaged with Cy7-labeled acidophilic algae (a), Cy7-labeled neutrophilic algae (b), or Cy7-labeled static acidophilic algae (c), and distribution in the GI tract was visualized over time. d,e. Measurement of the fluorescence intensity in the stomach (d) or small intestine and colon (e) at different timepoints (0.5 h, 2 h, 5 h, 10 h, and 24 h) after oral gavage (n = 3, mean + s.d.).

2.3.4 Biosafety of acidophilic algae in GI

To assess the safety of the acidophilic algae, we evaluated their toxicity profile both systemically and locally in the lower GI tract. A treatment dosage of 1 × 10^7 acidophilic algae was orally administered to mice, while untreated mice served as controls. A comprehensive blood chemistry panel and blood cell count were conducted 24 h afterward (Fig. 2.16a,b). There was no statistical difference between the untreated control and the algae treatment group in any of the 14 blood parameters and blood cell populations that were analyzed. Hematoxylin and eosin (H&E)-stained histological sections showed that the stomach and intestinal mucosa or submucosa maintained their integrity without any lymphocyte infiltration or signs of inflammation (Fig. 2.16c). Finally, histological analysis of the major organs, including the heart, liver, spleen, lungs, and kidneys, was performed (Fig. 2.16d). The appearance of all the organs was normal compared to healthy mice. Further studies will be required to comprehensively evaluate the impact of algae administration on other immune parameters, both local and systemic, across multiple timescales.

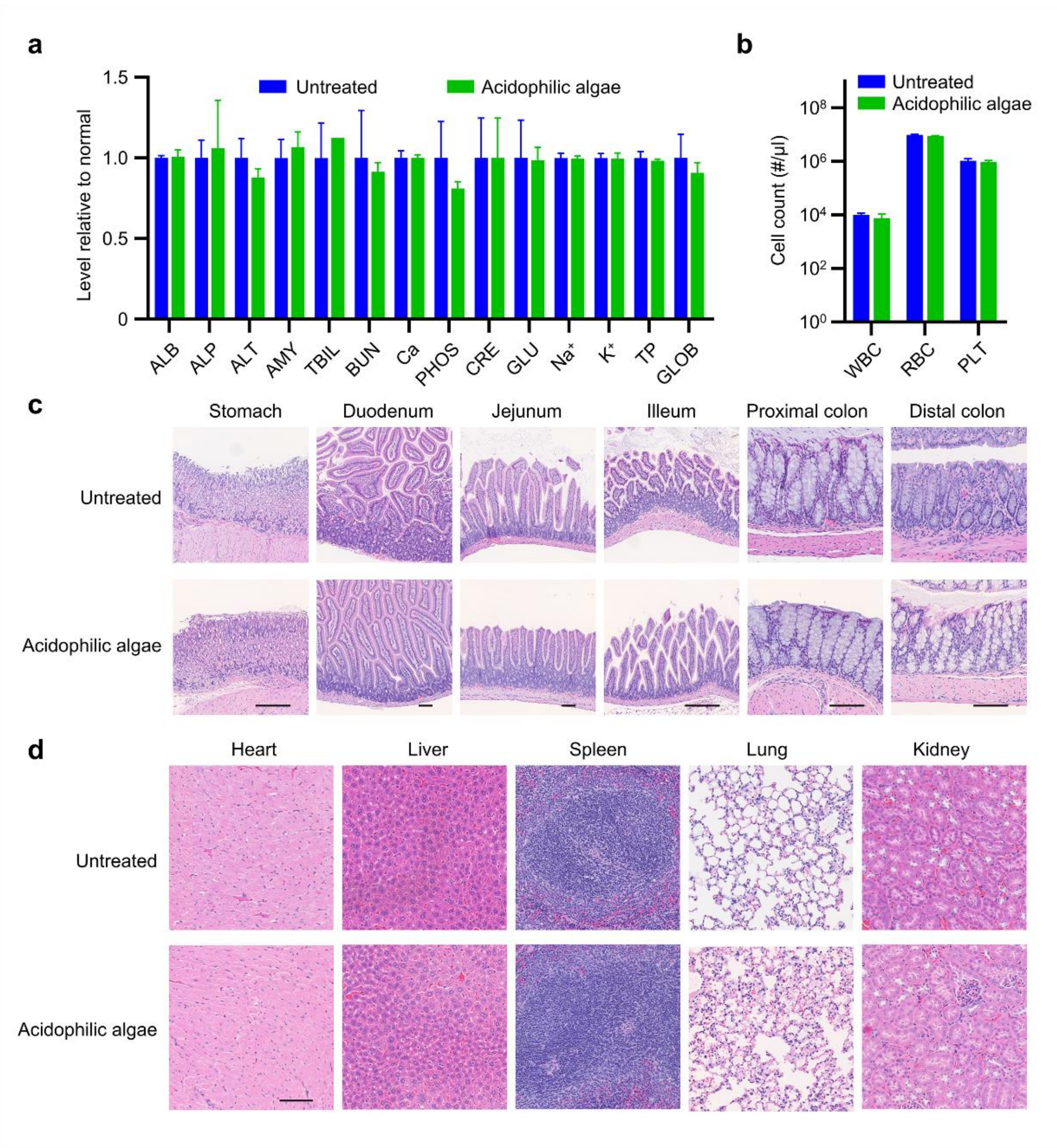

Figure 2.16 In vivo safety evaluation of acidophilic algae. a. Comprehensive blood chemistry panel for untreated mice or mice at 24 h after treatment with acidophilic algae micromotors (n = 3, mean + s.d.). Abbreviations: ALB, albumin; ALP, alkaline phosphatase; ALT, alanine transaminase; AMY, amylase; TBIL, total bilirubin; BUN, blood urea nitrogen; Ca, calcium; PHOS, phosphorus; CRE, creatinine; GLU, glucose; Na+, sodium; K+, potassium; TP, total protein; GLOB, globulin (calculated). b. Counts for various blood cells taken from untreated mice or mice at 24 h after treatment with acidophilic algae micromotors (n = 3, mean + s.d.). Abbreviations: WBC, white blood cells; RBC, red blood cells; PLT, platelets. c. Representative hematoxylin and eosin (H&E)-stained histology sections of different portions of the GI tract from untreated mice or mice at 24 h after treatment with acidophilic algae micromotors. Scale bar, 100 μm d. Representative H&E-stained histology sections of major organs from untreated mice or mice at 24 h after treatment with acidophilic algae micromotors. Scale bar, 100 μm.

2.3.5 Stomach delivery with acidophilic algae motors

Upon confirming the biodistribution and safety of acidophilic algae for GI administration, we evaluated the feasibility of leveraging them for cargo delivery. Poly(lactic-*co*-glycolic acid) (PLGA) nanoparticles were chosen as the model payload since they are attractive for therapeutic delivery applications with properties such as controlled and sustained drug release, high drug loading yield, and low toxicity[47]. To fabricate the acidophilic algae biohybrid motors, positively charged poly-l-lysine (PLL)-coated PLGA nanoparticles (denoted ‘PLLNP’) were attached to the negatively charged acidophilic algae surface via electrostatic interaction, thus generating PLLNP-loaded acidophilic algae biohybrid motors (denoted ‘acido-algae-PLLNP’) (Fig. 2.17a). The surface coating on the PLGA core was first optimized by tuning the incubation time between the nanoparticles and the PLL polyelectrolyte to yield PLLNP with a strong positive surface charge. The determination of zeta potential at different pH values is important for complexing two materials based on electrostatic interactions[48]. To this end, the surface charge of bare acidophilic algae and PLLNP was evaluated at pH values ranging from 1 to 11. It was found that the PLL coating could promote the effective binding of PLGA nanoparticles to algae at neutral pH, which was visualized by fluorescence microscopy (Fig. 2.17b). The algae were uniformly surrounded by 3,3'-dioctadecyloxacarbocyanine perchlorate (DiO; λex/λem = 484 nm/501 nm)-loaded PLLNP. A pseudocolored scanning electron microscopy (SEM) image illustrated the attachment of the nanoparticles onto the algae cell surface (Fig. 2.17c). The motion behavior of the acido-algae-PLLNP was characterized by measuring their speed under extreme acidic conditions at pH 1.5 (Fig. 2.17d). The decreased speed of the acido-algae-PLLNP (~50 μm/s) compared to bare acidophilic algae (~100 μm/s) could be attributed to the influence of the positively charged cargo on the flagella, as indicated by inconsistent (zigzag trajectory) movement patterns (Fig. 2.17e).

Next, we evaluated the gastric cargo delivery ability of the acido-algae-PLLNP biohybrid motors. A near-infrared dye, 1,1'-dioctadecyl-3,3,3',3'-tetramethylindotricarbocyanine iodide (DiR, λex/λem = 748 nm/780 nm), was encapsulated into PLLNP as a model payload. Prior to the animal studies, an in vitro study was conducted to assess the stability of cargo loading on the biohybrid motors. In the acido-algae-PLLNP formulation, released dye or unbound nanoparticles were hardly detected even after 24 h of incubation in HCl (pH 2) or simulated gastric fluid (pH 1.5), indicating highly stable cargo binding to the algae via electrostatic interactions, hydrogen bonding between PLL and the diverse functional groups present on the algae surface, and physical entrapment of nanoparticles by the highly porous structure of the algae cell wall. Then, acido-algae-PLLNP and PLLNP control (without algae) were orally administered to mice to study their biodistribution and retention. After 2 h, 5 h, and 10 h, the mice were euthanized, and their GI tracts were isolated for ex vivo imaging (Fig. 2.17f). Both acido-algae-PLLNP and PLLNP were mainly located in the stomach, which is attributed to the mucoadhesive property of the positively charged PLLNP[44]. However, the motion of the biohybrid motors enabled a higher chance of contact between the nanoparticles and the luminal lining, facilitating efficient cargo retention in the stomach. Such accumulation can be used to improve drug delivery and enhance tissue penetration, as was demonstrated previously using micromotors for oral vaccine delivery[49]. Quantification of the fluorescence intensity within the stomach supported the greatly improved retention of PLLNP when delivered by acido-algae-PLLNP biohybrid motors as opposed to in free form within the first 5 h after oral gavage (Fig. 2.17g).

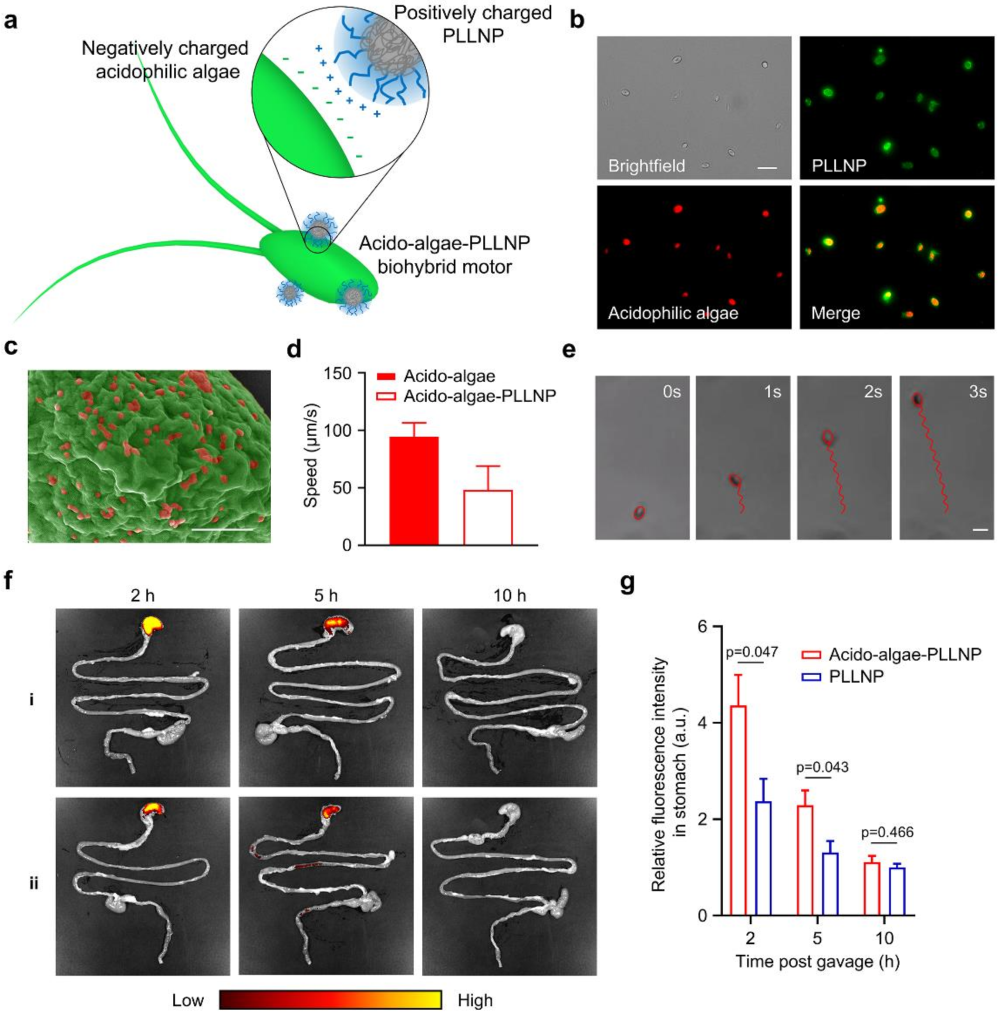

Figure 2.17 Acido-algae-PLLNP biohybrid motors for stomach delivery. a. Loading of PLLNP onto acidophilic algae motors by electrostatic interaction. b. Fluorescence microscopy images of acido-algae-PLLNP biohybrid motors. Red: acidophilic algae (chloroplast autofluorescence). Green: PLLNP (DiO). Scale bar, 20 µm. c. Pseudocolored SEM images of an acido-algae-PLLNP biohybrid motor. Scale bar, 1 µm. d. Speed comparison of acido-algae-PLLNP and bare acidophilic algae (denoted 'acido-algae' in the figure) at pH 1.5 (n = 20, mean + s.d.). e. Representative trajectories of the acido-algae-PLLNP biohybrid motor over a period of 3 s in HCl at pH 1.5. Scale bar, 10 µm. f. Ex vivo imaging of the GI tract at 2 h, 5 h, and 10 h after oral administration of acido-algae-PLLNP (i) or PLLNP (ii). g. Fluorescence intensity of DiR dye delivered by acido-algae-PLLNP or PLLNP in the stomach at 2 h, 5 h, and 10 h after oral gavage (n = 3, mean + s.d.).

2.3.6 Entire GI delivery with acidophilic algae motors

After confirming effective cargo delivery to the stomach by using mucoadhesive PLLNP attached to the surface of acidophilic algae motors, we sought to evaluate whether the acidophilic algae could be used to transport cargo throughout the entire GI tract given their effective distribution shown in Fig. 3. Instead of using positively charged PLLNP, we elected to employ PLGA cores with a cell membrane coating, which endows versatile surface functionality and biomimetic properties to nanocarriers[50]. Red blood cell membrane-coated PLGA nanoparticles (denoted 'RBCNP') were prepared based on a previously established protocol[51]. The hydrodynamic size and zeta potential of RBCNP were characterized by dynamic light scattering, indicating the slight increase in size and negative charge after membrane coating. The RBC membrane coating onto the PLGA surface was further verified by transmission electron microscopy (TEM), showing an intact core-shell structure. To achieve loading of RBCNP onto algae, a bioorthogonal conjugation approach using copper-free click chemistry was employed[52] (Fig. 2.18a). Briefly, the algae and RBCNP were separately functionalized with dibenzocyclooctyne-(polyethylene glycol)$_4$-N-hydroxysuccinimidyl ester (DBCO-PEG$_4$-NHS) and azido-PEG$_4$-NHS ester, respectively. The two components were then conjugated together by leveraging these newly introduced functional groups. The attachment of RBCNP to acidophilic algae (denoted 'acido-algae-RBCNP') was validated by a pseudocolored SEM image (Fig. 2.18b) and fluorescent imaging, confirming the effective binding between DiO dye-labeled RBCNP and the algal surface (Fig. 2.18c). Importantly, the covalent binding of RBCNP had minimal effects on the motion behavior (speed and tracking pattern) of the algae motors (Fig. 2.18d,e). After 24 h of incubation in acidic fluid, 90% of the fluorescence intensity of DiR-loaded RBCNP onto the algae surface was preserved, indicating the high binding stability between acidophilic algae and RBCNP in a harsh acidic environment.

Next, we evaluated the feasibility of using acido-algae-RBCNP biohybrid motors for delivery throughout the GI tract. DiR was loaded into RBCNP as a model payload to track nanoparticle localization at different GI sites in vivo. At 2 h, 5 h, and 10 h after oral administration of acido-algae-RBCNP and free RBCNP (without algae) with a similar amount of DiR loading, the GI tract was excised for ex vivo fluorescence imaging (Fig. 2.18f). Due to their acid tolerance and movement capabilities, the acido-algae-RBCNP motors were able to transport the RBCNP to the entire GI tract as opposed to only the stomach. The fluorescent signals from the active biohybrid motor group were more substantial in both the stomach and the small intestine at 2 h and remained stronger at 5 h and 10 h when compared with the free RBCNP group. Importantly, it should be noted that the 10 h cargo retention facilitated by the biohybrid motors was much longer than the gastric emptying time of a fluid meal[53]. A similar trend of improved GI payload retention by acido-algae-RBCNP was confirmed when quantifying the fluorescent signals, with 2-fold and 1.5-fold enhancement at 2 h and 5 h after oral gavage, respectively (Fig. 2.18g). These results confirmed that controlling the surface properties of the nanoparticle payload could selectively position the biohybrid motors in different regions of the GI tract.

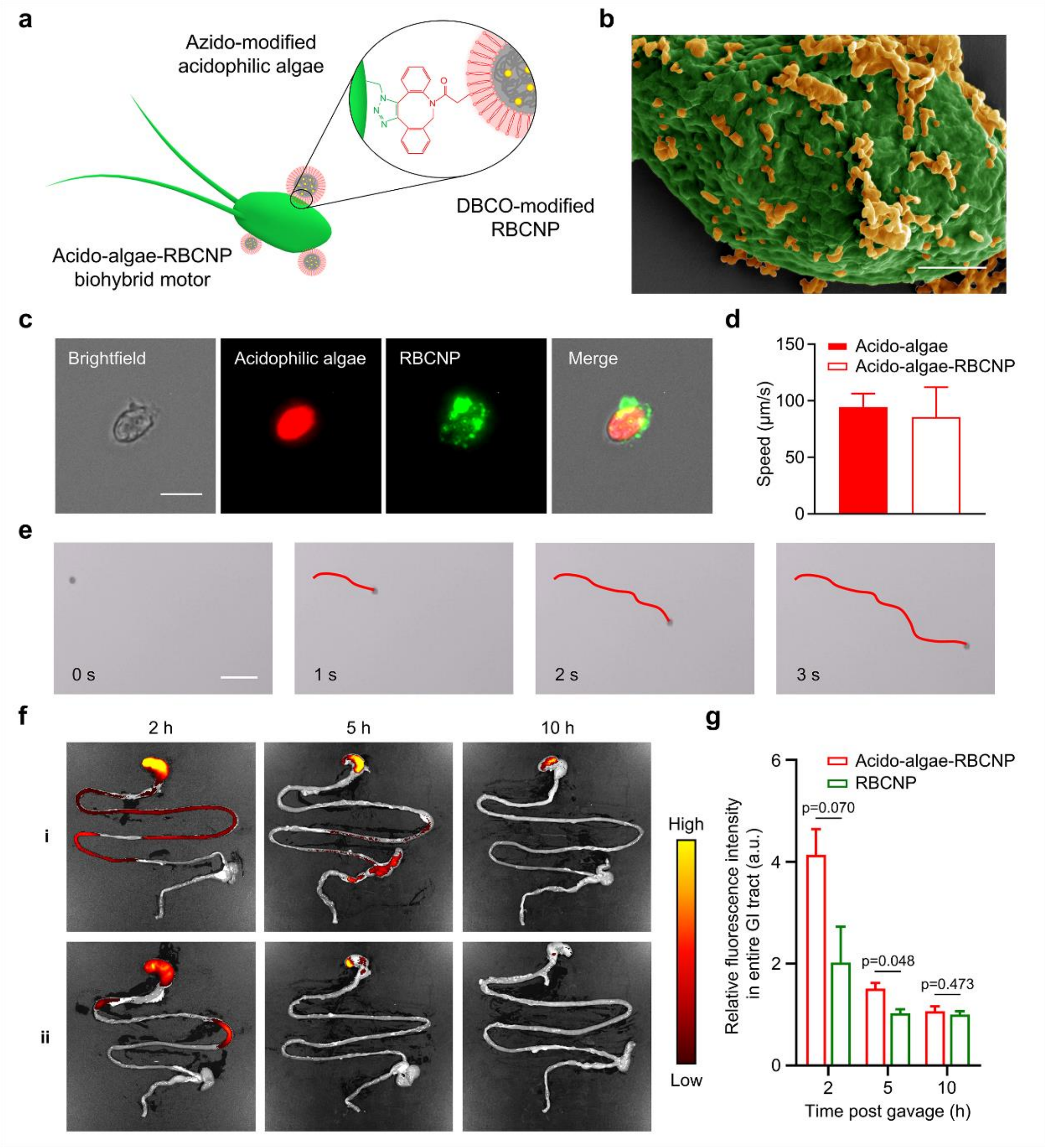

Figure 2.18 Acido-algae-RBCNP biohybrid motors for entire GI tract delivery. a. Loading of RBCNP onto acidophilic algae motors via click chemistry. b. Pseudocolored SEM image of an acido-algae-RBCNP biohybrid motor. Scale bar, 1 μm. c. Representative fluorescence microscopy images of an acido-algae-RBCNP biohybrid motor. Red: acidophilic algae (chloroplast autofluorescence). Green: RBCNP (DiO). Scale bar, 10 μm. d. Speed comparison of acido-algae-RBCNP and bare acidophilic algae (denoted 'acido-algae' in the figure) at pH 1.5 (n = 20, mean + s.d.). e. Representative trajectories of acido-algae-RBCNP biohybrid motor over a period of 3 s in HCl at pH 1.5. Scale bar, 50 μm. f. Ex vivo imaging of the GI tract at 2 h, 5 h, and 10 h after oral administration of acido-algae-RBCNP (i) or RBCNP (ii). g. Fluorescence intensity of DiR dye delivered by acido-algae-RBCNP or RBCNP in the entire GI at 2 h, 5 h, and 10 h after oral gavage (n = 3, mean + s.d.).

2.3.7 Discussion

In summary, we have reported on the first extremophile-based algae biohybrid motor for application in harsh conditions such as acidic biological fluid. Acidophilic *C. pitschmannii* algae were chosen based on their ability to effectively swim in highly acidic conditions. The unique adaptability and long-lasting self-propulsion of the acidophilic algae over a wide pH range (1.5-10) provided the natural micromotor essential flexibility for efficient performance in both gastric and intestinal fluid. In a murine model, oral administration of the acidophilic algae resulted in improved GI distribution and retention compared to neutrophilic algae and static acidophilic algae controls. By functionalizing the algae with cargo-loaded PLGA nanoparticles via different conjugation approaches, the resulting multifunctional biohybrid micromotors were able to facilitate cargo delivery to the stomach or the entire GI tract in vivo. Once inside the GI tract, the PLGA nanoparticles provide controlled and sustained drug release through the hydrolytic cleavage of their polyester backbones[54]. While the current surface attachment strategies were effective for loading drug onto the algae motors, other approaches such as the incorporation of small-molecule drugs inside the algae could be explored[55]. In addition, various drug payloads, including chemotherapeutics and biologics, could be incorporated to improve their therapeutic activity for local GI diseases[56]. Long-term biosafety monitoring needs to be performed prior to the clinical studies of the biohybrid motors to verify their lack of immunogenicity and toxicity. Looking forward, we envision decoration of the acidophilic algae with multiple functional units, including therapeutics, contrast agents, targeting moieties, and magnetic particles to create multifunctional microrobotic platforms with accurate maneuverability for targeted GI drug delivery. Overall, extremophile-based biohybrids offer considerable promise and open the door for diverse applications in harsh and inhospitable environments that are unsuitable for traditional microrobots.

2.3.8 Experimental section

Algae culture. The acidophilic algae *Chlamydomonas pitschmannii* (strain CPCC-354 wild-type) were obtained from the Canadian Phycological Culture Centre (CPCC). The algae were transferred from their original medium to modified acid medium (MAM, CPCC) and cultivated at room temperature under cycles of 12 h sunlight and 12 h darkness. The neutrophilic algae *Chlamydomonas reinhardtii* (strain CC-125 wild-type mt+) were obtained from the Chlamydomonas Resource Center. The algae were transferred from the agar plate to tris-acetate-phosphate (TAP) medium (Thermo Fisher Scientific) and cultured under the same conditions.

Preparation of dye-conjugated acidophilic algae. Acidophilic algae were transferred from the culture medium to 1× phosphate-buffered saline (PBS, Thermo Fisher Scientific) followed by 3 washes. Next, 10 μg/ml NHS-Cyanine7 (NHS-Cy7, Lumiprobe) was incubated with the algae at 1×10^7 per ml for 1 h at room temperature. After dye conjugation, the modified algae were washed with ultrapure water for the removal of the unreacted dye and resuspended in ultrapure water for further use. Static acidophilic algae were prepared through the dropwise addition of 1 M acetic acid (Sigma Aldrich) to active acidophilic algae. After 20 seconds, the pH value of the mixture was quickly neutralized to 7 by the addition of 1 M sodium hydroxide (Sigma Aldrich), and the algae were transferred into PBS. Then, the Cy7 dye conjugation was performed following a similar method as above. Neutrophilic algae were suspended in 10 mM 4-(2-hydroxyethyl)-1-piperazineethanesulfonic acid buffer (HEPES, Thermo Fisher Scientific) to complete the Cy7 conjugation.

Synthesis of fluorescent dye-loaded polymeric nanoparticles. The synthesis of polymeric nanoparticles was based on a previously reported nanoprecipitation method[51]. Briefly, 0.67 dl/g carboxyl-terminated 50:50 poly(lactic-*co*-glycolic) acid (PLGA, LACTEL Absorbable Polymers) at 20 mg/ml in 1 ml of acetone was added into 1 ml of 10 mM Tris-buffer. To fluorescently label the nanoparticles, 0.1 wt% of 3,3'-dioctadecyloxacarbocyanine perchlorate (DiO, λex/λem = 484 nm/501 nm; Thermo Fisher Scientific) was encapsulated into the PLGA cores. After nanoprecipitation, the organic solvent was evaporated under a vacuum for 1 h. Near-infrared dye-loaded polymeric nanoparticles for in vivo studies were prepared following a similar method by replacing DiO with 1,1'-dioctadecyl-3,3,3',3'-tetramethylindotricarbocyanine iodide (DiR, λex/λem = 748 nm/780 nm; Thermo Fisher Scientific).

Preparation of poly-l-lysine (PLL) coated nanoparticles (PLLNP). To prepare the PLGA nanoparticles coated with PLL (Sigma Aldrich), 10 mg/ml of preformed PLGA nanoparticles in ultrapure water were added dropwise into 1 ml of 0.05% w/v PLL under 700 rpm stirring for 2 h. Next, 5 washes were used to remove any free polyelectrolyte, and the PLLNP were resuspended in ultrapure water for further use. To characterize the size and zeta potential of the PLGA cores and PLLNP, the samples were tested using a Zetasizer MAL 1267090 (Malvern Panalytical).

Preparation of red blood cell (RBC) membrane-coated nanoparticles (RBCNP). RBCNP were prepared by a cell membrane cloaking technique[50,51]. RBC membrane was mixed with PLGA cores at a 1:1 weight ratio of membrane protein to PLGA polymer. The mixture was then sonicated using a Fisher Scientific FS30D ultrasonic bath sonicator for 3 min. The RBCNP were isolated by centrifugation for 5 min at 16,100*g* and washed 3 times with ultrapure water. To characterize the size and surface zeta potential of RBCNP, the samples were tested using a Zetasizer MAL 1267090. To characterize the morphology, the samples were deposited onto a carbon-coated 400-

mesh copper grid and stained with 1 wt% uranyl acetate (Electron Microscopy Sciences), followed by imaging on a JEOL 1200 EX II transmission electron microscope.

Preparation of acido-algae-PLLNP biohybrid motors. To attach PLLNP, 1×10^7 acidophilic algae were first isolated from MAM and resuspended in ultrapure water. Then, the PLLNP were mixed with algae for 30 min. After nanoparticle attachment, the resulting acido-algae-PLLNP biohybrid motors were washed 3 times and resuspended in ultrapure water.

Preparation of acido-algae-RBCNP biohybrid motors. To conjugate RBCNP onto algae, the acidophilic algae and RBCNP were linked using click chemistry. First, 1×10^7 algae were treated with 20 μM of dibenzocyclooctyne-(polyethylene glycol)$_4$-N-hydroxysuccinimidyl ester (DBCO-PEG$_4$-NHS, Click Chemistry Tools) for 1 h at room temperature. The RBCNP were incubated with 20 μM of azido-PEG$_4$-NHS (Click Chemistry Tools) for 1 h at room temperature. Both the algae and RBCNP were centrifuged and washed 3 times with ultrapure water to remove the unreacted NHS esters. Then, the modified algae and RBCNP were mixed and vortexed for 4 h to complete the click chemistry reaction. After conjugation, the resulting acido-algae-RBCNP biohybrid motors were separated by centrifugation at 800*g* for 3 min, followed by 3 washes.

Binding stability of acido-algae-PLLNP and acido-algae-RBCNP in acidic conditions. To test the binding stability between PLLNP and acidophilic algae after the formation of biohybrid motors, the acido-algae-PLLNP with DiR loading were incubated with two acidic conditions (simulated gastric fluid and HCl at pH 2) for 24 h. The detached PLLNP in the supernatant was removed by centrifugation at 800*g* for 3 min. Before and after incubation, the fluorescence intensity of PLLNP with DiR loading on the algae surface was measured by plate reader. The binding stability of acido-algae-RBCNP was evaluated following the same method.

Motion analysis. The speed of acidophilic algae, neutrophilic algae, fluorescein-conjugated algae motors, acido-algae-PLLNP biohybrid motors, and acido-algae-RBCNP biohybrid motors was analyzed in different media: modified acid medium (MAM, pH ~3.5), simulated gastric fluid (SGF, pH ~1.5, RICCA Chemical), simulated intestinal fluid (SIF, pH ~6.5, RICCA Chemical), 1× PBS (pH ~7.4), ultrapure water, pH-adjusted aqueous solutions (pH from 0 to 11), sulfuric acid (pH ~1.5, Sigma Aldrich), and nitric acid (pH ~1.5, Fisher Scientific). The motion of the acidophilic algae motors was also observed in HCl solution (pH ~1.5, Sigma Aldrich) at 0 h, 1 h, 4 h, 8 h, 24 h, and 72 h at room temperature (22 °C). Movies were captured by a Nikon Eclipse Ti-S/L100 inverted optical brightfield microscope coupled with 10× or 20× objectives and a Hamamatsu digital camera C11440 or by a Sony RX100 V camera on an Invitrogen EVOS FL fluorescence microscope with 20× or 40× objectives. An NIS Element tracking module was used to measure the speed of the motors in different media. To mimic the conditions in the stomach of mice, simulated gastric fluid containing 1 mg/ml of pepsin (Sigma Aldrich) was used to test the influence of enzymes on the motility of acidophilic algae. Speed was measured after incubation for 0 h, 1 h, 2 h, 4 h, and 8 h at body temperature (37 °C).

Viability of acidophilic algae motors. To evaluate the viability of acidophilic algae in solutions with different pH, algae were transferred from MAM to aqueous solutions with pH from 0 to 11 and incubated for 2 h at room temperature (22 °C). After incubation, algae motors were resuspended into 5 μM SYTOX green fluorescent probe (Thermo Fisher Scientific) for 1 h at room temperature (22 °C). The viability of the algae was determined by counting the live/dead ratio using an Invitrogen EVOS FL fluorescence microscope.

Characterization of acido-algae-PLLNP and acido-algae-RBCNP biohybrid motors. To visualize nanoparticle binding on the surface of the algae, PLGA cores were loaded beforehand with the fluorescent dye DiO. An Invitrogen EVOS FL microscope was used to capture the autofluorescence of algae chloroplasts in the Cy5 channel and DiO-encapsulated nanoparticles in the GFP channel. To further confirm the morphology of the acido-algae-PLLNP and acido-algae-RBCNP biohybrid motors, SEM imaging was performed. Briefly, the biohybrid motors were fixed with a 2.5% glutaraldehyde solution (Sigma Aldrich) overnight at 4 °C, followed by washing in ultrapure water. The samples were then sputtered with palladium for imaging on a Zeiss Sigma 500 SEM instrument with an accelerating voltage of 3 kV.

Animal care. Mice were housed in an animal facility at the University of California San Diego (UCSD) under federal, state, local, and National Institutes of Health (NIH) guidelines. Mice were maintained in standard housing with cycles of 12 h light and 12 h dark, ambient temperature, and normal humidity. All animal experiments were performed in accordance with NIH guidelines and approved by the Institutional Animal Care and Use Committee (IACUC) of UCSD.

Ex vivo GI tract imaging and retention quantification. To study GI tract distribution and retention, 8-week-old male CD-1 mice (Charles River Laboratories) were orally administered with Cy7-conjugated acidophilic algae, Cy7-conjugated static acidophilic algae, or Cy7-conjugated neutrophilic algae in 500 μl of PBS at a concentration of 1×10^7 per ml. At the predetermined time points (0.5 h, 2 h, 5 h, 10 h, and 24 h), the mice were euthanized, and their GI tracts were excised for analysis. To evaluate the performance of the biohybrid motors in vivo, the mice were orally administered with acido-algae-PLLNP, PLLNP, acido-algae-RBCNP or RBCNP. At predetermined time points (2 h, 5 h, and 10 h), the mice were euthanized, and their GI tracts were excised for analysis. Fluorescent ex vivo GI images were obtained with the Xenogen IVIS 200 system.

In vivo safety studies. 8-week-old male CD-1 mice were euthanized at 24 h after oral administration of algae motors in 500 μl of PBS at a concentration of 1×10^7 per ml. For the comprehensive chemistry panel, aliquots of blood were allowed to coagulate, and the serum was collected by centrifugation. To obtain blood cell counts, whole blood was collected into potassium EDTA collection tubes (Sarstedt). Analyses were conducted by the UCSD Animal Care Program Diagnostic Services Laboratory. To perform the histological analysis, different portions of the GI tract and major organs were sectioned and stained with H&E (Leica Biosystems), followed by imaging using a Hamamatsu Nanozoomer 2.0-HT slide scanning system.

Chapter 2.3, in full, is a reprint of the material as it may appear in Science Advances, 2022, by Fangyu Zhang, Zhengxing Li, Yaou Duan, Hao Luan, Lu Yin, Zhongyuan Guo, Chuanrui Chen, Mingyao Xu, Weiwei Gao, Ronnie H. Fang, Liangfang Zhang, Joseph Wang. The dissertation author was the primary investigator and author of this paper.

2.3.9 References

1. G.Z. Yang, J. Bellingham, P.E. Dupont, P. Fischer, L. Floridi, R. Full, N. Jacobstein, V. Kumar, M. McNutt, R. Merrifield, B.J. Nelson, The grand challenges of Science Robotics. *Sci. Robot.* **3**, eaar7650 (2018).

2. K.L. Smith Jr, A.D. Sherman, P.R. McGill, R.G. Henthorn, J. Ferreira, T.P. Connolly, C.L. Huffard, Abyssal Benthic Rover, an autonomous vehicle for long-term monitoring of deep-ocean processes. *Sci. Robot*. **6**, eabl4925 (2021).

3. H. Singh, T. Maksym, J. Wilkinson, G. Williams, Inexpensive, small AUVs for studying ice-covered polar environments. *Sci. Robot.* **2**, eaan4809 (2017).

4. J. Dupeyroux, J. R. Serres, S. Viollet, AntBot: A six-legged walking robot able to home like desert ants in outdoor environments. *Sci. Robot.* **4**, eaau0307 (2019).

5. A. Ghosh, P. Fischer, Controlled propulsion of artificial magnetic nanostructured propellers. *Nano Lett.* **9**, 2243-2245 (2009).

6. L. Zhang, J.J. Abbott, L. Dong, B.E. Kratochvil, D. Bell, B.J. Nelson, Artificial bacterial flagella: Fabrication and magnetic control. *Appl. Phys. Lett.* **94**, 064107 (2009).

7. B. Dai, J. Wang, Z. Xiong, X. Zhan, W. Dai, C.C. Li, S.P. Feng, J. Tang, Programmable artificial phototactic microswimmer. *Nat. Nanotechnol.* **11**, 1087-1092 (2016).

8. M. Xuan, Z. Wu, J. Shao, L. Dai, T. Si, Q. He, Near infrared light-powered Janus mesoporous silica nanoparticle motors. *J. Am. Chem. Soc.* **138**, 6492-6497 (2016).

9. W. Wang, S. Li, L. Mair, S. Ahmed, T.J. Huang, T.E. Mallouk, Acoustic propulsion of nanorod motors inside living cells. *Angew. Chem. Int. Ed.* **53**, 3201-3204 (2014).

10. A. A. Solovev, Y. Mei, E. Bermúdez Ureña, G. Huang, O. G. Schmidt, Catalytic microtubular jet engines self-propelled by accumulated gas bubbles. *Small* **5**, 1688-1692 (2009).

11. W.F. Paxton, K.C. Kistler, C.C. Olmeda, A. Sen, S.K. St. Angelo, Y. Cao, T.E. Mallouk, P.E. Lammert, V.H. Crespi, Catalytic nanomotors: autonomous movement of striped nanorods. *J. Am. Chem. Soc.* **126**, 13424-13431 (2004).

12. W. Gao, S. Sattayasamitsathit, J. Orozco, J. Wang, Highly efficient catalytic microengines: template electrosynthesis of polyaniline/platinum microtubes. *J. Am. Chem. Soc.* **133**, 11862-11864 (2011).

13. X. Ma, A. Jannasch, U.R. Albrecht, K. Hahn, A. Miguel-López, E. Schaffer, S. Sánchez, Enzyme-powered hollow mesoporous Janus nanomotors. *Nano Lett.* **15**, 7043-7050 (2015).

14. W. Gao, A. Pei, J. Wang, Water-driven micromotors. *ACS Nano* **6**, 8432-8438 (2012).

15. J. Wang, Nanomachines: fundamentals and applications. (Wiley-VCH, Weinheim, 2013).

16. M. Medina-Sánchez, L. Schwarz, A. K. Meyer, F. Hebenstreit, O. G. Schmidt, Cellular cargo delivery: Toward assisted fertilization by sperm-carrying micromotors. *Nano Lett.* **16**, 555-561 (2015).

17. D. B. Weibel, P. Garstecki, D. Ryan, W. R. DiLuzio, M. Mayer, J.E. Seto, G. M. Whitesides, Microoxen: Microorganisms to move microscale loads. *Proc. Natl. Acad. Sci. U.S.A.* **102**, 11963-11967 (2005).

18. Y. Alapan, O. Yasa, O. Schauer, J. Giltinan, A. F. Tabak, V. Sourjik, M. Sitti, Soft erythrocyte-based bacterial microswimmers for cargo delivery. *Sci. Robot.* **3**, eaar4423 (2018).

19. O. Felfoul, M. Mohammadi, S. Taherkhani, D. De Lanauze, Y. Z. Xu, D. Loghin, S. Essa, S. Jancik, D. Houle, M. Lafleur, L. Gaboury, M. Tabrizian, N. Kaou, M. Atkin, T. Vuong, G. Batist, N. Beauchemin, D. Radzioch, S. Martel, Magneto-aerotactic bacteria deliver drug-containing nanoliposomes to tumour hypoxic regions. *Nat. Nanotechnol*. **11**, 941-947 (2016).

20. F. Zhang, Z. Li, L. Yin, Q. Zhang, N. Askarinam, R. Mundaca-Uribe, F. Tehrani, E. Karshalev, W. Gao, L. Zhang, J. Wang, ACE2 receptor modified algae-based microrobot for removal of SARS-CoV-2 in wastewater. *J. Am. Chem. Soc.* **43**, 12194–12201 (2021).

21. B. E. F. de Ávila, P. Angsantikul, J. Li, W. Gao, L. Zhang, J. Wang. Micromotors go in vivo: from test tubes to live animals. *Adv. Funct. Mater.* **28**, 1705640. (2018).

22. Y. Alapan, U. Bozuyuk, P. Erkoc, A. C. Karacakol, M. Sitti, Multifunctional surface microrollers for targeted cargo delivery in physiological blood flow. *Sci. Robot.* **5**, eaba5726 (2020).

23. H. Zhang, Z. Li, C. Gao, X. Fan, Y. Pang, T. Li, Z. Wu, H. Xie, Q. He, Dual-responsive biohybrid neutrobots for active target delivery. *Sci Robot.* **6**, eaaz9519 (2021).

24. Z. Wu, J. Troll, H. H. Jeong, Q. Wei, M. Stang, F. Ziemssen, Z. Wang, M. Dong, S. Schnichels, T. Qiu, P. Fischer, A swarm of slippery micropropellers penetrates the vitreous body of the eye. *Sci. Adv.* **4**, eaat4388 (2018).

25. B. Wang, K. F. Chan, K. Yuan, Q. Wang, X. Xia, L. Yang, H. Ko, Y. X. J. Wang, J. J. Y. Sung, P. W. Y. Chiu, L. Zhang, Endoscopy-assisted magnetic navigation of biohybrid soft microrobots with rapid endoluminal delivery and imaging. *Sci. Robot.* **6**, eabd2813 (2021).

26. F. Zhang, J. Zhuang, Z. Li, H. Gong, B.E.F. de Ávila, Y. Duan, Q. Zhang, J. Zhou, L. Yin, E. Karshalev, W. Gao, V. Nizet, R. H. Fang, L. Zhang, J. Wang, Nanoparticle-modified microrobots for in vivo antibiotic delivery to treat acute bacterial pneumonia. *Nat. Mater.* **21,** 1324. (2022).

27. R. Mundaca-Uribe, E. Karshalev, B. E. F. de Ávila, X. Wei, B. Nguyen, I. Litvan, R. H. Fang, L. Zhang, J. Wang, A Microstirring Pill Enhances Bioavailability of Orally Administered Drugs. *Adv. Sci.* **8**, 2100389 (2021).

28. F. Zhang, Z. Li, Y. Duan, A. Abbas, R. Mundaca-Uribe, L. Yin, H. Luan, W. Gao, R. H. Fang, L. Zhang, J. Wang, Gastrointestinal tract drug delivery using algae motors embedded in a degradable capsule. *Sci. Robot.* **7**, eabo4160 (2022).

29. J. N. Chu, G. Traverso, Foundations of gastrointestinal-based drug delivery and future developments. *Nat. Rev. Gastroenterol. Hepatol.* **19**, 219-238 (2022).

30. A. M. Bellinger, M. Jafari, T. M. Grant, S. Zhang, H. C. Slater, E. A. Wenger, S. Mo, Y. A. L. Lee, H. Mazdiyasni, L. Kogan, R. Barman, C. Cleveland, L. Booth, T. Bensel, D. Minahan, H. M. Hurowitz, T. Tai, J. Daily, B. Nikolic, L. Wood, P. A. Eckhoff, R. Langer, G. Traverso, Oral, ultra–long-lasting drug delivery: Application toward malaria elimination goals. *Sci. Transl. Med.* **8**, 365ra157 (2016).

31. A. Abramson, E. Caffarel-Salvador, M. Khang, D. Dellal, D. Silverstein, Y. Gao, M. R. Frederiksen, A. Vegge, F. Hubálek, J. J. Water, A. V. Friderichsen, J. Fels, R. K. Kirk, C. Cleveland, J. Collins, S. Tamang, A. Hayward, T. Landh, S. T. Buckley, N. Roxhed, U. Rahbek, R. Langer, G. Traverso, An ingestible self-orienting system for oral delivery of macromolecules. *Science,* **363**, 611-615 (2019).

32. A. Abramson, M. R. Frederiksen, A. Vegge, B. Jensen, M. Poulsen, B. Mouridsen, M. O. Jespersen, R. K. Kirk, J. Windum, F. Hubálek, J. J. Water, J. Fels, S. B. Gunnarsson, A. Bohr, E. M. Straarup, M. W. H. Ley, X. Lu, J. Wainer, J. Collins, S. Tamang, K. Ishida, A. Hayward, P. Herskind, S. T. Buckley, N. Roxhed, R. Langer, U. Rahbek, G. Traverso, Oral delivery of systemic monoclonal antibodies, peptides and small molecules using gastric auto-injectors. *Nat. Biotechnol.* **40**, 103–109 (2022).

33. D. Walker, B. T. Käsdorf, H.-H. Jeong, O. Lieleg, P. Fischer, Enzymatically active biomimetic micropropellers for the penetration of mucin gels. *Sci. Adv.* **1**, e1500501 (2015).

34. W. Gao, M. D'Agostino, V. Garcia-Gradilla, J. Orozco, J. Wang, Multi-fuel driven janus micromotors. *Small* **9**, 467-471 (2013).

35. B. E. F. de Ávila, P. Angsantikul, J. Li, M. A. Lopez-Ramirez, D. E. Ramírez-Herrera, S. Thamphiwatana, C. Chen, J. Delezuk, R. Samakapiruk, V. Ramez, M. Obonyo, L. Zhang, J. Wang, Micromotor-enabled active drug delivery for in vivo treatment of stomach infection. *Nat. Commun.* **8**, 272 (2017).

36. W. Gao, R. Dong, S. Thamphiwatana, J. Li, W. Gao, L. Zhang, J. Wang, Artificial micromotors in the mouse's stomach: A step toward in vivo use of synthetic motors. *ACS Nano* **9**,117-123 (2015).

37. N. Merino, H.S. Aronson, D.P. Bojanova, J. Feyhl-Buska, M.L. Wong, S. Zhang, D. Giovannelli, Living at the extremes: extremophiles and the limits of life in a planetary context. *Front. Microbiol.* **10**, 780 (2019).

38. S. Hirooka, Y. Hirose, Y. Kanesaki, S. Higuchi, T. Fujiwara, R. Onuma, A. Era, R. Ohbayashi, A. Uzuka, H. Nozaki, H. Yoshikawa, Acidophilic green algal genome provides insights into adaptation to an acidic environment. *Proc. Natl. Acad. Sci. U.S.A.* **114**, E8304-E8313 (2017).

39. D. B. Johnson, Acidophilic algae isolated from mine-impacted environments and their roles in sustaining heterotrophic acidophiles. *Front. Microbiol.* **3**, 325 (2012).

40. W. Gross, Ecophysiology of algae living in highly acidic environments. *Hydrobiologia* **433**, 31-37 (2000).

41. A.P. Dean, A. Hartley, O.A. McIntosh, A. Smith, H.K. Feord, N.H. Holmberg, T. King, E. Yardley, K.N. White, J.K. Pittman, Metabolic adaptation of a Chlamydomonas acidophila strain isolated from acid mine drainage ponds with low eukaryotic diversity. *Sci. Total Environ.* **647**, 75-87 (2019).

42. M. M. Olaueson, P. M. Stokes, Responses of the acidophilic alga Euglena Mutabilis (Euglenophyceae) to carbon enrichment at pH 3. *J. Phycol.* **25**, 529-539 (1989).

43. Yasa, O., Erkoc, P., Alapan, Y. & Sitti, M. Microalga-powered microswimmers toward active cargo delivery. *Adv. Mater.* **30**, 1804130 (2018).

44. L. M. Ensign, R. Cone, J. Hanes, Oral drug delivery with polymeric nanoparticles: the gastrointestinal mucus barriers. *Adv. Drug Deliv. Rev.* **64**, 557-570 (2012).

45. A. Brodkorb, L. Egger, M. Alminger, P. Alvito, R. Assunção, S. Ballance, T. Bohn, C. Bourlieu-Lacanal, R. Boutrou, F. Carrière, A. Clemente, M. Corredig, D. Dupont, C. Dufour, C. Edwards, M. Golding, S. Karakaya, B. Kirkhus, S. Le Feunteun, U. Lesmes, A. Macierzanka, A. R. Mackie, C. Martins, S. Marze, D. J. McClements, O. Ménard, M. Minekus, R. Portmann, C. N. Santos, I. Souchon, R. P. Singh, G. E. Vegarud, M. S. J. Wickham, W. Weitschies, I. Recio, INFOGEST static in vitro simulation of gastrointestinal food digestion. *Nat. Protoc.* **14**, 991-1014 (2019).

46. M. Y. Inoue, K. Izawa, S. Kiryu, A. Tojo, K. Ohtomo, Diet and abdominal autofluorescence detected by in vivo fluorescence imaging of living mice. *Mol. Imaging* **7**, 7290 (2008).

47. M. N. Kamaly, Z. Xiao, P. M. Valencia, A. F. Radovic-Moreno, O. C. Farokhzad, Targeted polymeric therapeutic nanoparticles: design, development and clinical translation. *Chem. Soc. Rev.* **41**, 2971-3010 (2012).

48. M. S. Honary, F. Zahir, Effect of zeta potential on the properties of nano-drug delivery systems-a review (Part 1). *Trop. J. Pharm. Res.* **12**, 255-264 (2013).

49. X. Wei, M. Beltrán-Gastélum, E. Karshalev, Berta Esteban-Fernández de Á vila, J. Zhou, D. Ran, P. Angsantikul, R. H. Fang, J. Wang, L. Zhang. Biomimetic micromotor enables active delivery of antigens for oral vaccination. *Nano Lett.* **19**, 1914–1921 (2019).

50. R. H. Fang, A. V. Kroll, W. Gao, L. Zhang, Cell membrane coating nanotechnology. *Adv. Mater.* **30**, 1706759 (2018).

51. J.A. Copp, R.H. Fang, B.T. Luk, C.M.J. Hu, W. Gao, K. Zhang, and L. Zhang, Clearance of pathological antibodies using biomimetic nanoparticles. *Proc. Natl. Acad. Sci. U.S.A.* **111**, 13481-13486 (2014).

52. Q. Hu, W. Sun, J. Wang, H. Ruan, X. Zhang, Y. Ye, S. Shen, C. Wang, W. Lu, K. Cheng, G. Dotti, J. F. Zeidner, J. Wang, Z. Gu, Conjugation of haematopoietic stem cells and platelets decorated with anti-PD-1 antibodies augments anti-leukaemia efficacy. *Nat. Biomed. Eng.* **2**, 831 (2018).

53. S. Hellmig, F. Von Schöning, C. Gadow, S. Katsoulis, J. Hedderich, U.R. Fölsch, E. Stüber, Gastric emptying time of fluids and solids in healthy subjects determined by 13C breath tests: influence of age, sex and body mass index. *J. Gastroenterol. Hepatol.* **21**, 1832-1838 (2016).

54. H. K. Makadia, S. J. Siegel, Poly lactic-co-glycolic acid (PLGA) as biodegradable controlled drug delivery Carrier. *Polymers* **3**, 1377-1397 (2011).

55. J. M. Hyman, E. I. Geihe, B. M. Trantow, B. Parvin, P. A. Wender, A molecular method for the delivery of small molecules and proteins across the cell wall of algae using molecular transporters. *Proc. Natl. Acad. Sci. U.S.A.* **109**, 13225-13230 (2012).

56. C. Lautenschläger, C. Schmidt, D. Fischer, A. Stallmach, Drug delivery strategies in the therapy of inflammatory bowel disease. *Adv. Drug Deliv. Rev.* **71**, 58-76 (2014).

2.4 Microalgae microrobots for SARS-CoV-2 removal

2.4.1 Introduction

As an emerging coronavirus associated with formidable infectiousness and lethality, severe acute respiratory syndrome coronavirus 2 (SARS-CoV-2) can spread through multiple transmission routes, including direct airborne transmission from respiratory droplets or aerosols and indirect fomite transmission upon contacting contaminated subjects or surfaces.[1] While SARS-CoV-2 is known to infect the respiratory tract, it can also infect the gastrointestinal tract with a prolonged residence in fecal samples.[2] In addition to its presence in stool samples, SARS-CoV-2 has also been detected in domestic wastewater in sewage and downstream rivers.[3-5] These reports have raised concerns that wastewater could be a potential route of SARS-CoV-2 infection via fecal-oral transmission.[6,7] To minimize the risk of secondary transmission to humans, there remains an urgent need to develop wastewater treatment strategies for the effective removal of SARS-CoV-2. Several physical, chemical, and biological processes, including sedimentation, filtration, disinfection with UV or oxidants, and enzymatic degradation, have been proposed to tackle SARS-CoV-2 decontamination in wastewater.[8] While these conventional wastewater purification approaches are effective in general, it is still necessary to explore new techniques that are easy, fast, and effective in resolving the wastewater contamination issue of SARS-CoV-2.

We present here a biohybrid microrobot for the efficient removal of SARS-CoV-2 from contaminated aquatic media. Because of their robust self-propulsion ability and facile surface functionalization, microrobots offer a dynamic and powerful strategy for rapid decontamination of water matrices from a wide range of environmental pollutants, including dyes,[9,10] heavy metals,[11,12] oil,[13] pathogenic organisms,[14,15] nitroaromatic explosives,[16] and chemical and biological warfare agents.[17] Such movement of functional microrobots provides an enhanced collision/contact and adsorption of the target contaminants along with localized self-mixing as compared to their static counterparts, thus enabling efficient and rapid decomposition and accelerated "on-the-fly" removal of pollutants.[18,19] However, widespread environmental and defense applications of current synthetic microrobotic platforms have been hampered by their short life span, need for toxic fuels, or complex external actuation equipment, and restricted operating media. To address these challenges faced by synthetic microrobots, biohybrid microrobots, combining self-propelled microorganisms with functional biomaterials, have recently demonstrated significant promise for large-scale environmental remediation.[20−22]

The new microrobotic strategy for SARS-CoV-2 removal relies on angiotensin-converting enzyme 2 (ACE2) receptor functionalized algae microrobot (denoted "ACE2-algae-robot"). The ACE2 receptor is responsible for the recognition of the target virus with a high binding affinity to the S1 subunit of the viral spike protein and has been reported as an effective cellular receptor for SARS-CoV-2 toward diverse virus-related sensing,[23] therapeutic,[24] and neutralization[25] applications. Algae have been used for wastewater treatment[26] but not in connection to active microrobots or toward the management of SARS-CoV-2 contaminated water. Here we select Chlamydomonas reinhardtii as a model algae because of their attractive properties, including easy large-scale production, fast motion in diverse aqueous environments, long life span, and facile surface functionalization.[27,28] As illustrated in Figure 2.19a, the ACE2-algae-robot is fabricated using a click chemistry reaction for anchoring the ACE2 receptor onto the algae surface. The resulting ACE2-algae-robot displays fast movement (>100 μm/s) in various media, without compromising the intrinsic mobility of unmodified algae. Using SARS-CoV-2 spike protein (S protein) and pseudovirus as model contaminants, the moving ACE2 receptor on the algae surface leads to remarkable binding to the targets, enabling about 95% removal of the S protein and about 89% removal of SARS-CoV-2 pseudovirus from various testing wastewater (Figure 2.19b). The pseudovirus bears the same spike protein as the live SARS-CoV-2 virus and has been shown extremely useful for developing SARS-CoV-2 detection and neutralization technologies.[29] These results clearly illustrate the feasibility of using the biohybrid microrobot for large-scale “on-the-fly” decontamination of coronavirus and possibly other diverse environmental threats in wastewater.

2.4.2 Fabrication and characterization of the ACE2-Algae-Robots

Figure 1 schematically displays (a) the fabrication process of the ACE2 modified algae and (b) the targeting and removal of S protein and SARS-CoV-2 pseudovirus from wastewater. In the study, the ACE2 receptors were conjugated to the algae surface using a click chemistry approach. Specifically, the azide and dibenzocyclooctyne (DBCO) groups were conjugated to the ACE2 receptors and the algae, respectively, via the N-hydroxysuccinimide (NHS) ester reaction. The conjugated N_3 on the ACE2 receptors will then react effectively with the DBCO on the algae, resulting in the formation of the ACE2-algae-robot. Next, immunostaining was performed to visualize the ACE2 receptors attached on the algae surface. Here, Fluor488-conjugated anti-ACE2 antibody was used to label the ACE2 receptors on the algae. As illustrated in Figure 2.19c, the signals from immunostaining of fluorescent anti-ACE2 antibody in the GFP channel colocalized with those of the autofluorescence of algae in the Cy5 channel. The enlarged image in Figure 2.19d further indicates the coverage of ACE2 receptors on the algae surface. In addition, the unmodified algae incubated with fluorescent anti-ACE2 antibody exhibited a negligible change of GFP fluorescence intensity as compared to the bare algae alone (Figure 2.19e). In contrast, the ACE2-algae-robot incubated with fluorescent anti-ACE2 antibody showed a significant increase in fluorescent intensity as compared to the two control groups, reflecting the effective conjugation of ACE2 receptors onto the algae via click chemistry. The pseudocolored scanning electron microscopy (SEM) images further illustrate the ACE2-algae-robot before (Figure 2.19f) and after (Figure 2.19g) contact with SARS-CoV-2 pseudovirus. The bound virus particles can be clearly observed on the ACE2-algae-robot from the inset of SEM images in Figure 2.19g.

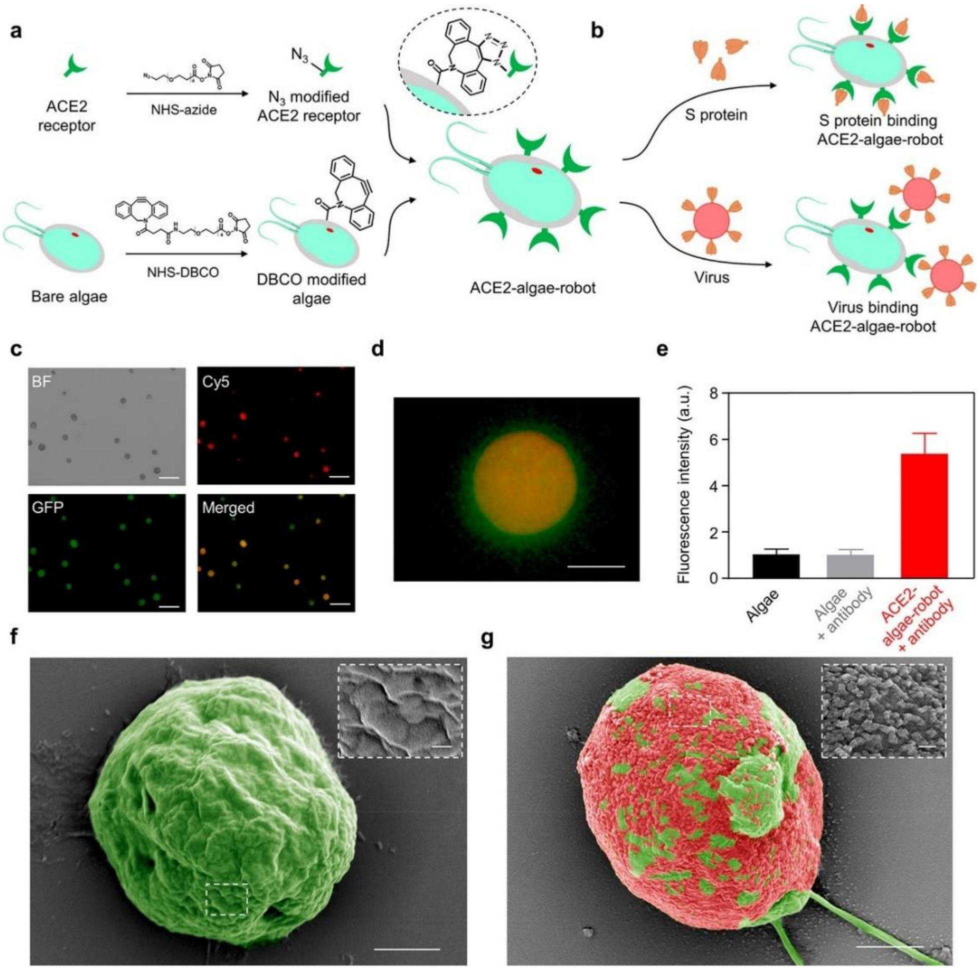

Figure 2.19 Fabrication and characterization of ACE2-algae-robot. (a) Schematic of the functionalization of microalgae with ACE2 receptor. (b) Schematic depicting the use of the ACE2-algae-robot for the binding and removal of spike protein and SARS-CoV-2 virus. (c) Brightfield, fluorescent, and merged images of the ACE2-algae-robot after immunostaining. Autofluorescence of natural algae chloroplast in Cy5 channel; immunostaining of Fluor488-conjugated anti-ACE2 antibody in GFP channel. Scale bar: 50 µm. (d) Enlarged fluorescence image from panel (c) clearly shows the full coverage of the ACE2 receptor onto the algae surface. Red core: chloroplast of the algae; green: Fluor488-conjugated anti-ACE2 antibody. Scale bar: 5 µm. (e) GFP fluorescence intensity of bare algae, bare algae with Fluor488-conjugated anti-ACE2 antibody, and the ACE2-algae-robot with Fluor488-conjugated anti-ACE2 antibody. (f,g) Pseudocolored scanning electron microscopy (SEM) images of the ACE2-algae-robot (f) before and (g) after contact with the virus. Green: ACE2-algae-robot; red: SARS-CoV-2 pseudovirus. Scale bar: 2 µm. Zoom-in images show the surface morphology of the ACE2-algae-robot (f) before and (g) after contact with the virus. Scale bar: 200 nm.

2.4.3 Motion behavior of ACE2-Algae-Robots in aquatic media

We next investigated the motion behavior of the biohybrid microrobot. After confirming the DBCO-NHS ester conjugation, the ACE2-algae-robot was fabricated by mixing DBCO modified algae with the azide-ACE2 receptor in DI water for 2 h. The speed of the DBCO-modified algae and the ACE2-algae-robot were measured to be 112 μm/s and 108 μm/s (∼11 body length/s), respectively, compared to 115 μm/s of the bare algae, indicating that the functionalization process has a negligible effect on the motion of the algae (Figure 2.20a). Once prepared in DI water, the ACE2-algae-robot was transferred into various aqueous media to test their mobility. As illustrated in Figure 2.20b, the ACE2-algae-robot displayed efficient motion (>100 μm/s) in TAP medium, 0.1 × PBS, drinking water, and river water without a need of any external fuel to propel the robot. In addition, the ACE2-algae-robot demonstrated long-lasting motion in both drinking and river water matrices (Figure 2.20c,d), indicating its capability for extended operation toward the removal of SARS-CoV-2 S protein and pseudovirus. The images in Figure 2.20e,f illustrate representative tracking trajectories of the individual ACE2-algae-robot, over a 2.5 s interval, at different times [0 h (i) and 24 h (ii)] in drinking and river water, respectively, reflecting the highly stable algae motion in these media.

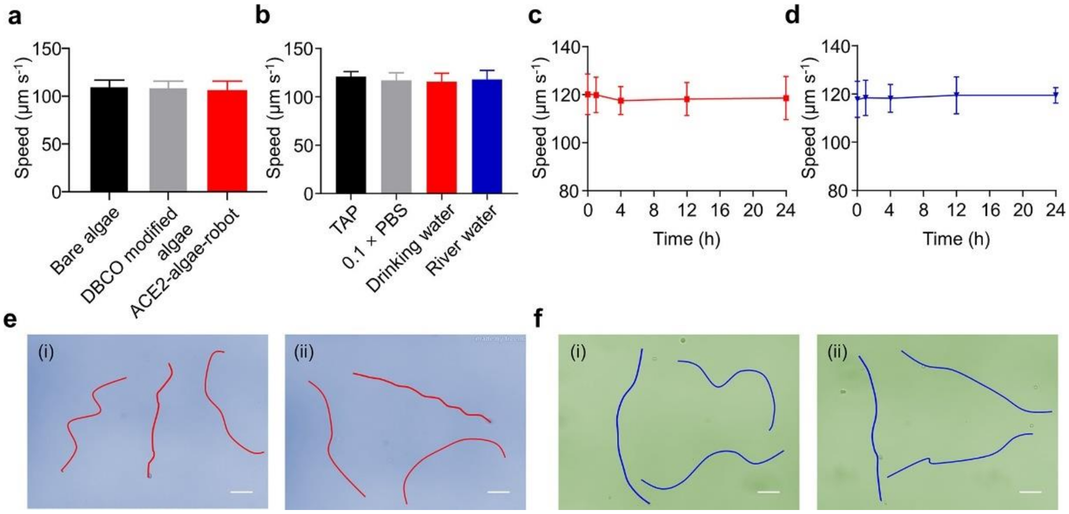

Figure 2.20 Motion behavior of the ACE2-algae-robot. (a) Effect of the algae functionalization upon its swimming behavior: speeds of bare algae, DBCO-modified algae, and the ACE2-algae-robot (n = 6; mean + s.d.). (b) Movement of the ACE2-algae-robot in different media: tris-acetate-phosphate medium (TAP), 0.1 × phosphate-buffered saline (PBS; diluted from 1 × PBS with DI water), drinking water, and river water (n = 6; mean + s.d.). (c,d) Speed of the ACE2-algae-robot at different time points (0, 1, 4, 12, and 24 h) in (c) drinking water and (d) river water (n = 6; mean ± s.d.). (e,f) Representative optical trajectories of the movement of the ACE2-algae-robot over 2.5 s motion in (e) drinking water and (f) river water obtained at (i) 0 h and (ii) 24 h. Scale bar: 40 μm.

2.4.4 Removal of SARS-CoV-2 Spike protein by ACE2-Algae-Robots

Figure 2.21a illustrates that the presence of viral S protein in the drinking water (red) and river water (blue) did not affect the mobility or the lifespan of the ACE2-algae-robot, which showed highly stable motion in both media for over 24 h operation. This was supported by the tracking trajectories of about 200 individual ACE2-algae-robots (during 0.6 s) after moving for 24 h in drinking water and river water, respectively (Figure 2.21b,c). The corresponding speed distribution indicates that 80% of algae moved faster than 100 μm/s. Such fast and continuous motion of the ACE2-algae-robot could accelerate its collision with viral S protein and thus improve the specific binding and removal of the target protein. Figure 2.21d examines the effect of ACE2-

algae-robot density on the kinetic removal efficiency of S protein from drinking water. As expected, the speed and efficiency of the removal process increased upon increasing the density of the microrobots, with 5×10^7 ml^{-1} ACE2-algae-robot removing 95% of 2.88 ng/mL S protein from the water sample within 6 h. To compare the S protein removal capability between different algae groups, the same density of algae (5×10^7 ml^{-1}) from different control groups, including the ACE2-algae-robot, static ACE2-algae (deflagellated algae with the ACE2 receptor modification), bare algae, and cell wall deficient algae, was added to 500 μL drinking water containing 2.88 ng/mL S protein. The ACE2-algae-robot shows highly efficient binding and 95% removal efficiency after 6 h continuous motion (Figure 2.21e,(i). In comparison, the active bare algae lacking ACE2 (Figure 2.21e,(ii) and static ACE2-algae (Figure 2.21e,(iii) displayed only 46% and 23% removal efficiency after 16 h operation, respectively, indicating the critical role of the ACE2 receptor modification and algae motion on the speed and efficiency of the S protein removal. The S protein removal by the bare algae is likely attributed to nonspecific binding associated with the presence of diverse functional groups (e.g., carboxyl or amino groups) on the algae surface.[30] The ACE2-algae-robot also exhibits effective S protein removal in various media, including DI water, drinking water, and river water, as indicated by the similar kinetic profiles in Figure 2.21f. These results reveal that the ACE2-algae-robot, with long-lasting motion and ACE2 receptor for S protein recognition, represents an attractive system to enhance environmental remediation in complex aqueous surroundings.

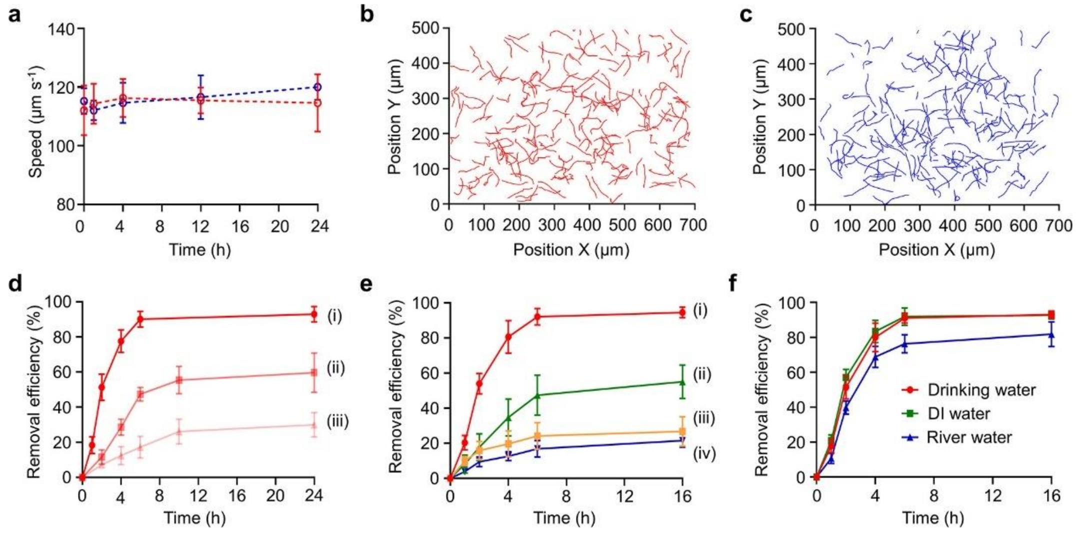

Figure 2.21 ACE2-algae-robot for the removal of SARS-CoV-2 spike protein. (a) Speed comparison of the ACE2-algae-robot in drinking water (red) and river water (blue) containing the spike protein (n = 6; mean ± s.d.). (b,c) Motion trajectory of the ACE2-algae-robot in (b) drinking water and (c) river water samples containing the spike protein. (d) Effect of the ACE2-algae-robot density on the spike protein removal kinetic profile in the drinking water. Algae input density: (i) 5×10^{7} ml^{-1}, (ii) 2×10^{7} ml^{-1}, and (iii) 5×10^{6} mL^{-1} (n = 3; mean ± s.d.). (e) Kinetic profile of the spike protein removal efficiency from drinking water with the treatment of the (i) ACE2-algae-robot, (ii) bare algae, (iii) static ACE2-algae, or (iv) cell wall deficient algae. (f) Kinetic profile of the spike protein removal efficiency by employing the ACE2-algae-robot in different media, including drinking water, DI water, and river water (n = 3; mean ± s.d.).

2.4.5 Removal of SARS-CoV-2 pseudovirus by ACE2-Algae-Robots

Following the effective removal of viral S protein, the next set of experiments examined the ability of the ACE2-algae-robot to remove SARS-CoV-2 pseudoviruses, which represents an effective alternative of live human SARS-CoV-2 virus for research to evaluate new antiviral technologies.[29] Figure 2.22a schematically illustrates the efficient removal of the SARS-CoV-2 pseudovirus from water samples using the ACE2-algae-robot. After ACE2-algae-robot treatment, the pseudoviruses are largely captured and removed from the solution, validated, and visualized by an NL-20 cell-based assay. The NL-20 cells remained nonfluorescent following 24 h incubation in pseudovirus contaminated water samples upon ACE2-algae-robot treatment, confirming the highly effective pseudovirus removal by the robot. In comparison, without the ACE2-algae-robot treatment, the cells displayed bright fluorescence, reflecting the pseudovirus entry and significant expression of fluorescent protein in the host cells. Figure 2.22b show the motion behavior (speed and lifespan) of the ACE2-algae-robot in various water matrices containing the SARS-CoV-2 pseudovirus. The biohybrid microrobot displays similar speed in these aqueous media, which is similar to that observed in Figure 2.22b without the pseudovirus, indicating that the presence of the pseudovirus does not hamper the movement of the ACE2-algae-robot.

Next, we investigated the effect of ACE2-algae-robot density on the removal efficiency of SARS-CoV-2 pseudovirus from drinking water. As shown in Figure 2.22c, the results demonstrated a gradual increase of the removal efficiency, 19% to 90%, upon increasing ACE2-algae-robot concentrations from 5×10^4 mL^{-1} to 5×10^7 mL^{-1}. The pseudovirus removal efficiency was also visualized by fluorescent imaging. As expected, the highest robot concentration resulted in a minimal fluorescent virus signal (Figure 2.22d). The ACE2-algae-robot also offers significant improvement (89%) in the removal of SARS-CoV-2 pseudovirus compared with control groups, including static ACE2-algae (31%), bare algae (63%), and cell-wall deficient algae (21%) (Figure 4e). These experiments were performed by immersing 2.5×10^5 of algae in a 50 μL drinking water sample containing 2×10^9 VG ml^{-1} (VG: viral genomes) pseudovirus for 16 h. In the control experiments, the viral binding capability of the bare algae is possibly attributed to both biosorption[30] and physical entrapment of the virus into the porous structure of the algae cell wall.[31] The fluorescence images in Figure 2.22f illustrate the minimal fluorescent virus signal with the ACE2-algae-robot treatment, corresponding to the virus removal efficiency data of Figure 2.22e. Furthermore, we evaluated and compared the virus removal kinetic profiles in drinking water treated with the ACE2-algae-robot, bare algae, or static ACE2-algae (Figure 2.22g). These data illustrate that the ACE2-algae-robot can effectively remove 85% of pseudovirus after 4 h treatment, compared to 60% and 18% for bare algae and static ACE2-algae, respectively. Therefore, each ACE2-algae-robot can bind to ∼340 VG of virus. Such results indicate the significant contributions of both the ACE2 receptor for virus targeting and the fast microrobot motion for contacting the virus toward highly efficient viral binding and removal. The representative fluorescence images also show the progression of the viral infection over time with samples treated with the ACE2-algae-robot (Figure 2.22h). Furthermore, the ACE2-algae-robot can be reused to reach 90% viral removal efficiency after five repeated cycles. A post-treatment of the ACE2-algae-robot by flocculant was performed to clean the robot in the water sample. The flocculant can isolate the ACE2-algae-robot from the water matrices without affecting the virus removal efficiency, holding considerable potential for practical future applications.

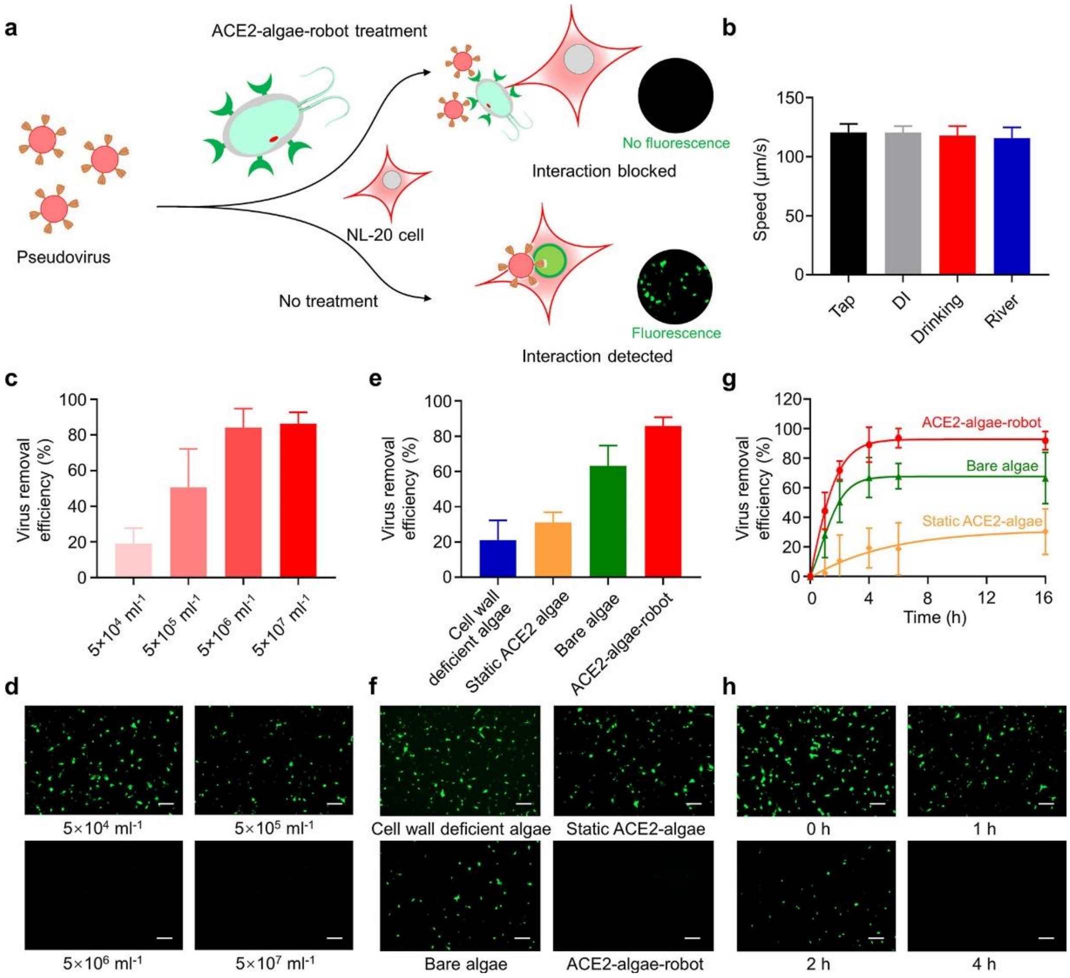

Figure 2.22 ACE2-algae-robot for the removal of SARS-CoV-2 pseudovirus. (a) Schematic illustrating the viral removal by the ACE2-algae-robot, which blocks the virus from entering cells. Inset: viral infection was indicated by expression of green fluorescent protein, whereas the virus treated by the ACE2-algae-robot shows low viral infection. (b) Speed comparison of the ACE2-algae-robot in TAP, DI water, drinking water, and river water containing 1×10^8 VG of the virus, (n = 3; mean ± s.d.). (c) Effect of the ACE2-algae-robot density on the efficiency of virus removal in drinking water. (d) Representative fluorescent images of NL-20 cells infected with virus treated by different densities of the ACE2-algae-robot. Scale bar: 100 μm. (e) Efficiency of the virus removal in drinking water with the treatment of the ACE2-algae-robot, bare algae, static ACE2-algae, or cell wall deficient algae. (f) Representative fluorescent images of NL-20 cells infected with the virus treated by the ACE2-algae-robot, bare algae, static ACE2-algae, and cell wall deficient algae. Scale bar: 100 μm. (g) Kinetic profile of the virus removal efficiency in drinking water with the treatment of the ACE2-algae-robot, bare algae, and static ACE2-algae (n = 3; mean ± s.d.). (h) Representative fluorescent images of NL-20 cells infected with the virus, which is treated by the ACE2-algae-robot for different times (0, 1, 2, and 4 h). Scale bar: 100 μm.

2.4.5 Discussion

In summary, we have developed an effective biohybrid microrobotic method to actively remove the SARS-CoV-2 spike protein and pseudovirus from various water matrices using ACE2 receptor-modified microalgae. The ACE2-algae-robot can be readily fabricated by an efficient click chemistry approach, without compromising the motion behavior of algae and the function of the ACE2 receptor. The resulting ACE2-algae-robot displays excellent motion ability in various water matrices and offers considerable potential to clean contaminated water samples. The binding and removal capability of the ACE2-algae-robot were demonstrated and characterized using both SARS-CoV-2 spike protein and SARS-CoV-2 pseudovirus, resulting in 95% and 89% removal efficiency, respectively, at the experimental conditions. Given the high concentration of viral load (2×10^9 VG ml^{-1}) in our experiment, the removal efficiency of 89% and binding capability of ∼340 VG $algae^{-1}$ represent a high efficacy compared to the traditional wastewater viral treatments.[32] The enhanced removal of the viral spike protein and pseudovirus is attributed to the continuous self-propulsion of the ACE2-algae-robot and corresponding mixing and collision with the target protein and virus. The reusability and post-treatment of the microrobot were also studied, demonstrating considerable promise for removing waterborne pathogenic viruses from contaminated water. Although current platform can reach 89% viral removal, it is difficult to directly convert viral concentration in wastewater to disease prevalence in hosts.[33] However, any reduction of viral load would have a positive correlation with the control of viral infectivity and the illness of patients.[34] The algae microrobots are expected to have greater mobility and longer lifetime in an open wastewater reservoir when compared to a confined test tube and thus hold considerable potential for future scaling-up applications. Given that new emerging SARS-CoV-2 variants show a similar binding mechanism and higher binding affinity with the ACE2 receptor,[35,36] the functionalized algae microrobotic platform is expected to efficiently remove different virus variants from wastewater. Overall, by relying on click chemistry to attach protein receptors onto natural algae surfaces, such a functionalized algae-based microrobot offers an attractive strategy for a variety of environmental remediation applications.

2.4.6 Experimental section

Algae culture. Green C. reinhardtii algae (strain CC-125 wild-type mt+) were obtained from the Chlamydomonas Resource Center. The algae were transferred from the agar plate to tris-acetate-phosphate (TAP) medium (Thermo Fisher Scientific) and cultivated at room temperature under cycles of 12 h sunlight and 12 h dark.

Preparation of ACE2-algae-robot. Bare algae were centrifuged at 500×g for 3 min and washed five times with ultrapure water to remove the TAP medium and then resuspended in ultrapure water. 1 ml of 1×10^7 ml-1 bare algae were treated with 20 μM DBCO-PEG4-NHS ester (Click Chemistry Tools) for 1 h at room temperature. Here, the presence of triple bonds on the algae surface was confirmed by adding 1 μM FAM azide, 5-isomer (Lumiprobe), and visualized by fluorescence microscopy. In parallel, 100 μl of 73 μg/ml ACE2 receptor (SinoBiological) was incubated with 20 μM azidoPEG4-NHS ester (Click Chemistry Tools) for 1 h at room temperature. As prepared azido-modified ACE2 receptor was concentrated by filtration at 4000×g for 10 min and washed three times with ultrapure water to remove free NHS ester through an ultrafilter with a 30 kDa molecular weight cut-off (Amicon Ultra 0.5mL Filters, Sigma Aldrich); DBCO-modified algae were centrifuged at 500×g for 3 min and washed five times with ultrapure water to remove unreacted NHS ester. The ACE2-algae-robot was fabricated by the incubation of azido-modified ACE2 receptor and DBCO-modified algae for 3 h via click chemistry. The resulting ACE2-algae-robots were centrifuged at 500×g for 3 min and washed 3 times with TAP and collected for further studies. To fabricate the static ACE2-algae, ACE2-algae-robot was incubated with 0.01M PBS for 30 min to remove the algae flagella.

Characterization of ACE2-algae-robot binding with SARS-CoV-2 pseudovirus. To perform scanning electron microscopy (SEM) characterization, ACE2-algae-robot binding with SARS-CoV-2 pseudovirus were fixed in 2.5% glutaraldehyde at 4 °C 2overnight and washed three times with ultrapure water before sputtering. The asprepared samples were sputtered with palladium before SEM characterization, and the SEM imaging was performed using an acceleration voltage of 3 KV (Zeiss Sigma 500 SEM instrument). The ACE2-algae-robot without SARS-CoV-2 pseudovirus was treated and examined using the same methodology. To determine the ACE2 receptor conjugation onto the algae, Fluor488-conjugated ACE2 antibody (R&D system) was chosen to label the ACE2 receptor on the algae. The immunostaining of antibody was visualized by fluorescence microscopy (EVOS FL) with two individual fluorescence channels, Cy5 and GFP, which corresponded to the autofluorescence of algae and Fluor488-conjugated anti-ACE2 antibody, respectively. The ACE2-algae-robot, with Fluor488-conjugated anti-ACE2 antibody, was resuspended in 1% BSA in PBS for flow cytometry analysis. Data were acquired with a BD FACSCanto II flow cytometer and analyzed using the FlowJo software.

Motion analysis of ACE2-algae-robot. The motion of ACE2-algae-robot, dibenzocyclooctyne (DBCO) modified algae and bare algae were analyzed in different media: tris-acetate-phosphate medium (TAP), 0.1×phosphate-buffered saline (PBS; diluted from 1×PBS with DI water), drinking water from Arrowhead Springs, river water from Peñasquitos Creek. After transferring to the drinking water or river water containing SARS-CoV-2 spike protein or pseudovirus, the speed of ACE2-algae-robot was evaluated at 0 h, 1 h, 4 h, 12 h, and 24 h. The movies of the motion were captured by an inverted optical microscope (Nikon Eclipse Instrument Inc. Ti-S/L 100) coupled with different microscope objectives (4x, 10x, and 20x), a Hamamatsu digital camera C11440, and NIS Elements AR 3.2 software. An NIS Element tracking module was used to measure the corresponding algae speed in different media.

Cell culture. Human bronchial epithelial non-tumoral cell line NL-20 (CLR-2503, American Type Culture Collection, ATCC) was cultured in HAM-F12 medium (Invitrogen) supplemented with 2.7 g/L glucose (Gibco), 4% fetal bovine serum (FBS), 0.1 mM non-essential amino acids (Gibco), 5 µg/ml of insulin (Sigma Aldrich), 10 ng/ml of epidermal growth factor (Sigma Aldrich), 1 µg/ml of transferrin (Sigma 3Aldrich), 500 ng/ml of hydrocortisone (Sigma Aldrich), 1% penicillin/streptomycin (Gibco) at 37 °C in a 5% CO2 environment. The cells were detached from culture flasks using 1× PBS containing 13.7 µL of 0.5 M ethylenediaminetetraacetic acid (EDTA) and 5% fetal bovine serum (FBS) at 37 °C and collected with centrifugation at 700×g for 5 min for further study.

Removal of SARS-CoV-2 spike protein. To explore the effect of ACE2-algae-robot density on the efficiency of spike protein removal, ACE2-algae-robot was incubated with 500 µl 2.88 ng/ml spike protein with different algae density of 5×10^7 ml^{-1}, 2×10^7 ml^{-1}, and 5×10^6 ml^{-1} in drinking water and tested the removal efficiency at 0 h, 1 h, 2 h, 4 h, 6 h, and 16 h. To explore the kinetic profiles of spike protein removal efficiency in drinking water, the bare algae, static ACE2-algae, and cell-wall deficient algae with a density of 5×10^7 ml^{-1} were incubated with 500 µl 2.88 ng/ml spike protein. 5 × 10^7 ml^{-1} ACE2-algae-robot were also incubated with 500 µl 2.88 ng/ml spike protein in different media, including DI water, drinking water, and river water, to study the environmental effect on the removal efficiency. To measure the spike protein removal efficiency, all the groups were centrifuged at 500×g for 3 min and quantified by SARS-CoV-2 spike RBD protein ELISA kits (ABclonal).

Removal of SARS-CoV-2 pseudovirus. To explore the effect of ACE2-algae-robot density on SARS-CoV-2 pseudovirus removal efficiency, ACE2-algae-robot was incubated with 50 µl 2 × 10^9 VG/ml SARS-CoV-2 pseudovirus (Montana Molecular) with different algae density of 5 × 10^4 ml^{-1}, 5 × 10^5 ml^{-1}, 5 × 10^6 ml^{-1}, and 5 × 10^7 ml^{-1} in drinking water for 16 h. To explore the kinetic profiles of SARS-CoV-2 pseudovirus removal efficiency in drinking water, the bare algae, static ACE2-algae and cell-wall deficient algae with a density of 5 × 10^6 ml^{-1} were incubated with the same amount of SARS-CoV-2 pseudovirus for 16 h. To explore the time dependence removal efficiency of SARS-CoV-2 pseudovirus in drinking water, 5 × 10^6 ml^{-1} ACE2-algae-robot was incubated with the same amount of SARS-CoV-2 pseudovirus in drinking water at room temperature for 0 h, 1 h, 2 h, 4 h, 6 h, 16 h, the bare algae and static ACE2-algae were treated with the same method. The method of reusability of ACE2-algae-robot 4was studied as before. For the post-treatment, 5 × 10^6 ml-1 ACE2-algae-robots were treated by 0.5% chitosan for 10 min. In comparison, the control groups were treated by 500×g centrifugation for 3 min. Before measuring SARS-CoV-2 pseudovirus removal efficiency, 15,000 NL-20 cells per well were seeded in a 96-well plate for 24 h at 37 °C in a 5% CO2 environment, and then the supernatant with unbound SARS-CoV-2 pseudovirus from each sample was incubated with the cells for 24 h. The fluorescence intensity of the mixture was analyzed by fluorescence microscopy and quantified using a BioTek Synergy Mx microplate reader.

Chapter 2.4, in full, is a reprint of the material as it appears in Journal of the American Chemical Society, 2021, by Fangyu Zhang, Zhengxing Li, Lu Yin, Qiangzhe Zhang, Nelly Askarinam, Rodolfo Mundaca-Uribe, Emil Karshalev, Weiwei Gao, Liangfang Zhang, Joseph Wang. The dissertation author was the primary investigator and author of this paper.

2.4.7 References

1. Zhang, R.; Li, Y.; Zhang, A. L.; Wang, Y.; Molina, M. J. Identifying airborne transmission as the dominant route for the spread of COVID-19. *Proc. Natl. Acad. Sci. U. S. A.* **117**, 14857–14863 (2020).

2. Wu, Y.; Guo, C.; Tang, L.; Hong, Z.; Zhou, J.; Dong, X.; Yin, H.; Xiao, Q.; Tang, Y.; Qu, X.; Kuang, L.; Fang, X.; Mishra, N.; Lu, J.; Shan, H.; Jiang, G.; Huang, X. Prolonged presence of SARS-CoV-2 viral RNA in faecal samples. *Lancet Gastroenterol. Hepatol.* **5**, 434–435 (2020).

3. Randazzo, W.; Truchado, P.; Cuevas-Ferrando, E.; Simón, P.; Allende, A.; Sánchez, G. SARS-CoV-2 RNA in wastewater anticipated COVID-19 occurrence in a low prevalence area. *Water Res.* **181**, 115942 (2020).

4. Haramoto, E.; Malla, B.; Thakali, O.; Kitajima, M. First environmental surveillance for the presence of SARS-CoV-2 RNA in wastewater and river water in Japan. *Sci. Total Environ.* **737**, 140405 (2020).

5. Guerrero-Latorre, L.; Ballesteros, I.; Villacrés-Granda, I.; Granda, M. G.; Freire-Paspuel, B.; Ríos-Touma, B. SARS-CoV-2 in river water: Implications in low sanitation countries. *Sci. Total Environ.* **743**, 140832 (2020).

6. Wu, F.; Zhang, J.; Xiao, A.; Gu, X.; Lee, W. L.; Armas, F.; Kauffman, K.; Hanage, W.; Matus, M.; Ghaeli, N. SARS-CoV-2 titers in wastewater are higher than expected from clinically confirmed cases. *Msystems* **5**, e00614-e00620 (2020).

7. Foladori, P.; Cutrupi, F.; Segata, N.; Manara, S.; Pinto, F.; Malpei, F.; Bruni, L.; La Rosa, G. SARS-CoV-2 from faeces to wastewater treatment: what do we know? A review. *Sci. Total Environ.* **743**, 140444 (2020).

8. Bogler, A.; Packman, A.; Furman, A.; Gross, A.; Kush-maro, A.; Ronen, A.; Dagot, C.; Hill, C.; Vaizel-Ohayon, D.; Mor-genroth, E. Rethinking wastewater risks and monitoring in light of the COVID-19 pandemic. *Nat. Sustainability* 3, 981-990 (2020).

9. Zhang, Q.; Dong, R.; Wu, Y.; Gao, W.; He, Z.; Ren, B. Light-Driven Au-WO3@C Janus Micromotors for Rapid Photodeg-radation of Dye Pollutants. *ACS Appl. Mater. Interfaces* **9**, 4674-4683 (2017).

10. Liang, C.; Zhan, C.; Zeng, F.; Xu, D.; Wang, Y.; Zhao, W.; Zhang, J.; Guo, J.; Feng, H.; Ma, X. Bilayer Tubular Micromotors for Simultaneous Environmental Monitoring and Remediation. *ACS Appl. Mater. Interfaces* **10**, 35099-35107 (2018).

11. Vilela, D.; Parmar, J.; Zeng, Y.; Zhao, Y.; Sánchez, S. Gra-phene-based microbots for toxic heavy metal removal and recov-ery from water. *Nano Lett.* **16**, 2860-2866 (2016).

12. Maric, T.; Mayorga‐Martinez, C. C.; Khezri, B.; Nasir, M. Z. M.; Chia, X.; Pumera, M. Nanorobots Constructed from Nanoclay: Using Nature to Create Self‐Propelled Autonomous Nanomachines. *Adv. Funct. Mater.* **28**, 1802762 (2018).

13. Mou, F.; Pan, D.; Chen, C.; Gao, Y.; Xu, L.; Guan, J. Mag-netically Modulated Pot‐Like MnFe2O4 Micromotors: Nanoparti-cle Assembly Fabrication and their Capability for Direct Oil Re-moval. *Adv. Funct. Mater.* **25**, 6173-6181 (2015).

14. Hoop, M.; Shen, Y.; Chen, X. Z.; Mushtaq, F.; Iuliano, L. M.; Sakar, M. S.; Petruska, A.; Loessner, M. J.; Nelson, B. J.; Pané, S. Magnetically driven silver‐coated nanocoils for efficient bacterial contact killing. *Adv. Funct. Mater.* **26**, 1063-1069 (2016).

15. Lin, Z.; Gao, C.; Wang, D.; He, Q. Bubble‐propelled Janus Gallium/Zinc Micromotors for Active Treatment of Bacterial In-fection. *Angew. Chem. Int. Ed.* **60**, 8750-8754 (2021).

16. Kong, L.; Ambrosi, A.; Nasir, M. Z. M.; Guan, J.; Pumera, M. Self‐Propelled 3D‐Printed "Aircraft Carrier" of Light‐Powered Smart Micromachines for Large‐Volume Nitroaromatic Explosives Removal. *Adv. Funct. Mater.* **29**, 1903872 (2019).

17. Li, J.; Singh, V. V.; Sattayasamitsathit, S.; Orozco, J.; Kaufmann, K.; Dong, R.; Gao, W.; Jurado-Sanchez, B.; Fedorak, Y.; Wang, J. Water-driven micromotors for rapid photocatalytic deg-radation of biological and chemical warfare agents. *ACS Nano* **8**, 11118-11125 (2014).

18. Gao, W.; Wang, J. The environmental impact of mi-cro/nanomachines: a review. *ACS Nano* **8**, 3170-3180 (2014).

19. Parmar, J.; Vilela, D.; Villa, K.; Wang, J.; Sanchez, S. Micro- and Nanomotors as Active Environmental Microcleaners and Sensors. *J. Am. Chem. Soc.* **140**, 9317-9331 (2018).

20. Zhang, Y.; Yan, K.; Ji, F.; Zhang, L. Enhanced Removal of Toxic Heavy Metals Using Swarming Biohybrid Adsorbents. *Adv. Funct. Mater.* **28**, 1806340 (2018).

21. Soto, F.; Lopez‐Ramirez, M. A.; Jeerapan, I.; Esteban-Fernández de Ávila. E. F.; Mishra, R. K.; Lu, X.; Chai, I.; Chen, C.; Kupor, D.; Nourhani, A.; Wang, J. Rotibot: Use of Rotifers as Self‐Propelling Biohybrid Microcleaners. *Adv. Funct. Mater.* **29**, 1900658 (2019).

22. Palagi, S.; Fischer, P. Bioinspired microrobots. *Nat. Rev. Mater.* **3**, 113-124 (2018).

23. Lee, J.-H.; Choi, M.; Jung, Y.; Lee, S. K.; Lee, C.-S.; Kim, J.; Kim, J.; Kim, N. H.; Kim, B.-T.; Kim, H. G. A novel rapid detection for SARS-CoV-2 spike 1 antigens using human angiotensin con-verting enzyme 2 (ACE2). *Biosens. Bioelectron.* **171**, 112715 (2021).

24. Huang, Y.; Yang, C.; Xu, X.-f.; Xu, W.; Liu, S.-w. Structur-al and functional properties of SARS-CoV-2 spike protein: poten-tial antivirus drug development for COVID-19. *Acta Pharmacol. Sin.* **41**, 1141-1149 (2020).

25. Glasgow, A.; Glasgow, J.; Limonta, D.; Solomon, P.; Lui, I.; Zhang, Y.; Nix, M. A.; Rettko, N. J.; Zha, S.; Yamin, R. Engineered ACE2 receptor traps potently neutralize SARS-CoV-2. *PNAS* **117**, 28046-28055 (2020).

26. Wollmann, F.; Dietze, S.; Ackermann, J. U.; Bley, T.; Walther, T.; Steingroewer, J.; Krujatz, F. Microalgae wastewater treatment: biological and technological approaches. *Eng. Life Sci.* **19**, 860-871 (2019).

27. Yasa, O.; Erkoc, P.; Alapan, Y.; Sitti, M. Microalga‐Powered Microswimmers toward Active Cargo Delivery. *Adv. Mater.* **30**, 1804130 (2018).

28. Silflow, C. D.; Lefebvre, P. A. Assembly and motility of eukaryotic cilia and flagella. Lessons from Chlamydomonas rein-hardtii. *Plant Physiol.* **127**, 1500-1507 (2001).

29. Xiong, H.-L.; Wu, Y.-T.; Cao, J.-L.; Yang, R.; Liu, Y.-X.; Ma, J.; Qiao, X.-Y.; Yao, X.-Y.; Zhang, B.-H.; Zhang, Y.-L. Robust neutralization assay based on SARS-CoV-2 S-protein-bearing ve-sicular stomatitis virus (VSV) pseudovirus and ACE2-overexpressing BHK21 cells. *Emerging Microbes Infect.* **9**, 2105-2113 (2020).

30. Bhatt, A.; Arora, P.; Prajapati, S. K., Can Algal Derived Bioactive Metabolites Serve as Potential Therapeutics for the Treatment of SARS-CoV-2 Like Viral Infection? *Front Microbiol.* **11**, 596374 (2020).

31. Goodenough, U. W.; Heuser, J. E., The Chlamydomonas cell wall and its constituent glycoproteins analyzed by the quick-freeze, deep-etch technique. *J. Cell Bio.* **101**, 1550-1568 (1985).

32. Carducci, A.; Battistini, R.; Rovini, E.; Verani, M., Viral removal by wastewater treatment: monitoring of indicators and pathogens. *Food Environ. Virol.* **1**, 85-91 (2009).

33. Larsen, D. A.; Wigginton, K. R., Tracking COVID-19 with wastewater. *Nat. Biotechnol.* **38**, 1151-1153 (2020).

34. Goyal, A.; Reeves, D. B.; Ojeda, E. F. C.; Mayer, B. T.; Schiffer, J. T., Slight reduction in SARS-CoV-2 exposure viral load due to masking results in a significant reduction in transmission with widespread implementation. *Sci. Rep.* **11**, 11838 (2021).

35. Zhou, D.; Dejnirattisai, W.; Supasa, P.; Liu, C.; Mentzer, A. J.; Ginn, H. M.; Zhao, Y.; Duyvesteyn, H. M.; Tuekprakhon, A.; Nutalai, R., Evidence of escape of SARS-CoV-2 variant B. 1.351 from natural and vaccine-induced sera. *Cell* **184**, 2348-2361 (2021).

36. Khan, A.; Zia, T.; Suleman, M.; Khan, T.; Ali, S. S.; Abbasi, A. A.; Mohammad, A.; Wei, D. Q., Higher infectivity of the SARS‐CoV‐2 new variants is associated with K417N/T, E484K, and N501Y mutants: An insight from structural data. *J. Cell. Physiol.* **236**, 7045-7057 (2021).

CHAPTER 3. CELL/CELL MEMBRANE-BASED BIOHYBRID MICROROBOTS

3.1 Macrophage–magnesium biohybrid microrobots for endotoxin neutralization

3.1.1 Introduction

The development of artificial micromotors that can convert energy to movement and forces has recently become a fascinating research area.[1-3] Improvements in the biocompatibility of the micromotor's materials have allowed them to perform some biomedical tasks, such as targeted drug delivery, precise surgery, biosensing, or toxin removal.[4-6] Among the different types of biocompatible micromotors, Mg-based Janus micromotors offer distinct advantages for in vivo applications owing to their autonomous propulsion in body fluids including gastric and intestinal fluids, cargo transport and release, and their transient biodegradability properties.[7-9] In recent years, Mg-based micromotors have thus been applied in a variety of biomedical applications, such as site-specific gastrointestinal tract delivery,[10] in vivo drug or antigen delivery,[11, 12] and collective and dynamic gastric delivery via micromotor pills.[13] While Mg micromotors have been widely tested for dynamic in vivo delivery applications, their ability to manipulate, carry, and transport living cells has not been explored.

Along the line of micromotor design, significant progress has been made recently toward creating biohybrid micromotors that combine cellular components and synthetic micro/nanoscale materials. Such cell-based micromotors offer considerable promise for diverse in vivo biomedical applications owing to their biocompatibility and biological functionality of the cellular component.[14] Live cells can thus be integrated with artificial substrates to produce functional biohybrid devices that possess new and improved capabilities. Such cell-based micromotors can be classified in two types. The first one relies on the intrinsic motility of live cells, such as spermatozoa,[15] bacteria,[16] and cardiomyocytes,[17] for transporting artificial material payloads. The microorganisms thus act as engines to form active biohybrid swimming systems powered by cellular actuation. The second type consists of cell-based materials, such as cell membranes, and synthetic micromotors that provide the motion. Such combination of micromotors with cell components confers the micromotor with cell-like properties[18,19] and improved biofunctionality.[20] Besides cell membrane-coated micromotors, various types of cells have also been used in biomedical applications due to their large drug loading capacity,[21] natural homing tendency toward inflammation sites,[22] and easy genetic engineering for gene delivery.[23] The combination of intact cells and engineered motors has resulted in several cell-based biohybrid micromotor designs for diverse applications, including stem cell-based motors for drug delivery,[24] red blood cell-motors for on-demand cargo delivery,[25] and NIH 3T3 cell-based motors for precise control and patterning.[26] Although such cell-based motors have demonstrated clear advantages as drug delivery carriers, it will be particularly interesting to explore the possibility of integrating intact live cells with biocompatible and biodegradable artificial micromotors, such as the Mg-based micromotors, to form a biohybrid motor system, which can potentially be applied for in vivo operations.

Herein, we present a new approach, combining living macrophage (MΦ) cells with Mg micromotors to prepare MΦ–Mg hybrid motors, which possess the powerful propulsion of the Mg micromotors and preserve the biological function of the cells. As a critical cell in the innate immune system, MΦs play a major role in the regulation of homeostasis,[27] can swallow and digest pathogens,[28] and have specific receptors for biotoxins such as endotoxins.[29] The new biohybrid micromotors are fabricated by coating Mg microparticles with titanium dioxide (TiO2) and a poly(l-lysine) (PLL) layer, and attaching the MΦ to the outer PLL coating via electrostatic interactions. The resulting MΦ–Mg biohybrid motors maintain the functionality and viability of MΦ cells and offer efficient transport of the living cells. Numerical modeling of the propulsion dynamics of the resulting MΦ–Mg dimer motor is in good agreement with the experimental observations. In addition, the viability and biological function of the attached MΦ are retained and the cell can bind and neutralize pathogenic toxins, such as endotoxins. Overall, this work presents an attractive method to fabricate a biohybrid micromotor, consisting of whole cells attached onto autonomously propelled synthetic micromotors. While the new biohybrid strategy is demonstrated here using MΦs as model living cells, it could be readily expanded to other types of cells that possess different functionalities.

3.1.2 Fabrication and characterization of MΦ–Mg motors

The new biohybrid strategy for moving whole living cells in biological media consists of utilizing a synthetic Mg-based micromotor while retaining the viability, integrity, and function of the cells. We used MΦ as a model living cell owing to its critical role as an immune cell. The design of the new biohybrid motor relies on the attachment of MΦs to Mg micromotors via electrostatic attraction between the negatively charged cell membrane and the positively charged outer PLL coating on the Mg micromotor. Such interaction ensures that the open area of the Mg micromotor remains exposed to the biological fluid for efficient bubble propulsion. The fabrication protocol, illustrated in Figure 1A, consists of modifying Mg/TiO2 micromotors (commonly $\approx$20 µm size) with 0.01% PLL coating over a glass slide (Figure 3.1a, steps 1 and 2). Subsequently, the PLL-modified Mg micromotors and MΦs were suspended in Dulbecco's modified eagle medium

(DMEM) and incubated for 1 h at 4 °C (Figure 3.1a, step 3). It should be noted that the MΦs remained stable on the PLL motor surface after longer times. After the incubation, the MΦ–Mg motors were washed to eliminate all the unbound cells. Subsequently, the MΦ–Mg motors were released and placed in an acidic environment, where the motors propelled spontaneously due to the reaction between the Mg core and the protons present in the acidic fluid, which generates a hydrogen bubble tail and propulsion thrust (Figure 3.1a, step 4).

Figure 3.1b (left side) shows a scanning electron microscopy (SEM) image of a MΦ–Mg motor, displaying the binding between a MΦ cell and a Mg micromotor (pseudocolored in pink and green, respectively) with its opening exposed to ambient medium. Energy-dispersive X-ray spectroscopy (EDX) images illustrate the presence and elemental distribution of Mg and Ti within the micromotor structure (Figure 3.1b, right). The aperture observed in the Ti mapping image corresponds to the opening in the TiO2 shell produced during the atomic layer deposition (ALD) process. The motion of the MΦ–Mg motors was evaluated using simulated gastric fluid (pH 1.3), which led to the generation of hydrogen bubbles and corresponding thrust. Figure 1C displays a microscopy image of a MΦ–Mg motor moving in simulated gastric fluid, showing the MΦ (pseudocolored in pink) attached to the Mg micromotor, along with the corresponding hydrogen bubble tail. The MΦ–Mg motors displayed a lifetime of $\approx$5 min, characteristic of the gradual Mg depletion,[13] with an average speed of 127.3 μm s^{-1}. It should be noted that the MΦ cells remained attached firmly to the MΦ–Mg motors throughout these experiments, reflecting their strong binding to the PLL motor layer.

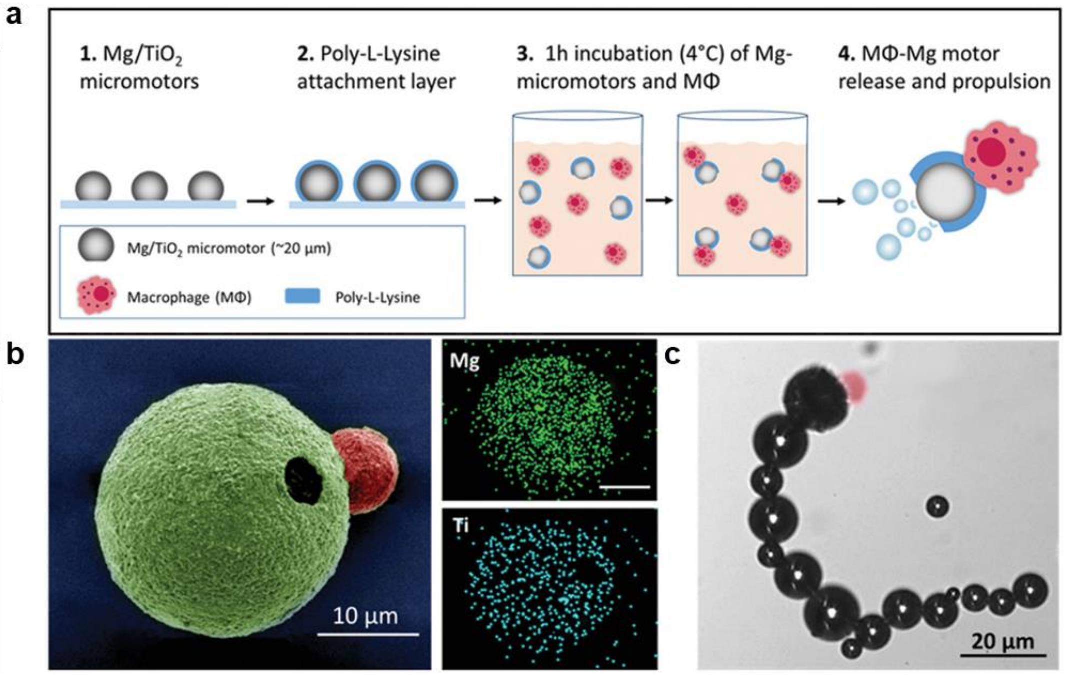

Figure 3.1 MΦ–Mg micromotor preparation and structural characterization. a, Schematic of the preparation of the MΦ–Mg motor: 1) ALD of TiO2 over Mg microparticles; 2) Deposition of a PLL layer over the Mg/TiO2 micromotors; 3) Incubation of Mg-micromotors and MΦs for 1 h at 4 °C; 4) MΦ–Mg motor release and propulsion in simulated gastric fluid (pH 1.3). b, Left: SEM image of a MΦ–Mg motor (Mg-micromotor is pseudocolored in green and MΦ is pseudocolored in pink); Right: EDX images showing the distribution of elemental Mg (green) and Ti (cyan). c, Microscopy image displaying the motion of a MΦ–Mg motor in gastric fluid simulant (pH 1.3); the MΦ is pseudocolored in pink.

3.1.3 Motion characteristics of MΦ–Mg motors

The propulsion characteristics of the resulting MΦ–Mg motors were evaluated in vitro in simulated gastric acid. The schematic and the microscopy images shown in Figure 3.2a display the movement of MΦ–Mg motors with a motor diameter of: i) 20–25 μm or ii) 10–15 μm. Efficient hydrogen bubble generation propelled the Mg micromotor and MΦ–Mg motor in simulated gastric fluid (Figure 3.2b and microscopy images at 1 min). Once the Mg motor core was dissolved fully (i.e., completion of the Mg-proton reaction), only open TiO2 shells remained (Figure 3.2c), and the propulsion was halted while the MΦ remained attached to the resulting shell (images at 3 min).

Figure 3.2d schematically illustrates the biohybrid structure with the MΦ attached to the Mg microparticle. The motion behavior of the MΦ–Mg motor primarily depends on the dynamic characteristics of the biohybrid micromotor, the position of the MΦ on the Mg microparticle and the ratio of the effective radius of the MΦ $R_{M\Phi}$ to the Mg microparticle radius R_{Mg}, defined by:

$$\lambda = \frac{\mathrm{RM\Phi}}{\mathrm{RMg}} = \frac{\mathrm{dM\Phi}}{\mathrm{dMg}} \qquad (1)$$

where $d_{M\Phi}$ and d_{Mg} are the effective diameters of MΦ and Mg microparticle, respectively.

For a typical MΦ–Mg dimer motor of length $l \cong 30$ μm, moving with speed $v \cong 100$ μm s^{-1} in a fluid of density $\rho \cong 1000$ kg m^{-3} and viscosity $\mu \cong 8.9 \times 10^{-4}$ Pa s, the Reynolds number is $Re = \rho l v/\mu \cong 0.003 \ll 1$. In the low Reynolds number regime, the fluid flow is governed by Stokes equation and the MΦ–Mg dimer motor velocity is linearly proportional to the force exerted on the motor. Approximating the Mg microparticle and MΦ as spheres, and employing a zeroth-order approximation by adding up the hydrodynamics effect of the spherical particles independently, the speed of the MΦ–Mg motor v_{dimer} relates to the speed of the bare Mg micromotor v_{Mg} by

$$v_{\mathrm{diameter}} = \frac{1}{1+\lambda} v_{\mathrm{Mg}} \qquad (2)$$

where the relative size $\lambda = d_{M\Phi}/d_{Mg}$ is the ratio of the effective diameter of the MΦ, $d_{M\Phi}$ to the Mg diameter d_{Mg}. In the limit of a very large MΦ compared to the Mg microparticle ($\lambda >> 1$), the micromotor's driving force is not strong enough to effectively move the MΦ. Practically, in this regime the MΦ engulfs the micromotor and there will be no motion. On the other hand, for very large micromotors ($\lambda << 1$) the MΦ–Mg motor moves with a speed close to that of the bare Mg micromotor. Our experimental regime is between these two extremes.

To compare the modeling prediction with experimental results, we averaged the MΦ–Mg motor velocity and their Mg micromotor and MΦ radii for dimers with the micromotor diameter in the range of 23−44 µm from the experimental data. We obtained an average velocity of $v_{dimer} \cong 127.3 \pm 6.1$ µm s^{-1}, and average diameters for bare Mg micromotor $d_{Mg} \cong 33$ µm, and $d_{M\Phi} \cong 10.6$ µm ($\lambda \cong 0.32$). To compare our model with the experimental data, we fitted first a linear regression for bare Mg micromotors as a function of their velocities. For diameter $d_{Mg} = 33$ µm the linear fit gives a value of $v_{Mg} = 167$ µm s^{-1} for bare Mg micromotor velocity. Plugging this value in Equation 2 along with $\lambda = 0.32$, our model approximates a dimer velocity to be $v_{dimer} = 126.5$ µm s^{-1}, which is very close to the experimental velocity value ($v_{dimer} = 127.3 \pm 6.1$ µm s^{-1}). The model can qualitatively explain the behavior of the dimers due to the nature of the zeroth order approximation. A good agreement is observed between the model and the experimental data despite the approximation of Mg microparticle and MΦ as perfect spheres and the fluctuations in the experimental data.

The experimental average speed for bare Mg micromotors in the range of 20–25 µm and 10–15 µm in simulated gastric fluid was measured, obtaining values of 190.5 ± 13.24 and 62.8 ± 4.3 µm s^{-1}, respectively, and were compared to the speed of MΦ–Mg motors at 1 min time, with average speeds of 136.3 ± 17.9 and 19.9 ± 2.1 µm s^{-1}, respectively (Figure 3.2e). The corresponding theoretical values from Equation 2 for a MΦ–Mg motor with MΦ of diameter $d_{M\Phi}$ = 15 µm are 114.294 and 28.545 µm s^{-1} using Mg micromotors of 20–25 and 10–15 µm, respectively. The observed MΦ–Mg motor velocities correspond to a relative speed of about five body lengths per second, indicating that these biohybrid motors can rapidly react and move in the gastric fluid. In addition, no propulsion movement was observed when the MΦs were attached to 5 µm Mg micromotors.

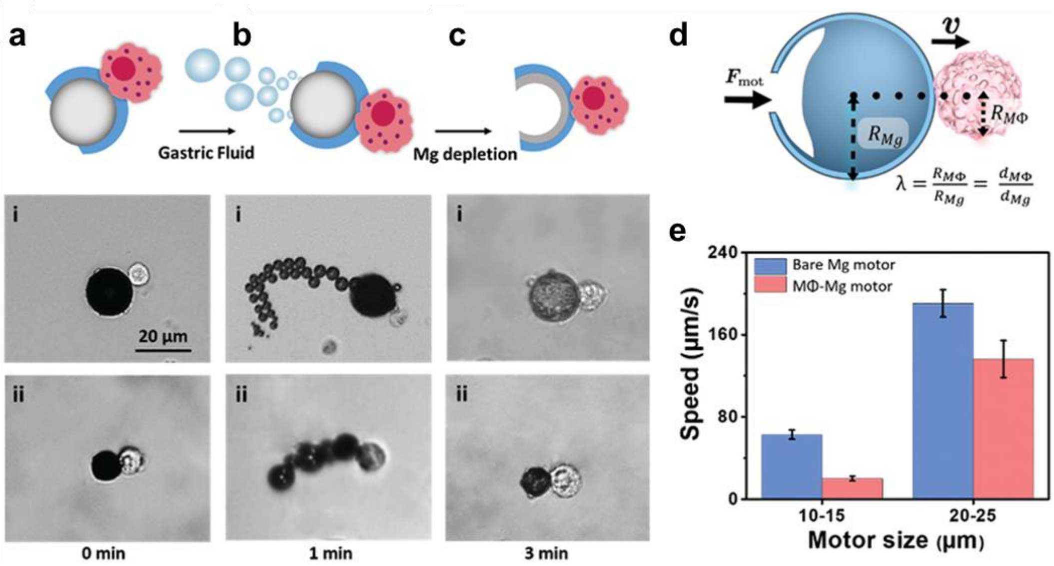

Figure 3.2 Propulsion characteristics of MΦ–Mg motors. a, Schematic and microscopy images of a MΦ–Mg micromotor with motor diameters of: i) 20–25 µm or ii) 10–15 µm at time = 0 min. b, Schematic and microscopy images of a MΦ–Mg micromotor with motor diameters of: i) 20–25 µm or ii) 10–15 µm propelling in gastric fluid solutions at time = 1 min. c, Schematic of the MΦ–Mg shell (with partial Mg depletion) at time = 3 min, along with microscopy images of a MΦ–Mg shell corresponding to the two motor sizes (i, ii) at time = 3 min. d, Modeling of the dynamics of a dimer where a MΦ of an effective radius RMΦ is attached to a Mg-based micromotor with radius of RMg (following partial Mg depletion). e, Comparison of the speed of 10–15 µm and 20–25 µm Mg motors and MΦ–Mg motors in the gastric fluid simulant (values defined at time = 1 min).

3.1.4 Size-dependent interaction of MΦs with polystyrene (PS) microparticles.

Since the MΦ–Mg biohybrid motor design is based on the interaction between MΦs and Mg micromotors, it is essential to verify that these cells do not engulf the motors after the binding process. Few studies have examined the relation between the particle size and its engulfment by MΦ.30 In this work, we studied the size-dependent engulfment by MΦs using polystyrene (PS) microparticles with four different size ranges (1–2, 4–5, 10–12, and 20–25 µm) as model particles in the size range of the Mg micromotors. Figure 3.3 displays bright-field, fluorescence (green channel, FITC dye), and merged images corresponding to MΦs incubated with the different sized PS microparticles. It is observed that the 1–2 and 4–5 µm PS microparticles were internalized by the MΦs, while the bigger PS microparticles (10–12, and 20–25 µm) just interacted with the outer membrane of the MΦs without being internalized. These results not only explain why no propulsion was observed using Mg micromotors smaller than 5 µm, but also indicate that Mg micromotors larger than 5 µm are essential for realizing MΦ–Mg biohybrid motors.

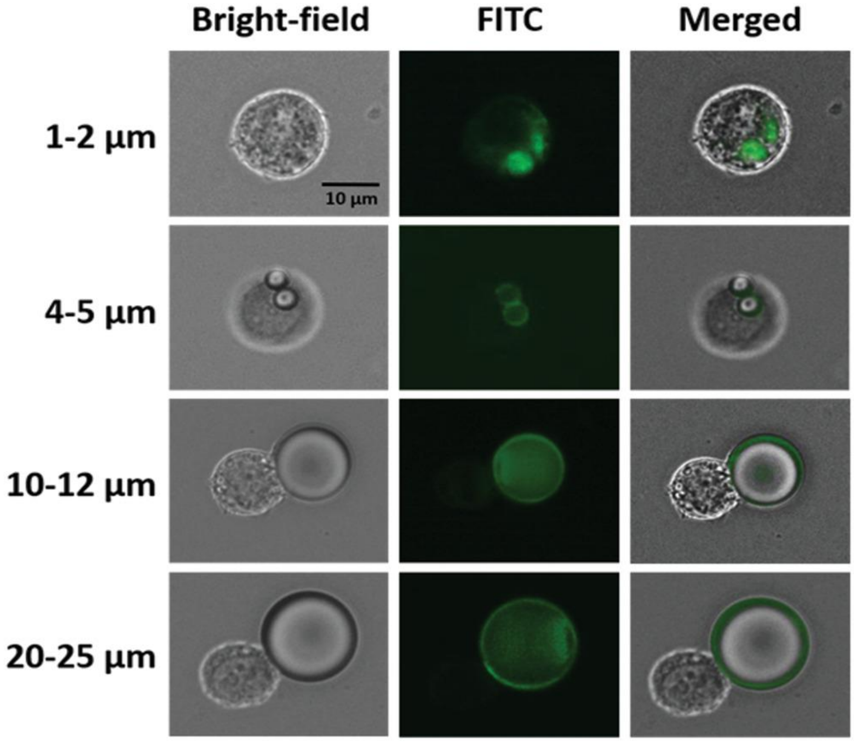

Figure 3.3 Mimic the interaction of MΦs with Mg motors. For fluorescence imaging, the PS particles were labeled with FITC dye (green color). Small PS particles (<10 µm) were prone to be engulfed by the MΦ while large particles attached on the cell membrane of the MΦ (not internalized).

3.1.5 Endotoxin (LPS) binding with MΦ–Mg motors.

Another important factor to consider in the fabrication of the MΦ–Mg motors is the cell viability and functionality of MΦ cells following the different modification steps. To test these, Calcein AM (λex/λem, 488 and 520 nm, respectively) and lipopolysaccharide (LPS) conjugated with Alexa Fluor594 (λex/λem, 590 and 617 nm, respectively) were used to evaluate the cell viability and functionality, respectively. Figure 3.4 demonstrates that the MΦ attached to the micromotor showed a strong green fluorescence, which is consistent with the free MΦ, and indicates that the motor conjugation process does not affect the cell viability. In addition, the LPS binding capability of the MΦ was mostly retained after the modification process, as the MΦ conjugated with the motor showed comparable fluorescence intensity after incubating with LPS conjugates. Further studies were performed to evaluate the viability of the attached MΦs after the micromotor reaction in gastric fluid simulant. The results (shown in Figure S3 in the Supporting Information) demonstrate that the MΦs remained viable, retaining all their biological functions after being exposed to gastric fluid for 5 min, 1 h, 2 h, and 4 h, confirming the good stability of the system. Overall, these results demonstrate that the motor conjugation process does not affect either the cell viability or the membrane functional proteins, and that the attached MΦ is not damaged due to the hybrid biomotor fabrication process.

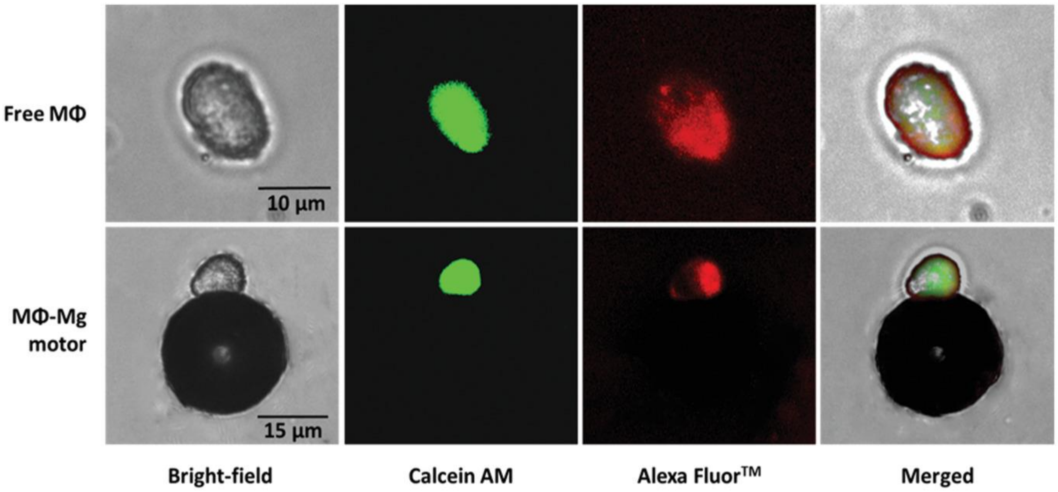

Figure 3.4 Cell viability and functionality of MΦ–Mg motors Microscopy images of a free MΦ (top) and a MΦ–Mg motor (bottom) after 30 min incubation with Calcein AM (λex/λem, 488 and 520 nm) and LPS labeled with Alexa Fluor594 (λex/λem, 590 and 617 nm), in DMEM medium at 37 °C.

3.1.6 Endotoxin (LPS) neutralization with MΦ–Mg motors.

As was stated before, it is essential that the MΦs maintain their viability and biological functionality after binding to the Mg micromotors. Specifically, MΦs have the ability to bind and neutralize endotoxins. LPS is a hazardous endotoxin released from the membrane of Gram-negative bacteria, which can induce strong inflammatory response[31] and has a preponderant role in the development of sepsis.[32, 33] Since this is one of the most important roles of MΦs in the body, it is critical to ensure that these cells are still functional and retain their endotoxin binding ability. Figure 3.5a illustrates an active MΦ–Mg motor binding to the endotoxin released by Escherichia coli. Aiming to test the ability of the MΦ–Mg motor to neutralize LPS, to illustrate the cell functionality after its binding with the Mg micromotors, we thus performed in vitro LPS binding and neutralization experiments. For this study, 0.25 EU (units of endotoxin) were used for each group. First, the maximum LPS binding capacity of a fixed amount of MΦs (1×10^6) was examined by titrating the concentration of LPS, finding that 1×10^6 MΦs can neutralize 0.25 EU LPS after 1 h incubation with periodic shaking. Then, the LPS binding ability of MΦ–Mg motors was compared to that of free MΦs (used as a positive control). In addition, DMEM medium was used as a negative control. After incubation, remaining LPS quantification was carried out using ToxinSensor chromogenic LAL endotoxin assay kit following the manufacturer's guideline. The results showed that following 5 min reaction, the MΦ–Mg motors removed 66.82 ± 6.31% of LPS from the system, around 13% more than free MΦs (53.34 ± 4.48%). For a better understanding, these data are graphed in Figure 3.5b in terms of remaining LPS, where the lowest value is obtained with the MΦ–Mg motors as demonstrated by the statistical analysis. This can be explained by the fact that using the MΦ–Mg motors, the MΦ receptor is rapidly moving through the solution, keeping the reaction under constant stirring and thus binding more LPS, while the free MΦs are present in suspension. These results illustrate that this new biohybrid motor maintains the natural biological function of MΦs.

To gain insights into the characterization of this new biohybrid motor, a time-dependence study was carried out, in which the performance of the MΦ–Mg motors and the free MΦs toward binding LPS at different time points was evaluated (Figure 3.5c). After 2 min of reaction, MΦ–Mg motors neutralized nearly 45% of the LPS, after 5 min almost a 56%, and after 10 min around 66%. Since the micromotor velocity tends to be higher during the initial 2 min, the best performance of this new biohybrid is expected during this period, which is consistent with the obtained data.

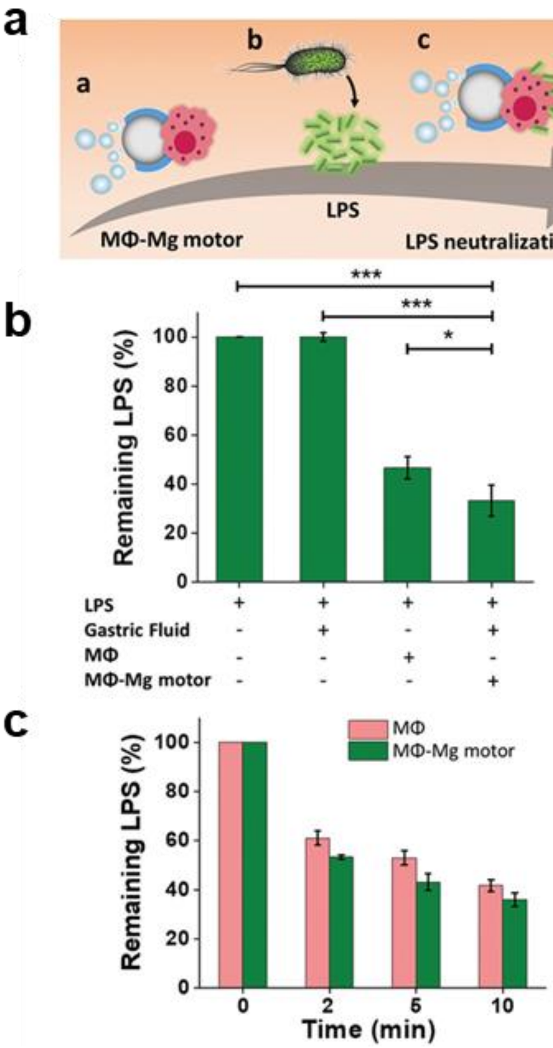

Figure 3.5 Endotoxin (LPS) neutralization with MΦ–Mg motors. a, Schematic illustration of using MΦ–Mg motors to neutralize LPS produced by bacteria: a) MΦ–Mg motors propelling in a bacterial culture medium; b) LPS released by E. coli bacteria; c) LPS neutralization by MΦ–Mg motors. b, LPS removal with MΦ–Mg motors in comparison with free MΦs. Error bars estimated as a triple of SD (n = 3). Bars represent median values. $^*P < 0.05$, $^{***}P < 0.001$. c, Evaluation of MΦ–Mg motor toxin neutralization performance at different times and comparison with free MΦs.

3.1.7 Discussion

We have reported the fabrication and unique property of a biohybrid MΦ–Mg motor, combining a Mg-based micromotor with a living MΦ cell. The resulting MΦ–Mg motors were able to propel in acidic environment, reaching average speeds of 127.3 µm s−1, which was in agreement with numerical modeling based on dynamic characteristics of the micromotor, such as its relative size and position of the MΦ on the micromotor. The formation of the MΦ–Mg motors is dependent on the size of the Mg micromotors; larger than 10 µm Mg micromotors resulted in MΦs attaching to the motor surface, but smaller than 5 µm Mg micromotors would be engulfed by the MΦs. The propulsion behavior of the Mg micromotors enabled movement of the whole MΦ–Mg motors and thus rapid transport of the attached MΦs, while retaining the viability and biological functionality of their source cells, as indicated from the endotoxin neutralization study. While MΦs were used in this work, the new biohybrid strategy represents a platform technology and should be generalizable to other types of cells for other specific application purposes.

3.1.8 Experimental section

Mg Micromotors Fabrication: Mg-based micromotors were prepared using commercial magnesium (Mg) microparticles (catalog #FMW20, TangShan WeiHao Magnesium Powder Co.; average size, 20 and 10 µm) as the core. The Mg microparticles were initially washed with acetone to remove impurities. After drying under N_2 flow the Mg microparticles were dispersed onto glass slides (2 mg of Mg microparticles per glass slide) and coated with TiO_2 by ALD (at 100 °C for

3000 cycles) using a Beneq TFS 200 atomic layer deposition system. This deposition allowed for leaving a small opening at the contact point of the particle to the surface of the glass slide.

MΦ–Mg Motor Fabrication: To fabricate the MΦ–Mg motor, the Mg micromotors were coated with 100 µL of 0.01% (w/v) PLL solution prepared in water (Sigma-Aldrich, P8920) to allow for better binding to the MΦs. This PLL coating was distributed around 80% of the surface of the Mg micromotor, thus facilitating later interactions with MΦs at 1:1 ratio. J774.A1 mouse MΦs (diameter in suspension, 10–16 µm) were purchased from the American Type Culture Collection (ATCC). Then, the modified micromotors were collected from the glass slide by gently scratching and washed 2 times with ethanol and Dulbecco's modified Eagle medium (DMEM), with 3 min centrifugation at 3000 rpm between each washing step. Finally, 2 mg of these micromotors and 1 mL of MΦs (1×10^6 cells per mL of DMEM) were incubated at 4 °C for 1 h to allow the attachment of MΦs with Mg motors to form MΦ–Mg motors. Subsequently, the MΦ–Mg motors were washed three times with DMEM to remove all the unbound cells.

MΦ–Mg Motor Characterization: Bright-field, fluorescence, and merged images of the MΦ–Mg motors were obtained with an EVOS FL microscope coupled with 20× and 40× objectives and a fluorescence filter for green light excitation. Scanning electron microscopy (SEM) images were captured using a FEI Quanta 250 ESEM instrument (Hillsboro, Oregon, USA), using an acceleration voltage of 10 kV. Energy-Dispersive X-Ray Spectroscopy (EDX) mapping analysis was carried out with an Oxford EDS detector attached to SEM instrument and controlled by Pathfinder software.

MΦ–Mg Motor Propulsion: The MΦ–Mg motor propulsion was evaluated using simulated gastric fluid (Sigma-Aldrich, 0 1651), which was diluted 10 times and supplemented with 0.2% Triton X-

100 (Fisher Scientific, FairLawn, NJ, USA) as a surfactant. To capture videos of the motion of the MΦ–Mg motor, an inverted optical microscope (Nikon Eclipse Instrument Inc. Ti-S/L100) coupled with different microscope objectives (10×, 20×, and 40×), a Hamamatsu digital camera C11440, and NIS Elements AR 3.2 software was used. An NIS Element tracking module was used to measure the speed.

MΦ-Particle Interaction Study: Polystyrene (PS) particles were washed two times with ethanol through centrifugation at 3000 rpm for 3 min each; then the microparticles were transferred to DMEM medium, washed two times with this medium, and incubated in a 0.01% PLL solution which was labeled with the fluorescein (FITC) dye for visualization. The PS microparticles and MΦs were incubated in DMEM for 1 h at 4 °C and observed under the optical and fluorescence microscope.

MΦ Viability and Functionality Study: Calcein AM ($\lambda_{ex}/\lambda_{ex}$, 488/520 nm, respectively) (ThermoFisher Scientific, C3100 MP), Lipopolysaccharides from *Escherichia coli* Serotype 055:B5, and Alexa Fluor 594 conjugates ($\lambda_{ex}/\lambda_{ex}$, 590/617 nm, respectively) (ThermoFisher Scientific, L23353) were used to study cell viability and LPS binding functionality simultaneously. In the study, 2 mg of MΦs-Mg motors, 3×10^{-6} M of Calcein AM, and 1 EU mL^{-1} of LPS conjugate with alexa fluor were incubated at 37 °C for 30 min in DMEM, homogenizing every 5 min; then, free cells and MΦs–Mg motors were analyzed using an EVOS FL microscope coupled with 20× and 40× microscopes objectives and fluorescence filters for green and red light excitation. Calcein AM was used for studying the MΦ viability after reaction and propulsion in gastric fluid simulant. The MΦ–Mg motors were exposed to the gastric fluid simulant during different times.

Then, MΦ–Mg motors were incubated with Calcein AM at 37 °C for 30 min and microscopy images were taken to evaluate the cell viability.

Endotoxin Binding and Neutralization: To evaluate the in vitro endotoxin (LPS) binding and neutralization, 2 mg of MΦ–Mg motors and 0.25 EU of LPS were left reacting in acidic medium for 5 min; free MΦs (1 × 10^6 cell per mL) were used as positive control and DMEM as negative control. After the reaction was completed, the sample was centrifuged at 1400 rpm for 3 min to spin down the cells together with the Mg micromotors. To quantify LPS in the supernatant, the Toxisensor chromogenic LAL endotoxin assay kit (Cat. No. L00350) was used. The binding and neutralization capacity of the MΦ–Mg motor was calculated by deducting the remaining LPS in the supernatant.

Chapter 3.1, in full, is a reprint of the material as it appears in Advanced Materials, 2019, by Fangyu Zhang, Rodolfo Mundaca-Uribe, Hua Gong, Berta Esteban-Fernández de Ávila, Mara Beltrán-Gastélum, Emil Karshalev, Amir Nourhani, Yao Tong, Bryan Nguyen, Mathieu Gallot, Yue Zhang, Liangfang Zhang, Joseph Wang. The dissertation author was the primary investigator and author of this paper.

3.1.9 References

1. H. Wang, M. Pumera, *Chem. Rev.* **115**, 8704 (2015).

2. J. Wang, Nanomachines: Fundamentals and Applications, John Wiley & Sons, Weinheim, 2013.

3. X. Z. Chen, M. Hoop, F. Mushtaq, E. Siringil, C. Hu, B. J. Nelson, S. Pane, *Appl. Mater. Today* **9**, 37 (2017).

4. B. Esteban-Fernández de Ávila, P. Angsantikul, D. E. Ramírez-Herrera, F. Soto, H. Teymourian, D. Dehaini, Y. Chen, L. Zhang, J. Wang, *Sci. Rob.* **3**, eaat0485 (2018).

5. F. Mou, C. Chen, Q. Zhong, Y. Yin, H. Ma, J. Guan, *ACS Appl. Mater. Interfaces* **6**, 9897 (2014).

6. J. Li, B. Esteban-Fernández de Ávila, W. Gao, L. Zhang, J. Wang, *Sci. Rob.* **2**, eaam6431 (2017).

7. Z. Wu, T. Li, W. Gao, T. Xu, B. Jurado-Sánchez, J. Li, W. Gao, Q. He, L. Zhang, J. Wang, *Adv. Funct. Mater.* **25**, 3881 (2015).

8. C. Chen, E. Karshalev, J. Li, F. Soto, R. Castillo, I. Campos, F. Mou, J. Guan, J. Wang, *ACS Nano* **10**, 10389 (2016).

9. Y. Sun, M. Li, R. Duan, D. Zhang, H. Zhang, B. Song, B. Dong, *Adv. Mater. Technol.* **3**, 1800208 (2018).

10. J. Li, S. Thamphiwatana, W. Liu, B. Esteban-Fernández de Ávila, P. Angsantikul, E. Sandraz, J. Wang, T. Xu, F. Soto, V. Ramez, X. Wang, W. Gao, L. Zhang, J. Wang, *ACS Nano* **10**, 9536 (2016).

11. B. Esteban-Fernández de Ávila, P. Angsantikul, J. Li, M. A. Lopez-Ramirez, D. E. Ramírez-Herrera, S. Thamphiwatana, C. Chen, J. Delezuk, R. Samakapiruk, V. Ramez, M. Obonyo, L. Zhang, J. Wang, *Nat. Commun.* **8**, 272 (2017).

12. X. Wei, M. Beltrán-Gastélum, E. Karshalev, B. Esteban-Fernandez de Avila, J. Zhou, D. Ran, P. Angsantikul, R. H. Fang, J. Wang, L. Zhang, *Nano Lett.* **19**, 1914 (2019).

13. E. Karshalev, B. Esteban-Fernández de Ávila, M. Beltrán-Gastélum, P. Angsantikul, S. Tang, R. Mundaca-Uribe, F. Zhang, J. Zhao, L. Zhang, J. Wang, *ACS Nano* **12**, 8397 (2018).

14. B. Esteban-Fernandez de Avila, W. Gao, E. Karshalev, L. Zhang, J. Wang, *Acc. Chem. Res.* **51**, 1901 (2018).

15. V. Magdanz, S. Sanchez, O. G. Schmidt, *Adv. Mater.* **25**, 6581 (2013).

16. B.-W. Park, J. Zhuang, O. Yasa, M. Sitti, *ACS Nano* **11**, 8910 (2017).

17. B. J. Williams, S. V. Anand, J. Rajagopalan, M. T. Saif, *Nat. Commun.* **5**, 3081 (2014).

18. J. Shao, M. Xuan, H. Zhang, X. Lin, Z. Wu, Q. He, *Angew. Chem.* **129**, 13115 (2017).

19. J. Shao, M. Abdelghani, G. Shen, S. Cao, D. S. Williams, J. C. Van Hest, *ACS Nano*, **12**, 4877 (2018).

20. J. Li, P. Angsantikul, W. Liu, B. Esteban-Fernández de Ávila, X. Chang, E. Sandraz, Y. Liang, S. Zhu, Y. Zhang, C. Chen, W. Gao, L. Zhang, J. Wang, *Adv. Mater.* **30**, 1704800 (2018).

21. M. Hamidi, A. Zarrin, M. Foroozesh, S. Mohammadi-Samani, *J. Controlled Release* **118**, 145 (2007).

22. B. Burke, S. Sumner, N. Maitland, C. Lewis, *J. Leukocyte. Biol.* **72**, 417 (2002).

23. M. Studeny, F. C. Marini, J. L. Dembinski, C. Zompetta, M. Cabreira-Hansen, B. N. Bekele, R. E. Champlin, M. Andreeff, *JNCI J. Natl Cancer Inst.* **96**, 1593 (2004).

24. J. Li, X. Li, T. Luo, R. Wang, C. Liu, S. Chen, D. Li, J. Yue, S.-h. Cheng, D. Sun, *Sci. Rob.* **3**, eaat8829 (2018).

25. Y. Alapan, O. Yasa, O. Schauer, J. Giltinan, A. F. Tabak, V. Sourjik, M. Sitti, *Sci. Rob.* **3**, eaar4423 (2018).

3.2 Enzyme-powered Janus platelet microrobots for active and targeted drug delivery

3.2.1 Introduction

Evolved with distinctive features such as low immunogenicity, long life span, and binding specificity, natural cells have proven highly advantageous as carriers of therapeutic and diagnostic agents.[1–3] For example, platelets are tiny, anucleate cells derived from the megakaryocyte of the bone marrow. Because of the relatively short life span of an individual platelet (around 8 to 10 days), billions of new platelets are produced daily to maintain normal platelet counts.[4] The large volume and surface area of platelets facilitate efficient drug loading. With their combined abundancy, fast replenishment, high drug loading efficiency, and specific binding to biological threats, platelets have been considered an attractive platform for targeted drug delivery.[5–9] However, vital cells, such as red blood cells (RBCs) and platelets, are immobile and rely on blood flow and passive diffusion to reach their desired destination, which may limit their overall binding, transport, and therapeutic efficacy when used as drug carriers. Transforming these passive cell systems into active and mobile delivery platforms is expected to open up new opportunities. Such a change in the operation of nanoscale systems from passive to active has been recently demonstrated with impressive benefits[10–22], including prolonged intestinal retention[12] and accelerated detoxification[22].

The use of micro/nanomachines that convert energy to propulsive force offers a viable route for realizing active cell-based delivery systems.[23–26] Recent efforts toward cell-motor hybrid platforms can be classified into two main categories on the basis of the propulsion mechanism. The first category of cell robots relies on the propulsion by external fields, where cells are integrated with active components that respond to external stimulations (i.e., magnetic, acoustic, etc.).[27–31] Such externally propelled cell systems may experience constraints, such as the need for complex actuation equipment. The second category of cell-motor systems operates autonomously, relying on self-propelled micromotors interfaced with functional cells.[22, 32, 33] For instance, natural cells such as RBCs and macrophages have been attached to bacteria or magnesium (Mg)–based micromotors, respectively.[22, 33] However, several concerns of biohybrid systems may limit their utility in practical clinical settings. For example, the pathogenicity and immunogenicity of bacteria may compromise the biocompatibility of bacteria-based platforms. Toxic propulsion fuels (e.g., H2O2) or short motor lifetimes (e.g., Mg-based micromotors) are additional barriers for diverse biomedical applications. Therefore, a fully biocompatible and biodegradable cell robot, capable of long-lasting self-propulsion in biological fuel, is highly desirable.

With the aforementioned design considerations, the use of enzymes to modify live cell motors represents an attractive approach, given their ability to convert their substrate biofuel into a driving force.[34–37] Enzyme-based micro/nanomotors, relying on biocatalytic reactions of widely available biocompatible fuel substrates, can thus be used for practical biomedical applications. Such enzymes integrated onto micro/nanostructures can generate sufficient power in biological media containing their substrate fuel to overcome random Brownian motion and display efficient propulsion without requiring external fuels.[38–40] Although early studies reported on the successful non-Janus modification of inorganic micro/nanospheres with enzymes to achieve propulsion[37, 41–43], breaking the symmetry to obtain a Janus structure is essential for achieving asymmetric driving force and generating efficient directional propulsion. The ability to immobilize enzymes onto cell surfaces has been proven viable for various applications[44–46], but reports on an active self-propelled cell motor based on enzyme modification of a cell surface in a Janus manner are scarce.

Here, we present urease-powered Janus platelet micromotors (JPL-motors) prepared by immobilizing the enzyme asymmetrically onto the surface of natural platelets (Fig. 1). As a major type of circulating blood cells, platelets offer multifunctionality in response to various microenvironments (i.e., hemostasis, inflammation, angiogenesis, wound healing, etc.) and specific binding to biological threats (cancer cells, bacteria, etc.) due to the versatile receptors on their surface.[4, 47, 48] The JPL-motors developed in the present study leverage the intrinsic binding specificity and capacity of platelets to other biological subjects[7, 49] for developing a new generation of targeted platelet micromotor powered by biocatalytic reactions of bioavailable fuels. By preserving the biological and structural features of regular platelets, the resulting JPL-motors have a wide range of platelet-like functions that other synthetic motors cannot achieve, for instance, specific binding and targeted delivery to cancer cells and bacteria.

The JPL-motors were fabricated by partially blocking the platelet surface through attachment of the platelets to a poly(l-lysine) (PLL)–modified surface in a commercial 12-well plate, followed by modifying the unblocked platelet surface with urease via a biotin-streptavidin-biotin binding complex (Fig. 3.6a). The biocatalytic reaction of the surface-bound urease in the presence of urea fuel generates an effective propulsion force through a chemophoretic mechanism. The resulting JPL-motors thus show efficient motion in diverse biological fluids in the presence of urea and significant propulsion enhancement in comparison with urease fully modified (non-Janus) platelets (denoted as “non-JPLs”), reflecting their asymmetrical structure. Our study demonstrates that the urease modification has a negligible effect on the functional proteins present on the platelet surface. This allows us to design a targeted platform on the basis of the intrinsic and specific binding of platelets to biological targets. The effective propulsion of the resulting JPL-motors in the presence of the urea fuel shows accelerated binding with cancer cells and bacteria and improved therapeutic efficacy of JPL-motors loaded with the model anticancer and antibiotic drugs, respectively. The integration of platelets with the urease biocatalytic engine enables the creation of an endogenous, biocompatible, and biodegradable cell robot that has the intrinsic properties of platelets along with the ability to self-propel. The cell surface engineering used for preparing the Janus urease coating represents a facile and robust method to asymmetrically functionalize the surface of natural cells. Such surface functionalization holds considerable potential for developing advanced cell robots. Using the body's own cellular materials as building blocks bestows the cell robots with capabilities to meet the rigorous properties required for biological applications, including superb biocompatibility, natural targeting ability, and high cargo-carrying capacity. These unique features would enable the cell robots for diverse biomedical applications including drug delivery, immunotherapy, and detoxification. Although the concept of creating enzyme-powered cell motors via an asymmetric biocatalytic cell coating has been presented here in connection to urease-modified platelet cells, it could be readily expanded for developing a multitude of self-propelled cell-based micromotors with diverse biofunctionalities based on different natural cells and enzyme modifications.

3.2.2 Fabrication and characterization of JPL-motors

The JPL-motors were fabricated in a commercial PLL-modified 12-well plate. PLL is a positively charged amino acid polymer with lysine residues that are commonly used to coat tissue culture vessels to promote the nonspecific attachment of negatively charged cells or proteins through electrostatic interactions.[22, 50] To accomplish the asymmetric surface modification, platelets were attached first to the PLL surface through centrifugation and further incubated for an hour. The centrifugation allowed partial platelet immersion into the PLL layer on the 12-well plate bottom, whereas the following incubation reinforced electrostatic attachment between the positively charged PLL surface and the negatively charged platelet membrane. This process enabled the partial blocking of the platelet membrane and allowed the subsequent Janus urease immobilization. As shown in Fig. 3.6a, the primary amines of the cell membrane proteins provided stable anchorage for cell surface engineering.[44]

Then, sulfo–N-hydroxysuccinimide (NHS)–biotin, streptavidin, and urease-biotin were sequentially introduced to modify the platelet surface with urease (see Materials and Methods). Last, the resulting JPL-motors were dissociated from the PLL surface and suspended in phosphate-buffered saline (PBS) at 4°C until use. Using strong noncovalent binding interactions, the biotin-streptavidin-biotin complex provided a robust connection between the platelets and urease, ensuring high stability of the resulting cell robots in diverse biological environments.

The fabricated JPL-motors were characterized first by fluorescence microscopy using Cyanine5 [Cy5; excitation (Ex)/emission (Em) = 646/662 nm]–labeled urease. The optical and fluorescent images of JPL-motors with Cy5-labeled urease demonstrate the monolayer distribution of JPL-motors on the well plate surface before pipetting. Further measurement of the JPL-motor sizes verified that about 82% of the JPL-motors are within a narrow size range of 1.4 to 2.6 μm. The fluorescent image (i) of the Cy5 channel in Fig. 3.6b shows the Janus distribution of urease on JPL-motors. The merged image (ii) of the bright-field and Cy5 channels confirmed the effective localization of urease on JPL-motors and further verified the successful Janus modification of urease on platelet membranes as displayed by the asymmetric localization of the Cy5 fluorescent dye on the platelet surface. Moreover, the fabricated JPL-motors maintained the characteristic shape of platelets, revealing no damage to the cell morphology during the modification process or detachment of JPL-motors from the PLL substrate. The modification feasibility and efficiency of urease was further explored by flow cytometry analysis. As shown in Fig. 3.6c, around 96% of JPL-motors were Cy5 positive, whereas the Cy5 signal was not observed in control experiments involving unmodified PLs or Janus modification of platelets without using biotinylated urease or streptavidin. Such results further demonstrate the successful modification of urease on the JPL-motors. We also examined whether the JPL-motors remained as activated platelets, which is directly related to the inherent properties of platelets, such as their specific binding capability. Expression of P-selectin, a hallmark platelet activation marker, was thus evaluated among rest platelets (freshly isolated platelets without activation), unmodified but activated platelets, and JPL-motors. The results of flow cytometry analysis, displayed in Fig. 3.6d, reveal that the P-selectin expression for both unmodified PLs and JPL-motors was significantly enhanced in comparison with that of rest platelets, indicating that the platelets used for fabricating the JPL-motors were activated and unaltered by the urease modification. Furthermore, we investigated the effect of cell surface engineering on the protein content of JPL-motors. A bicinchoninic acid (BCA) protein assay was performed, as shown in Fig. 3.6e. The protein content of JPL-motors was slightly higher than that of unmodified PLs at the same cell concentration (5×10^{11} cells/ml), which may be ascribed to the additional molecules (i.e., biotin) and proteins (i.e., streptavidin and urease) on the JPL-motor membrane. On the basis of the protein quantification, we also estimated the amount of urease per JPL-motor, which corresponds to 136 ± 25 molecules. Details of these calculations are given in the Supplementary Materials. Gel electrophoresis analysis of Fig. 3.6f illustrates that the protein profile of JPL-motors matches closely to that of unmodified PLs at the same protein concentration. However, the bands of the attached streptavidin or urease moieties cannot be found in the gel electrophoresis analysis because of their significantly lower amounts compared with those of proteins existing on the platelet surface. These results demonstrate that the platelet surface can be modified with urease without altering its protein profile, which is a prerequisite for subsequent biomedical applications of JPL-motors.

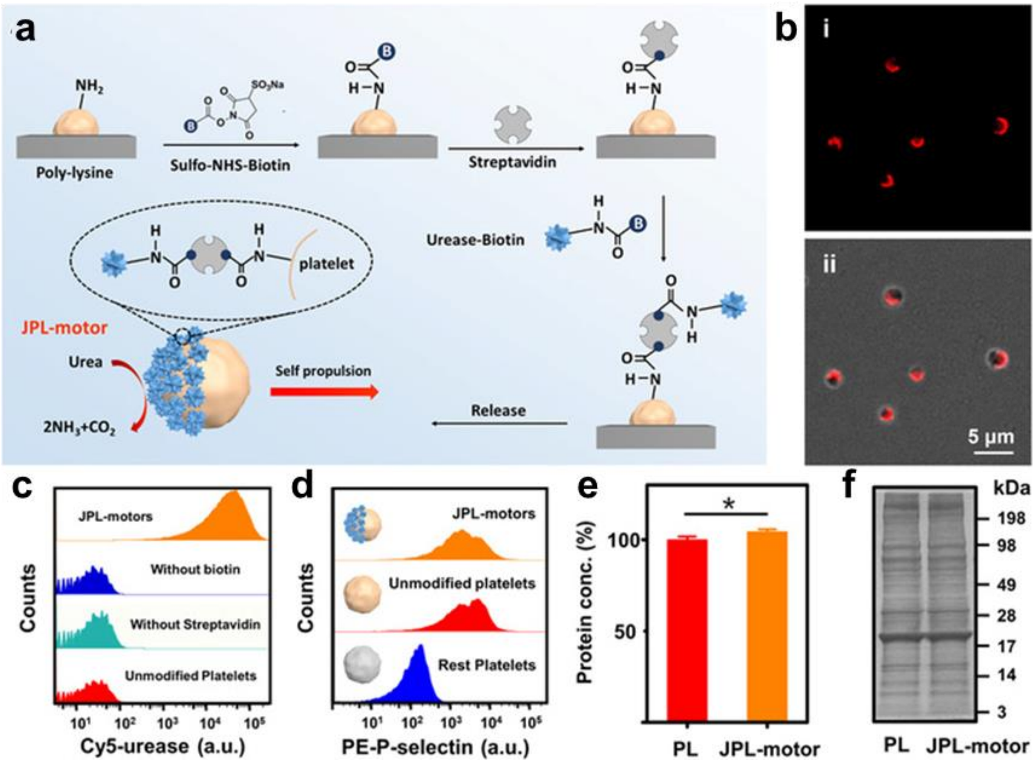

Figure 3.6 Fabrication and characterization of JPL-motors. a, Schematic of the fabrication of JPL-motors. Platelets were attached first to a PLL surface and then modified with urease via a biotin-streptavidin-biotin binding complex. b, Fluorescent (i) and merged (ii) images of Cy5 and bright-field channels of JPL-motors with Cy5-labeled urease. c, Representative flow cytometry histograms of Cy5-labeled urease under different conditions: JPL-motors (orange) and control experiments with unmodified platelets (red) and Janus modification of platelets without using biotin on urease (blue) or streptavidin (cyan). a.u., arbitrary units. d, Representative flow cytometry histograms of the platelet activation marker P-selectin on JPL-motors (orange), unmodified platelets (red), and resting platelets (blue). e, Quantification of the protein content of unmodified platelets (PL; red) and JPL-motors (orange) (both 5×10^{11} cells/ml), stored in 1× PBS at 4°C for 24 hours. Error bars represent SDs from three independent measurements. The mean protein amount of unmodified platelets was normalized to 100% ($^*P < 0.05$, t test). f, SDS–polyacrylamide gel electrophoresis analysis of proteins presented on unmodified platelets (PL) and JPL-motors. The samples were run at equal protein content and stained with Coomassie blue.

3.2.3 Propulsion performance of JPL-motors and non-JPLs

The Janus distribution of urease over the platelet surface results in asymmetric biocatalytic decomposition of urea into ammonia and carbon dioxide, as illustrated in Fig. 1A and the following Eq. 1:

$$(NH2)_2CO+H_2O \xrightarrow{urease} CO_2+2NH_3 \quad (1)$$

Subsequently, a concentration gradient and active directional flow of reaction products around JPL-motors are generated, which drives the JPL-motor to undergo self-diffusiophoretic propulsion. The propulsion data were acquired by optical tracking of individual micromotor samples. Figure 3.7a displays the typical tracking trajectories of JPL-motors in the presence of varying urea concentrations (0, 50, 100, and 200 mM) in PBS and illustrates the enhanced motion with increasing urea fuel concentrations. On the basis of the X-Y coordinates of the micromotor trajectories, taken from the optical tracking, the mean-squared displacement (MSD) was calculated as a function of the time interval (Δt) along with different concentrations. In Fig. 3.7b, the MSD increases linearly with time in low fuel concentration. This behavior changed at higher urea concentrations (100 and 200 mM), starting off as linear and shifting to parabolic, reflecting the effective directional motion of the cell robots under these conditions. Aiming at using JPL-motors in practical biomedical applications, we also examined the propulsion behavior of the motors in biologically relevant environments. As illustrated in Fig. 3.7c, the motion behavior of the cell robots in Dulbecco’s modified Eagle medium (DMEM), blood, and simulated urine in the presence of 100 mM urea is comparable with their movement in PBS. The effective diffusion coefficient (Deff) was estimated by fitting the MSD curves to Eq. 2

$$\mathrm{MSD}(\Delta \mathrm{t})=4D_{eff}\,\Delta \mathrm{t} \quad (2)$$

where D_{eff} represents the effective diffusion coefficient and Δt represents the time interval[51, 52]. The corresponding Deff is shown in Fig. 3.7d. Such propulsion behavior of the JPL-motors in various media further demonstrates the robustness of the Janus modification under different conditions toward expanded possibilities in diverse environments. We also explored the propulsion behavior of unmodified PLs in aforementioned biological fluids containing 100 mM urea. As expected, in the absence of immobilized urease engine, only a Brownian motion was observed in the different media. Because the Brownian motion is affected only by the temperature and the viscosity of the fluid, the unmodified PLs (lacking the urease engine) are expected to display Brownian motion independent of the presence of urea. We also examined the lifetime of the JPL-motors. The JPL-motors still displayed effective propulsion after 30 min at a urea concentration of 100 mM compared with their initial motion. Such biocatalytic propulsion with long life span holds great potential for addressing the requirement of practical applications. The observed path decrease is largely due to the depletion of the urea fuel, whereas the slow translational diffusion of the attached urease enzymes on cell membrane might also contribute to the path decrease by breaking the asymmetric enzyme distribution on the JPL-motors.

Several studies have reported that non-Janus coating of enzymes on polystyrene particles[37] or mesoporous silica nanoparticles[41–43] could enhance diffusive motion due to the unbalanced distribution of enzymes on the surface. Here, non-JPLs were also fabricated (see Materials and Methods) to compare their propulsion behavior with that of JPL-motors. The characterizations of non-JPLs with Cy5-labeled urease are presented. The fluorescence intensity of Cy5-labeled urease can be observed uniformly over the surface of the platelets. The successful fabrication of non-JPLs is further confirmed by flow cytometry analyses, demonstrating that the non-JPLs display a strong Cy5 signal (~99%) compared with the unmodified PLs. Compared with the images shown in Fig. 3.6b, such results further validated our methodology for Janus cell surface engineering. The optical tracking trajectories and calculated MSD of non-JPLs were shown in Fig. 3.7 (e and f, respectively), where an increase in displacement was observed upon increasing the urea concentration. However, as expected, JPL-motors displayed a more efficient propulsion and larger MSD compared with the corresponding non-JPLs. This difference was attributed to the asymmetric propulsion force generated by JPL-motors and was further confirmed by the Deff and speed. Figure 3.7g compares the calculated *Deff* of JPL-motors and non-JPLs. Although no major difference was observed in the absence of fuel, in the presence of urea, the Deff of JPL-motors was approximately two times higher compared with that of non-JPLs at the same fuel concentration. A similar trend was observed in Fig. 3.7h when comparing the speed obtained from optical tracking, with the JPL-motors displaying a higher speed (1.62-fold) than non-JPLs at 200 mM urea. Overall, these results demonstrate that JPL-motors exhibit effective movement in various biological media in the presence of urea and enhanced propulsion compared with non-JPLs, reflecting the stronger net propulsion force generated by the asymmetric enzyme distribution on the cell surface.

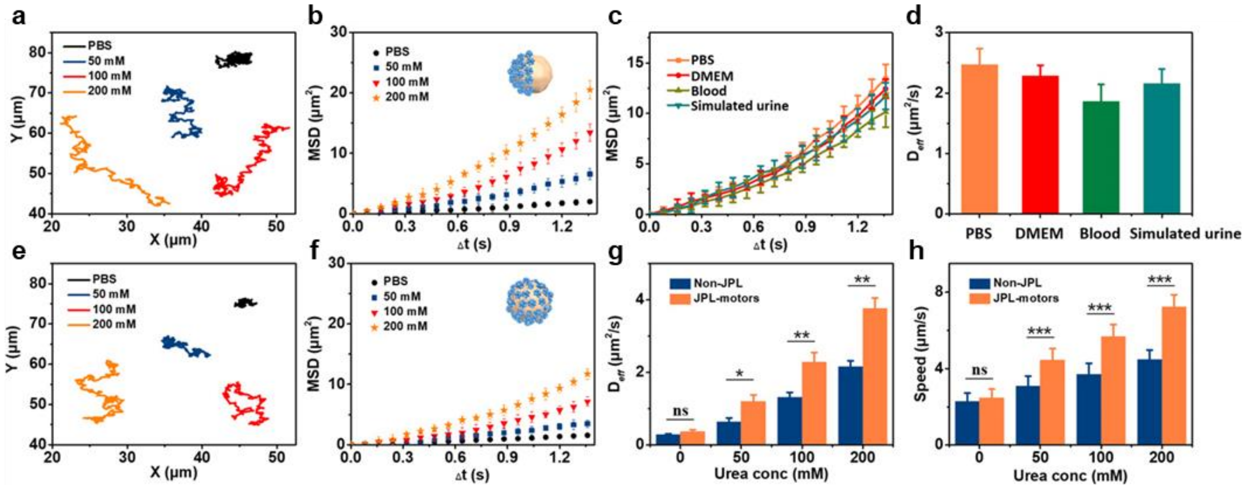

Figure 3.7 Motion behavior of JPL-motors. a,b, Optical tracking trajectories (over 20 s) and MSD of JPL-motors in PBS solution with different urea concentrations [n = 15; mean ± standard error of the mean (SEM)]. c,d, MSD and corresponding *Deff* of JPL-motors in various media at the same urea concentration (100 mM) (n = 15; mean ± SEM). e,f, Optical tracking trajectories (20 s) and MSD of the non-JPLs in PBS solution with different urea concentrations. g,h, Comparisons of the *Deff* (n = 15; mean ± SEM) and speed (n = 15; mean ± SD) of JPL-motors and non-JPLs in the presence of different urea concentrations. $*P < 0.05$, $**P < 0.01$, and $***P < 0.001$; ns, no statistical significance; t test.

3.2.1 In vitro anticancer drug delivery of JPL-motors

The successful fabrication of JPL-motors and their effective propulsion in diverse biological fluids allowed us to investigate their use in biological applications. Considering that platelets play crucial roles in cancer metastasis, including interacting directly with cancer cells[47], the active targeted JPL-motor platform holds great potential to improve drug delivery to cancer cells. Here, the breast cancer cell MDA-MB-231, known for its interaction with platelets[53], was used as a model to evaluate the anticancer activity of chemodrug-loaded JPL-motors (Fig. 3.8a). We first examined the specific adhesion of JPL-motors to cancer cells. Figure 3.8b presents a scanning electron microscope (SEM) image illustrating the adhesion and aggregation of JPL-motors (pseudocolored in pink) on an MDA-MB-231 cell (pseudocolored in purple) after 10 min of incubation at a urea concentration of 100 mM. Such specific binding is also demonstrated by fluorescent microscopy. JPL-motors and MDA-MB-231 cells were labeled with Cy5 and Hoechst 33342 (Ex/Em = 361/497 nm) dyes, respectively. Figure 3.8c shows the bright-field (i) and fluorescent (ii to iv) images of JPL-motors (iii, red) attached onto an MDA-MB-231 cell (ii, blue). The adhesion of cancer cells with PLs and RBCs has been used as positive and negative controls, respectively, to further explore the effect of the urease modification on the binding affinity of platelets. JPL-motors, PLs, and RBCs have thus been labeled with 1,1'-dioctadecyl-3,3,3',3'-tetramethylindodicarbocyanine (DiD; Ex/Em = 648/668 nm) and incubated for 30 min with MDA-MB-231 cells at the ratio of 10:1, followed by flow cytometry analysis. Both the JPL-motors and PLs displayed comparable DiD positive (~96%), whereas no DiD signal was observed for the negative RBC control. These data demonstrate that the enzyme modification of JPL-motors has no influence on the intrinsic adhesion properties of platelets, which is in agreement with the results of Fig. 3.6d and allows the design of JPL-motor–based targeted delivery platforms.

After confirming the specific binding capability of JPL-motors with MDA-MB-231 cells, the antitumor efficacy of drug-loaded JPL-motors was evaluated. Doxorubicin (DOX), a widely used chemotherapeutic drug, was selected for this study. The drugs are expected to be loaded onto the platelet cell through both electrostatic absorption and cellular endocytosis[54–56]. Initially, the capability of JPL-motors to load DOX was confirmed by fluorescent microscopy. Then, the loading capacity was explored with increasing inputs of DOX. In Fig. 3.8d, JPL-motors showed comparable loading capacity to unmodified PLs, indicating that the surface modification only has a slight effect on drug encapsulation. The maximum loading amount was obtained with 25 μM input concentration of DOX, corresponding to a 20% loading efficiency per 10^8 cells (Fig. 3.8d), whereas larger DOX concentrations provided lower loading efficiencies. We also explored the propulsion behavior of DOX-loaded JPL-motors. Only slight differences in trajectory and MSD were observed between DOX-loaded JPL-motors and unloaded JPL-motors, reflecting the effective propulsion of the drug-loaded cell robot platform. Subsequently, the DOX release from JPL-motors was analyzed over 24 hours at two different pH values. The JPL-motors displayed a similar and comparable DOX release behavior compared with PLs (Fig. 3.8e). The enhanced DOX release within 24 hours at a lower pH 5.0, compared with that at the physiological pH 7.4, might be due to the destabilization and protein denaturation of the platelet membrane at a lower pH value[57]. Enhanced release at low pH may facilitate effective drug delivery to tumors with their acidic microenvironments. Before evaluating the anticancer efficacy of DOX-loaded JPL-motors, the binding efficiency of cancer cells with JPL-motors or unmodified PLs was analyzed. Both JPL-motors and unmodified PLs were labeled with DiD and then incubated with MDA-MB-231 cells at 100 mM urea for different periods (5 min, 10 min, 30 min, 1 hour, 2 hours, and 4 hours). The optimized centrifugation speed of 100 relative centrifugal force (rcf) per minute was chosen to isolate the resulting aggregates from the free JPL-motors, PLs, and cancer cells. Then, the fluorescence intensity of DiD was measured. A rapid increase in fluorescence was observed within 30 min for JPL-motors, followed by a gradual saturation in signal (Fig. 3.8f). In contrast, MDA-MB-231 cells cultured with unmodified PLs showed a much slower fluorescent signal increase, demonstrating that the active motion can accelerate the specific adhesion between JPL-motors and cancer cells. The incubation time with the maximum difference of binding efficiency was 10 min, where the fluorescence intensity of DiD in JPL-motors reached a 2.55-fold increase compared with that of passive unmodified PLs. Subsequently, anticancer efficacy was evaluated on the basis of the optimized incubation time. Figure 3G displays the viability of MDA-MB-231 cells cultured at various conditions for 10 min and then isolated for another 24 hours of incubation. Three urea concentrations (0, 50, and 100 mM) were examined for each condition. Incubation with PBS or urea only (control in Fig. 3G) and JPL-motors without DOX loading (JPL-motor in Fig. 3.8g) were performed as negative controls and resulted in a negligible influence on cell viability, indicating the biocompatibility of JPL-motors and their propulsion fuel. When treated with free DOX, cancer cells displayed around 80% cell viability (DOX in Fig. 3.8g). Lower viability (~70%) was observed for MDA-MB-231 cells treated with DOX-loaded unmodified PLs (PL-DOX in Fig. 3.8g). It is also shown that different urea concentrations have negligible effects on cell growth for both free DOX and PL-DOX groups. In comparison, cells treated with DOX-loaded JPL-motors (JPL-motor–DOX in Fig. 3.8g) exhibited a substantial decrease in viability upon increasing the urea concentration. Forty percent cell viability was achieved at 100 mM urea, which is a 1.75-fold decrease compared with PL-DOX. The effective propulsion of JPL-motors thus accelerated their binding with cancer cells and enhanced local DOX concentration for improved anticancer effects (Fig. 3.8g). Overall, these results demonstrate that our cell robot therapeutic platform, with self-propulsion in the presence of urea, is capable of accelerating specific adhesion to cancer cells and enhancing anticancer efficacy.

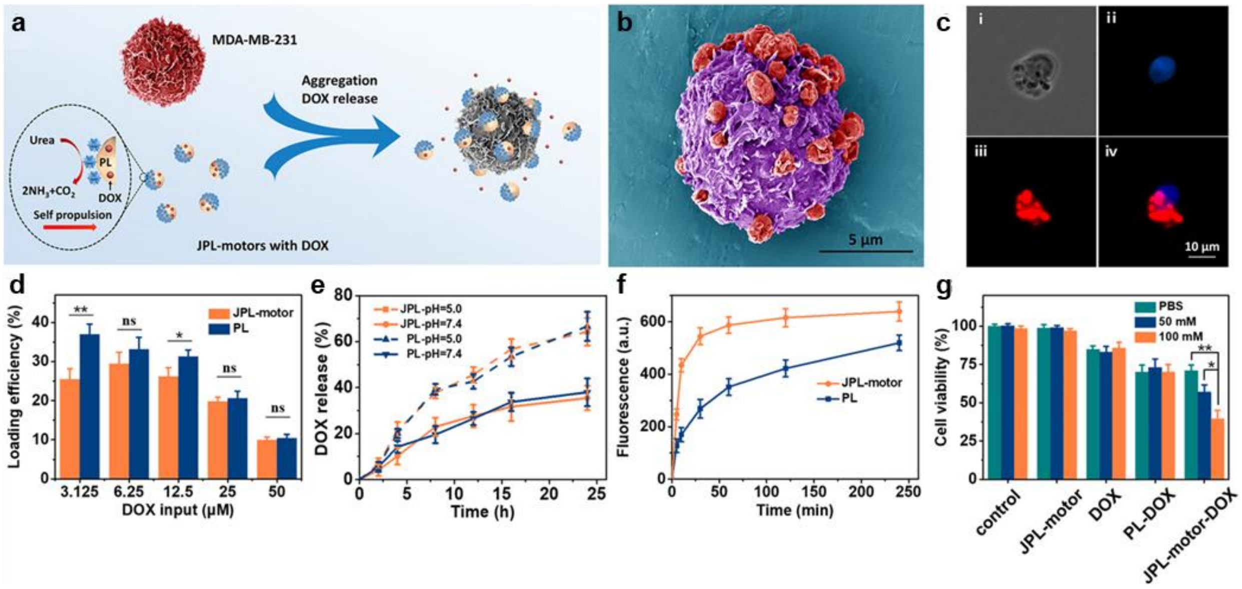

Figure 3.8 Enhanced binding and anticancer activity of chemodrug-loaded JPL-motors. a, Schematic of JPL-motor–DOX for cancer-targeted delivery. MDA-MB-231 breast cancer cells were selected as a model cell line. b, Pseudocolored SEM image of numerous JPL-motors (red) attached to an MDA-MB-231 cell (purple). c, Bright-field (i) and fluorescent (ii to iv) images showing the binding between an MDA-MB-231 cell and JPL-motors, labeled with Hoechst 33342 (ii, blue) and Cy5 (iii, red), respectively. Overlay of the two channels is shown in (iv). d, Loading efficiency of JPL-motors and unmodified platelets (PLs) at various DOX initial inputs (n = 3; mean ± SD). $*P < 0.05$ and $**P < 0.01$, t test. e, Cumulative release of DOX from DOX-loaded JPL-motors and unmodified platelets (PLs) at pH 5.0 or 7.4 over 24 hours (n = 3; mean ± SD). f, Comparison of the fluorescence intensity of MDA-MB-231 cells after incubation with DiD-labeled JPL-motors or unmodified platelets (PLs) over different periods of time at 100 mM urea (n = 3; mean ± SD). g, Viability of MDA-MB-231 cells after incubation with control solutions (only PBS or urea), JPL-motors, free DOX, PL-DOX, and JPL-motor–DOX at the same DOX concentration of 10 µM at various urea concentrations (0, 50, and 100 mM) for 10 min and separated for another 24 hours of incubation (n = 3; mean ± SD). $*P < 0.05$ and $**P < 0.01$, t test.

3.2.4 In vitro antibacterial drug delivery of JPL-motors

Encouraged by the enhanced anticancer efficacy of DOX-loaded JPL-motors, we explored whether this active therapeutic platform could be generalized to other payloads and biological threats. Here, we investigated the potential antibacterial application of JPL-motors by taking advantage of the platelets' high binding affinity to certain bacteria.[49, 58] We chose Escherichia coli, known to bind to platelets[59], as the model bacteria to assess the JPL-motor–bacterium interactions (Fig. 3.9a). Figure 3.9b displays an SEM image of the adhesion between a JPL-motor (pseudocolored in green) and E. coli (pseudocolored in pink) after 5 min of incubation at 100 mM urea. The platelet aggregation induced by E. coli was also shown. To further verify the motor-bacterium binding, we labeled the JPL-motors and E. coli with Cy5 and 4′,6-diamidino-2-phenylindole (DAPI; Ex/Em = 358/461 nm), respectively. The bright-field (i) and fluorescent images (ii to iv) of the E. coli (ii, blue) and JPL-motor (iii, red) aggregates are shown in Fig. 3.9c, revealing the binding affinity between E. coli and the cell robots. We further quantified the specific binding of JPL-motors with E. coli along with the binding to PLs serving as control. Both JPL-motors and PLs (labeled with DiD) were incubated with E. coli (labeled with DAPI) for 30 min at the ratio of 1:5. The binding percentage was estimated by manually counting 10 representative images taken from each sample. Only a slight difference in the binding level is observed for both JPL-motors and PLs, indicating that the Janus modification has a negligible influence on the binding affinity of platelets to bacteria. The demonstrated binding ability of the JPL-motors to cancer cells and bacteria relies on the numerous protein receptors on the surface of platelets. For example, bacteria can bind with the platelet Toll-like receptors, leading to the activation and aggregation of platelets.[49, 58] Platelet receptors, such as αIIbβ3, P-selectin, and α6β1, are responsible for the PL binding with cancer cells.[47] These biological receptor-ligand interactions enable the recognition and binding of platelets to the target cells. Because platelets express many unique functional receptors on its membrane that other cells, such as RBCs, do not express, our

JPL-motors are expected to target a wide range of biological threats that have binding affinity with platelets.

Ciprofloxacin (Cip), an antibiotic used to treat a wide variety of Gram-negative bacterial infections[60], was used for antibacterial evaluation. The drug loading capacity was first analyzed. The loading amount of JPL-motors increased with the Cip input, reaching the maximum loading at 12.5 μg/ml input concentration of Cip, corresponding to a loading efficiency of ~27% (Fig. 3.9d). Increasing the Cip input to 25 μg/ml resulted in a smaller loading efficiency. It was also observed that Cip-loaded JPL-motors exhibited propulsion comparable with their unloaded counterparts. Subsequently, Cip release was measured over 24 hours at two pH values (Fig. 3.9e). Similar to the DOX formulation, JPL-motors and PLs exhibit a negligible difference in the amounts of released Cip at each pH value. Moreover, at pH 5.0, both JPL-motors and PLs displayed a nearly twofold higher Cip release compared with pH 7.4. The binding efficiency of JPL-motors or PLs to E. coli was also explored. DiD-labeled JPL-motors or unmodified PLs were cultured with E. coli at 100 mM urea for different incubation times, followed by centrifugation at an optimized centrifugation speed of 600 rcf/min and washing steps to separate the resulting aggregates and remove the free JPL-motors or unmodified PLs. The increase of DiD fluorescence intensity in the aggregates was measured and calculated in the same way as above. JPL-motors induced a rapid fluorescence increase in comparison with non-JPLs (Fig 3.9f). The maximum difference in signal was achieved at 5 min, which was chosen as the incubation time for the following antimicrobial efficacy evaluation. This difference is attributed to the active motion of JPL-motors, leading to rapid adhesion to E. coli. To test the antibacterial effectiveness, an E. coli suspension [2 × 10^5 colony-forming units (CFU) per milliliter] was incubated with free Cip (Cip in Fig. 3.9g), unmodified PLs loaded with Cip (PL-Cip in Fig. 4G), and JPL-motors loaded with

Cip (JPL-motor–Cip in Fig. 3.9g) at the same drug concentration (10 μg/ml) with different urea concentrations for 5 min. The bacteria were then collected through centrifugation and transferred to fresh LB broth for a subsequent 24-hour incubation. The negative controls were also performed by mixing E. coli with PBS or urea only (control in Fig. 3.9g) or JPL-motors without Cip (JPL-motor in Fig. 4G), revealing a negligible effect on bacteria colonization. Only JPL-motors display a urea concentration–dependent bacteria inhibitory effect with the lowest optical density (0.4) at 600 nm (OD600) with 100 mM urea, which is around 3.6- and 2.1-fold lower than that of Cip and PL-Cip, respectively. The significant antibacterial effect of JPL-motors reflects their self-propulsion in the presence of urea, which accelerates adhesion to bacteria and induces higher local Cip concentrations. Overall, these results indicate that the effective propulsion and the specific binding of our cell robots to bacteria significantly improve their antibacterial efficacy compared with passive systems.

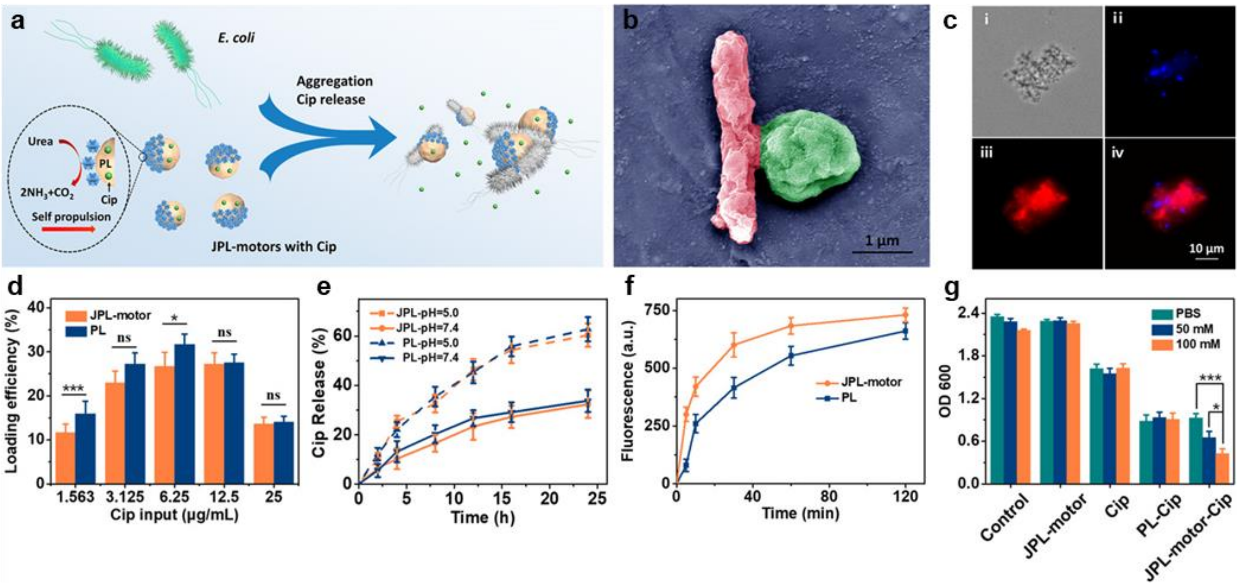

Figure 3.9 Enhanced binding and antibacterial activity of antibiotic-loaded JPL-motors. a, Schematic of JPL-motor–Cip for bacterium-targeted delivery. E. coli was selected as a model bacterium. b, Pseudocolored SEM image of the binding between the JPL-motor (green) and E. coli (red). c, Bright-field (i) and fluorescent (ii to iv) images of the binding between E. coli and JPL-motors, labeled with DAPI (ii, blue) and Cy5 (iii, red), respectively. The merged image of two channels is shown in (iv). d, Loading efficiency of JPL-motors and unmodified platelets (PLs) at various Cip initial inputs (n = 3; mean ± SD). *P < 0.05 and ***P < 0.001, t test. e, Cumulative released percentage of Cip from Cip-loaded JPL-motors and unmodified platelets (PLs) at pH 5.0 or 7.4 over 24 hours (n = 3; mean ± SD). f, Comparison of fluorescence intensity of E. coli after incubation with DiD-labeled JPL-motors or unmodified platelets (PLs over different periods of time at 100 mM urea) (n = 3; mean ± SD). g, OD600 of E. coli after culture with control solutions (only PBS or urea), JPL-motors, free Cip, PL-Cip, and JPL-motor–Cip at the same Cip concentration of 10 µg/ml at various urea concentrations (0, 50, and 100 mM) for 5 min and separated for another 24 hours of incubation (n = 3; mean ± SD). *P < 0.05 and ***P < 0.001, t test.

3.2.5 Discussion

Several challenges facing existing cell robot systems may hinder their practical use for biomedical applications. The first concern for biohybrids is biocompatibility. For example, live bacterium–driven microswimmers may induce an immune response.[33] The second issue is the potential toxicity of the propulsion fuel, for instance, the use of H2O2 during the manipulation of breast cancer cells.[32] Thus, there is demand for alternative biocompatible platforms and fuels to expand the biomedical prospects of micromotors. Another challenge in the application of biohybrid micromotors in biological environments is the limited motor life span. Despite good biocompatibility and biodegradability of Mg-based biohybrid micromotors, they still suffer from a short lifetime (~2 min), which compromises their application in certain environments.[12, 22, 61] On the other hand, although fuel-free propulsion mechanisms, based on the use of external acoustic or magnetic fields, have shown impressive performance in actuating and controlling micromotors for in vivo tests, these systems require relatively complex actuation systems and have limited tissue penetration. To overcome these limitations, we have demonstrated a platelet cell robot powered by urease with autonomous and long-lasting propulsion in the presence of urea, triggered by the corresponding enzymatic fuel decomposition that obviates the need for motor actuation. The integration of the endogenous enzyme with platelet cells yields a fully biocompatible cell robot system. The biofunctionality of platelet cells combined with an efficient motor results in an attractive platform with unique synergistic capabilities that can be useful for a broad range of biomedical applications. Moreover, the urea fuel is a common biological substrate readily available in the body, especially in the urinary system, making these types of microenvironments an attractive choice for initial clinical investigation. The methodology developed here leads to a facile and robust route to asymmetrically modify cell surfaces with urease. The Janus structure is highly preferable for achieving asymmetric driving force and active motion compared with complete enzymatic coverage of the entire cell membrane. The current Janus cell modification was realized by attaching platelets onto a PLL-modified substrate to block the attached platelet surface and modifying the exposed cell membrane with urease via a biotin-streptavidin-biotin binding interaction. The asymmetric distribution of urease on JPL-motors, demonstrated by fluorescent imaging using Cy5-labeled urease, results in an asymmetric propulsion force and leads to greatly enhanced movement in the presence of urea compared with non-JPLs. The ability to overcome Brownian motion and achieve effective propulsion enables the integration of asymmetrically engineered platelets into the microrobotic community to expand the design, functionality, and versatility of microrobots on the basis of the Janus modification and intrinsic properties of platelets.[14] The cell surface engineering route has a negligible effect on the functional proteins of platelet membrane, endowing JPL-motors with the unique capabilities of drug loading and specific binding to biological threats. The effective propulsion of JPL-motors in the presence of urea significantly enhances their binding efficiency to cancer cells and bacteria, and this, in turn, improves the in vitro therapeutic efficacy compared with passive unmodified PLs. These improvements can lead to decreased drug dosages, which can ultimately reduce unwanted side effects. Cell surface engineering transforms cells into active micromotors and can be readily generalized to other types of cells (e.g., RBCs and T cells) or enzymes (e.g., catalase and glucose oxidase) to open up a wide range of new biomedical opportunities.

The findings from this work illustrate a concept of using enzyme asymmetrically modified natural cells as live cellular robots for active and targeted delivery. The platform combines the merits of biocompatibility and functions of natural cells with active propulsion ability empowered by biological enzymes. In terms of potential medical applications, these cell robots can be readily expanded to carry other types of therapeutic or diagnostic payloads or to achieve a mission other than active delivery such as biodetoxification. The production and regulation of urea are crucial for various metabolic processes in the human body. The normal urea concentration in human blood ranges from 2.5 to 6.5 mM. In other biofluids, such as urine, the level of urea is significantly higher. Despite the large urea fluctuations in urine (ranging from 102 to 835 mM), this biofluid is particularly suitable for the propulsion of JPL-motors. The bioavailable propulsion fuel of the JPL-motors makes the platform amenable to future biomedical applications such as treatment of urinary tract infection or bladder cancer. Although the ammonia product of the biocatalytic decomposition of urea may contribute to a higher local pH and potential cytotoxic effect, such effects were reported to be controllable by adjusting the input of urease-powered micromotors for in vitro bladder cancer therapy.[42] This study demonstrated the safe in vivo application of urease-powered micromotors for bladder cancer treatment using an optimized motor concentration displaying low toxicity. Future in vivo studies and applications will require precise control to manipulate the cell robots to perform complex tasks in dynamic environments. Coupled with new functionalization and propulsion strategies, real-time tracking and imaging of the cell robots inside the body remain challenges that need to be addressed in parallel to the development of cell robots. In addition, directional movement of living cells induced by chemotaxis is critical for practical applications in biological systems.[62] Investigating the effect of concentration gradients of substrates on the propulsion of Janus cell robots holds considerable potential for designing multifunctional platforms with autonomous movement in response to complex environments. Overall, the Janus modification of cell surfaces offers an inspiring and versatile avenue for transforming passive cells into active cell robots. Such a strategy paves the way for efficient biocompatible cell robot platforms that meet the rigorous requirements of clinical biomedical applications.

3.2.6 Experimental section

Preparation of urease-biotin-Cy5. Urease (Sigma-Aldrich) was first dissolved in PBS (1×; pH 7.4) at 1 mg/ml. Sulfo-NHS-biotin (200 μl; 16.6 μM; ProteoChem) was then mixed with urease solution (200 μl, 1 mg/ml) and reacted for 30 min with gentle shake at room temperature. Subsequently, 4 μl of sulfo-Cy5 NHS ester (sulfo-NHS-Cy5; 1 mM; Lumiprobe) was added for another 30-min incubation. Last, the modified urease was purified four times with PBS through a 100-kDa filter (Millipore) with centrifugation at 1500 rcf for 3 min. The resulting urease-biotin-Cy5 was dispersed in 400 μl of PBS and stored at 4°C until use.

Fabrication of JPL-motors. Human platelets were purified from platelet-rich plasma (San Diego Blood Bank). JPL-motors were prepared in commercial 12-well plates modified with PLL (Corning). Platelets (10^9 cells) suspended in 400 μl of PBS were added to a 12-well plate and spun down to the PLL surface with a 3-min centrifugation at 900 rcf. After 1 hour of incubation at room temperature, the supernatant was removed and the plate was washed three times with PBS to remove all the unattached platelets. Afterward, the attached platelets were reacted with sulfo-NHS-biotin (166 μM), streptavidin (ProSpec; 166 μM), and urease-biotin-Cy5 (described above) for 1 hour, respectively. Three washes with PBS were needed for the removal of free agents between each reaction. Last, the resulting JPL-motors were disassociated from the PLL surface by pipetting gently and repeatedly, followed by two PBS washes. The micromotors were suspended in PBS and stored at 4°C until use.

Fabrication of non-JPLs. The reactions were performed in 1.7-ml Eppendorf tubes (Corning). Platelets were modified with the same chemicals at the same ratios as the fabrication of JPL-motors. The resulting non-JPLs were dispersed in PBS and stored at 4°C until use.

Characterization of JPL-motors. The Janus coating of urease onto the platelet surface was characterized by the fluorescent imaging of Cy5. All the bright-field, fluorescence, and merged images were captured using an EVOS FL microscope with a 40× objective. Flow cytometry analyses were also applied to evaluate the successful modification and binding efficiency of Cy5-labeled urease using a Becton Dickinson FACSCanto II flow cytometer. PLs, platelet modification without using biotinylated urease or streptavidin, were used as control experiments. P-selectin was selected to characterize the platelet activation. Resting platelets, PLs, and JPL-motors at a density of 10^6/ml were all incubated with 5 μl of phycoerythrin-labeled P-selectin (BioLegend) for 30 min, after which they were washed with PBS three times before flow cytometry analysis.

To compare the protein profile of the platelets before and after modification, both JPL-motors and PLs were centrifuged and resuspended in 1× PBS three times. Then, a BCA assay (Thermo Fisher Scientific) was used to quantify the membrane proteins on the JPL-motors as per the manufacturer's instructions. Gel electrophoresis followed by protein staining with Coomassie blue was also performed. PLs and JPL-motors containing equivalent total proteins were prepared in lithium dodecyl sulfate sample loading buffer (Invitrogen). The samples were then separated on a 4 to 12% bis-tris 17-well Mini Gel in Mops running buffer using a Novex XCell SureLock electrophoresis system (Life Technologies). Last, the protein columns were stained with Coomassie blue according to the manufacturer's protocol.

Propulsion study. All the experiments were performed in PBS solution by mixing JPL-motors with urea solution at the desired concentrations. A cover slide was applied to avoid the drifting effect. The propulsion videos were captured using an inverted optical microscope (Eclipse Ti-S/L100, Nikon Instruments Inc.) with a 40× microscope objective. The propulsion analysis was performed with NIS-Elements AR 3.2 software. The simulated urine was prepared according to the protocol described in a previous report.[63] Briefly, 0.073 g of NaCl, 0.040 g of KCl, 0.028 g of CaCl2·2H2O, 0.056 g of Na2SO4, 0.035 g of KH2PO4, 0.025 g of NH4Cl, and 0.15 g of urea were added to 25 ml of deionized water to obtain the simulated urine with 100 mM urea for investigating the propulsion behavior of JPL-motors in this medium.

Binding of JPL-motors with bacteria and cancer cells. SEM images of JPL-motors binding with E. coli and MDA-MB-231 breast cancer cells were performed on an Apreo high-resolution instrument (FEI, Hillsboro, OR, USA) with an accelerating voltage of 10 kV. Binding was further confirmed by fluorescent imaging. The breast cancer cell, MDA-MB-231, was labeled with Hoechst 33342 (Invitrogen), and the E. coli (DH5α) was labeled with DAPI (Sigma-Aldrich). All the bright-field, fluorescence, and merged images were captured using an EVOS FL microscope coupled with a 20× objective.

To explore the effect of urease modification on platelets' adhesion to cancer cells, PLs and RBCs were used as positive and negative controls, respectively. The JPL-motors, PLs, and RBCs at the cell concentration of 10^8 cells/ml were all labeled with DiD dye (1 μg/ml) for 30 min at room temperature. Then, the resulting suspension was centrifuged (1500 rcf, 3 min) to remove the free dyes by washing three times with PBS. The binding assay was conducted by incubating the DiD-labeled JPL-motors, PLs, and RBCs with MDA-MB-231 cells at the ratio of 10:1 for 30 min at the room temperature, followed by flow cytometry analysis to quantify the binding efficiency to MDA-MB-231.

To quantify the specific binding of JPL-motors and PLs to E. coli, both JPL-motors and PLs (10^{12} cells/ml) were first labeled with DiD (1 μg/ml) for 30 min at room temperature, followed by washing three times and centrifugation (1500 rcf, 3 min). E. coli (3×10^9 cells/ml) was labeled with DAPI (1 μg/ml) for 30 min at room temperature. The free dye was then removed through three washing steps with centrifugation at 5900 rcf for 5 min. The DiD-labeled JPL-motors and PLs were incubated with E. coli at the ratio of 1:5 for 30 min at room temperature, followed by microscopy imaging. The percentage of JPL-motors or PLs that bind to E. coli was quantified by manually counting 10 representative images taken for each sample.

The binding efficiency of JPL-motors and PLs with E. coli and MDA-MB-231 cells in the presence of urea was also evaluated. JPL-motors and PLs (10^{12} cells/ml) were first labeled with DiD (1 μg/ml), followed by washing steps to remove free dyes. DiD-labeled JPL-motors and PLs (10^{12} cells/ml) were then mixed with bacteria (3×10^9 cells/ml) at the ratio of 1:15 and cancer cells (10^5 cells/ml) at the ratio of 1:5 for different periods in the presence of 100 mM urea. The resulting aggregates of platelets and E. coli were separated by centrifugation at 600 rcf for 3 min and washed with PBS two times. The aggregates of platelets and MDA-MB-231 cells were collected with a 3-min centrifugation at 100 rcf, followed by two PBS washes. The aggregates were suspended in PBS and transferred to a 96-well plate. The binding efficiency was determined by the fluorescent intensity of DiD, measured with a BioTek Synergy Mx microplate reader.

DOX or Cip loading and release from JPL-motors. A total of 200 μl of DOX (Sigma-Aldrich) or Cip (Sigma-Aldrich), with different initial drug input concentrations (DOX input: 3.125, 6.25, 12.5, 25, and 50 μM; Cip input: 1.563, 3.125, 6.25, 12.5, and 25 μg/ml), was incubated with JPL-motors or PLs (10^8 cells) at 37°C for 1 hour, followed by removal of the free drug by two washes at 2300 rcf for 3 min. Then, drug-loaded JPL-motors were suspended in 200 μl of PBS for further use. The concentration of DOX (Ex/Em = 488/594 nm) and Cip (Ex/Em = 280/425 nm) were quantified by their fluorescent intensities measured by a BioTek Synergy Mx microplate reader. The loading efficiency was determined as the amount of the loaded drug divided by the drug input. The drug release was performed with 200 μl of fresh JPL-motor loaded with DOX or Cip at pH 5.0 or 7.4.

In vitro anticancer activity of DOX-loaded JPL-motors. The MDA-MB-231 cells (10^6 cells) were first incubated with PBS or urea only (negative controls), free DOX, PL-DOX, and JPL-motor–DOX at the same DOX concentration of 10 μM with different urea concentrations (0, 50, and 100 mM) for 10 min in 1.7-ml Eppendorf tubes. Then, the cancer cells were isolated by centrifugation at 100 rcf for 3 min and washed two times with PBS. The collected cells were further incubated with fresh DMEM in a 96-well plate at 37°C for 24 hours. After that, an MTS (Promega) [3-(4,5-dimethylthiazol-2-yl)-5-(3-carboxymethoxyphenyl)-2-(4-sulfophenyl)-2H-tetrazolium] assay was conducted to evaluate cell viability based on the manufacturer's protocol. The absorbance at 490 nm was read using a BioTek Synergy Mx microplate reader.

In vitro antibacterial activity of Cip-loaded JPL-motors. Typically, E. coli (2×10^6 CFU/ml) was mixed with PBS or urea only (negative controls), free Cip, PL-Cip, and JPL-motor–Cip at the same Cip concentration of 10 μg/ml with different urea concentrations (0, 50, and 100 mM) for 5 min. Then, the bacteria were collected by centrifugation at 600 rcf for 3 min and washed two times with PBS. The bacteria were then transferred to 1 ml of LB broth (Luria-Bertani, BD Difco) and cultured for 24 hours at 37°C. Last, the bacterial colonies were counted by measuring their absorbance at 600 nm (OD600).

Chapter 3.2, in full, is a reprint of the material as it appears in Science Robotics, 2020, by Songsong Tang, Fangyu Zhang, Hua Gong, Fanan. Wei, Jia. Zhuang, Emil Karshalev, Berta Esteban-Fernández de Ávila, Chuying Huang, Zhidong Zhou, Zhengxing Li, Lu Yin, Haifeng Dong, Ronnie H. Fang, Xueji Zhang, Liangfang Zhang, Joseph Wang. The dissertation author was the primary investigator and author of this paper.

3.2.7 References

1. F. Pierigè, S. Serafini, L. Rossi, M. Magnani, Cell-based drug delivery. *Adv. Drug Deliv. Rev.* 60, 286–295 (2008).

2. L. A. L. Fliervoet, E. Mastrobattista, Drug delivery with living cells. *Adv. Drug Deliv. Rev.* 106, 63–72 (2016).

3. T. Burnouf, P.-A. Burnouf, Y.-W. Wu, E.-Y. Chuang, L.-S. Lu, H. Goubran, Circulatory-cellmediated nanotherapeutic approaches in disease targeting. *Drug Discov. Today* 23, 934–943 (2018).

4. J. W. Semple, J. E. Italiano Jr., J. Freedman, Platelets and the immune continuum. *Nat. Rev. Immunol.* 11, 264–274 (2011).

5. S. Sarkar, M. A. Alam, J. Shaw, A. Kr. Dasgupta, Drug delivery using platelet cancer cell interaction. *Pharm. Res.* 30, 2785–2794 (2013).

6. P. Xu, H. Zuo, B. Chen, R. Wang, A. Ahmed, Y. Hu, J. Ouyang, Doxorubicin-loaded platelets as a smart drug delivery system: An improved therapy for lymphoma. *Sci. Rep.* 7, 42632 (2017).

7. Z. Li, S. Hu, K. Cheng, Platelets and their biomimetics for regenerative medicine and cancer therapies. *J. Mater. Chem.* B 6, 7354–7365 (2018).

8. M. Demers, D. D. Wagner, Targeting platelet function to improve drug delivery. *Oncoimmunology* 1, 100–102 (2012).

9. Q. Shi, R. R. Montgomery, Platelets as delivery systems for disease treatments. *Adv. Drug Deliv. Rev.* 62, 1196–1203 (2010).

10. A. M. Fennimore, T. D. Yuzvinsky, W.-Q. Han, M. S. Fuhrer, J. Cumings, A. Zettl, Rotational actuators based on carbon nanotubes. *Nature* 424, 408–410 (2003).

11. J. Xi, J. J. Schmidt, C. D. Montemagno, Self-assembled microdevices driven by muscle. *Nat. Mater.* 4, 180–184 (2005).

12. B. Esteban-Fernández de Ávila, P. Angsantikul, J. Li, M. Angel Lopez-Ramirez, D. E. Ramírez-Herrera, S. Thamphiwatana, C. Chen, J. Delezuk, R. Samakapiruk, V. Ramez, M. Obonyo, L. Zhang, J. Wang, Micromotor-enabled active drug delivery for in vivo treatment of stomach infection. *Nat. Commun.* 8, 272 (2017).

13. J. T. Kim, U. Choudhury, H.-H. Jeong, P. Fischer, Nanodiamonds that swim. Adv. Mater. 29, 1701024 (2017).

14. J. Li, B. Esteban-Fernández de Ávila, W. Gao, L. Zhang, J. Wang, Micro/nanorobots for biomedicine: Delivery, surgery, sensing, and detoxification. *Sci. Robot.* 2, eaam6431 (2017).

15. Z. Wu, J. Troll, H.-H. Jeong, Q. Wei, M. Stang, F. Ziemssen, Z. Wang, M. Dong, S. Schnichels, T. Qiu, P. Fischer, A swarm of slippery micropropellers penetrates the vitreous body of the eye. *Sci. Adv.* 4, eaat4388 (2018).

16. W. Wang, W. Duan, A. Sen, T. E. Mallouk, Catalytically powered dynamic assembly of rod-shaped nanomotors and passive tracer particles. Proc. Natl. Acad. Sci. U.S.A. 110, 17744–17749 (2013).

17. V. Magdanz, M. Medina-Sánchez, L. Schwarz, H. Xu, J. Elgeti, O. G. Schmidt, Spermatozoa as functional components of robotic microswimmers. *Adv. Mater.* 29, 1606301 (2017).

18. F. Peng, Y. Tu, D. A. Wilson, Micro/nanomotors towards in vivo application: Cell, tissue and biofluid. *Chem. Soc. Rev.* 46, 5289–5310 (2017).

19. K. Kim, J. Guo, Z. Liang, D. Fan, Artificial micro/nanomachines for bioapplications: Biochemical delivery and diagnostic sensing. Adv. Funct. Mater. 28, 1705867 (2018).

20. X. Yan, Q. Zhou, M. Vincent, Y. Deng, J. Yu, J. Xu, T. Xu, T. Tang, L. Bian, Y.-X. J. Wang, K. Kostarelos, L. Zhang, Multifunctional biohybrid magnetite microrobots for imagingguided therapy. *Sci. Robot.* 2, eaaq1155 (2017).

21. M. Pal, N. Somalwar, A. Singh, R. Bhat, S. M. Eswarappa, D. K. Saini, A. Ghosh, Maneuverability of magnetic nanomotors inside living cells. *Adv. Mater.* 30, e1800429 (2018).

22. F. Zhang, R. Mundaca-Uribe, H. Gong, B. Esteban-Fernández de Ávila, M. Beltrán-Gastélum, E. Karshalev, A. Nourhani, Y. Tong, B. Nguyen, M. Gallot, Y. Zhang, L. Zhang, J. Wang, A

macrophage-magnesium hybrid biomotor: Fabrication and characterization. *Adv. Mater.* 31, e1901828 (2019).

23. H. Wang, M. Pumera, Micro/nanomachines and living biosystems: From simple interactions to microcyborgs. *Adv. Funct. Mater.* 28, 1705421 (2018).

24. L. Schwarz, M. Medina-Sánchez, O. G. Schmidt, Hybrid biomicromotors. *Appl. Phys. Rev.* 4, 031301 (2017).

25. C. Gao, Z. Lin, X. Lin, Q. He, Cell membrane–camouflaged colloid motors for biomedical applications. *Adv. Therap.* 1, 1800056 (2018).

26. X. Z. Chen, B. Jang, D. Ahmed, C. Hu, C. De Marco, M. Hoop, F. Mushtaq, B. J. Nelson, S. Pané, Small-scale machines driven by external power sources. *Adv. Mater.* 30, e1705061 (2018).

27. Z. Wu, T. Li, J. Li, W. Gao, T. Xu, C. Christianson, W. Gao, M. Galarnyk, Q. He, L. Zhang, J. Wang, Turning erythrocytes into functional micromotors. *ACS Nano* 8, 12041–12048 (2014).
28. S. Jeon, S. Kim, S. Ha, S. Lee, E. Kim, S. Y. Kim, S. H. Park, J. H. Jeon, S. W. Kim, C. Moon, B. J. Nelson, J.-y. Kim, S.-W. Yu, H. Choi, Magnetically actuated microrobots as a platform for stem cell transplantation. *Sci. Robot.* 4, eaav4317 (2019).

29. Z. Lin, X. Fan, M. Sun, C. Gao, Q. He, H. Xie, Magnetically actuated peanut colloid motors for cell manipulation and patterning. *ACS Nano* 12, 2539–2545 (2018).

30. J. Li, X. Li, T. Luo, R. Wang, C. Liu, S. Chen, D. Li, J. Yue, S.-h. Cheng, D. Sun, Development of a magnetic microrobot for carrying and delivering targeted cells. *Sci. Robot.* 3, eaat8829 (2018).

31. Z. Wu, B. Esteban-Fernández de Ávila, A. Martín, C. Christianson, W. Gao, S. K. Thamphiwatana, A. Escarpa, Q. He, L. Zhang, J. Wang, RBC micromotors carrying multiple cargos towards potential theranostic applications. *Nanoscale* 7, 13680–13686 (2015).

32. K. Villa, L. Krejčová, F. Novotný, Z. Heger, Z. Sofer, M. Pumera, Cooperative multifunctional self-propelled paramagnetic microrobots with chemical handles for cell manipulation and drug delivery. *Adv. Funct. Mater*. 28, 1804343 (2018).

33. Y. Alapan, O. Yasa, O. Schauer, J. Giltinan, A. F. Tabak, V. Sourjik, M. Sitti, Soft erythrocytebased bacterial microswimmers for cargo delivery. *Sci. Robot.* 3, eaar4423 (2018).
34. I.-A. Pavel, A.-I. Bunea, S. David, S. Gáspár, Nanorods with biocatalytically induced self-electrophoresis. *ChemCatChem* 6, 866–872 (2014).

35. P. S. Schattling, M. A. Ramos-Docampo, V. Salgueiriño, B. Städler, Double-fueled janus swimmers with magnetotactic behavior. *ACS Nano* 11, 3973–3983 (2017).

36. T. Patiño, X. Arqué, R. Mestre, L. Palacios, S. Sánchez, Fundamental aspects of enzymepowered micro-and nanoswimmers. *Acc. Chem. Res.* 51, 2662–2671 (2018).

37. K. K. Dey, X. Zhao, B. M. Tansi, W. J. Méndez-Ortiz, U. M. Córdova-Figueroa, R. Golestanian, A. Sen, Micromotors powered by enzyme catalysis. *Nano Lett.* 15, 8311–8315 (2015).

38. S. Keller, S. P. Teora, G. X. Hu, M. Nijemeisland, D. A. Wilson, High-throughput design of biocompatible enzyme-based hydrogel microparticles with autonomous movement. *Angew. Chem. Int. Ed.* 57, 9814–9817 (2018).

39. X. Arqué, A. Romero-Rivera, F. Feixas, T. Patiño, S. Osuna, S. Sánchez, Intrinsic enzymatic properties modulate the self-propulsion of micromotors. *Nat. Commun.* 10, 2826 (2019).

40. P. Schattling, B. Thingholm, B. Städler, Enhanced diffusion of glucose-fueled Janus particles. *Chem. Mater.* 27, 7412–7418 (2015).

41. A. C. Hortelão, T. Patiño, A. Perez-Jiménez, À. Blanco, S. Sánchez, Enzyme-powered nanobots enhance anticancer drug delivery. *Adv. Funct. Mater.* 28, 1705086 (2018).

42. A. C. Hortelão, R. Carrascosa, N. Murillo-Cremaes, T. Patiño, S. Sánchez, Targeting 3d bladder cancer spheroids with urease-powered nanomotors. *ACS Nano* 13, 429–439 (2018).

43. T. Patiño, N. Feiner-Gracia, X. Arqué, A. Miguel-López, A. Jannasch, T. Stumpp, E. Schäffer, L. Albertazzi, S. Sánchez, Influence of enzyme quantity and distribution on the selfpropulsion of non-Janus urease-powered micromotors. *J. Am. Chem. Soc.* 140, 7896–7903 (2018).

44. J. Park, B. Andrade, Y. Seo, M.-J. Kim, S. C. Zimmerman, H. Kong, Engineering the surface of therapeutic "living" cells. *Chem. Rev.* 118, 1664–1690 (2018).

45. S. Abbina, E. M. J. Siren, H. Moon, J. N. Kizhakkedathu, Surface engineering for cell-based therapies: Techniques for manipulating mammalian cell surfaces. *ACS Biomater Sci. Eng.* 4, 3658–3677 (2017).

46. J. Niu, D. J. Lunn, A. Pusuluri, J. I. Yoo, M. A. O'Malley, S. Mitragotri, H. T. Soh, C. J. Hawker, Engineering live cell surfaces with functional polymers via cytocompatible controlled radical polymerization. *Nat. Chem.* 9, 537–545 (2017).

47. D. G. Menter, S. C. Tucker, S. Kopetz, A. K. Sood, J. D. Crissman, K. V. Honn, Platelets and cancer: A casual or causal relationship: Revisited. *Cancer Metastasis Rev.* 33, 231–269 (2014).

48. O. Garraud, Editorial: Platelets as immune cells in physiology and immunopathology. *Front. Immunol.* 6, 274 (2015).

49. S. W. Kerrigan, D. Cox, Platelet–bacterial interactions. *Cell. Mol. Life Sci.* 67, 513–523 (2010).

50. H. Lu, L. Guo, N. Kawazoe, T. Tateishi, G. Chen, Effects of poly(L-lysine), poly(acrylic acid) and poly(ethylene glycol) on the adhesion, proliferation and chondrogenic differentiation of human mesenchymal stem cells. *J. Biomater. Sci. Polym. Ed.* 20, 577–589 (2009).

51. J. R. Howse, R. A. L. Jones, A. J. Ryan, T. Gough, R. Vafabakhsh, R. Golestanian, Self-motile colloidal particles: From directed propulsion to random walk. *Phys. Rev. Lett.* 99, 048102 (2007).

52. G. Dunderdale, S. Ebbens, P. Fairclough, J. Howse, Importance of particle tracking and calculating the mean-squared displacement in distinguishing nanopropulsion from other processes. *Langmuir* 28, 10997–11006 (2012).

53. J. Suchanski, J. Grzegrzolka, T. Owczarek, P. Pasikowski, A. Piotrowska, B. Kocbach, A. Nowak, P. Dziegiel, A. Wojnar, M. Ugorski, Sulfatide decreases the resistance to stress-induced apoptosis and increases P-selectin-mediated adhesion: A two-edged sword in breast cancer progression. *Breast Cancer Res.* 20, 133 (2018).

54. P. Mohan, N. Rapoport, Doxorubicin as a molecular nanotheranostic agent: Effect of doxorubicin encapsulation in micelles or nanoemulsions on the ultrasound-mediated intracellular delivery and nuclear trafficking. *Mol. Pharm.* 7, 1959–1973 (2010).

55. S. V. Blokhina, A. V. Sharapova, M. V. Ol'khovich, T. V. Volkova, G. L. Perlovich, Solubility, lipophilicity and membrane permeability of some fluoroquinolone antimicrobials. *Eur. J. Pharm. Sci.* 93, 29–37 (2016).

56. M. Banerjee, S. W. Whiteheart, The ins and outs of endocytic trafficking in platelet functions. *Curr. Opin. Hematol.* 24, 467–474 (2017).

57. E. Baumann, W. Linß, M. Fröhner, G. Stoya, W. Richter, Ph-induced denaturation of spectrin changes the interaction of membrane proteins in erythrocyte ghosts. Biochemical and electron microscopic evidence. *Ann. Anat.* 176, 93–99 (1994).

58. J. R. Fitzgerald, T. J. Foster, D. Cox, The interaction of bacterial pathogens with platelets. *Nat. Rev. Microbiol.* 4, 445–457 (2006).

59. C. N. Watson, S. W. Kerrigan, D. Cox, I. R. Henderson, S. P. Watson, M. Arman, Human platelet activation by Escherichia coli: Roles for fcγriia and integrin αiibβ3. *Platelets* 27, 535–540 (2016).

60. R. J. Fass, Efficacy and safety of oral ciprofloxacin for treatment of serious urinary tract infections. *Antimicrob. Agents Chemother.* 31, 148–150 (1987).

61. F. Mou, C. Chen, H. Ma, Y. Yin, Q. Wu, J. Guan, Self-propelled micromotors driven by the magnesium–water reaction and their hemolytic properties. *Angew. Chem. Int. Ed.* 52, 7208–7212 (2013).

62. A. Somasundar, S. Ghosh, F. Mohajerani, L. N. Massenburg, T. Yang, P. S. Cremer, D. Velegol, A. Sen, Positive and negative chemotaxis of enzyme-coated liposome motors. *Nat. Nanotechnol.* 14, 1129–1134 (2019).

63. P. Batista Deroco, F. Campanhã Vicentini, G. Gabriel Oliveira, R. C. Rocha-Filho, O. Fatibello-Filho, Square-wave voltammetric determination of hydroxychloroquine in pharmaceutical and synthetic urine samples using a cathodically pretreated boron-doped diamond electrode. *J. Electroanal. Chem.* 719, 19–23 (2014).

3.3 Ultrasould-triggered RBC membrane-coated nanorobots for intracellular oxygen transport

3.3.1 Introduction

Gas molecules have essential physiological and pathological roles, impacting various signaling and metabolic pathways. Simple gas molecules such as nitric oxide,[1,2] carbon monoxide,[3,4] hydrogen sulfide,[5] and hydrogen[6] have been studied extensively. The transport of gas molecules in appropriate amounts to corresponding tissue sites is critical for positive health outcomes, ranging from heart protection[7] and neuronal repair[8] to regulation of blood pressure[9] and inflammation.[10] Among a variety of gas molecules being routinely transported during metabolism, oxygen is the most essential for life maintenance. Hypoxia, the decrease in oxygen levels below normal physiological levels, has been shown to play a critical role in the progression of different diseases.[11] The majority of cellular activities require energy in the form of oxygen, and prolonged and severe hypoxia results in cell death.[12] It is thus crucial to maintain sufficient oxygen availability to cells and tissues.[13] When oxygen levels are critically low, the infusion of donated red blood cells (RBCs) is a life-saving measure for patients with significant blood loss. However, due to significant strain on available resources and infrastructure,[14] tremendous efforts have been devoted to the development of viable alternatives to human RBCs for oxygen delivery.[15,16] Toward this goal, materials with high oxygen solubility have been used as nano/microcarriers for effective blood circulation and deep tissue penetration.[17,18] In particular, perfluorocarbon (PFC)-based oxygen nanocarriers offer many intrinsic benefits, such as high loading capacity, facile release profile, and relative small size.[19–21] RBC membrane-coated PFC nanoemulsions (RBC-PFC) have recently been reported as a viable candidate for blood substitutes.[22] The formulated biomimetic

RBC-PFC could be stored at room temperature for several months and demonstrated high capacity for oxygen delivery. Notably, the RBC-PFC formulation was able to attenuate the effects of hypoxia in vitro and could fully resuscitate mice in a model of hemorrhagic shock. The biomimetic surface coating of the natural RBC membrane also helped to improve biocompatibility and minimize immunogenicity. Nevertheless, by solely relying on passive circulation and diffusion, the current delivery platforms are not able to actively and effectively localize oxygen to ischemic tissues and hypoxic cells, resulting in suboptimal delivery efficiency.

Over the past decade, researchers have reported on active delivery methods using nano/micromotors, which consist of synthetic nano/microscale structures of different shapes and materials that can convert different energy inputs into mechanical motion.[23–25] The nano/micromotor field has been growing rapidly and has started to demonstrate great promise for medical applications such as active delivery of therapeutic payloads, fast sensing of important disease markers, accelerated detoxification of human fluids, and cargo-transport toward and into cells.[26–32] Specifically, acoustically propelled nanomotors have demonstrated major advantages for active intracellular delivery and actuation.[33,34] These nanomotors are based on gold nanowires (AuNWs), which can display rapid propulsion under an ultrasound (US) field.[32,35,36] The gold surface allows facile modification and functionalization of the nanomotors with therapeutic payloads or specific receptors. Then, the acoustic propulsion enables the concentration of nanomotors around target cells, their rapid penetration through cellular membranes, continuous motor motion within the intracellular space, and finally the active delivery of the payloads. Such acoustic propulsion and fast cell internalization have proven useful for accelerating a variety of intracellular processes. For example, US-powered nanomotors have been utilized for rapid intracellular delivery of therapeutic proteins,[37,38] fast miRNA sensing inside cancer cells,[39] and enhanced siRNA delivery accelerating gene silencing.[40] The capabilities demonstrated by US-propelled nanomotors for active intracellular delivery and actuation shed light on a wide range of potential biomedical applications. Nonetheless, most of the payloads delivered by acoustic nanomotors have been large biomolecules, with no attention given to gas delivery. Thus, we anticipated that combining the mobile nanomotor with an oxygen delivery nanocarrier would lead to the active intracellular delivery of small gas molecules by nanomotor technology.

In this work we describe a nanomotor-based gas delivery strategy for active intracellular oxygen delivery. Our approach took advantage of the combination of the rapid acoustic propulsion of AuNW nanomotors with the high oxygen loading capacity of RBC-PFC, enabling oxygen delivery to the intracellular space of J774 macrophage cells and helping maintain their viability when cultured under hypoxic conditions. Briefly, positively charged poly-l-lysine (PLL)-modified AuNWs were functionalized with negatively charged RBC-PFC via electrostatic interactions; then, the resulting RBC-PFC-loaded nanomotors (denoted as Motor-PFC) were propelled under a US field and actively incorporated into J774 macrophages. Upon entering the cells, the oxygen loaded in the Motor-PFC was sustainably released intracellularly under hypoxic culture conditions, helping to maintain the cell viability against hypoxia. As indicated above, while different platforms have been designed for oxygen delivery, the present active acoustic nanomotor strategy offers significant advantages in terms of cellular penetration and intracellular delivery toward maintaining sufficient oxygen availability to cells. This approach combines the active acoustic motor delivery with the high oxygen-carrying capacity of synthetic PFC and the biocompatibility of the natural cell membrane. These advantages make the Motor-PFC platform an attractive candidate for biomedical applications. While the present proof-of-concept study demonstrates active intracellular oxygen delivery to macrophages, a variety of other versatile gas-loaded nanocarriers could be combined with acoustic nanomotors for intracellular delivery of different therapeutic gases.

3.3.2 Fabrication and characterization of Motor-PFC

Figure 3.10a schematically illustrates the stepwise surface modification of a AuNW nanomotor for the loading of the RBC-PFC oxygen carrier. Initially, the AuNW was functionalized with a self-assembled monolayer of 3-mercaptopropionic acid (MPA), introducing negatively charged carboxyl moieties to the nanomotor surface. A positively charged poly-l-lysine layer was then incorporated onto the AuNW/MPA surface via electrostatic interactions. Finally, the RBC-PFC, fabricated according to an early work,[22] were immobilized onto the AuNW/MPA/PLL surface by further electrostatic interactions with the outer PLL layer, leveraging the attraction between the negatively charged RBC membrane surface and the positively charged PLL nanomotor surface. As shown in Figure 3.10b, the resulting Motor-PFC could be effectively propelled under an acoustic field and actively incorporated into J774 macrophage cells upon a 5 min US treatment. The efficient nanomotor movement under the US field enables effective cell membrane penetration.[38] Upon internalization, the Motor-PFC released the dissolved oxygen under hypoxic culture conditions. The efficiency of the active nanomotor-assisted oxygen delivery could be visualized directly by using fluorescent microscopy. Image-iT Green hypoxia reagent-labeled cells remained nonfluorescent following a 72 h incubation, confirming the oxygen release and prolonged maintenance of the cell viability (Figure 1c, left). In contrast, without the Motor-PFC treatment, the cell displayed a bright fluorescent color, reflecting the significant amount of accumulated hypoxic stress (Figure 3.10c, right).

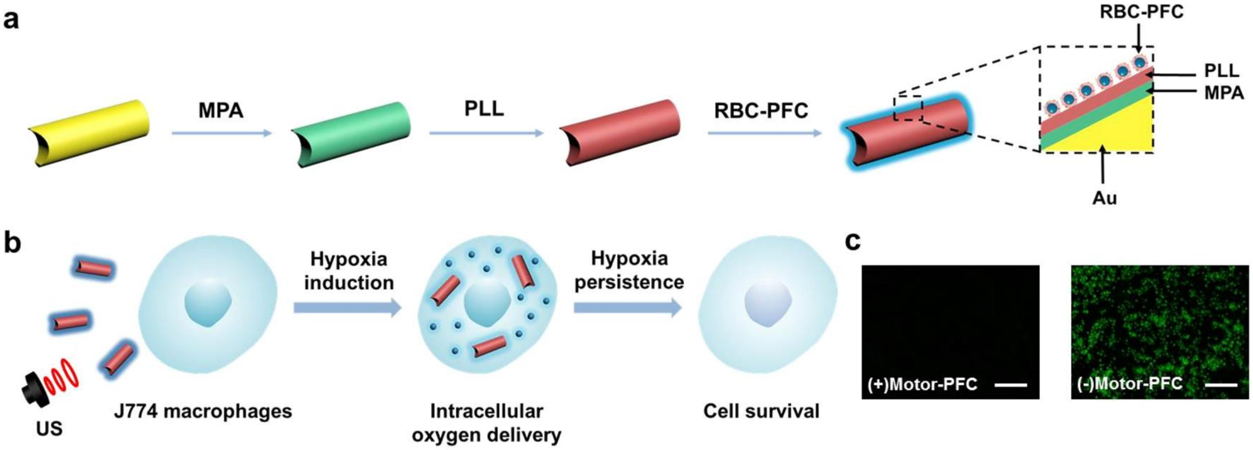

Figure 3.10 Motor-PFC for intracellular oxygen delivery system. a, Loading of RBC-PFC onto a AuNW nanomotor surface (Motor-PFC) along with a schematic dissection of the preparation processes: AuNW is first modifed with 3-mercaptopropionic acid (MPA), followed by coating with a poly-l-lysine (PLL) layer. Preformed RBC-PFC nanoemulsions are then attached onto the outer surface of the motors to prepare Motor-PFC. b, Acoustically assisted intracellular oxygen delivery to J774 macrophages by Motor-PFC, which help cells preserve appropriate oxygen level and maintain viability in hypoxic conditions. c, Intracellular hypoxic stress was indicated by green fluorescence marker, whereas the cells treated by Motor-PFC maintain low hypoxic stress. Scale bars: 100 μm.

The RBC-PFC nanoemulsion formulation is based on the one described earlier with small modifications.[22] The resulting RBC-PFC nanoemulsions have a diameter of ∼170 nm. To gain further insights into the morphology and integrity of the RBC-PFC nanoemulsion, we performed confocal fluorescence imaging of dual-labeled RBC-PFC nanoemulsions (Figure 3.11a). Scanning electron microscopy (SEM) was carried out to characterize the structural morphology of the Motor-PFC. The SEM imaging (Figure 3.11b, left) showed that RBC-PFC was bound onto the structure of a AuNW that was 2 μm in length and 400 nm in diameter. Energy-dispersive X-ray (EDX) spectroscopy mapping analysis was also conducted (Figure 3.11b), confirming the presence of gold (Au), sulfur (S), phosphorus (P), and fluorine (F), corresponding to the nanomotor core, MPA coating, RBC membrane, and PFC, respectively. To further characterize the efficient RBC-PFC immobilization onto the surface of the AuNW nanomotors, the RBC membrane was labeled with the fluorescent dye 1,1'-dioctadecyl-3,3,3',3'-tetramethylindodicarbocyanine (DiD) before immobilization onto the AuNW/MPA/PLL nanomotors. Figure 3.11c shows bright-field, fluorescent (Cy5 channel), and merged images of a group of Motor-PFC (from left to right, respectively). The microscopy images demonstrated the successful immobilization of the DiD-labeled RBC-PFC onto the surface of the AuNW nanomotors. The stepwise surface modification of the AuNW nanomotors was further confirmed by measuring the corresponding zeta potentials (Figure 3.11d). The introduction of the MPA carboxyl layer was confirmed by the change to a more negative zeta potential value (from −10.4 mV to −25.7 mV). The following modifications with the positively charged PLL and negatively charged RBC-PFC layers were also confirmed by the corresponding zeta potential values (18.1 and −30.1 mV, respectively). The zeta potential value obtained from the resulting Motor-PFC was nearly identical to that observed for RBC-PFC alone, used as a positive control. These results were in agreement with a previous study on RBC membrane-coated PFC cores.[22] The loading capability of RBC-PFC on AuNWs was evaluated using different amounts of nanomotors (Figure 3.11e). Samples containing different amounts of nanomotors were incubated with 1 mg/mL of RBC-PFC solution for 1 h, and then the protein content from the RBC membrane was calculated. The results demonstrated a gradual protein increase that correlated with the number of nanomotors, from 0.67 μg to 6.5 μg of protein for AuNW nanomotors at concentrations of 6.5×10^4/mL and 5.2×10^5/mL of, respectively.

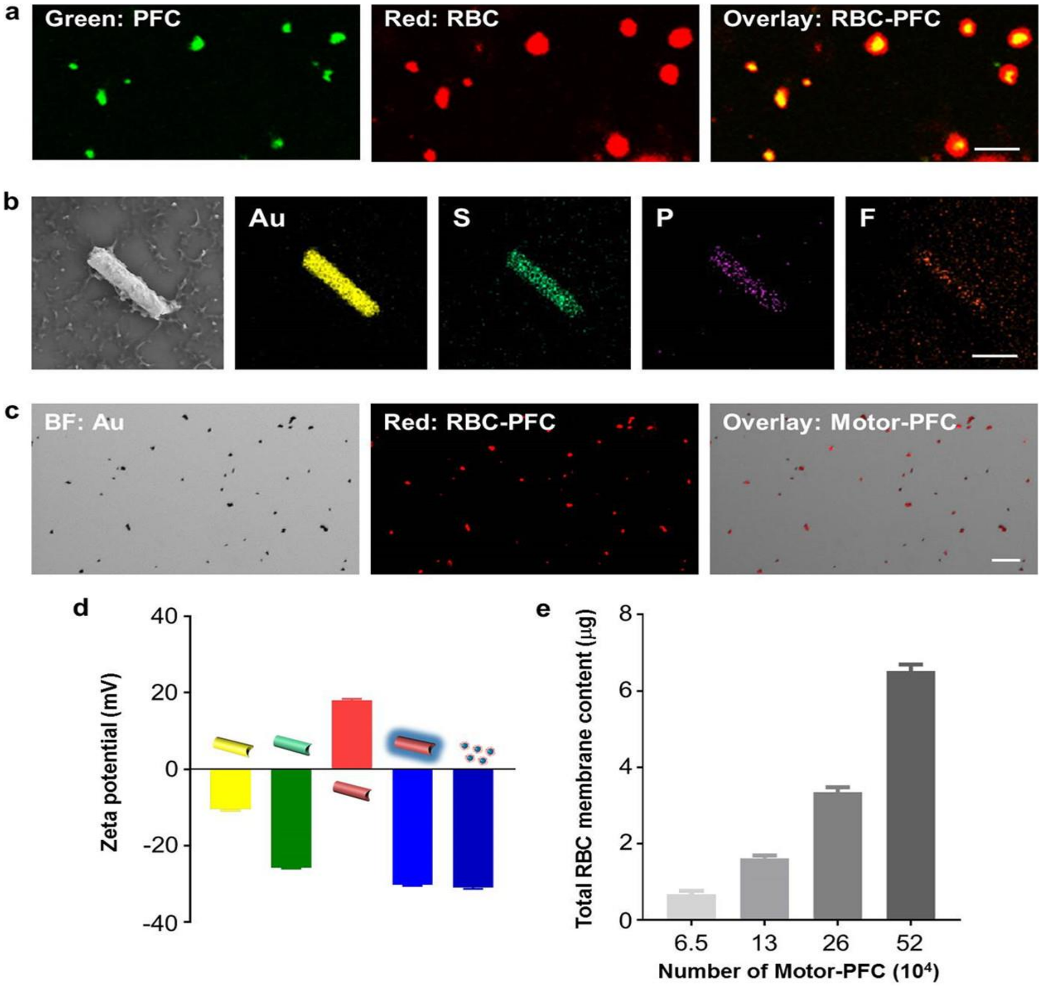

Figure 3.11 Structural characterization of Motor-PFC. a, Confocal fluorescence imaging of dual-labeled RBC-PFC; the RBC membrane was labeled with DiD (red), and the PFC core was labeled with BODIPY (green). Scale bar: 500 nm. b, Scanning electron microscopy (SEM) image of a Motor-PFC and corresponding energy-dispersive X-ray spectroscopy (EDX) analysis showing the distribution of Au (yellow), S (green), P (purple), and F (orange). Scale bar: 1 μm. c, Bright-field, fluorescent, and merged images of a group of Motor-PFC; the RBC membrane was labeled with DiD to help visualization (red). Scale bar: 10 μm. d, Zeta potential of sequential modification of Motor-PFC (from left to right): bare AuNW, MPA-modified AuNW, PLL-modified AuNW, RBC-PFC-bound AuNW, and free RBC-PFC (n = 3, mean ± SD). e, Total RBC content on different numbers of Motor-PFC, measured by lipoprotein content from the RBC membrane (n = 3, mean ± SD).

3.3.3 Propulsion of Motor-PFC

Next, we characterized the propulsion of Motor-PFC in water under an acoustic field. The propulsion performance of the Motor-PFC was compared to that of the unmodified AuNWs (without RBC-PFC) at different ultrasound voltages. The histogram shown in Figure 3.12a displays the increase of the average Motor-PFC speed from 28.5 μm/s at 2 V, to 49.8 μm/s at 4 V, to 73.5 μm/s at 6 V. The bare nanomotors displayed overall higher average speeds (53.0, 77.8, and 107.8 μm/s at 2, 4, and 6 V, respectively). The slight speed decrease observed with the Motor-PFC was attributed to the acoustic streaming change around the nanomotor after binding with the RBC-PFC. In low Reynolds number fluid under an ultrasound field, the motion of the nanomotor is dominated by the Stokes law. (35) The acoustic driving force is equal to the Stokes drag force, which can be calculated from the following equation:

$$F_{driving} = F_{stokes} = \frac{2\pi\eta L U}{\ln\left(\frac{L}{a}\right) - 0.5} \quad (1)$$

where η is the viscosity coefficient, L and a are the length and radius of the Motor-PFC, respectively, and U is the velocity of the motor under ultrasound (6 V, 2.66 Hz). When RBC-PFC attached to the AuNW, the radius of the Motor-PFC increased to about 350 nm compared to 200 nm of the bare motor. Therefore, as expected from eq 1, the speed of the Motor-PFC decreased compared to the bare motor under the same acoustic pressure.

Despite the small effect that the loaded RBC-PFC has on the nanomotor propulsion, the movement of the Motor-PFC provided sufficient thrust for effective penetration through the cell membrane for further internalization and delivery of oxygen molecules, as it will be illustrated below. Figure 3.12b shows representative tracking trajectories of individual Motor-PFC at the different studied voltages within a 1 s interval in water. In accordance with earlier observations, the distance and speed increased dramatically with applied voltage (more than doubling between 2 and 6 V).

The binding stability of the RBC-PFC on the AuNWs after acoustic propulsion was then evaluated (Figure 3c). For this study, DiD-labeled RBC (red) and BODIPY-labeled PFC (green), prepared as in a previous study,[22] were used for nanomotor modification. Microscopic optical and fluorescent images of Motor-PFC before and after applying the acoustic field (top and bottom rows, respectively) were taken. The merged fluorescence images displayed in the top row demonstrate the binding of RBC-PFC onto the AuNW nanomotors (Figure 3.12c top, in orange). The Motor-PFC was then allowed to propel in water for 5 min under an acoustic field (6 V and 2.66 Hz). The fluorescent and overlay images (Figure 3.12c bottom) demonstrate that the RBC-PFC remained stable on the nanomotor surface following acoustic propulsion, verifying the good stability of the system, as desired for its application for intracellular oxygen delivery.

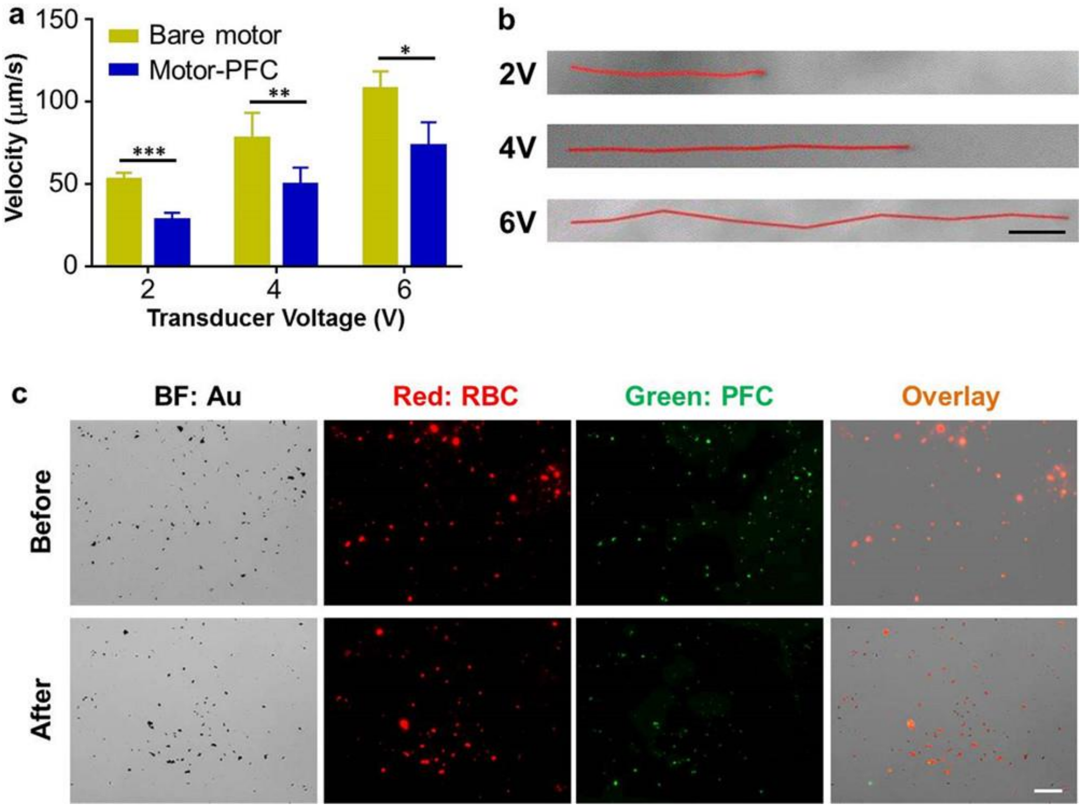

Figure 3.12 Motion behavior characterization of Motor-PFC. a, Comparison of the speed of bare motors and Motor-PFC at different US voltages (2, 4, and 6 V; 2.66 MHz) in water (n = 3, mean ± SD). $*p < 0.05$, $**p < 0.01$, $***p < 0.001$; t test. b, Tracking trajectories of Motor-PFC at different voltages within a 1 s interval in water. Scale bar: 10 μm. c, Verification of the Motor-PFC integrity before (top) and after (bottom) 5 min US propulsion (6 V, 2.66 MHz). The AuNW motor was visualized under bright-field (BF); the RBC membrane was labeled with DiD (red), and the PFC was labeled with BODIPY (green) for fluorescent imaging. Scale bar: 20 μm.

3.3.4 Oxygen delivery kinetics using US-driven Motor-PFC

We further examined the oxygen delivery capacity and kinetics of the Motor-PFC by following our previously reported protocol.[22] Specifically, a volume of water was first deoxygenated by nitrogen purging, and various samples were injected into the closed system. The corresponding dissolved oxygen (DO) levels were monitored over time (Figure 3.13a). We first evaluated the oxygen release profiles in the absence of a US field. Owing to the high oxygen loading capacity of PFC, Motor-PFC presented similar DO kinetics compared with RBC-PFC (1.7 mg/L) when normalized to the same RBC-PFC content (Figure 3.13a, empty red circles versus empty blue triangles). On the basis of this oxygen saturated value, we calculated the total loading capacity of our Motor-PFC to be 0.4 pg/motor. In contrast, bare motors displayed a basal level of oxygen release, which was similar to the regular water control (0.7 mg/L), due to the lack of any oxygen loading (Figure 3.13a, empty purple diamonds). Subsequently, we examined whether the DO kinetics of Motor-PFC could be expedited by applying a US field. Interestingly, the Motor-PFC demonstrated a faster oxygen release pattern under US, reflecting the impact of nanomotor motion in promoting fast mass exchange with the surrounding environment (Figure 3.13a, red circles). Not surprisingly, in the absence of nanomotor propulsion, free RBC-PFC (not bound to AuNWs) exposed to the US field did not display accelerated DO kinetics (Figure 3.13a, full blue triangles). On the other hand, despite the fast propulsion of bare AuNWs under the US field, minimal oxygen release was observed under these conditions due to the absence of the RBC-PFC oxygen reservoir (Figure 3.13a, purple diamonds). We also quantified the time required to reach kinetic equilibrium in each condition (Figure 3.13b). Here, we define equilibrium as the state when the level of dissolved oxygen reaches a plateau with no further increase. Similarly, we define the time to equilibrium as the time taken to reach such a plateau. The US-propelled Motor-PFC reached the kinetic equilibrium within 40 s, while more than 80 s was needed under static conditions. Moreover, we compared the DO levels of each sample in the first 40 s, which clearly demonstrated that Motor-PFC under US showed the highest DO level and the most favorable release profile at each examined time point (Figure 3.13c).

Furthermore, we found that the oxygen delivery profiles could be finely manipulated by adjusting the US voltage, as shown in Figure 3.13d. Specifically, by increasing the applied US voltage, the oxygen could be released into the environment in a faster manner. With the Motor-PFC, it only took 40 s for oxygen levels to reach equilibrium using a 6 V US field, compared to 56 and 72 s for under 4 and 2 V fields, respectively (Figure 3.13e). In terms of DO levels, Motor-PFC under 6 V US outperformed the nanomotor under lower voltages at each time point (Figure 3.13f). Overall, these results highlight the essential roles of the RBC-PFC and the US propulsion in the hybrid nanomotor system, with the RBC-PFC offering high oxygen loading, while the AuNW nanomotors accelerated the oxygen transport and release. Furthermore, these data also demonstrate that the oxygen release rate can be controlled by tuning the US voltage.

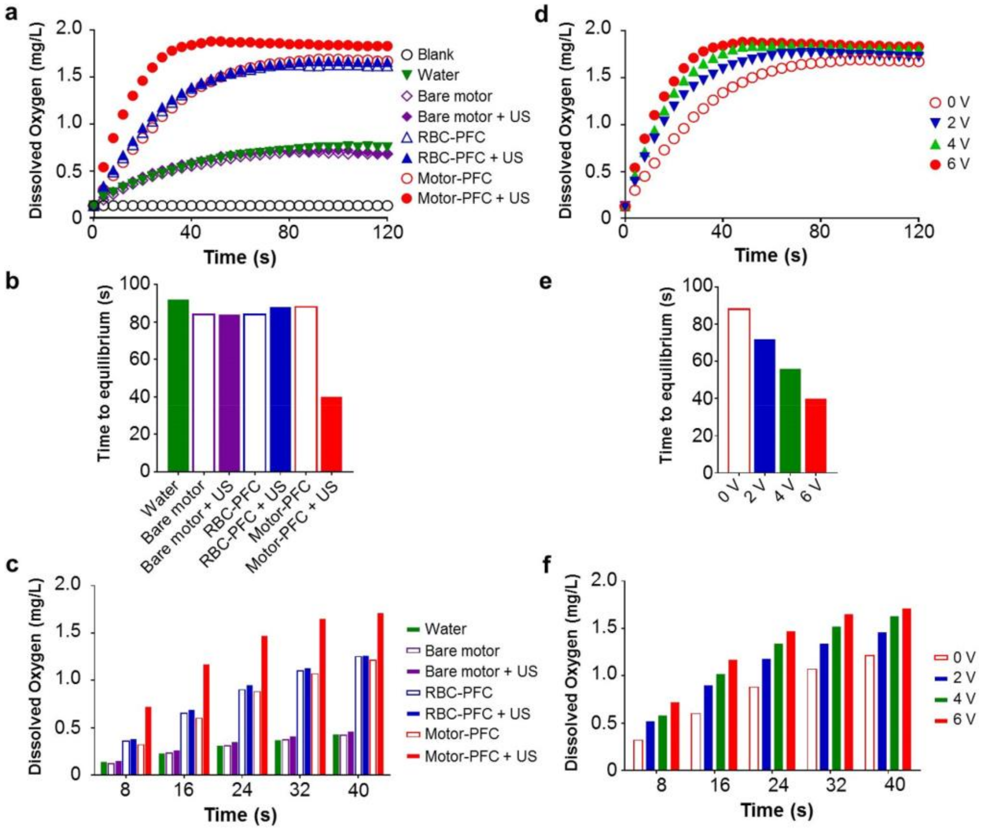

Figure 3.13 Oxygen delivery kinetics of Motor-PFC. a, Dissolved oxygen kinetics after the addition of oxygenated water, bare motor (with or without US), RBC-PFC (with or without US), and Motor-PFC (with or without US) into deoxygenated water. The US field was applied at 6 V. b, Time to reach kinetic equilibrium of each sample indicated in (a). c, Dissolved oxygen levels within the first 40 s of each sample indicated in (a). d, Dissolved kinetics after the addition of Motor-PFC into deoxygenated water at different US voltages. e, Time to reach kinetic equilibrium of each sample indicated in (d) at different US voltages. f, Dissolved oxygen levels within the first 40 s of each sample indicated in (d) at different US voltages. A constant US frequency of 2.66 MHz was used in all experiments.

3.3.5 US-driven Motor-PFC for intracellular oxygen delivery

After validating the oxygen delivery capability of Motor-PFC bestowed by the synergistic effects of both components (RBC-PFC and US-propelled AuNW), we assessed the ability of this dynamic nanomotor system for intracellular oxygen delivery into hypoxic cells. Murine J774 macrophages were selected for this study due to their ability to be cultured in suspension, which helps to increase motor–cell contacts and facilitate penetration by US-powered Motor-PFC through the cell membrane and subsequent intracellular oxygen delivery. More importantly, macrophages have high sensitivity to oxygen and a prompt response to hypoxia, which has been well characterized by their significant biological functions against inflammation and relationships with tumor growth.[41,42] In the present experimental setup, the Motor-PFC was first brought to a levitation plane by the acoustic radiation force exerted on the nanowire motor.[43] After levitation, the local acoustic streaming effects arising from the shape asymmetric property of AuNWs can lead to the small amplitude oscillation in a standing wave, which is translated into motion of the Motor-PFC in a direction perpendicular to the acoustic wave.[44] The motion of the Motor-PFC provides thrust toward the cell, and the driving force contributes to the active macrophage penetration and internalization.

First, we evaluated the US-driven intracellular oxygen delivery to cells under hypoxic conditions (Figure 3.14). Specifically, J774 cells were suspended at 4 million cells/mL, followed by the addition of the Motor-PFC. Then, the cell/nanomotor suspension was exposed to the US field for 5 min. During the treatment, the ultrasound field provided energy for the Motor-PFC propulsion, generating the force beneficial for cell poration. The driving force of the US-powered Motor-PFC can be estimated to be around 2.1pN based on eq 1. After the application of the US field, we tested the viability of the motor-treated cells by a cell proliferation assay and compared it to that of the untreated cells over a given time period, observing minimal difference between the two groups (data not shown). The cells were washed extensively to remove all unbound nanomotors, leaving only the internalized nanomotors for analysis. The ultimate proof for the effective penetration through the cell membrane and subsequent internalization of Motor-PFC into J774 cells has been demonstrated by optical imaging (Figure 3.14a). For example, the optical image on the left shows clearly that the US-propulsion greatly enhances the Motor-PFC penetration and internalization into J774 cells, as indicated from the presence of several Motor-PFC within the cell. The image was taken right after performing the ultrasound treatment for 5 min. In contrast, no nanomotors were found in J774 cells treated with the same motors but in the absence of ultrasound (Figure 3.14a right panel), as expected from the short treatment time (5 min).

The cells were then cultured under hypoxic conditions for varying amounts of time (i.e., 24, 48, 72 h), and the effects on cell viability were assessed by an MTS cell viability assay. Notably, the active Motor-PFC was capable of preserving cell viability even after long periods of hypoxia induction, with near 85% cell recovery throughout the study (Figure 3.14b, red line). In contrast, only ∼30–40% cell recovery was observed over a 72 h period for all control groups, including the RBC-PFC under US (i.e., without the AuNW carrier). We attributed the benefits (85% cell recovery) of the US-driven Motor-PFC system to the sustained oxygen release from the internalized nanomotors. Under hypoxic conditions, the nanomotors localizing in the cytoplasm could release sufficient oxygen to mitigate the negative effects. In contrast, without applying the US field, most of the Motor-PFC in suspension would be removed, leading to an inability to maintain the cell viability. In contrast, RBC-PFC is not able to achieve such restoration efficiency since it could not effectively penetrate the plasma membrane. Only a small portion of RBC-PFC was attached to the cells during the US treatment, resulting in slightly improved cell viability. Although bare motors could penetrate the cell plasma membrane, they lacked RBC-PFC and oxygen delivery capacity. The intracellular oxygen delivery efficiency to hypoxic cells was also visualized fluorescently by staining the cells with a commercial detection reagent (Figure 3.14c).

In general, significant fluorescent signals were observed in cells subjected to hypoxia over time, and only the intracellular oxygen delivery by US-driven Motor-PFC resulted in the absence of this signal. The two data sets do show good correlation: whereas cells without any treatment present most hypoxic stress and lower cell survival, the Motor-PFC-treated cells demonstrate minimum hypoxic stress and best survival. Thus, the relief of hypoxia should be the main reason for the significantly higher viability of the cells treated by Motor-PFC under US, highlighting again the significant role of the active oxygen delivery capability of the Motor-PFC. Finally, we evaluated the impact of Motor-PFC concentration on the protective effects of the formulation (Figure 3.14d). At the highest concentration tested, minimal reduction in cell viability was observed. Fluorescence microscopy measuring hypoxia levels matched well with the cell viability data (Figure 3.14e). It is noteworthy that the intracellular delivery efficiency could be further optimized by increasing the loading of RBC-PFC onto the AuNWs or by adding more Motor-PFC to the cell suspension.

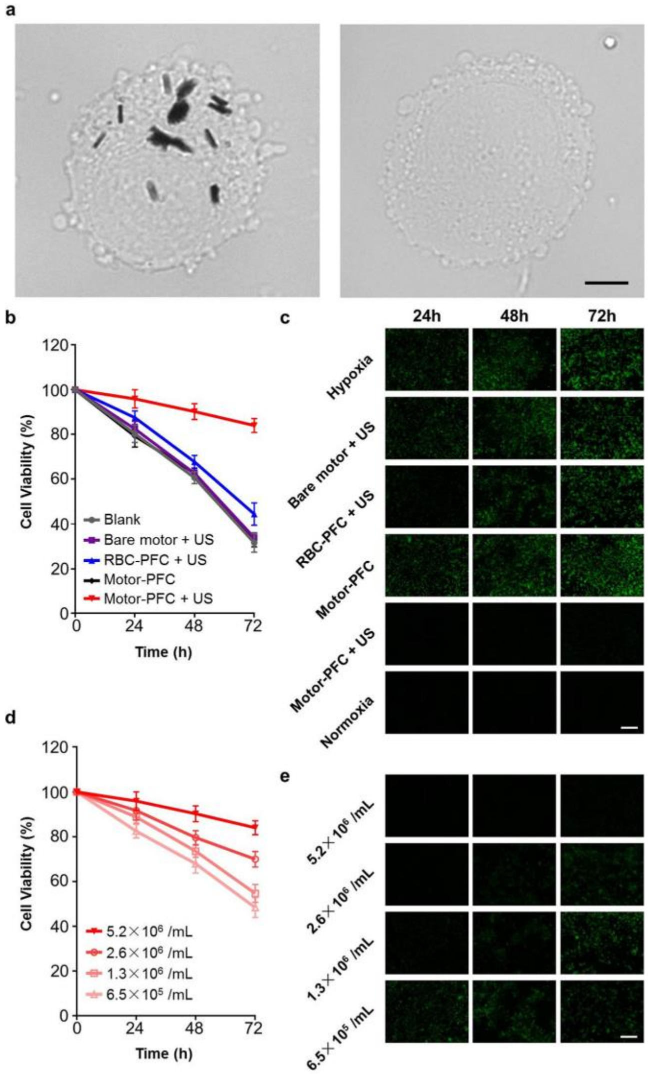

Figure 3.14 Intracellular oxygen delivery using acoustically propelled Motor-PFC. a, Motor-PFC internalization into J774 cells treated with 5 min of US (left) or without US (right); cells imaged under optical microscope. Scale bar: 5 μm. b, Viability of J774 cells after incubation with different treatment conditions and then being subjected to hypoxia. Cells were incubated under hypoxic conditions for 24, 48, or 72 h and then normalized to corresponding viability in normoxia (n = 4, mean ± SD). c, Fluorescence microscopy of J774 cells after incubation with different treatment conditions and then being subjected to hypoxia. Cells were labeled with Image-iT Green hypoxia reagent (green) for visualization. Images were taken at 24, 48, and 72 h. Scale bar, 100 μm. d, Viability of J774 cells after incubation with Motor-PFC at different input concentrations and then being subjected to hypoxia. Cells were incubated under hypoxic conditions for 24, 48, or 72 h and then normalized to corresponding viability in normoxia (n = 4, mean ± SD). e, Fluorescence microscopy of J774 cells after incubation with Motor-PFC at different input concentrations and then being subjected to hypoxia. Cells were labeled with Image-iT Green hypoxia reagent (green) for visualization. Images were taken at 24, 48, and 72 h. Scale bar: 100 μm.

3.3.6 Discussion

We have presented an effective method to actively deliver oxygen inside living cells using US-propelled nanomotors modified with biomimetic RBC-PFC nanoemulsions. The RBC-PFC, possessing a high oxygen loading capacity, was readily functionalized onto the nanomotor surface without affecting the acoustic propulsion. Oxygen release kinetic studies indicated that the US-driven Motor-PFC formulation could release oxygen significantly faster compared to other controls (i.e., same Motor-PFC under static conditions). The oxygen release rate could also be tuned by adjusting the ultrasound intensity. We also confirmed that the combination of synthetic AuNW nanomotors with oxygen-carrying RBC-PFC nanoemulsions enabled direct and efficient intracellular oxygen delivery inside J774 macrophage cells, which significantly improved cell viability. Notably, the Motor-PFC could penetrate through the cell membrane and deliver oxygen into cells under hypoxia, maintaining 85% cell viability after 72 h, compared to 45% with free RBC-PFC and 30% with their static counterparts. Such motor-based oxygen delivery could also be used to target other cell types, such as tumor cells for therapeutic purposes such as photodynamic therapy and cardiac muscle cells for myocardial oxygen consumption. While this nanomotor-based intracellular delivery platform is still in its early stage and future system optimization is needed before leveraging this delivery strategy into clinical settings, this proof-of-concept work clearly demonstrates the advantages of the nanomotor-based system for in vitro intracellular oxygen delivery. Future studies will aim at optimizing this nanomotor-based oxygen delivery system toward application at local hypoxic tissue sites. Meanwhile, these findings demonstrate that Motor-PFC can act as a powerful oxygen delivery vehicle with considerable promise for future therapeutic applications. While oxygen was selected here as a model gas molecule, we anticipate that this work will encourage the nanomotor-based dynamic intracellular delivery of other therapeutic gas molecules toward diverse biomedical applications. By reducing the size of the AuNW motors, switching to other biocompatible motor systems, or discovering alternative active delivery mechanisms, we envision it is possible to design advanced motor systems for oxygen delivery in more practical scenarios.

3.3.7 Experimental section

Reagents and Materials. Polycarbonate (PC) membranes (400 nm pore size) were supplied from Whatman (cat. No.110407). Gold- and silver-plating solutions (Orotemp 24 RTU RACK and 1025 RTU at 4.5 Troy/gallon) were purchased from Technic Inc. (Anaheim, CA, USA). 3-Mercaptopropionic acid, poly-l-lysine, and PFC (perfluorooctyl bromide) were purchased from Sigma-Aldrich. Methylene chloride (HPLC grade) was obtained from Fisher Scientific. Human O-positive RBCs were obtained from the San Diego Blood Bank. DiD and Image-iT Green hypoxia reagent were obtained from Invitrogen. BODIPY PFC staining dye was synthesized using a previously reported approach.[45] J774 macrophages (TIB-67; American Type Culture Collection) were maintained in Dulbecco's modified Eagle medium (DMEM, HyClone) supplemented with 10% fetal bovine serum (HyClone) and 1% penicillin–streptomycin (Gibco). CellTiter AQueous One Solution cell proliferation assay was obtained from Promega.

Preparation of AuNW Nanomotor. The AuNW nanomotors were fabricated by a template-assisted electrodeposition method. A 400 nm diameter porous PC membrane was first sputtered with a thin layer of gold. The membrane was then assembled in a Teflon plating cell and served as a working electrode using aluminum foil as an electrical contact for subsequent electrodeposition. A thin sacrificial silver layer was initially electrodeposited into the PC membrane using a charge of 0.1 C and a potential of −0.9 V (versus Ag/AgCl reference electrode and a Pt wire as a counter electrode). Then, Au was electroplated using a gold plating solution at −1 V (versus Ag/AgCl) with a charge of 2 C. The sputtered gold layer was removed by mechanical polishing with cotton tip applicators soaked with 3–4 μm aluminate powder. The silver sacrificial layer was then removed by a quick chemical etching using an 8 M HNO3 solution. The removal of this sacrificial layer helped to form the concave shape in one end of the AuNW. Subsequently, the membrane was dissolved in a pure methylene chloride solution for 30 min under vigorous shaking for complete release of the AuNWs. The resulting nanomotors were separated from the solution by centrifugation at 4600g for 3 min and washed twice with isopropanol, ethanol, and ultrapure water. Between each step, the nanomotor was mixed with the desired solvent and briefly sonicated to ensure the complete dispersion in the solvent. All AuNWs were stored in 1 mL of ultrapure water at room temperature until use.

Preparation of RBC-PFC. RBC-PFC was prepared following a previously reported method. (22) Specifically, RBC membrane ghosts were obtained by hypotonic lysis. The RBC membrane was suspended at a final protein concentration of 2 mg/mL. To prepare RBC-PFC, 50 μL of the PFC was mixed with 2 mL of RBC membrane solution, followed by emulsification on ice using a Fisher Scientific 150E Digital Sonic Dismembrator for 2 min with an on/off interval of 2 s/1 s. The resulting RBC-PFC was centrifuged at 600g for 5 min to remove the excess membrane vesicles, followed by resuspension in 1 mL of water. For fluorescent imaging of the RBC-PFC, dual-labeled samples were immobilized on glass slides with Tissue-Tek OCT compound (Sakura Finetek) and visualized using an Olympus FV1000 confocal microscope.

Preparation of Motor-PFC. Motor-PFC were prepared by the immobilization of the RBC-PFC onto the surface of AuNWs. First, 100 µL of AuNWs were mixed with 5 µL of 11.5 M MPA solution and kept stirring overnight to successfully form the self-assembled monolayer on the nanomotor surface. The resulting MPA-AuNWs were washed twice with ultrapure water and then incubated with 100 µL of a 0.01% PLL solution for 2 h under vigorous shaking, aiming to obtain a positively charged PLL coating on the AuNWs. Finally, the resulting PLL-AuNWs were incubated with 100 µL of RBC-PFC at 37 °C for 1 h to obtain Motor-PFC. The nanomotors were washed with ultrapure water between each modification step (centrifuging at 4600g for 3 min).

Characterization of Motor-PFC. A SEM image of Motor-PFC was obtained with a Zeiss Sigma 500 scanning electron microscope instrument using an acceleration voltage of 10 kV. EDX mapping analysis was performed using an Oxford EDX detector attached to a SEM instrument and operated by Pathfinder software. Bright-field and fluorescent images of Motor-PFC modified with BODIPY-labeled PFC and DiD-labeled RBC membrane were captured using an EVOS FL microscope. Zeta potential measurements were conducted by a Malvern Instruments Zetasizer Nano ZS. The RBC-PFC loading was determined by a Pierce BCA protein assay kit (Thermo Scientific).

Ultrasound Equipment and Propulsion Studies. The acoustic cell setup consisted of a piezoelectric transducer (Ferroperm PZ26 disk 10 mm diameter, 0.5 mm thickness) responsible for the generation of ultrasound waves, attached by conductive epoxy glue to the bottom center of a steel plate (50 × 50 × 0.94 mm3); then the steel plate was covered with a 240 µm Kapton tape protective layer with a sample reservoir at the center (5 mm). A glass slide was used to cover the reservoir for ultrasound reflection and to protect the sample. A continuous ultrasound sine wave was applied via a piezoelectric transducer, through an Agilent 15 MHz arbitrary waveform generator, connected to a homemade power amplifier. All propulsion experiments were conducted by applying a continuous sine waveform that had a frequency of 2.66 MHz and an amplitude of 2.0, 4.0, or 6.0 V (voltage at the output of the function generator). Videos were captured using a Cool SNAP HQ2 camera, with 20× and 40× objectives and acquired at 10 frames per second using the Metamorph 7.1 software (Molecular Devices, Sunnyvale, CA, USA). The particle displacement image stacking was performed using ImageJ software and Flow Trace Plugin.

Dissolved Oxygen Kinetics. A measurement apparatus was built by a 20 mL glass vial with a foam cap, which was sealed in place using Parafilm (Bemis). Three holes were cut into the foam cap in order to accommodate with a syringe for nanomotor injection, an oxygen probe, and a plastic pipet for degassing. An acoustic cell setup was attached by conductive epoxy glue to the bottom center of the glass vial. Before the start of each experiment, 1 mL of water was added to the vial, and purged with nitrogen to remove dissolved oxygen. When the dissolved oxygen meter was stable, 1 mL of Motor-PFC was injected into the bottom of the vial under ultrasound with a frequency of 2.66 MHz and an amplitude of 6.0 V. The control experiment (RBC-PFC or bare motor) with ultrasound was conducted under the same conditions as the Motor-PFC with normalized concentration. The static controls, oxygen release of Motor-PFC, RBC-PFC, bare motor, and water without ultrasound were employed in the same conditions. Intensity-dependent oxygen release of Motor-PFC was conducted at various amplitudes (2.0, 4.0, and 6.0 V; keeping the frequency constant at 2.66 MHz).

Intracellular Oxygen Delivery. J774 cells cultured in suspension (2.5 μL, containing ∼10 000 cells) were treated with Motor-PFC (2.5 μL, 1.3×10^4 motors) during 5 min in the ultrasound setup

(6 V, 2.66 MHz, 5 min). The 5 min treatment time was chosen based on previous reports. (38) In order to obtain enough cells for the following studies, the US treatment was repeated multiple times (20 times) for every control experiment, and the treated cells were combined at the very end. The resulting cell–nanomotor suspension (∼100 μL) was collected in an Eppendorf tube. After leaving undisturbed for 5 min at room temperature, the unbound Motor-PFC was removed and the settled cells were resuspended in 100 μL of DMEM medium. An EVOS FL microscope with a 100× oil objective lens was used to image the motor internalization to the cells. A 5 μL amount of cells was transferred to the well of a 96-well plate containing 95 μL of culturing medium. The cells were then incubated under hypoxic conditions (1% O2/5% CO2/94% N2) in a Thermo Scientific Forma Series 3 WJ incubator. Cells were examined at certain time points (i.e., 24, 48, 72 h) by a cell viability assay and hypoxia imaging. Specifically, cell viability was quantified using a CellTiter AQueous One Solution cell proliferation assay (Promega) following the manufacturer's instructions, and cells were stained by Image-iT Green hypoxia reagent and imaged using an EVOS FL microscope. Normoxic control cells were incubated under normoxic conditions (20% O2/5% CO2/75% N2) in a Thermo Scientific Heracell 150i incubator. For static control of Motor-PFC, the ultrasound treatment was omitted.

Chapter 3.3, in full, is a reprint of the material as it appears in ACS Nano, 2019, by Fangyu Zhang, Jia. Zhuang, Berta Esteban-Fernández de Ávila, Songsong Tang, Qiangzhe Zhang, Ronnie H. Fang, Liangfang Zhang, Joseph Wang. The dissertation author was the primary investigator and author of this paper.

3.3.8 References

1. Wang, R. Gasotransmitters: Growing Pains and Joys. *Trends Biochem. Sci.* 39, 227−232 (2014).

2. Carpenter, A. W.; Schoenfisch, M. H. Nitric Oxide Release: Part II. Therapeutic Applications. *Chem. Soc. Rev.* 41, 3742−3752 (2012).

3. Motterlini, R.; Otterbein, L. E. The Therapeutic Potential of Carbon Monoxide. *Nat. Rev. Drug Discovery* 9, 728−743 (2010).

4. García-Gallego, S.; Bernardes, G. J. L. Carbon-Monoxide-Releasing Molecules for the Delivery of Therapeutic CO In Vivo. *Angew. Chem., Int. Ed.* 53, 9712−9721 (2014).

5. Cooper, C. E.; Brown, G. C. The Inhibition of Mitochondrial Cytochrome Oxidase by The Gases Carbon Monoxide, Nitric Oxide, Hydrogen Cyanide and Hydrogen Sulfide: Chemical Mechanism and Physiological Significance. *J. Bioenerg. Biomembr.* 40, 533−539 (2008).

6. Ohsawa, I.; Ishikawa, M.; Takahashi, K.; Watanabe, M.; Nishimaki, K.; Yamagata, K.; Katsura, K.-i.; Katayama, Y.; Asoh, S.; Ohta, S. Hydrogen Acts as A Therapeutic Antioxidant by Selectively Reducing Cytotoxic Oxygen Radicals. *Nat. Med.* 13, 688−694 (2007).

7. Andreadou, I.; Iliodromitis, E. K.; Rassaf, T.; Schulz, R.; Papapetropoulos, A.; Ferdinandy, P. The Role of Gasotransmitters NO, H2S and CO in Myocardial Ischaemia/Reperfusion Injury and Cardioprotection by Preconditioning, Postconditioning and Remote Conditioning. *Br. J. Pharmacol.* 172, 1587−1606 (2015).

8. Shefa, U.; Yeo, S. G.; Kim, M.-S.; Song, I. O.; Jung, J.; Jeong, N. Y.; Huh, Y. Role of Gasotransmitters in Oxidative Stresses, Neuroinflammation, and Neuronal Repair. *BioMed Res. Int.* 2017, 1−15 (2017).

9. Zoccali, C.; Catalano, C.; Rastelli, S. Blood Pressure Control: Hydrogen Sulfide, A New Gasotransmitter, Takes Stage. *Nephrol. Dial. Transplant.* 24, 1394−1396 (2009).

10. Shatalin, K.; Shatalina, E.; Mironov, A.; Nudler, E. H2S: A Universal Defense Against Antibiotics in Bacteria. *Science* 334, 986−990 (2011).

11. Owen, J.; McEwan, C.; Nesbitt, H.; Bovornchutichai, P.; Averre, R.; Borden, M.; McHale, A. P.; Callan, J. F.; Stride, E. Reducing Tumour Hypoxia via Oral Administration of Oxygen Nanobubbles. *PLoS One* 11, No. e0168088 (2016).

12. Harris, A. L. Hypoxia --- A Key Regulatory Factor in Tumour Growth. *Nat. Rev. Cancer* 2, 38−47 (2002).

13. Vincent, J.-L.; De Backer, D. Oxygen Transport --- The Oxygen Delivery Controversy. *Intensive Care Med.* 30, 1990−1996 (2004).

14. Beliën, J.; Forcé, H. Supply Chain Management of Blood Products: A Literature Review. Eur. *J. Oper. Res.* 217, 1−16 (2012).

15. Buehler, P. W.; D'Agnillo, F.; Schaer, D. J. Hemoglobin-Based Oxygen Carriers: from Mechanisms of Toxicity and Clearance to Rational Drug Design. *Trends Mol. Med.* 16, 447−457 (2010).

16. Castro, C. I.; Briceno, J. C. Perfluorocarbon-Based Oxygen Carriers: Review of Products and Trials. *Artif. Organs* 34, 622−634 (2010).

17. Riess, J. G. Oxygen Carriers ("Blood Substitutes") Raison d'Etre, Chemistry, and Some Physiology Blut ist ein ganz besondrer Saft. *Chem. Rev.* 101, 2797−2920. (2001).

18. Winslow, R. M. Blood Substitutes. *Adv. Drug Delivery Rev.* 40, 131−142 (2000).

19. Riess, J. G. Perfluorocarbon-Based Oxygen Delivery. Artif. Cells Blood Substit. *Biotechnol* 34, 567−580 (2006).

20. Lowe, K. C. Engineering Blood: Synthetic Substitutes from Fluorinated Compounds. *Tissue Eng.* 9, 389−399 (2003).
21. Riess, J. G. Understanding The Fundamentals of Perfluorocarbons and Perfluorocarbon Emulsions Relevant to In Vivo Oxygen Delivery. *Artif. Cells Blood Substit. Biotechnol.* 33, 47−63 (2005).

22. Zhuang, J.; Ying, M.; Spiekermann, K.; Holay, M.; Zhang, Y.; Chen, F.; Gong, H.; Lee, J. H.; Gao, W.; Fang, R. H.; Zhang, L. Biomimetic Nanoemulsions for Oxygen Delivery In Vivo. *Adv. Mater.* 30, 1804693 (2018).

23. Wang, J. Nanomachines: Fundamentals and Applications; Wiley- VCH: Weinheim, Germany, (2013).

24. Wang, H.; Pumera, M. Emerging Materials for The Fabrication of Micro/Nanomotors. *Nanoscale* 9, 2109−2116 (2017).

25. Chen, X.-Z.; Hoop, M.; Mushtaq, F.; Siringil, E.; Hu, C.; Nelson, B. J.; Pané, S. Recent Developments in Magnetically Driven Micro- and Nanorobots. *Appl. Mater. Today* 9, 37−48 (2017).

26. Li, J.; Esteban-Fernández de Ávila, B.; Gao, W.; Zhang, L.; Wang, J. Micro/Nanorobots for Biomedicine: Delivery, Surgery, Sensing, and Detoxification. *Sci. Robot.* 2, eaam6431 (2017).

27. Gao, W.; de Ávila, B. E.-F.; Zhang, L.; Wang, J. Targeting and Isolation of Cancer Cells Using Micro/Nanomotors. *Adv. Drug Delivery Rev.* 125, 94−101 (2018).

28. Esteban-Fernández de Ávila, B.; Angsantikul, P.; Li, J.; Gao, W.; Zhang, L.; Wang, J. Micromotors Go In Vivo: From Test Tubes to Live Animals. *Adv. Funct. Mater.* 28, 1705640 (2018).

29. Chałupniak, A.; Morales-Narváez, E.; Merkoçi, A. Micro and Nanomotors in Diagnostics. *Adv. Drug Delivery Rev.* 95, 104−116 (2015).

30. Hortelão, A. C.; Carrascosa, R.; Murillo-Cremaes, N.; Patiño, T.; Sánchez, S. Targeting 3D Bladder Cancer Spheroids with Urease- Powered Nanomotors. *ACS Nano* 13, 429−439 (2019).

31. Wang, H.; Pumera, M. Micro/Nanomachines and Living Biosystems: From Simple Interactions to Microcyborgs. *Adv. Funct. Mater.* 28, 1705421 (2018).

32. Xu, T.; Xu, L.-P.; Zhang, X. Ultrasound Propulsion of Micro-/Nanomotors. *Appl. Mater. Today* 9, 493−503 (2017).

33. Campuzano, S.; Esteban-Fernández de Ávila, B.; Yáñez-Sedeño,P.; Pingarrón, J. M.; Wang, J. Nano/Microvehicles for Efficient Delivery and (Bio)Sensing at the Cellular Level. *Chem. Sci.* 8, 6750−6763 (2017).

34. Wang, W.; Li, S.; Mair, L.; Ahmed, S.; Huang, T. J.; Mallouk, T. E. Acoustic Propulsion of Nanorod Motors Inside Living Cells. *Angew. Chem., Int. Ed.* 53, 3201−3204 (2014).

35. Wang, W.; Castro, L. A.; Hoyos, M.; Mallouk, T. E. Autonomous Motion of Metallic Microrods Propelled by Ultrasound. *ACS Nano* 6, 6122−6132 (2012).

36. Ahmed, S.; Wang, W.; Bai, L.; Gentekos, D. T.; Hoyos, M.; Mallouk, T. E. Density and Shape Effects in the Acoustic Propulsion of Bimetallic Nanorod Motors. *ACS Nano* 10, 4763−4769 (2016).

37. Esteban-Fernández de Ávila, B.; Ramírez-Herrera, D. E.; Campuzano, S.; Angsantikul, P.; Zhang, L.; Wang, J. Nanomotor- Enabled pH-Responsive Intracellular Delivery of Caspase-3: Toward Rapid Cell Apoptosis. *ACS Nano* 11, 5367−5374 (2017).

38. Hansen-Bruhn, M.; de Ávila, B. E.-F.; Beltrán-Gastélum, M.; Zhao, J.; Ramírez-Herrera, D. E.; Angsantikul, P.; Vesterager Gothelf, K.; Zhang, L.; Wang, J. Active Intracellular Delivery of a Cas9/sgRNA Complex Using Ultrasound-Propelled Nanomotors. *Angew. Chem., Int. Ed.* 57, 2657−2661 (2018).

39. Esteban-Fernández de Ávila, B.; Martín, A.; Soto, F.; Lopez- Ramirez, M. A.; Campuzano, S.; Vásquez-Machado, G. M.; Gao, W.; Zhang, L.; Wang, J. Single Cell Real-Time miRNAs Sensing Based on Nanomotors. *ACS Nano* 9, 6756−6764 (2015).

40. Esteban-Fernández de Ávila, B.; Angell, C.; Soto, F.; Lopez- Ramirez, M. A.; Báez, D. F.; Xie, S.; Wang, J.; Chen, Y. Acoustically Propelled Nanomotors for Intracellular siRNA Delivery. *ACS Nano* 10, 4997−5005 (2016).

41. Egners, A.; Erdem, M.; Cramer, T. The Response of Macrophages and Neutrophils to Hypoxia in the Context of Cancer and Other Inflammatory Diseases. *Mediators Inflammation* 2016, 2053646 (2016).

42. Henze, A.-T.; Mazzone, M. The Impact of Hypoxia on Tumor- Associated Macrophages. *J. Clin. Invest.* 126, 3672−3679 (2016).

43. Doinikov, A. A. Acoustic Radiation Pressure on A Rigid Sphere in A Viscous Fluid. *Proc. R. Soc. London, Ser.* A 447, 447−466 (1994).

44. Nadal, F.; Lauga, E. Asymmetric Steady Streaming as A Mechanism for Acoustic Propulsion of Rigid Bodies. *Phys. Fluids* 26, 082001 (2014).

45. Laudien, J.; Naglav, D.; Groβ-Heitfeld, C.; Ferenz, K. B.; de Groot, H.; Mayer, C.; Schulz, S.; Schnepf, A.; Kirsch, M. Perfluorodecalin-Soluble Fluorescent Dyes for The Monitoring of Circulating Nanocapsules with Intravital Fluorescence Microscopy. *J. Microencapsulation* 31, 738−745 (2014).

CHAPTER 4. SUMMARY AND PERSPECTIVES

4.1 Summary

The purpose of this dissertation was to demonstrate some of the unique capabilities and applications of cell-based autonomously propelled microrobots. The following are the dissertation's major accomplishments:

(1) Design and fabrication of versatile surface functionalized algae-based biohybrid microrobots for biomedical and environmental applications. In the first example, antibiotic-loaded cell membrane-coated polymeric nanoparticle were functionalized to the surface of algae via click chemistry for the formation of biohybrid microrobots. In a mouse model of acute *Pseudomonas aeruginosa* pneumonia, the algae robots are capable of delivering antibiotics to deep lungs, reducing the bacteria burden and substantially lessening animal mortality, with negligible toxicity. The distinct advantages of microrobots for acute pneumonia treatment are mainly attributed to the self-propulsion of algae in the local environment where they can escape the alveolar macrophage engulfment and prolong the action of the drug. In the second example, living algae-based microrobots were encapsulated in a protective oral capsule for gastrointestinal tract drug delivery. When orally administered in vivo into mice, the algae robots substantially improved GI distribution of the dye payload compared with traditional magnesium-based micromotors, which are limited by short propulsion lifetimes, and they also enhanced retention of a model chemotherapeutic payload in the GI tract compared with a passive nanoparticle formulation. In the third example, the algae-based microrobot is fabricated by using click chemistry to functionalize microalgae with angiotensin-converting enzyme 2 (ACE2) receptor against the SARS-CoV-2

spike protein. The movement of the ACE2 receptor functionalized algae-robot offers effective “on-the-fly” removal of SARS-CoV-2 spike proteins and SARS-CoV-2 pseudovirus.

(2) Selection of appropriate microorganisms with good motility, long lifetime, and adaptability in low pH for construction of biohybrid microrobots and use for application in extremely acidic conditions. We used acidophilic algae for its ability to swim in acidic conditions capability at pH down to 1.5 and further demonstrated the creation of biohybrid microrobots by loading different synthetic nanoparticles for practical biomedical application. By tuning the surface properties of cargos, it is possible to modulate their precise gastrointestinal localization.

(3) Integration of blood cells and cell components with synthetic actuation materials for the development of cell-based microrobots with effective propulsion in versatile biofluid and specific biomedical operations. For example, utilizing the efficient propulsion of magnesium microrobots in biofluid, the macrophage-magnesium hybrid microrobots can achieve high endotoxin removal compared to the static cell counterparts. Applying the enzyme conversion in physiological surroundings, urease linked platelet can yield enhanced motion and improved capabilities for anti-bacteria and anti-cancer treatment. Taking advantage of fast movement and cell membrane penetration ability of gold nanowire microrobots under ultrasound, red blood cell membrane coated oxygen-loaded PFCs which are modified to the gold nanowire surface can realize intracellular oxygen delivery in vitro.

4.2 Perspectives

During the past decade, microrobotic research has been based on the principle of simplicity in design, powering, and fabrication of autonomous robotic systems. This choice in the design was required, as typical macroscale robotic strategies present a particular challenge to adapt to small scales. Looking forward, research should transition away from the current standards of microrobots based on simple geometries (spheres, wires, and hollow tubes) and rigid homogeneous materials into modular designs embedded with hybrid and soft material compositions. The microrobots will not only be built from building blocks present in the environment or transported by them, but they will also be able to do this collectively by communicating and even joining together to form complex assemblies. Additionally, sensing can happen by a mechanical signal due to a gripper or soft and deformable extensions. Loading and unloading cargo is of great importance for any task driven microrobot. Being able to communicate to a microscopic robot which cargo to pick up, navigate and drop it off at a targeted location with high temporal accuracy is crucial for the future. Now that our ideal microrobot can move and sense its environment, it is important to make sure it can communicate and cooperate with its fellow active partners. Again, whether through chemical cues or electromagnetic/sound wave interactions, microscopic robots can “talk” to each other in a variety of ways to form simple swarms or change their behavior to perform specific tasks that a single microrobot cannot do. Integrating smart materials gradients in the microrobot composition and design could introduce time delay and dynamic behavior that induce oscillating behaviors. Finally, we envision these structures will get closer and closer to their living analogues. Thus, we see that putting on-board synthesis micro factories as an absolute necessity. Then, our micro/nanorobots could process fuels or reagents into useful molecules and more building blocks, whether making in situ adhesive, such as mollusks or DNA kill sequences, to just name a few. With such complex synthesis and assembly capabilities microrobots might become closer to animal counterparts with different parent and child types of microrobots or even one generation releasing another or even making replicas of itself.

We should also consider that the next decade is essential for the future of microrobotics. Currently, most efforts are focused on very narrow research. It is clear that realizing the vision of intelligent microrobots and expanding their scope require the close collaboration of researchers in diverse fields ranging from materials science, robotics, chemistry, and artificial intelligence. Commercialization will help to drive the research. Thus, researchers should consider problem selection, aim at tackling unmet needs, and think outside the box. It is impossible to imagine how microscopic robots will look in the next few years, but just like the development of microprocessors, miniaturization of everyday tools could have a profound impact on future technological revolutions.

Chapter 4.2 is based, in part, on the material as it appears in Chemical Reviews, 2021, by Fernando Soto, Emil Karshalev, Fangyu Zhang, Berta Esteban Fernandez de Avila, Amir Nourhani, and Joseph Wang. The dissertation author was the primary investigator and author of this paper.